TOWARDS A FUNDAMENTAL UNDERSTANDING OF ENERGY-EFFICIENT, PLASMA-BASED CO_2 CONVERSION

Omar Biondo

July 3rd 2023

Faculty of Science
Department of Chemistry

Department of Applied Physics

Towards a fundamental understanding of energy-efficient, plasma-based CO_2 conversion

PhD thesis submitted for the degree of Doctor of Science: Chemistry at the University of Antwerp and for the degree of Doctor at the Eindhoven University of Technology to be defended by Omar Biondo

Supervisors:
Professor Annemie Bogaerts (University of Antwerp)
Professor Gerard van Rooij (Eindhoven University of Technology)

Antwerp, 2023

Acknowledgements

And here I am, writing the acknowledgements section of my doctorate thesis. This journey seemed very short and very long at the same time. It has been a roller-coaster ride of experiences and profound inner transformation. I am so grateful to my supervisors, **Annemie and Gerard**, for believing in me and having given me the opportunity to challenge myself with an international and interdisciplinary doctorate. Your passion and mentoring have inspired, and still do, my way of approaching every difficulty and new research insight, calming down my impulsiveness but without compromising on enthusiasm. Probably, the greatest achievement of this doctorate is that I am still very enthusiastic about doing research, despite all the difficulties we encountered during the last 3.5 years. And this, I owe it especially to your solid example of passion and drive. I have learned so much from you and I still have a lot more to learn, so I hope we will keep working together during the coming years.

Of course, I would have not gotten this far if I had not met **Cristina, Ester and Francesco** during my master thesis. You made me discover and nurture the passion for doing research. The two years I shared with you in Padova have been life-changing and unforgettable. I want to thank also **Alessio, Ana, Andrea Rossa, Giulia, Goran, Mubbshir** and many others for the fun and inspiring time we shared. I cannot express how much I miss those moments.

The covid pandemic greatly affected my interactions with the rest of the group, and when we were allowed to come back to our offices, I moved to Eindhoven for my secondment. Nevertheless, I had the great pleasure to meet so many fantastic people and friends. Everything started when I met **Amin, Claudia, Hamid, Fanny, Kevin, James, Maryam and Sean**. Thanks to you guys, I felt welcomed since the very first day of work and enjoyed many moments before the pandemic started. Luckily, some of you were still there when I came back to my office on November 2021, while others have unfortunately left. Since then, the group have expanded and evolved quite a lot, until someone ended up eating in the corridor because our tiny coffee room was fully packed. I want to thank **Bart, Björn, Callie, Claudia, Colin, Ed, Eline, Elise, Elizabeth, Greg, Hamid, Ivan, Joachim, Joran, Josh, Yury, Mahdi, Matthew, Pepijn, Rani, Robin, Roel, Sara, Shangkun, Stein, Stijn and, of course, Annemie** for turning our crumbling, grey building into a thriving, flowery meadow, where you guys are the flowers. I want to thank also **Diana, Iza, Jeroen, Radu, Sander, Valeria and Wouter** for sharing with me many coffee breaks and fun moments, in and out the university. It is certainly not the quality of your coffee, which is quite questionable, that brings me to walk through the door of your offices, but rather the light that you spread, even during the saddest winter days.

Speaking of coffee, DIFFER has definitely the best coffee I have ever tried in the north of the Alps, along with advanced and intriguing lab facilities. There I must also thank many people, especially **Alex, Ashley, Cas, Margherita and Qin**. Without you, I would have been able to overcome the frustration deriving from experiments not working, promised devices not delivered and living with 10+ (I have never been actually able to count all of them) fist-year bachelor students. But, most important, I would have not enjoyed any exciting discussion in front of a proper-sized, black coffee. Also, thanks to **Aron, Martijn, Michel, Vu**, and their group leader **Stefan** for the essential technical support during the setting up of the experiments and for the troubleshooting. Last but not the least, thanks a lot **Cas** for the experiments at IntSF, and **Richard** for the kind permission of using your setup and the discussion of the results.

During my PhD I have been lucky enough to pay a research visit at IST Lisbon and get to know another thriving and beautiful group of researchers and people. I want to thank **Chloé, Daan, Duarte, Lex, Maik, Pedro, Tiago Dias, Tiago Silva and Vasco** for the inspiring discussions and enjoyable moments, making me feel like at home. Six weeks have flown by really too fast, and I regret that I was not able to fully benefit from your great expertise. Despite the short time, Portugal will always have a place in my heart.

Lisbon has also been one of the several occasions where I could join the PIONEER family. We indeed had many occasions to see each other, especially online, thanks to the much-hated and much-mentioned covid pandemic, which made our mobility plans less international than they should have been. However, every moment with you guys has been remarkable, and I wish I could have more. I want to thank **Ashley, Beatrice, Carolina, Domenico, Chloé, Golshid, Harry, Jairo, Yuxiang, Maik, Marzia, Minh, Toine,** and the whole PIONEER consortium for creating a wonderful environment, where science and amusement can coexist.

Besides the covid pandemic and many other difficulties that naturally come along with a PhD, a huge challenge has been moving away from my own land, family and friends. The distance is not insurmountable at all (thanks Ryanair!), but it is felt plenty. A huge thanks goes to my family, especially to **Rita, Moreno, Daniela, Renata, Manuel, Radames, Luca, Alessia, Gloria,** and my dearest friends **Lisa, Federico, Ilaria, Davide, Giorgia, Nicolò, Aurora, Stefano, Adua, Massimiliano and Carolina.** Thank you so much, from the bottom of my heart. You never miss to make me feel your true love and great support, wherever I am. I want also to thank **Manrico**, who supported me throughtout the ride with his great competence and immense kindness, allowing me to bring home the best possible results from this journey and merging professional growth with personal development and improvement.

Finally, I want to thank **Julio**, who was with me for most of the ride. You were there during all highs and (especially) lows, and you have never backed down from supporting me. Your love made the journey much easier and the fact that we found ourselves willing to continue spending time and create new projects together fills me with joy. I hope we will keep walking side by side through the next adventures, towards a bright future, possibly with a couple of dogs and cats.

Summary

Plasma-based CO_2 conversion is worldwide gaining increasing interest. The aim of this work is to find potential pathways to improve the energy efficiency of plasma-based CO_2 conversion beyond what is feasible in thermodynamic equilibrium. To do so, we use a combination of modeling and experiments to better understand the underlying mechanisms of CO_2 conversion, ranging from non-thermal to thermal equilibrium conditions.

The status of development of plasma-based CO_2 splitting and its combination with other reactions is introduced in Chapter 1. Zero-dimensional (0D) chemical kinetics modelling, describing the detailed plasma chemistry, is developed to explore the vibrational kinetics of CO_2, as the latter is known to play a crucial role in the energy-efficient CO_2 conversion. The 0D model is explained in detail in Chapter 2 and applied in Chapter 4, where it is successfully validated against pulsed CO_2 glow discharge experiments, enabling the reconstruction of the complex dynamics underlying gas heating in a pure CO_2 discharge. This paves the way towards the study of gas heating in more complex gas mixtures, such as CO_2 plasmas with high dissociation degrees. Since gas heating has a strong effect on vibrational excitation, Chapter 4 represents a substantial step forward in the definition of the experimental conditions suitable for vibrationally-enhanced CO_2 splitting in a plasma.

Energy-efficient, plasma-based CO_2 conversion can also be obtained upon the addition of a reactive carbon bed in the post-discharge region. The reaction between solid carbon and O_2 to form CO allows to both reduce the separation costs and increase the selectivity towards CO, thus, increasing the energy efficiency of the overall conversion process. In this regard, a novel 0D model to infer the mechanism underlying the performance of the carbon bed over time is developed within this thesis. The model is explained in Chapter 2, while the experimental setup is described in Chapter 3, and the results are presented in Chapter 5. The model outcome indicates that gas temperature and oxygen complexes formed at the surface of solid carbon play a fundamental and interdependent role. These findings open the way towards further optimization of the coupling between plasma and carbon bed.

Experimentally, it has been demonstrated that warm plasmas (e.g. microwave or gliding arc plasmas) can yield very high energy efficiency for CO_2 conversion, but typically only at reduced pressure. For industrial application, it will be important to realize such good energy

efficiency at atmospheric pressure as well. However, recent experiments illustrate that microwave plasmas at atmospheric pressure are too close to thermal conditions to achieve a high energy efficiency.

Hence, a comprehensive set of advanced diagnostics is used in this thesis to characterize the plasma and the reactor performance, focusing on CO_2 and CO_2/CH_4 microwave discharges, as described in Chapter 3. In particular, laser scattering is coupled with optical emission imaging to reconstruct the shape of the plasma and link it with the evolution of electron density and temperature, and gas temperature. The results lead to a deeper understanding of the mechanism of power concentration with increasing pressure, typical of plasmas in most gases, as presented in Chapter 6, which is of great importance for model validation and understanding of reactor performance.

In a complex chemistry such as dry reforming of methane (CO_2/CH_4), transport of reactive species is essential to define the performance of the reactor and achieve the desired outputs. On this matter, the electron and heavy-particle properties of the CO_2 and CO_2/CH_4 microwave discharge are characterized for two different flow configurations, i.e. forward vortex (FV) and reverse vortex (RV), which exhibit different core transport mechanisms, i.e. flow-independent diffusion and flow-dependent convection, respectively. In addition, the effect of the gas flow dynamics on the reactor performance is determined by gas chromatography. The results, presented in Chapter 7, show that the RV flow configuration enables control of the process selectivity towards gaseous or solid products, e.g. by inhibiting the deposition of solid carbon inside the reactor, even in pure CH_4 experiments.

This thesis adds to the state-of-the-art by providing a deeper insight in the underlying mechanisms governing plasma-based CO_2 conversion, under a wide range of experimental conditions and in combination with other thermodynamically challenging reactions. Chapter 8 details how the results of this thesis can be used to direct future research efforts to improve both conversion and energy efficiency.

Samenvatting (Dutch Summary)

Plasma-gebaseerde CO_2 conversie krijgt wereldwijd steeds meer belangstelling. Het doel van dit werk is de mogelijkheden te onderzoeken om de energie-efficiëntie van plasma-gebaseerde CO_2 conversie verder te verbeteren dan mogelijk is bij thermodynamisch evenwicht. In deze thesis gebruiken wij een combinatie van computationele modellering en experimenten om de onderliggende mechanismen van CO_2 conversie beter te begrijpen, variërend van niet-thermische tot thermische evenwichtsvoorwaarden.

De stand van de ontwikkeling van plasma-gebaseerde CO_2 conversie en zijn combinatie met andere reacties wordt geïntroduceerd in Hoofdstuk 1. Nul-dimensionale (0D) chemische kinetische modellering, met een beschrijving van de gedetailleerde plasmachemie, is ontwikkeld om de vibrationele kinetiek van CO_2 te bekijken, aangezien deze laatste een cruciale rol kan spelen in de energie-efficiëntie van CO_2 conversie. Het 0D model wordt uitgelegd in Hoofdstuk 2, en toegepast in Hoofdstuk 4, waar het met succes gevalideerd wordt aan de hand van experimenten met een gepulseerde CO_2 glimontladingsplasma. Hierdoor wordt het reconstrueren van de complexe dynamiek van gasverwarming in een zuiver CO_2 plasma mogelijk. Dit zet ook de deur open voor de studie van gasverwarming in complexere gasmengsels zoals CO_2 plasma met hoge dissociatie-graden. Vermits gasverwarming een sterk effect heeft op vibrationele excitatie, betekent Hoofdstuk 4 een substantiële stap voorwaarts voor de omschrijving van de experimentele condities geschikt voor vibrationeel-geactiveerde CO_2 conversie in een plasma.

Energie-efficiënte, plasma-gebaseerde CO_2 conversie kan ook worden verkregen na de toevoeging van een reactief koolstofbed na het plasma. De reactie tussen het koolstof en O_2 om CO te produceren maakt het mogelijk om de scheidingskosten te verminderen en de selectiviteit naar CO te doen toenemen. Daarmee is de energie-efficiëntie van de conversie verbeterd. In dit verband is een innovatief 0D model binnen deze thesis ontwikkeld om de onderliggende mechanismen van de prestaties van het koolstofbed in functie van de tijd af te leiden. Het model wordt uitgelegd in Hoofdstuk 2, terwijl de experimentele opstelling beschreven wordt in Hoofdstuk 3, en de resultaten gepresenteerd worden in Hoofdstuk 5. Het modelresultaat geeft aan dat de gastemperatuur en oppervlakte-zuurstofcomplexen aan het koolstofbed een fundamentele en onderling afhankelijke rol spelen. Deze bevindingen openen de weg naar verdere optimalisatie van de koppeling tussen het plasma en het koolstofbed.

Experimenteel is aangetoond dat warm plasma (bijv. Microgolf en/of gliding arc plasma) zeer hoge energie-efficiëntie kan opleveren voor CO_2 conversie, maar meestal alleen bij gereduceerde druk. Voor industriële toepassing het is belangrijk om goede energie-efficiëntie te verkrijgen bij atmosferische druk. Toch illustreren recente experimenten dat microgolf plasma bij atmosferische druk te dicht bij thermische omstandigheden is om een hoge energie-efficiëntie te bereiken.

Vandaar dat een uitgebreide reeks geavanceerde diagnostiek in deze thesis wordt gebruikt voor het karakteriseren van het plasma en de prestaties van de reactor, met een focus op CO_2 and CO_2/CH_4 microgolf plasma, zoals beschreven in Hoofdstuk 3. Laserlichtverstrooiing en optische emissie beeldvorming zijn gekoppeld om het plasma te reconstrueren en de vorm te linken met de evolutie van de elektronendichtheid en -temperatuur, en gastemperatuur. De uitkomsten leiden tot een dieper begrip van de mechanism van vermogensconcentratie met toenemende druk, typisch voor plasma in de meeste gassen, zoals beschreven in Hoofdstuk 6, wat van groot belang is voor modelvalidatie en begrip van de prestaties van de reactor.

In een complexe chemie als “dry reforming” van methaan (CO_2/CH_4) is transport van reactieve stoffen essentieel om de prestaties van de reactor te definiëren en de gewenste output te bereiken. In dat verband zijn de eigenschappen van de elektronen en neutrale deeltjesbundel gekarakteriseerd voor twee verschillende gasstromingsconfiguraties, d.w.z. forward vortex (FV) and reverse vortex (FV), die verschillende transportmechanismen tussen het centrum van het plasma en de periferie vertonen, d.w.z. respectievelijk stroom-afhankelijke convectie en stroom-onafhankelijke diffusie. Verder wordt het effect van de gasstromingsdynamica op de prestatie van de reactor bepaald met behulp van gaschromatografie. De resultaten, beschreven in Hoofdstuk 7, laten zien dat de RV stromingsconfiguratie controle over de selectiviteit van het process naar gasvormige of vaste producten biedt, bijv. door het remmen van de afzetting van vaste koolstof in de reactor, zelfs in experimenten met zuivere CH_4.

Deze thesis streeft ernaar om een dieper inzicht te verschaffen in de onderliggende mechanismen van plasma-gebaseerde CO_2 conversie, t.o.v. wat reeds gekend is, onder een brede waaier van experimentele omstandigheden en in combinatie met andere thermodynamisch uitdagende reacties. De resultaten van deze thesis kunnen toekomstige onderzoeksinspanningen helpen sturen op de sleutelfactoren voor energie-efficiënte conversie, zoals beschreven in Hoofdstuk 8.

Table of contents

List of abbreviations

0D	Zero-dimensional
AC	Alternating current
APGD	Atmospheric pressure glow discharge
BET	Brunauer-Emmett-Teller
CCS	Carbon capture and storage
CCU	Carbon capture and utilization
C_p	Heat capacity at constant pressure
$C_{p,\mathrm{nonreactive}}$	Non-reactive component of the heat capacity at constant pressure
$C_{p,\mathrm{reactive}}$	Reactive component of the heat capacity at constant pressure
$C_{p,\mathrm{tot}}$	Total heat capacity at constant pressure
C(s)	Active carbon site
c-s	Cross sections
C(s)-O	Oxygen atom chemisorbed at an active carbon site
DBD	Dielectric barrier discharge
DFT	Density functional theory
DIFFER	Dutch Institute for Fundamental Energy Research
DRM	Dry reforming of methane
EEDF	Electron energy distribution function
E/N	Reduced electric field
EU	European Union
e-V	Electron-impact vibrational excitation
FV	Forward vortex
FWHM	Full width at half maximum
GA	Gliding arc
GAP	Gliding arc plasmatron
GC	Gas chromatography
GHG	Greenhouse gas
ΔH°_{R}	Reaction enthalpy
k	Rate coefficient
k_B	Bolztmann constant
κ	Heat conductivity
$\kappa_{\mathrm{nonreactive}}$	Non-reactive component of the heat conductivity
$\kappa_{\mathrm{reactive}}$	Reactive component of the heat conductivity
κ_{tot}	Total heat conductivity

LIF	Laser-induced fluorescence
LoKI	LisbOn Kinetics
MPT	Microwave plasma torch
MW	Microwave
NDIR	Non-dispersive infrared
n_e	Electron density
NRP	Nanosecond repetitively pulsed
OES	Optical emission spectroscopy
P	Power
p	Pressure
QCT	*Quasi-classical* trajectory
q_te	Specific energy input in thermodynamic equilibrium
RBR	Reverse Boudouard reaction
RF	Radiofrequency
RV	Reverse vortex
SB	Sharma-Brau
SEI	Specific energy input
SEM	Scanning electron microscopy
slm	Standard liters per minute
SSH	Schwartz-Slawsky-Herzfeld
t	Time
T_1	Temperature of the symmetric stretching mode of CO_2
T_{12}	Temperature of the symmetric levels of CO_2
T_2	Temperature of the bending mode of CO_2
T_3	Temperature of the asymmetric stretching mode of CO_2
TCD	Thermal conductivity detector
T_e	Electron temperature
T_g	Gas temperature
TGA	Thermogravimetric analysis
TGA-MS	Thermogravimetric analysis coupled with mass spectrometry
t_res	Gas residence time
TRL	Technology readiness level
T_rot	Rotational temperature
TSA	Total surface area
v_1	Symmetric stretching mode of CO_2
v_2	Bending mode of CO_2
v_3	Asymmetric stretching mode of CO_2
VDF	Vibrational distribution function

V_R	Reactor volume
V-T	Vibration-translation
V-V	Vibration-vibration
V-V-T	Vibration-vibration-translation

Chapter 1 Introduction

1.1 CO_2 upcycling in response to the climate and energy crisis

Carbon dioxide emissions are considered the origin of climate change. Therefore, their reduction is highly desirable and the society is put under particular pressure to find a solution before long. Model simulations suggested that CO_2 increase in the atmosphere will have a direct impact on Northern Hemisphere summer temperature, heat stress, and tropical precipitation extremes[1]. It has been pointed out that temperature targets alone are insufficient to limit the risks associated with anthropogenic emissions[2,3]. Indeed, the existing fossil-fuel energy infrastructure will emit about 658 Gt CO_2 by 2050, if operated in a *business as usual* way, which will lead the global temperature increase to exceed the 1.5 °C target[4]. Around 54% of these emissions comes from the power sector, which puts more pressure on the need of decarbonizing the power production.

The European Union (EU) is currently facing a complex geopolitical crisis, which is threatening the energy transition strategy and its energy security[5]. High dependence on gas imports is one of the EU's biggest problems. Recent gas shortages have led to higher prices, driving up the cost of electricity on the market last fall and winter. The equivalent of 25% of current EU gas imports from Russia could be saved by 2030 through the renovation and electrification of residential buildings, according to the European Climate Foundation[6]. Under the REPowerEU plan, an additional 35 TWh could be generated through renewable energy projects within this year, reducing natural gas use by more than 6 billion cubic meters[7,8].

Under this pressure, the development of alternatives to the use of fossil carbon has become a priority in many countries. Renewable energy is expected to contribute to half of the growth in global energy supplies and become the largest source of power by 2040[9]. As a drawback, renewable energy sources have intermittent production rates and are inherently not well balanced with the fluctuations in the electricity demand, as depicted in Figure 1.1.

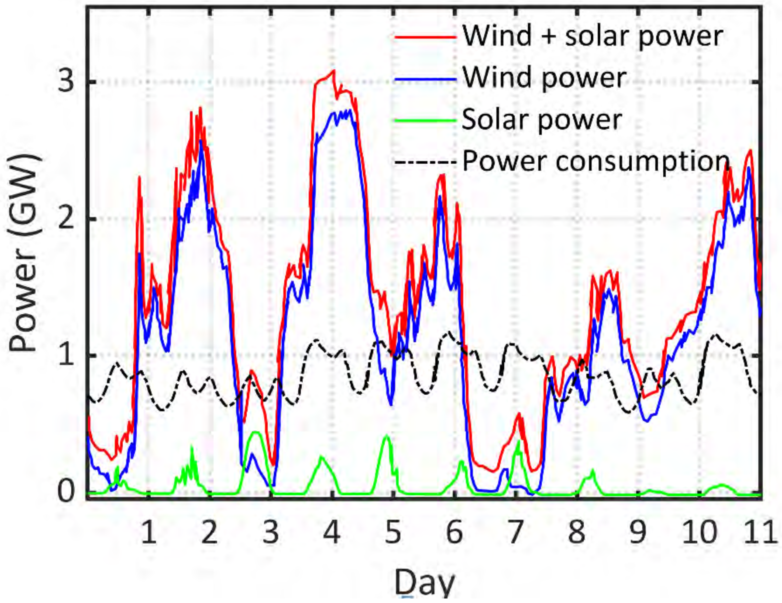

Figure 1.1. Predicted fluctuations in the production of renewable energy (from wind and solar sources) and consumption on eleven days in a row for Lower Austria. Digitalized from[10].

More specific, conventional fossil-based sources are still needed to supplement periods of shortage (e.g. reduced daylight during winter, absence of wind, drought) in electricity demand. On the other hand, when the production exceeds the demand, the generation of renewable energy cannot be fully exploited and has to be lowered, causing economical losses[11]. Therefore, the development of technologies able to simultaneously reduce CO_2 emissions and store the excess of renewable energy into chemical bonds of fuels is of vital importance.

Since 2015, with the Paris agreement, there have been multiple efforts towards the implementation of low-carbon energy production, in order to pursue the net-zero target, in at least 20 countries in the world. A net-zero emissions energy system does not add any CO_2 to the atmosphere[12]. There are different ways of approaching the issue of reducing CO_2 emissions. For instance, H_2 has the highest possible energy density and its use features CO_2-free emissions. However, hydrogen-based energy production is limited by the storage capacity of the available facilities, due to the very low volumetric density of H_2. Such a drawback can be overcome with the development of the offshore geological storage of hydrogen in sub-sea reservoirs[13]. Alternatively, CO_2 can be either captured and stored (known as CCS) or captured and utilized into valuable chemicals, useful for a wide range of industrial applications. This approach, known as *CCU - CO_2 Capture and Utilization* is very promising, as CO_2 becomes then a renewable resource of energy for various applications.

Especially, CO_2 utilization as feedstock for fuels represents a major route for decarbonisation[14].

Direct CO_2 splitting (equation (1.1)) is highly endothermic and requires a lot of energy in thermo-catalytic processes, i.e. temperatures of at least 2000 K at atmospheric pressure[15]:

$$CO_2 \rightarrow CO + 1/2\ O_2, \text{ with } \Delta H^{\circ}_{R} = 283 \text{ kJ/mol (or 2.9 eV/molecule)}. \quad (1.1)$$

The net reaction (1.1) is initiated by breaking the O=CO bond:

$$CO_2 + M \rightarrow CO + O + M, \text{ with } \Delta H^{\circ}_{R} = 534 \text{ kJ/mol (or 5.5 eV/molecule)}. \quad (1.2)$$

The CO produced can be used in e.g., the Fischer-Tropsch process to produce liquid hydrocarbons or in methanol synthesis[16]. Upcycling of CO_2 into value-added products represents a substantially untapped opportunity to tackle environmental issues and point towards energy independence of the European economy.

1.2 Plasma-based CO_2 conversion

Amongst all the technologies capable of converting CO_2 into CO, plasma technology is promising due to (i) its high process versatility, allowing performing different types of reactions in combination with CO_2 splitting (e.g. dry reforming of methane, CO_2 hydrogenation or CO_2 methanation); (ii) the intrinsic low investment and operating costs (depending on the type of plasma reactor); (iii) the rare earth metal-free operation; (iv) its scalability; and (v) being easily combined with various kinds of renewable energy[17]. Due to its unique and highly-reactive composition (high-energy free electrons, excited molecules/atoms, radicals and ions, as well as photons), plasma offers a route to convert CO_2 with high energy efficiency and operation flexibility, and at mild conditions (ambient pressure and temperature), as demonstrated in numerous studies[18]. For instance, pure CO_2 dissociation was investigated with dielectric barrier discharges (DBDs), which are one of most common types of non-thermal plasmas for CO_2 conversion[15,19,20]. Notwithstanding this, DBDs provide low energy efficiency (around 10%)[15]. Under typical conditions for DBDs, i.e. reduced electric field of 200 Td (Townsend; 1 Td = 10^{-21} V m^2)[15] and electron temperature higher than 5 eV[21], only ca. 10% of the electron energy is deposited into the CO_2 vibrational degrees of freedom, which are known to promote dissociation through the most efficient pathway[15]. Therefore, intensive research has been conducted on the applicability of so-called *warm* plasmas, which are plasmas close to thermal equilibrium, but with non-equilibrium electron kinetics. The particular operating conditions of these plasmas allow combining advantages of both thermal (high gas temperature) and non-thermal (vibrational excitation) systems[15,22]. With this aim, *warm* plasmas such as microwave (MW) plasmas[23–25], radio-frequency (RF) plasmas[26,27], (2D) gliding arc (GA) plasmas[28,29] or (3D) GA plasmas at atmospheric pressure[30–32], were investigated for more efficient CO_2 conversion, providing promising results. An overview of the experimental results that were reported in literature, up to 2017, for the various plasmas mentioned above is shown in Figure 1.2. For more detailed information, we refer to Snoeckx and Bogaerts[15].

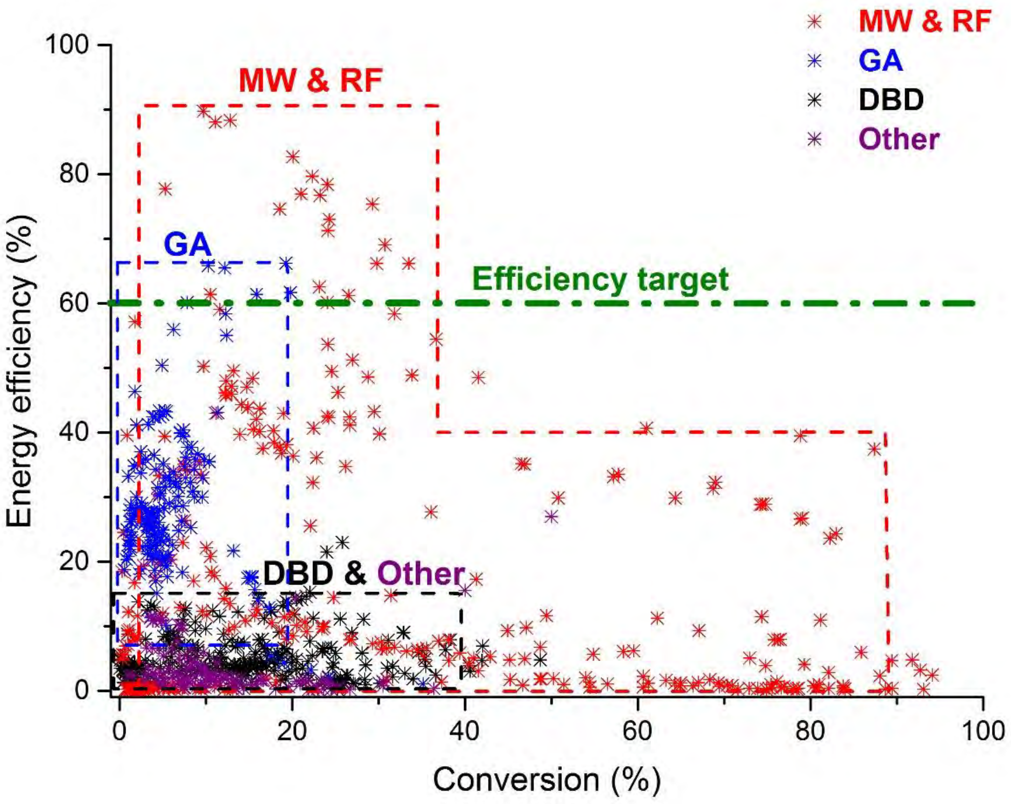

Figure 1.2. Comparison of experimental CO_2 conversion and energy efficiency of different plasma reactors, reported in literature. The 60% efficiency target is also indicated. Taken from Snoeckx and Bogaerts[15].

Figure 1.2 shows that the highest energy efficiencies were reported for MW plasmas in the 1980s. These efficiencies reach 80% for subsonic flows, and 90% with a supersonic flow[33–35]. However, so far, these reported efficiencies have not been reproduced. More recent experiments show maximum energy efficiencies around 50% for MW discharges[25,36,37]. All experiments that were reporting such high energy efficiencies were performed at reduced pressures of 100-600 mbar. These pressures are not optimal for industrial application since there would be an additional energy cost to reducing the pressure. For atmospheric pressure, Spencer *et al.*[38] obtained maximum energy efficiencies of 20%, and new experimental values were reported for MW discharges at atmospheric pressure since Figure 1.2 was published. Particularly, energy efficiencies of 28.9% with 11.8% conversion[39] and 50% with 9% conversion[40] were achieved without any catalysts.

Despite the encouraging results, plasma technology for CO_2 conversion is still at low technological readiness level (TRL 3-4; lab scale), although D-CRBN, a spin-off of the University of Antwerp, is currently bringing the technology to TRL 5-6. However, plasma is a well-established technology for lighting, surface cleaning, etching, film deposition and polymerization at industrial level[41,42]. Moreover, non-thermal plasma stands out as a promising alternative to the widely used oxidation processes for water and flue gas treatment[43] and can be a suitable tool for nanomaterial processing, analytical chemistry, sterilization, disinfection, medicine and food safety[44]. Given the wide range of applications for which the technology is well established, plasma has a great potential to support CCU strategies and help overcoming the climate and energy crisis. However, more research is needed to further improve the capabilities of plasma-based CO_2 conversion in terms of (i) energy efficiency, (ii) conversion, and (iii) product selectivity. In this regard, this thesis is aimed to take some steps forward in the understanding of the key factors, with a special care towards the underlying chemical and physical mechanisms. In the next section, the main chemical pathways for CO_2 conversion are analyzed with respect to the energy efficiency.

1.3 Strategies towards energy-efficient CO_2 plasma splitting

Depending on the experimental conditions, different pathways to dissociate CO_2 can be activated, each characterized by a specific energy threshold for dissociation. Thus, their contributions to the dissociation rate will determine the overall energy efficiency of the process. The main dissociation pathways are illustrated in Figure 1.3.

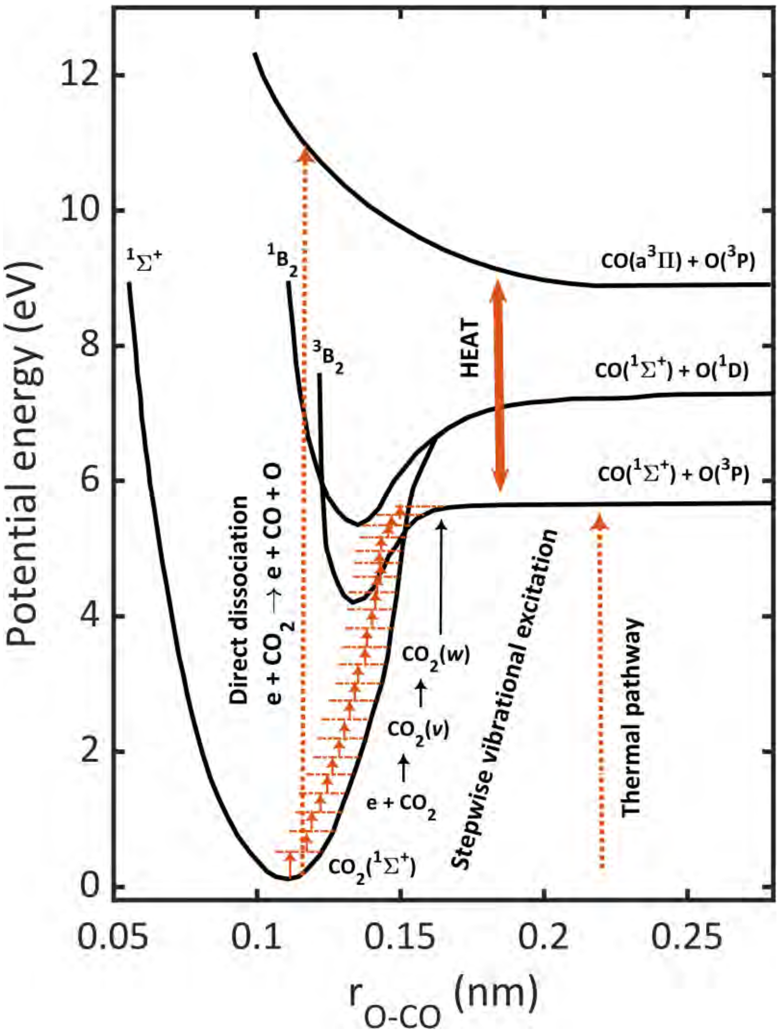

Figure 1.3. Potential energy diagram (as a function of one O–CO bond length) that illustrates the molecular physics behind three variants of CO_2 dissociation, namely the thermal pathway, the stepwise vibrational excitation and the electron-impact direct dissociation. The schematic is adapted from[17,36].

The reactions leading to CO_2 dissociation by direct electron impact require a high amount of energy, typically about 7 eV and 10 eV for the main dissociative channels, and involve a significant amount of heat to be released. The theoretical maximum energy efficiency for this dissociation pathway is ca. 17.5%[45]. Electron-impact CO_2 dissociation is typical for DBD and corona discharges, which exhibit energy efficiencies lower than 17.5% (cf. Figure 1.2), far below the target of 60%. However, it is possible to reduce the energy cost for dissociation to ca. 5.5 eV, hence improving the overall energy efficiency, by taking advantage of non-equilibrium conditions, resulting mainly from collisions of highly vibrating molecules previously excited by the electrons from the discharge[46]. Particularly, the stepwise vibrational excitation of the asymmetric stretching mode of CO_2 (v_3) up to the dissociation limit, also called *ladder-climbing* mechanism, can be the key for a highly efficient CO_2 conversion into CO[46]. The negative anharmonicity of v_3 (i.e. the level spacing decreases for higher levels)[47] promotes the overpopulation of the higher levels through vibration-vibration (V-V) collisions, eventually leading to splitting of the molecule[48,49]. If this process can be exploited, for instance in MW and GA plasmas at specific conditions (e.g., reduced pressure or power pulsing), this can explain the higher energy efficiency in these plasma types (cf. Figure 1.2). However, T_g should be maintained low in order to avoid vibration-translation (V-T) relaxation and conserve an effective *ladder-climbing*[46]. In this thesis, a self-consistent kinetic model is developed to infer the gas heating dynamics in pure CO_2, low-pressure discharges. The model is described in detail in Chapter 2 (Section 2.2) and is then validated against experimental work published for a pulsed CO_2 glow discharge[50]. Compared to the wide array of CO_2 plasma kinetic models reported in the literature, the 0D model presented in this study is for the first time validated for both the active phase of the discharge and its afterglow. The model outcome and the gained insights are reported and discussed in Chapter 4.

The thermal pathway, represented by equation 1.2 above, shares the same energy threshold as the *ladder-climbing* mechanism. However, the former requires temperatures above ca. 3000 K, meaning that a lot of energy has to be spent to heat up the gas first, thus increasing the energy cost. *Warm* plasmas, with T_g = 3000-4000 K (or more in case of discharge contraction[51]), are typically characterized by thermal equilibrium conversion[36,52–55]. Under these conditions, high conversion rates and energy efficiencies of up to 80% and 50% (close to the theoretical efficiency limit ∼52%, with no CO losses in back-reactions[15]), respectively, were achieved[25,37]. Nevertheless, the thermal pathway for CO_2 cannot explain alone the energy efficiencies higher than 80% reported for the splitting of CO_2 in the past[33–35]. Recently, van de Steeg *et al.*[56] proposed a redefinition of the thermal limit to 70% for the energy efficiency, proving that the combination of fast transport and high energy deposition in the plasma core can result in a local chemical non-equilibrium, where additional CO_2 dissociation through the O-CO_2 association might occur. However, a 70% energy efficiency is still lower than the previous experimental observations[33–35]. Motivated by these observations, this thesis focuses on the application of *warm* plasmas, with a special attention to the fundamentals underlying the reactor performance. Moreover, the thesis goes beyond the study of pure CO_2 splitting, as explained in the next sections.

1.4 Alternative routes

A limitation for energy-efficient CO_2 conversion in *warm* plasmas is the backward (recombination) reaction of CO with O atoms or O_2 molecules, forming CO_2 again. Thus, fast removal of the O atoms from the mixture is crucial to maximize the conversion and energy efficiency. This was demonstrated by modeling in a classical GA plasma[57] and by a combination of modeling and experiments in a MW discharge[56]. Experimentally, the removal of oxygen can be achieved by combining CO_2 splitting with a (gas or solid) co-reactant, which converts it into value-added compounds, quenching the back-reactions. With the aim of gathering more insights, this thesis focuses on a fundamental investigation of the combination of CO_2 *warm* plasmas with solid carbon (section 1.4.1) and CH_4 (section 1.4.2).

1.4.1 Solid carbon as co-reactant

CO_2 conversion using solid carbon (biochar) as a solid reactant, also known as CO_2 gasification of biochar, is a widely investigated process that combines CO_2 utilization and solid waste valorisation, thus expanding the horizon of CCU technologies[58,59]. In effect, this process represents a model for the study of the gasification of more complex and heterogeneous solid wastes, which requires the development of time-consuming models or machine learning methods[60]. The reaction of CO_2 with carbon is known as the reverse Boudouard reaction (RBR) (equation (1.3))[59]:

$$CO_2(g) + C(s) \leftrightarrow 2CO(g), \text{ with } \Delta H^{\circ}_R = 172 \text{ kJ/mol.} \tag{1.3}$$

The stoichiometry and reversibility of this reaction was first identified by Boudouard in 1899[61]. As indicated by the large positive enthalpy, the RBR is highly endothermic and the equilibrium lies far to the left to produce CO_2 as the dominant product[62]. However, at high temperatures (typically > 1000 K), the reaction proceeds spontaneously to produce CO[58]. Several gasification heat sources to favour the RBR rate have been studied, e.g. conventional convective heating[59], solar-driven gasification[63,64] and microwave-driven CO_2

gasification[62,65,66]. Especially MW heating[62,65,66] allowed to decrease the activation energy for CO_2 gasification by 60-70% and to reach energy efficiencies of 45% at laboratory scale[67]. Recently, a few groups investigated the RBR with solid carbon driven by different kinds of plasmas and showed very interesting results[68–72], summarized in Table 1.1.

Table 1.1. List of experimental studies on the plasma-based CO_2 gasification of chars, including the gasified char type, the plasma source, the maximum conversion (X) and the applied power.

Gasified char	Plasma source	Max. X (%)	Gasification time (s)	Power (kW)	Reference
Coke	Thermal arc	94.2[a]	-	14	Liu *et al.*[68]
Coke	Thermal arc	95[a]	-	14	Li *et al.*[69]
Coconut shell	GA Plasmatron	21.3	ca. 30	-	Huang *et al.*[70]
Carbonized biomass	GA Plasmatron	27.1	ca. 30	-	Zhang *et al.*[71]
Coconut shell	MW plasma torch	75[a]	-	1.8	Wu *et al.*[72]

[a] for CO_2/Argon mixtures.

Thermal plasmas, in combination with char gasification, stand out for the very high conversion rates, along with energy efficiencies surpassing the efficiency target of 60%[68,69]. However, as a drawback, argon had to be added to CO_2 in the feed mixture, in order to sustain the discharge and protect the cathode from carbon contamination[73]. The additional separation (for the products) and recovery (for argon) steps will need to be included, which will also increase the cost, thereby reducing the energy efficiency[74]. Considering that the fraction of argon is larger than 50% in the experiments with the highest CO_2 conversion[68,69,72], the reduction in energy efficiency can be substantial. Alternatively, *warm* plasmas such as GA Plasmatron (GAP) provide good conversion and energy efficiencies (up to 35%), without argon addition, although only for a very short time[70,71]. The mechanism underlying the transient effect of the carbon bed is not yet addressed in the literature. Therefore, a novel kinetic model for CO_2 gasification of carbon is developed within this thesis and described in Chapter 2 (Section 2.3). The kinetic model, combined with experiments, is then used in Chapter 5 to analyse the contribution of the RBR and the mechanisms underlying the deactivation of the carbon bed over time.

As mentioned earlier, O/O_2 removal from the gas mixture is essential to prevent recombination reactions, reforming CO_2. Only a few methods are described in literature, such as the use of hollow fiber membranes permeable to O/O_2, which is then removed using a sweep gas[75], the use of zeolites[76,77] and electrochemical oxygen separation[78]. A promising route, also mentioned above, is to use solid carbon after the plasma reactor, which can be oxidized by O and/or O_2 to produce CO, allowing (i) to consume the undesirable O/O_2 and (ii) to enrich the exhaust in CO, beneficial for the applications. This process is also known as O/O_2 gasification of carbon and has been investigated for decades, both experimentally and computationally[79–82]. Oxygen scavenging not only increases CO_2 conversion and energy efficiency by quenching recombination, but also reduces the energy cost that would be needed for the separation of O_2 from CO. O_2-free CO is highly desirable to be directly used in industrial applications, like the Fischer-Tropsch process as mentioned above. The effectiveness of this process in the post-discharge region of a *warm* plasma is evaluated in Chapter 5. Thus far, research focused on high-purity, carbon materials. However, the final goal is the combination of CO_2 and solid waste upcycling, with lower C content, which might lead to the formation of other undesired gaseous by-products other than O_2, limiting the purity of the output CO stream. While the investigation of the effect of low-purity, carbon materials on the product composition goes beyond the purpose of this thesis, more experimental and computational efforts will be required before the process can be proposed for industrialization.

1.4.2 Dry reforming of methane

CO_2 and CH_4 are by far the most important greenhouse gases (GHGs) and are currently responsible for ca. 82% of the radiative forcing[83]. In the context of reducing GHG emissions, plasma can be used to produce syngas (H_2 and CO) by upcycling CO_2 and CH_4 through the so-called plasma-assisted dry reforming of methane (DRM)[15,84–86]:

$$CO_2 + CH_4 \rightarrow 2CO + 2H_2, \text{ with } \Delta H^{\circ}_R = 247.3 \text{ kJ/mol} \tag{1.4}$$

This process is highly energy consuming because CO_2 is a highly oxidized, thermodynamically stable molecule, and its reaction partner, CH_4, also requires high temperatures to activate its strong chemical bonds. Hence, the process needs to be carried out at high temperatures (900-1200 K) in the presence of a catalyst, typically containing Ni, Co, precious metals or Mo_2C as the active phase[87,88]. To date, a true amalgam of environmental and economical motivations exist, such as the conversion of the greenhouse gas CO_2, the capability of using biogas as a feedstock, the search for a convenient way to liquefy CH_4 for easier transport, and the availability of cheap CH_4 through shale gas[15]. At the current status of development, plasma-based DRM has been so far only validated in lab tests and there is much work ahead to bring it up to a higher maturity level (technology readiness level, TRL = 1-4)[89]. An overview of the experimental results reported in the literature is given in Figure 1.4.

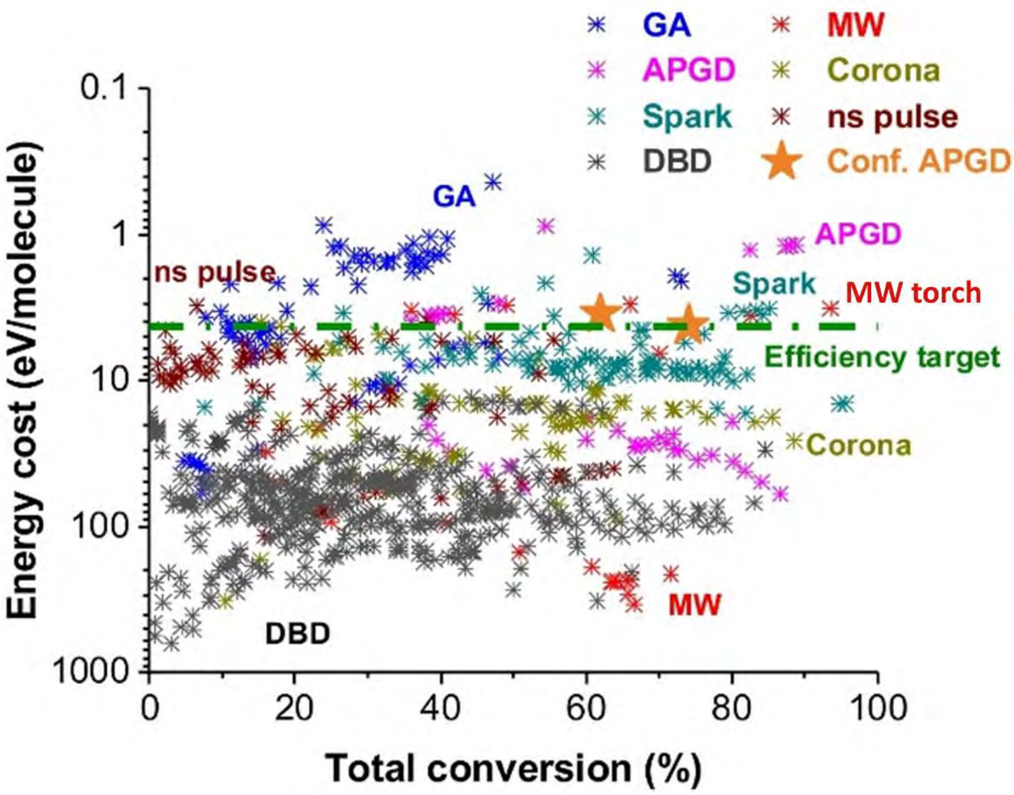

Figure 1.4. Overview of energy cost vs total conversion (i.e. the weighted average of CO_2 and CH_4 conversions), for a large number of different plasma reactors, collected from literature by Snoeckx and Bogaerts[15] and updated by Wanten et al.[86] The efficiency target is defined as the energy cost that should be reached in order to be competitive with classical DRM and other emerging technologies for producing syngas.

Figure 1.4 shows that *warm* plasmas can provide both low energy cost and high conversion rates, although little research has been thus far conducted compared to the widely studied DBDs. Amongst the *warm* plasmas that were investigated, atmospheric pressure glow discharges (APGDs)[86,90] and MW plasma torches[91,92] stand out for the most promising results, attributed to the reactor design and/or plasma characteristics[86]. Particularly, reactor design has been poorly studied in the context of plasma-based DRM, especially for *warm* plasmas. However, its essential role in determining the reactor performance was demonstrated by a combination of experiments and modeling in DBD reactors[93–95] and an arc plasma[96]. In MW discharges, the effect of the reactor design in DRM was not yet established, and the modeling of these plasmas is particularly challenging due to their high inhomogeneity. Nevertheless, a few self-consistent models were developed to study the plasma behavior in similar gas mixtures such as H_2/CH_4 MW discharges for chemical vapor deposition[97–99]. The origin of such inhomogeneity is investigated with a combination of advanced diagnostics within the framework of this thesis, and the main results are reported in Chapter 6. In particular, the outcome of this investigation will be of great help in future modeling efforts dealing with complex chemistry environments such as DRM.

Syngas production from DRM is typically accompanied by the formation of H_2O, small hydrocarbons and solid carbon, depending on the CO_2/CH_4 ratio[15,86]. Their presence can be explained by the occurrence of side reactions, which further complicate the overall picture. Particularly, in the next sections, we focus our attention on non-oxidative coupling of CH_4 to C_2 hydrocarbons and on CH_4 pyrolysis to H_2 and solid carbon, whose contribution is essential to explain the experimental results of Chapter 7.

1.4.2 (a) Non-oxidative coupling to C_2 hydrocarbons[1]

CO_2 is often investigated as an oxidant softer than O_2 for light alkane partial oxidation reactions[100,101]. Its use as an oxygen source for light alkane activation is attractive due to the high content of CO_2 in biogas[102] and due to the rise of vast new shale gas resources[103]. Non-oxidative coupling to C_2 hydrocarbons is a side reaction of DRM, in which C_2H_6 and C_2H_4 can be produced according to Equations 1.5 and 1.6:

$$2CH_4 + CO_2 \rightarrow C_2H_6 + H_2O + CO, \text{ with } \Delta H^\circ_R = 111.9 \text{ kJ/mol} \tag{1.5}$$

$$2CH_4 + 2CO_2 \rightarrow C_2H_4 + 2H_2O + 2CO, \text{ with } \Delta H^\circ_R = 287 \text{ kJ/mol.} \tag{1.6}$$

---

[1] This paragraph is included in:
Meta-analysis of CO_2 conversion, energy efficiency and other performance data of plasma-catalysis reactors with the open access PIONEER database
A. Salden, M. Budde, C. A. Garcia-Soto, O. Biondo, J. Barauna, M. Faedda, B. Musig, C. Fromentin, M. Nguyen-Quang, H. Philpott, G. Hasrack, D. Aceto, Y. Cai, F. Azzolina Jury, A. Bogaerts, P. Da Costa, R. Engeln, M. E. Gálvez, T. Gans, T. Garcia, V. Guerra, C. Henriques, M. Motak, M. V. Navarro, V. I. Parvulescu, G. van Rooij, B. Samojeden, A. Sobota, P. Tosi, X. Tu, and O. Guaitella
Submitted to Journal of Energy Chemistry on May 22, 2023

The endothermicity of these reactions implies that the use of CO_2 as an oxidant requires more energy than the non-oxidative coupling driven by O_2, which is exothermic, with reaction enthalpy of -221 kJ/mol to produce C_2H_6 and -370.5 kJ/mol to produce C_2H_4[101]. To increase conversion and decrease reaction temperature, plasma technology has been proposed for CO_2/CH_4 activation. However, the main product of CO_2/CH_4 discharges is typically syngas, as in Equation 1.4 above, which can be converted to C_2 hydrocarbons via the Fischer-Tropsch synthesis[104].

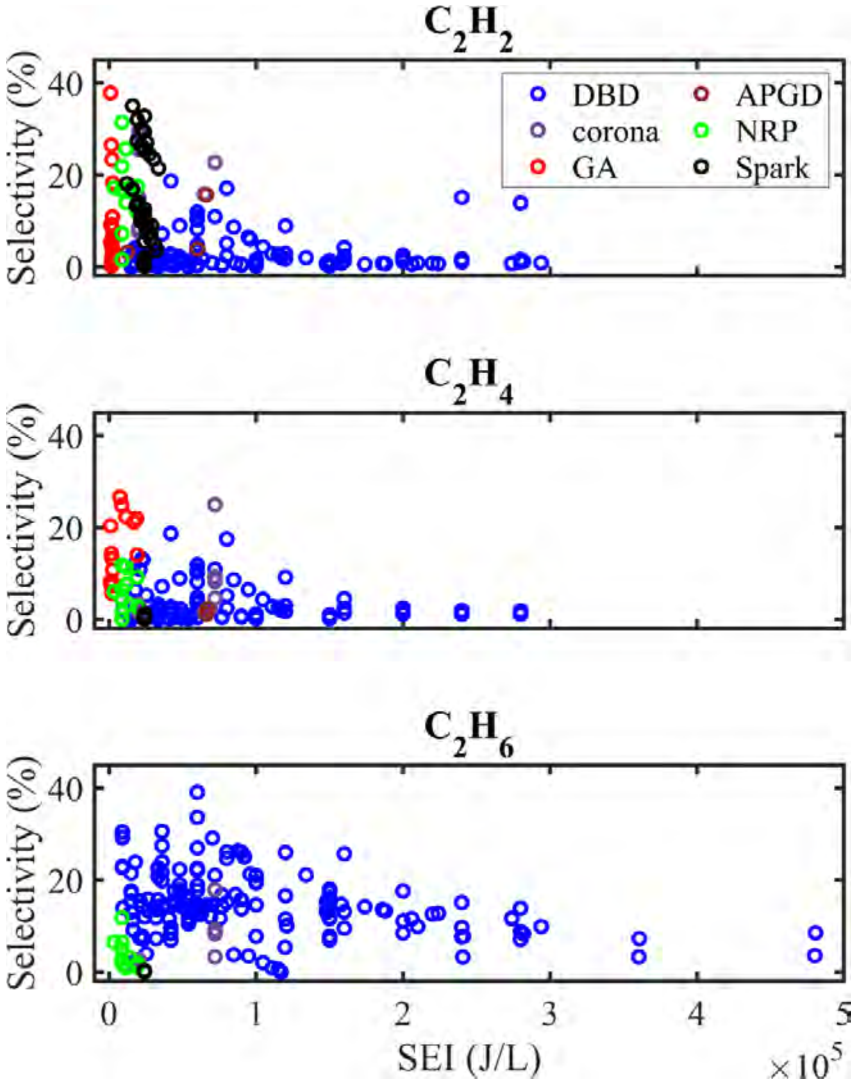

Figure 1.5. Selectivity to the main C_2 hydrocarbons as a function of the SEI for different plasma types (i.e. dielectric barrier discharges (DBD), corona, gliding arc (GA), atmospheric pressure glow discharge (APGD), nanosecond repetitively pulsed (NRP) and spark discharges), taken from the PIONEER database for CO_2/CH_4 discharges.

In this regard, the direct non-oxidative pathway tries to eliminate the second step by converting the reactants immediately into hydrocarbons[15]. The specific energy input (SEI = input power/feed flow rate) is the major determining factor for the conversion and energy cost, as well as for the selectivity towards desired products, as it combines the effects of power and residence time[15]. Moreover, the SEI is easier to calculate than the energy efficiency for DRM, as the latter requires that all the reaction products are known and that an overall stoichiometric equation for the process is written[15,105]. Therefore, we plot the selectivity towards the main C_2 hydrocarbons, for different types of plasmas collected from the literature, as a function of the SEI in Figure 1.5. In alternative, a traditional conversion vs selectivity plot might be more informative of the reactor performance for the production of light hydrocarbons. However, one must plot the selectivity as a function of either the conversion of one of the two reactants or the total conversion (see Figure 1.4 above), which has been recently accepted as a performance indicator within the plasma community and is therefore not yet widely reported in the DRM literature.

Figure 1.5 shows that for all C_2 hydrocarbons the maximum selectivity is reached at low SEI values and, beyond that, the selectivity tends to 0%. In effect, Snoeckx and Bogaerts[15] reviewed the literature available up to 2017 and found that the selectivity to C_2 hydrocarbons tends to increase with the feed flow rate and, thus, with decreasing SEI, in line with Figure 1.5. Moreover, maximum selectivities to C_2H_2 and C_2H_4 are typically achieved by *warm* discharges (i.e. GA and spark discharges in Figure 1.5), whereas C_2H_6 is significantly produced only by non-thermal discharges (i.e. DBD and corona discharge in Figure 1.5). The SEI is generally much larger in DBD than in *warm* plasmas; therefore, the inclination of the former towards higher C_2H_6 selectivity seems counterintuitive. In *warm* plasmas, higher SEI generally promotes the pyrolysis to solid carbon and H_2 (Eq. 1.7 below) due to higher gas temperature and/or residence time[55,106]. However, DBDs typically feature a filamentary behavior, meaning that the actual gas residence time in the microdischarges is much lower than the overall gas residence time in the DBD reactor, and that only a fraction of the gas flow actually gets in contact with the discharge. Hence, the filamentary regime enables both low gas temperature and high SEI, resulting in more electron impact dissociation and three-body recombination processes, thus driving the selectivity towards C_2H_6 and higher hydrocarbons[107]. However, C_2H_4 is more valuable than C_2H_6 for the chemical industry, and Figure 1.5 shows that *warm* plasmas may provide good selectivity at low SEI (and thus low energy cost), although little research has been carried out so far. With the aim to further corroborate the suitability of *warm* discharges for CH_4 coupling to C_2 hydrocarbons (especially C_2H_4), we test the MW reactor available at DIFFER and report the results, compared against the literature, in Chapter 7.

1.4.2 (b) Solid carbon deposition

Operations in CO_2/CH_4 activated mixtures are susceptible to solid carbon deposition and its detrimental effect on the discharge and catalyst stability. A lot of research is still ongoing towards modified catalysts to circumvent deactivation due to solid carbon deposition, which was originally also a big problem for the currently widely adopted steam reforming of methane[15]. Solid carbon can of course be formed by a variety of reactions. Apart from the forward Boudouard reaction (CO disproportionation; see equation 1.3 above), another thermodynamically favored reaction that results in solid carbon buildup is CH_4 pyrolysis[108,109]:

$$CH_4(g) \rightarrow C(s) + 2H_2(g), \text{ with } \Delta H^{\circ}_R = 74.9 \text{ kJ/mol.} \quad (1.7)$$

At high temperatures and elevated pressure, non-catalytic reactions in the gas phase play an essential role in the formation of higher hydrocarbons. CH_4 can be converted directly to hydrocarbons by thermally induced coupling reactions at high temperatures[110,111]. The stepwise dehydrogenation of CH_4 can be explained by free-radical mechanisms[111]. Modeling of the homogeneous gas-phase reactions between CH_4 and O_2 achieved satisfactory agreement with the experimental data on the products C_2H_6 and C_2H_4 above 1000 K[112,113]. From these and other literature results, it can be concluded that hydrocarbon molecules may undergo either pure or oxygen-supported pyrolysis with the formation of small hydrocarbon radicals[108]. The principal reaction pathway of the carbon deposition generally follows the Kassel mechanism[109,114]:

$$2CH_4(g) \rightarrow C_2H_6(g) + H_2(g), \text{ with } \Delta H^{\circ}_R = 67.5 \text{ kJ/mol} \quad (1.8)$$

$$C_2H_6(g) \rightarrow C_2H_4(g) + H_2(g), \text{ with } \Delta H^{\circ}_R = 135 \text{ kJ/mol} \quad (1.9)$$

$$C_2H_4(g) \rightarrow C_2H_2(g) + H_2(g), \text{ with } \Delta H^{\circ}_R = 173.7 \text{ kJ/mol} \quad (1.10)$$

$$C_2H_2(g) \rightarrow 2C(s)+ H_2(g), \text{ with } \Delta H^{\circ}_R = -228.8 \text{ kJ/mol} \quad (1.11)$$

Primary C_2H_6 is produced through CH_4 dehydrogenation to CH_3 radicals and subsequent CH_3 recombination; then, a cascade of dehydrogenation reactions to ethylene, acetylene and eventually to solid carbon takes place. However, the rate of formation of C_2H_4 (characteristic time of 10^{-6}-10^{-5} s) and C_2H_2 (10^{-4}-10^{-3} s) is much faster than the complete decomposition to H_2 and solid carbon (> 10^{-3} s)[109,115], thus control over the gas residence time in the hot plasma zone may be beneficial to control the deposition process. In order to verify this, we test for the first time the effect of the gas flow configuration in the performance of a MW discharge for DRM. The results are presented and discussed in Chapter 7, demonstrating the critical role played by the flow geometry in controlling carbon deposition.

1.5 Aim of the thesis

The previous sections illustrate that, while significant progress has been made in the understanding of the critical parameters for energy-efficient CO_2 conversion, some research gaps remain. Particularly, the attainability of efficient non-thermal vs thermal conversion is still a focal point of discussion within the plasma community (Section 1.3) and therefore is a key topic of study in this work. The current state-of-the-art of plasma-based CO_2 conversion indicates that there are still unexplored avenues for process optimization (Section 1.4). On this matter, the literature lacks a fundamental understanding and this thesis aims to provide an essential step forward towards a deeper grasp of the underlying mechanisms. Hence, the aim of this thesis can be summarized in the all-encompassing goal:

From fundamental understanding towards efficient, plasma-based CO_2 conversion.

In Chapter 2 and 3, the theoretical background and the experimental aspects are discussed, respectively. Chapter 2 includes a detailed description of the construction of chemical kinetic models used in the framework of this thesis. Subsequently, in Chapter 3, the advanced diagnostics employed for the characterization of the plasma and the reactor performance is briefly introduced.

From Chapter 4 on, this thesis adds to the state-of-the-art by answering several research questions:

- *What is the potential significance of vibrational excitation for CO_2 dissociation?*

The feasibility of the so-called *ladder-climbing* up to the dissociation limit of CO_2 has thus far not been established due to the lack of a reliable benchmark for validation. In Chapter 4, the 0D kinetic model described in Chapter 2 is applied to reproduce the vibrational and gas temperature evolution, measured in conditions that are theoretically suitable to sustain a strong vibrational excitation. The verification of the new kinetic scheme allow studying the CO_2 vibrational and electronic kinetics and their role into the gas heating dynamics. Since the storage of energy in the vibrational energy distribution function is highly temperature-dependent, this study will enable to indirectly unveil the potential for vibrationally enhanced dissociation, without a full description of the *ladder-climbing*. The results of Chapter 4 will have an impact on steering future research addressing vibrational excitation as a way to improve the energy efficiency of the process.

- *Why is the beneficial effect of the carbon bed transient?*

CO_2 conversion and energy efficiency, along with O_2-free CO production, can be achieved with a post-plasma carbon bed, as previously demonstrated in literature[68–72]. However, gasification reactions consume the solid reactant, which needs to be replaced with fresh pellets. Therefore, an innovative silo system, described in Chapter 3, has been developed in our research group, but it is not yet providing a performance improvement stable over time, and the beneficial effect of the system is found to be transient, as explained in Chapter 5. This unexpected behavior calls for more insight to identify the relevant underlying mechanisms, in order to exploit the full potential. In this thesis, a novel 0D kinetic model, described in Chapter 2, is developed to explain the experimental trends in Chapter 5. The results will provide detailed insights into the underlying chemistry needed to understand and overcome the deactivation of the carbon bed over time.

- *What is the effect of CH_4 concentration on the CH_4-CO_2 discharge parameters?*

In CO_2 *warm* plasmas, the trajectory of O atoms determines to which extent recombination reactions (which form CO_2 again) can be prevented. The onset of plasma contraction, which has been thoroughly studied in the last decades, establishes strong temperature gradients within the discharge zone, triggering fast core-periphery transport. We define this phenomenon as power concentration, because it is more than just discharge contraction, but it also involves changes in heavy-particle properties within the reaction zone and, therefore, it affects the productivity of the reactor. In this perspective, understanding the contraction dynamics becomes of great importance, especially in complex gas mixtures (e.g., DRM) where control over the selectivity towards desired products is essential. Thus, in Chapter 6, the evolution of the discharge volume with pressure in DRM is characterized for the first time. The results will have important implications for the development of self-consistent fluid models, essential for understanding the complex nature of MW plasmas.

- *Can we avoid solid carbon deposition in low-ratio CO_2/CH_4 MW discharges?*

Energy efficiency is defined by the chemical bonds where the input energy is stored. Therefore, being able to steer the selectivity towards the desired products means having control on the energy efficiency of the process. Plasma-based DRM, and also the classical process, are both generally characterized by high carbon deposition at low CO_2/CH_4 ratios, hampering stable operations and reducing the selectivity towards gaseous products. From the analysis of the literature emerges that the gas flow dynamics may be at play in controlling solid carbon deposition. However, this has never been addressed so far and becomes one of the key aspects of novelty of this thesis. The characterization of the performance and the fundamental properties of a MW in reverse vortex flow configuration will establish the framework for understanding gas-phase solid carbon formation and subsequent deposition. The results will provide an alternative solution to the problem, with implications extending to the valorization of CH_4 in e.g., non-oxidative coupling to higher hydrocarbons.

Chapter 2 Kinetic modelling

2.1 The CO_2 vibrational levels

The CO_2 molecule has 3N - 5 = 4 vibrational normal modes: the v_1 symmetric stretching, the doubly degenerate v_2 bending, and the v_3 asymmetric stretching mode, as illustrated in Figure 2.1**.**

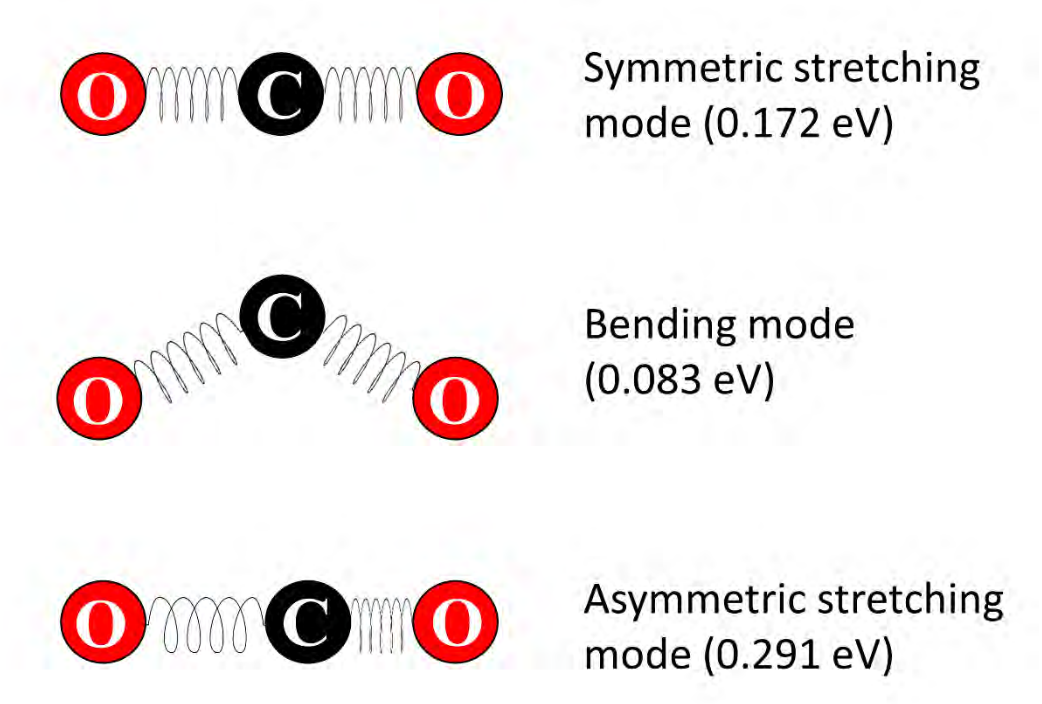

Figure 2.1. Vibrational modes of CO_2 molecules: symmetric stretching mode v_1, double degenerated bending mode v_2 and asymmetric stretching mode v_3.

The vibrational energy of a CO_2 vibrational level can be estimated through the anharmonic oscillator approximation[116], described by the following equation[117]:

$$\frac{E(v_1,v_2,l_2,v_3)}{hc} = \sum_{k=1}^{3} \omega_k \left(v_k + \frac{d_k}{2}\right) + \sum_{k=1}^{3} \sum_{j\geq k}^{3} \chi_{kj} \left(v_k + \frac{d_k}{2}\right)\left(v_j + \frac{d_j}{2}\right) + \sum_{k=1}^{3} \sum_{j\geq k}^{3} \sum_{w\geq j}^{3} y_{kjw} \left(v_k + \frac{d_k}{2}\right)\left(v_j + \frac{d_j}{2}\right)\left(v_w + \frac{d_w}{2}\right) + g_{22} l_2^2, \quad (2.1)$$

where c is the speed of light, h is the Planck constant, ω_k, χ_{kj}, γ_{kjw}, g_{22} are fitted anharmonic constants (taken from[118] and reported in Table 2.1), d_k defines the degeneration of the vibrational mode ($d_1 = d_3 = 1$ and $d_2 = 2$) and v_k (with k = 1-3) represent the quantum numbers for v_2 and v_3, respectively.

Table 2.1. Spectroscopic constants for the calculation of energy levels using expression (2.1), obtained from Chedin[118].

Constant	Value (cm^{-1})
ω_1	1335.87915
ω_2	667.20435
ω_3	2361.64697
χ_{11}	-2.99262
χ_{12}	-5.27638
χ_{13}	-19.14044
χ_{ll}	-1.01428
χ_{22}	1.58003
χ_{23}	-12.54184
χ_{33}	-12.50330
γ_{111}	0.02422
γ_{112}	0.00816
γ_{113}	-0.07736
γ_{1ll}	0.06316
γ_{122}	-0.05166
γ_{123}	0.09561
γ_{133}	0.06142
γ_{2ll}	0.00702
γ_{222}	-0.00471
γ_{3ll}	0.02587
γ_{223}	-0.02052
γ_{233}	0.01834
γ_{333}	0.00631

.

Note that expression (2.1) is modified, compared to[117], to include a number of additional spectroscopic constants (namely γ_{kjw}) introduced by Chedin[118]. The author calculated also ω_k, χ_{kj} and g_{22}, which differ somehow from the constants provided by Suzuki[117] and previously used for the calculation of the vibrational energy[48,119]. In the early 90's, Császár[120] and Martin *et al.*[121] found the spectroscopic constants obtained by algebraic contact transformation from Chedin[118] to be the most reliable to compute the quartic force field of CO_2. In addition, they provide a better agreement with the available spectroscopic constants reported by Courtoy[122], and, therefore, we chose them for the calculation of the vibrational energies in this study.

The quantum number l_2 in expression (2.1) characterizes the angular momentum projection of bending vibrations onto the molecular axis. This number can take the following values:

$$l_2 = v_2, v_2 - 2, v_2 - 4, \ldots, 1 \text{ or } 0, \tag{2.2}$$

depending if v_2 is odd or even[123]. Finally, with these four quantum numbers, one can specify any CO_2 vibrational level via the notation $CO_2(v_1 v_2^{l_2} v_3)$, also known as Herzberg's notation.

In the present work, we took into account the so-called accidental Fermi resonance[123–126] among CO_2 vibrational levels with nearly the same vibrational energy. More specific, the interaction between $(v_1, v_2^{l_2}, v_3)$ and $((v_1 - 1),(v_2 + 2)^{l_2},v_3)$ leads to a perturbation. These levels, in fact, "repel" each other, meaning that one of them is shifted up and the other down, thus the actual levels are not accurately described by the expression (2.1). It is important to note that in a symmetric molecule, such as CO_2, the Fermi resonance can happen only between levels with the same quantum number l_2, which arises from the symmetry type of the eigenfunctions describing these vibrational levels[117,123,127]. More on the calculation of the energy correction of perturbed levels can be found in the study of Amat and Pimbert[128] and van den Bekerom *et al.*[47]. In this study, the CO_2 vibrational levels under Fermi resonance are considered as one single effective level, following the same approach as in[124,129]. The energy of this effective vibrational level is determined through the average of the energies of all the individual vibrational levels in the effective level, calculated using the anharmonic oscillator approximation (2.1), while its statistical weight is determined through the sum of the statistical weights of the individual states. These effective levels are denoted in this work by $CO_2(v_1, v_2^{l_2}, v_3, f)$, where the v_1, v_2 and v_3 quantum numbers correspond to the level with the highest v_1; the ranking number f is always equal to $v_1 + 1$ and indicates how many individual levels are accounted for in the effective level. For instance, the level $CO_2(20^003)$ stands for the coupling of the three individual levels $CO_2(20^00)$, $CO_2(12^00)$ and $CO_2(04^00)$. The statistical weight g_v of a coupled level $CO_2(v_1, v_2^{l_2}, v_3, f)$ is determined by the sum of the statistical weights of the various individual levels and only depends on the l_2 quantum number, being 1 for $l_2 = 0$, and 2 (corresponding to two possible directions of rotation) otherwise. For example, the statistical weight of the $CO_2(20^003)$ level is 3, i.e. $g_v = 1 + 1 + 1$. In the purpose of keeping consistency in the notations, the levels that are not coupled by Fermi resonance are still represented by $CO_2(v_1, v_2^{l_2}, v_3, f)$, using $f = 1$.

As a follow-up of previous modelling efforts, this study includes the 72 vibrational levels introduced by[119,130] and extends the description of the symmetric (v_{12}, i.e. symmetric stretching and bending modes) levels of CO_2, resulting in a total of 101 vibrational levels, which are listed in Table A1 in Appendix A. In particular, the model comprises a full description of the symmetric levels up to 0.5 eV and all the possible combinations with the first five asymmetric levels. Indeed, we do not include all asymmetric mode vibrational levels, as we do not focus on the ladder climbing up to the dissociation limit. In addition, four extra symmetric levels are added to extend the description up to 0.6 eV. Such an extension is intended to fully identify the role of v_{12} on the excitation of v_3 and on the heating dynamics, as explained later in the results section.

2.2 Description of the CO_2 kinetic model[2]

The kinetic model developed within this thesis is the result of a collaboration between the research groups N-PRiME (IST Lisbon) and PLASMANT (Antwerp). The aim of such collaboration is the establishment of a common procedure to construct a detailed chemistry set for CO_2 low-pressure pulsed direct current discharges and infer the main pathways characterizing the heating dynamics in this type of discharges. The verification of the model was first tested and carried out using the LoKI (LisbOn Kinetics) simulation tool[131,132]. In this step, we systematically added the vibrational states of CO_2 and the corresponding reactions. Concurrently, we performed simple calculations of the vibrational distribution function (VDF) to verify the correctness of the implementation. The same procedure was then repeated with the ZDPlasKin code[133], validating the procedure. After the inspection on the vibrational chemistry of CO_2, the model was implemented in the

---

[2] This model was used in the following paper:
Insights into the limitations to vibrational excitation of CO_2: validation of a kinetic model with pulsed glow discharge experiments
O.Biondo, C. Fromentin, T. Silva, V. Guerra, G. van Rooij, A. Bogaerts
Plasma Sources Sci. Technol., 31, 074003 (2022)
https://doi.org/10.1088/1361-6595/ac8019

ZDPlasKin code that was used to obtain the results shown here. A description of the 0D kinetic model, solved with ZDPlasKin, is offered in section 2.2.1. The main steps towards the construction of a detailed chemistry set are (i) the construction of a complete and consistent set of cross sections (c-s) describing the relevant interactions between electrons and heavy gas species (see section 2.2.2); and (ii) the implementation of scaling laws to calculate the rate coefficients for vibration-vibration (V-V) and vibration-translation (V-T) exchanges (see section 2.2.3), for which the experimental values are unknown. Moreover, section 2.2.4 is dedicated to the inclusion of the relaxation of electronic states in the model. The complete set of reactions solved by the model can be found in Table A2 in Appendix A. The input parameters to the simulations are the discharge pressure, the pulse length, the tube radius and length from experiments[50]. For the simulations presented in section 4.2.1, the experimental gas temperature (T_g) profile is used, along with the time-dependent electron density profile estimated from the measured temporal variations of the discharge current and a reduced electric field (E/N = electric field/gas number density) of 55 Td (Townsend; 1 Td = 10^{-21} V m^2), as described by[130]. The simulations with self-consistent calculation of T_g are described in section 2.2.5 and the outcome is presented and discussed in section 4.2.2. In addition, we tested the model for E/N = 90 Td, as suggested by our calculations presented in section 2.2.6.

2.2.1 Zero-dimensional simulations

The present modelling study has been performed using the ZDPlasKin[133] simulation tool, which provides a self-consistent description of both electron and heavy species kinetics in the plasma. The 0D simulations were run with a pressure fixed at 6.7 mbar and an initial flow rate of 166 sccm of CO_2 at 300 K, in order to reproduce the experimental conditions for the *single-pulse* measurements presented by Klarenaar *et al.*[50]. Both pressure and mass flow rate are kept constant throughout the simulation. Thus, the density of each gas-phase species is multiplied by $p(t = 0)/p(t)$, where p is the pressure in the reactor. Also the velocity u is updated as $u = \dot{m}(t = 0)/(\rho(t) \times A)$, where $\dot{m}$ is the mass flow rate, ρ is the gas density and A is the cross-sectional area of the simulated volume. This is done at every time-step during the simulation. Such modifications are necessary to account for the gas expansion due to increasing temperature and molar flow rate upon dissociation of CO_2 into CO and ½ O_2 in the plasma. Both effects are incorporated in the variable $\beta(t)$, the gas expansion factor, which is defined by

$$\beta(t) = \frac{M(t = 0)T_g(t = 0)}{M(t)T_g(t)} \qquad (2.3)$$

with M being the total number of particles. $\beta(t)$ is initially equal to 1 and decreases when the gas expands and it is included in the calculation of the conversion and product yields. After specifying the initial parameters, the Boltzmann solver BOLSIG+[134], which is included in the ZDPlasKin tool, is used to calculate the electron energy distribution function (EEDF) using estimated values for E/N and the electron density (n_e) while simulating the active part of the discharge. E/N can be either estimated directly from the experiments or self-consistently calculated from the estimated values of power density (see section 3.6) using Joule's law: $P_{dep} = \sigma E^2 = \sigma N^2(E/N)^2$, with σ being the conductivity, which is given by $\sigma = en_e\mu_e$. The electron mobility μ_e is obtained from the Boltzmann solver, and e is the elementary charge. In the afterglow, E/N and n_e are set to zero, because the power deposition is equal to zero and electron impact processes are expected to have a negligible contribution. For the calculation of the EEDF, it is necessary to specify the scattering cross sections (c-s) for electrons colliding with the heavy species in the plasma, along with the initial gas composition and pressure. Once the EEDF is computed, the macroscopic electron properties such as electron temperature (T_e) or rate coefficients for the electron-impact reactions are obtained and provided to the chemistry module of the ZDPlasKin tool. At this point, the 0D model solves the temporal evolution of the different species densities according to the following equation,

$$\frac{dn_s}{dt} = \sum_j R_j\left[a_{sj}^R - a_{sj}^L\right] = \sum_j \left(k_j \prod_l n_l\right)\left[a_{sj}^R - a_{sj}^L\right] \qquad (2.4)$$

in which n_s refers to the density of the species s, index j refers to reaction j and index l refers to the different reactants of reaction j. a_{sj}^R and a_{sj}^L are the right- and left-hand side stoichiometric coefficients of species s, respectively, taking part in reaction j, k_j is the reaction rate coefficient, and $R_j = k_j \prod_l n_l$, is the reaction rate, with $\prod_l n_l$ being the product of densities n_l of species present on the left side of reaction j. BOLSIG+ and the chemistry module are iteratively called to calculate the electron-impact rate coefficients and species densities, respectively, and to update the EEDF and the gas composition in a consistent way. For the chemistry module of the simulation, it is necessary to give as input a chemistry set with the reactions that need to be tested. The systematic addition of the relevant reactions and rate coefficients is detailed in the following sections.

The model described here features the self-consistent calculation of T_3 and T_{12}, which are calculated based on the population of $CO_2(00^011)$ and $CO_2(10^002)$, respectively. Thanks to the close energies of levels in Fermi resonance with non-Fermi bending levels, and to the similarity of the rate coefficients involving these states, it has been shown that T_{12} is a good descriptor of the excitation of both v_1 and v_2[50]. In both cases, the vibrational temperature is obtained from

$$T_v = \frac{-E_1}{k_B \times \ln(n_1/n_0)}, \tag{2.5}$$

where E_1 is the energy of the first v_3 level for T_3 or of the first v_{12} level for T_{12}, with n_1 being the corresponding density, n_0 being the ground-state density of CO_2 and k_B the Boltzmann constant in J K^{-1}. Moreover, the self-consistent calculation of T_g is also implemented and applied to validate the heating mechanism proposed. More details on this calculation are given in section 2.2.5.

2.2.2 Electron kinetics

The first step to develop a kinetic model for a gaseous discharge is the selection of a complete and consistent set of c-s to describe the electron kinetics. The electrons gain energy from the electric field and subsequently redistribute it among different energy channels. Firstly, the EEDF is calculated by solving the steady-state, homogeneous electron Boltzmann equation in the two-term expansion approximation[135]. The electron Boltzmann equation is solved taking into account elastic and inelastic collisions between electrons and $CO_2(X_1\Sigma^+)$ molecules, including vibrational excitation energy losses (corresponding either to the excitation of individual levels or of groups of vibrational levels), superelastic collisions with CO_2 vibrationally excited states, excitation of two groups of electronic states, and ionization. Moreover, complete sets of c-s are incorporated for the dissociation products, namely CO, O and O_2, despite the splitting of CO_2 is very limited under the conditions of study here. The choice of the electron impact c-s set was made upon comparison against the swarm parameters, more specifically the reduced electron mobility and the reduced Townsend effective ionization coefficient. In this context, the electron impact c-s set in[135] provides a very good agreement with the experimental swarm parameters. The inclusion of higher vibrational levels leads to a deviation of the calculated reduced electron mobility in the range of E/N = 20-100 Td, which is relevant to this study and thus poses a threat to the correctness of the simulations. Hence, only the collisional processes contained in the electron impact c-s set of [135] have been used for the numerical solution of the electron Boltzmann equation and the calculation of the EEDF. The set of c-s is available at the IST-Lisbon database published at LXCat and are described in detail in[135]. Once the EEDF is known, the rate coefficients for each electron-impact excitation process from a state *i* to a state *j* are given by

$$C_{ij} = \sqrt{2/m_e} \int_0^{\infty} u\sigma_{ij}\,(u) f(u) du, \tag{2.6}$$

where m_e is the electron mass, *u* is the electron energy, σ_{ij} is the electron c-s and *f*(*u*) is the EEDF.

In the context of electron-impact vibrational excitation (e-V), the transitions from the ground state to the higher vibrationally excited levels that are not included in any of the c-s from the data set[130,135], i.e. j = 2, 3, 4, 5 and i = 0 in v_3, are calculated using the Fridman approximation[46]. The calculation is based on the following semi-empirical formula:

$$C_{ij} = \exp[-\alpha(j - i - 1)/1 + \beta i] C_{01}. \tag{2.7}$$

This expression allows the scaling of the rate coefficients C_{ij} for any transition between vibrational levels *i* and *j*, provided that the rate coefficient C_{01} is known. The magnitude of the rate coefficient is altered depending on the parameters α and β, specific of each plasma species. In the case of CO_2, $\alpha = 0.5$ for v_3 and the value of β is unknown[46]. Therefore, for the rate coefficients for the stepwise excitation of levels *j* from $i > 0$, we have chosen to set $\beta = 0$ for simplicity (i.e. the magnitude of C_{01} will be equal to C_{12}). The rate constants C_{ji} for superelastic collisions are obtained from the principle of detailed balance[136]

$$C_{ji} = \exp(- E_{ij}/T_e)(g_i/g_j) C_{ij}, \tag{2.8}$$

where $E_{ij} = E_j - E_i$ are the threshold energies for the corresponding excitations, and g_i and g_j are the statistical weights of level *i* and *j*. The shift in threshold due to the anharmonicity of the oscillator is taken into account in the detailed balance, where the real energy threshold of the transition is considered.

In order to verify the correctness of the approach, we added the c-s systematically to the data set, along with the calculation of the corresponding electron-impact vibrational excitation (e-V) rate coefficients, and tested the kinetic model with a Maxwellian EEDF, ensuring that all the vibrational levels included in the model follow a Boltzmann distribution with T_e. The list of the e-V processes included in this study is available in Grofulović *et al.*[130]. This bring us to the inclusion of the V-V and V-T reactions to the model, which is outlined in the next section.

2.2.3 Vibrational kinetics

A proper investigation of the underlying mechanisms of the heating dynamics in a gas discharge demands a detailed description of the vibrational energy exchanges between molecules. Here, these exchanges are categorized as follows: (i) nearly resonant collisions, with a transfer of vibrational energy from one molecule to another (V-V); (ii) non-resonant collisions, with inter-molecule energy exchange and loss of the energy defect to translational degrees of freedom (V-V-T); and (iii) non-resonant collisions, with intra-molecule loss of vibrational energy transferred to translational energy (V-T). The corresponding state-specific rate constants are taken from the survey of Blauer and Nickerson[124]. Nevertheless, this is not sufficient for a full characterization of the vibrational kinetics, since the rate coefficients of the transitions involving higher levels are missing. Several theories have been developed to calculate the state-specific rate constants for vibrational energy exchange in molecular collisions[137]. Approximate, reduced-dimension methods, such as the Schwartz-Slawsky-Herzfeld (SSH) theory for V-T relaxation[138], the Rapp-Englander-Golden theory for V-V relaxation[139] and the Sharma-Brau (SB) theory for V-V relaxation induced by long-range forces[140], are very popular for their simplicity. A more accurate approach can be based on the Forced Harmonic Oscillator theory[141–143], which is the extension to higher order terms of the same kinetic theory the SSH first order approximation is built on. Recently, *quasi-classical* trajectory (QCT) calculations have also been developed and improved in terms of computational effort, offering a good compromise between calculation time and accuracy[144]. QCT techniques are the only viable approach to full-dimensional dynamics and to the calculation of state-to-state collisional c-s for systems having more than four atoms, such as CO_2-CO_2 collisions[145]. For instance, Lombardi *et al.*[146] applied QCT and potential energy surface techniques to the CO_2-CO_2 collision system. The authors found that intermolecular transfers essentially involve rotational and vibrational exchanges, while intramolecular energy transfers efficiently redistribute the energy between symmetric stretching and bending modes, with the asymmetric stretching being fully decoupled if the symmetric levels of the molecule are not sufficiently excited.

In this study, we computed the fundamental transitions given by Blauer and Nickerson[124] and scaled the remaining rate coefficients based on the SSH scaling as described in Capitelli[136] and following an approach similar to Kozák and Bogaerts[48] and Silva *et al.*[129].

Additionally, we found that the list of vibrational energy exchanges of Blauer and Nickerson[124] is lacking some important reactions to fully depict the vibrational relaxation processes occurring under the conditions of study. To address this issue, we had to add vibrational exchanges with rate coefficients provided by different literature references and retrieved under different experimental conditions or even computationally calculated. Thus, we believe that this step, along with the selection of the electron impact c-s, represents a major source of uncertainties and, therefore, requires special attention. For instance, we included the nearly resonant collisional up-pumping process along v_3, given by

$$CO_2(00^011) + CO_2(00^011) \leftrightarrow CO_2(00^001) + CO_2(00^021), \qquad (2.9)$$

with the rate coefficients computed applying the SB theory by Silva *et al.*[129]. The rate coefficients for the transitions within higher v_3 levels were obtained with the SB formulation described in Jeffers and Kelley[147], which should be valid for low excitation conditions, i.e. low power input, where $v_3^{max} = 5$ and T_g remains low. Other CO_2 V-V reactions similar to (2.9),

$$CO_2(00^011) + CO_2(01^101) \leftrightarrow CO_2(00^001) + CO_2(01^111), \qquad (2.10)$$

$$CO_2(10^012) + CO_2(00^001) \leftrightarrow CO_2(10^002) + CO_2(00^011), \qquad (2.11)$$

are also incorporated in the model, with the rate coefficients derived from[148].

The survey of Blauer and Nickerson[124] provides the rate coefficients for only one V-V-T transition, i.e.

$$CO_2(00^011) + CO_2(00^001) \leftrightarrow CO_2(10^002) + CO_2(01^101) + 495.77\ K, \qquad (2.12)$$

where $CO_2(10^002)$ is the effective level resulting from $CO_2(02^00)$ and $CO_2(10^00)$, which are strongly coupled by Fermi resonance, as detailed above in section 2. Notwithstanding that, reaction (2.12) can also result in

$$CO_2(00^011) + CO_2(00^001) \leftrightarrow CO_2(02^201) + CO_2(01^101) + 495.93\ K, \qquad (2.13)$$

leading to a transfer of energy from v_3 to pure v_2 levels[149,150]. The branching ratio between (2.12) and (2.13) is unknown. However, Lepoutre *at al.*[149] suggested that the average number of v_2 quanta produced by deactivation of $CO_2(00^011)$ is equal to 2.8 in the 190-300 K temperature range. Nevertheless, this value may decrease as T_g increases[151], indicating that the deactivation of v_3 leads to the excitation of both $CO_2(10^002)$ and $CO_2(02^201)$. With this in mind, we included both (2.12) and (2.13), assuming a branching ratio of 50:50. The rate coefficient for (2.13) was measured to be $k(T_g) = 3.6 \times 10^{-13}\exp(-1660/T_g + 176948/T_g^2)$ by Lepoutre *et al.*[149], as reported in Lopez-Puertas and Taylor[152]. This rate coefficient differs from the one given in Blauer and Nickerson[124] for reaction (2.12). The difference is shown in Figure 2.2, where the rate coefficients for (2.12) and (2.13) are plotted as a function of T_g, in the interval of interest for this modelling study.

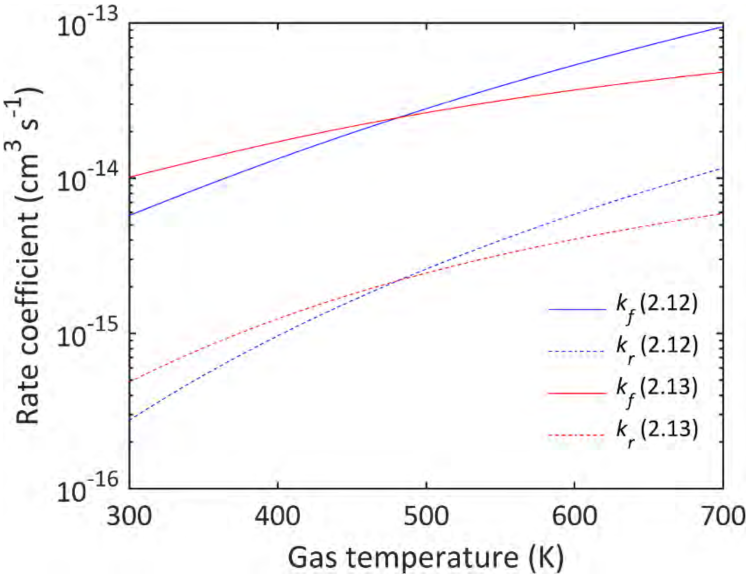

Figure 2.2. Plot of the forward (k_f) and reverse (k_r) rate coefficients for (2.12)[124]*, and for (2.13), measured by Lepoutre et al.*[149]*, as a function of the gas temperature. The reverse rate coefficients are calculated according to the principle of detailed balance*[136]*.*

The comparison displayed in Figure 2.2 shows that important deviations arise at $T_g < 400$ K. However, both rate coefficients converge at ca. 480 K, which is right in the middle of the temperature range of study here, although they deviate again at higher temperatures. Moreover, Lepoutre *et al.*[149] measured the deactivation of $CO_2(00^011)$ (2.13) in a low T_g range (190-300 K), which is relevant for the study of radiative transfer processes in the middle atmosphere. Therefore, their rate coefficient may not describe with sufficient accuracy the role of (2.13) at higher T_g. Following this reasoning, and for consistency with the other vibrational exchanges included in this study, we kept the rate coefficient of (2.13) equal to the one of (2.12), and we scaled it for the higher levels using the SSH theory.

At this point, we would like to emphasize that the SSH and SB theories are affected by limitations at high temperatures ($T_g > 1200$ K) and high vibrational quantum numbers ($v_n > 5$), which may potentially lead to overestimation of the computed rate coefficients[126].

However, these limitations do not pose a threat to the reliability of the calculations presented here since the experimental measurements[50], used for the validation of the model, were obtained in a low excitation regime, resulting in $T_g^{max} \cong 650$ K.

Starting from the foundations laid by Silva *et al.*[129], we extended the vibrational description to 101 levels, accounting for a total of ca. 450 V-T, 600 V-V-T and 1700 V-V direct reactions. All the rate coefficients associated with these reactions are fitted from the following expressions dependent on T_g[124]:

$$k(\mathrm{cm^3\ s^{-1}}) = 1.660 \times 10^{-24} \exp(A + BT_g^{1/3} + CT_g^{2/3}), \tag{2.14}$$

where A, B, and C are fitting constants.

The inverse reaction rate coefficients are computed from the principle of detailed balance[136]. Further details on the principles and the procedure to construct the vibrational chemistry used in this study can be found in Silva *et al.*[129].

Another important V-T reaction included in this work is the deactivation of v_3 (2.15) and v_2 (2.16) levels by collision with oxygen atoms (V-T O)[153]:

$$CO_2(00^011) + O \leftrightarrow CO_2(0v^v01) + O, \tag{2.15}$$

with $v \in \{2, 3, 4\}$, and

$$CO_2(0v^v01) + O \leftrightarrow CO_2(0w^w01) + O, \tag{2.16}$$

with $v \in \{1, 2, 3, 4\}$ and $w = v - 1$. The rate coefficients of reactions (2.15) and (2.16) are assumed to be independent of v and given by $k_{v_3\text{-}O} = 2 \times 10^{-13}\sqrt{T_g/300}\ \mathrm{cm^3\ s^{-1}}$ and $k_{v_2\text{-}O} = 2 \times 10^{-12}\sqrt{T_g/300}\ \mathrm{cm^3\ s^{-1}}$, respectively[152]. Because of their high rate coefficients, these reactions represent a very efficient quenching mechanism of vibrationally excited CO_2, which can significantly affect the VDF of v_3 and the heating dynamics, even at relatively low concentrations of O atoms[154] (see section 4.2.2). The deactivation of higher v_3 and v_2 levels, as well as of mixed levels, is included without any scaling of the corresponding rate coefficients.

The vibrational excitation of the dissociation products of CO_2, i.e. CO and O_2, is not taken into account in this study, since the dissociation degree is very low (< 0.7% with E/N = 90

Td). Its influence on the vibrational excitation of CO_2 will be investigated in a future study, with experimental conditions under which the dissociation degree in the plasma is not negligible.

As we did for the implementation of the e-V transitions, here we added systematically the vibrational exchanges while verifying the correctness of the procedure. In this case, the inspection was done by running a simulation with a very low n_e and T_e as input parameters, thus the VDF must be in a Boltzmann distribution with T_g set in the model, if the implementation of new reactions is correct.

2.2.4 Relaxation of electronic states

Along with V-T relaxation, the relaxation of electronically excited molecules can be responsible for the onset of gas heating at the beginning of the discharge pulse. Fast gas heating is typical of pulsed regimes[155–157] and is described as an abrupt increase in T_g occurring due to fast transfer of energy from electronic to translational degrees of freedom[158]. This mechanism can consume an important fraction of the energy deposited by the electrons onto molecules, limiting the performance and efficiency of the reactor. However, little attention has been paid to the mechanism of fast gas heating in CO_2 non-equilibrium discharges. We believe that fast gas heating has been disregarded by the modelling investigations of such discharges due to assumptions made on E/N and the description of electronic states, which is still very challenging in the case of CO_2. However, in this study, we aim to demonstrate that the role of electronic states is not limited to the promotion of CO_2 dissociation, under the typical conditions of operation in low-pressure pulsed glow discharges (i.e. E/N = 50-90 Td, T_e = 2-3 eV), but can also contribute to fast gas heating. The contribution of the relaxation of $O(^1D)$ and $CO(a^3\Pi)$ excited states was recently studied by Pokrovskiy *et al.*[157] in a nanosecond pulsed discharge with high specific deposited energy (~1.2 eV/molecule). This led to the estimation of E/N $\cong$ 150-250 Td, thereby a significant part of the discharge energy goes to electronic excitation. The authors well described the phenomenon of fast gas heating with a 1D axisymmetric model, validating their kinetic scheme with experimental results. In their model, the rate of direct electron-impact dissociation of CO_2, to give $O(^1D)$ and $CO(a^3\Pi)$ as products, along with the corresponding ground states $O(^3P)$ and $CO(^1\Sigma^+)$, is calculated from (2.6) by using Phelps c-s for electronic excitation, with threshold energy of 7 and 10.5 eV[159] for

$$CO_2 + e \rightarrow CO(^1\Sigma^+) + O(^1D) + e \tag{2.17}$$

and

$$CO_2 + e \rightarrow CO(a^3\Pi) + O(^3P) + e, \tag{2.18}$$

respectively. This choice was motivated by the observations of Babaeva and Naidis[45], who compared estimates of the CO_2 conversion efficiency, obtained using Phelps[159] or Polak[160] c-s for dissociation, with available experimental data. As an outcome, the authors[45] suggested the use of one of the two Phelps c-s, either with 7 or 10.5 eV threshold energy, as they provided a better agreement with the measured conversion efficiencies than Polak c-s, which underestimate the efficiency. A plot of the c-s from Phelps[159] and Polak[160] as a function of the electron energy is provided in Figure 2.3. However, the sum of both Phelps c-s leads to overestimation of the conversion[45] and yet it is necessary to accurately compute the EEDF[135]. Moreover, the use of Phelps c-s for CO_2 dissociation is only recommended for $E/N > 90$ Td, larger than the focus of this study. On the other hand, previous contributions[161,162] underlined the importance of Polak c-s via numerical modelling and experiments for $E/N < 100$ Td. These c-s describe dissociation reactions (2.17) and (2.18), with energy threshold of ca. 7.5 and 11.9 eV, respectively.

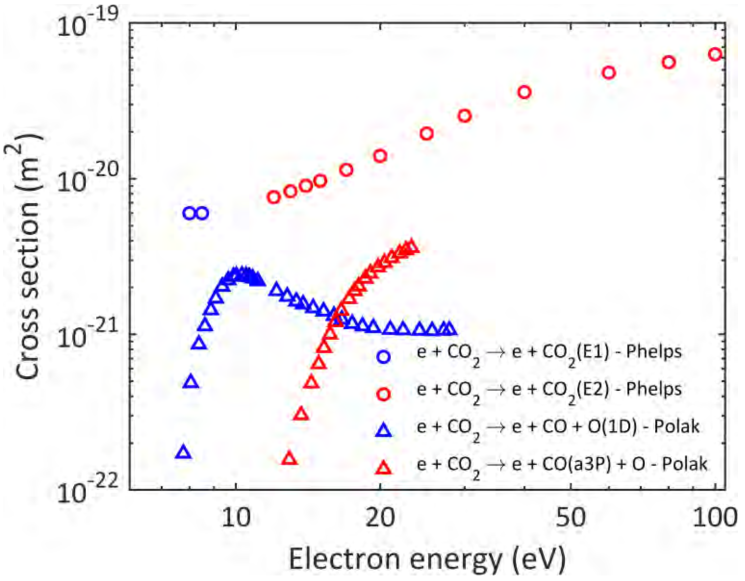

Figure 2.3. Phelps[159] and Polak[160] cross sections for electronic excitation and dissociation, respectively, as a function of the electron energy. $CO_2(E1)$ and $CO_2(E2)$ represent a group of electronic states with a threshold energy of 7 and 10.5 eV, respectively [159].

The comparison between the magnitude of Phelps and Polak c-s, depicted in Figure 2.3, indicates that the former set likely includes pure electronic excitation channels beyond electron-impact dissociation. This further encouraged us to use Polak c-s for the calculation of the CO_2 dissociation rate. However, as anticipated earlier, Phelps c-s are needed to compute the EEDF as they assure a valid prediction of the swarm parameters when used in a two-term Boltzmann solver and for $E/N < 1000$ Td[135]. In particular, the replacement of the Phelps with the Polak set leads to miscalculation of the reduced Townsend effective ionization coefficient, highlighting that some electron energy losses, which are not ascribable to dissociation, are missing in Polak c-s[153]. Therefore, considering the above observations, we kept the Phelps c-s for the excitation to CO_2(E1) and CO_2(E2), which are already integral part of the LXCat set[135] used in this work, solely for the calculation of the EEDF and, thus, of the E/N, as recommended in Grofulović *et al.*[135] and used in Silva *et al.*[163]. However, we used the Polak set for the calculation of the rate of electron-impact CO_2 dissociation and a new set, derived from the subtraction of the Polak to the Phelps c-s, for the rate of excitation of CO_2 to CO_2(E1) and CO_2(E2). This has been done with the assumption that the fraction of electron energy that is not spent into dissociation goes into electronic excitation[161,162] and, subsequently into heat. The approximation on the calculation of the rate coefficients for electronic excitation of CO_2 is needed in order to reduce any possible overestimation on the total production of electronic states due to the sum of Polak's c-s (for dissociative states only) and Phelps' c-s (where dissociative states are likely to be already included). We believe that the model could be further optimized with a deeper knowledge on the nature of the electronic states of CO_2 and by having a complete set of c-s for CO_2 which allows to discriminate between dissociative, radiative and non-radiative (whose collisional quenching releases heat) electronic states.

The electronic states included in our model are listed in Table 2.2.

Table 2.2. Electronic states included in the model and their energy thresholds.

Electronic state	Energy threshold (eV)
CO_2(E1)	7
CO_2(E2)	10.5
$CO(a^3\Pi)$	6
$O(^1D)$	1.96

The inclusion of $O(^1D)$ and $CO(a^3\Pi)$ is motivated by their formation as consequence of reactions (2.17) and (2.18). The relaxation rate coefficients for these species can be found in Table A2 in Appendix A, and more information is available in Silva *et al.*[163]. The exact composition of the lumped $CO_2(E1)$ and $CO_2(E2)$ excited states is unknown, and there is a lack of kinetic data for the relaxation of electronically excited CO_2 molecules in literature. Therefore, we adopted a relaxation rate coefficient equal to the sum of $CO(a^3\Pi) + CO_2 \rightarrow CO + CO_2$ and $CO(a^3\Pi) + CO_2 \rightarrow CO + CO + O$, assuming that CO_2 excited states behave similarly to $CO(a^3\Pi)$. Deeper investigation and characterization of the electronic excitation and relaxation of CO_2 are urgently needed to reduce the number of approximations required for modelling the heating dynamics.

2.2.5 Self-consistent calculation of T_g

The results presented in section 4.2.2 were obtained with simulations featuring the self-consistent calculation of T_g. To this end, the model solves the following heat balance equation

$$N\frac{\gamma k_B}{\gamma - 1}\frac{dT_g}{dt} = P_{el} + \sum_j R_j \Delta H_j - P_{ext} \tag{2.19}$$

where N is the total heavy-particle density, $\gamma = c_p/c_v$ is the ratio of specific heats, P_{el} is the gas heating power density due to elastic electron-neutral collisions, ΔH_j is the heat released (or consumed) in reaction j, and P_{ext} is the power density loss due to exchanges with the surroundings. For CO_2, c_p is taken from Silva *et al.*[164], who estimated it based on Vesovic *et al.*[165], and $c_v = c_p - k_B$.

Considering a gas discharge under isobaric conditions and assuming that the heat conduction is the dominant cooling mechanism, we considered the external cooling term as follows

$$P_{ext} = 8\lambda(T_g - T_w)/r^2, \tag{2.20}$$

in which λ is the gas thermal conductivity, and T_w is the wall temperature taken as 300 K. In this work, the gas thermal conductivity is $\lambda(T_g) = (0.071T_g - 2.33) \times 10^{-3}$ W m^{-1} K^{-1} as used by previous modeling studies[55,164,166] and estimated from Chase[167] for CO_2. The radius of the reactor r is set to 1 cm[50].

The contribution of reaction *j* to the gas heating (HR_j, in K s^{-1}) is recorded throughout the simulation according to the following expression, derived from the heat balance equation

$$HR_j = (R_j \Delta H_j / N)(\gamma - 1/\gamma k_B) \ . \tag{2.21}$$

Analogously, the electron energy loss rate ($EELR_j$, in eV s^{-1}) is computed as follows:

$$EELR_j = (ER_j \Delta \mathrm{E}_j / N)(\gamma - 1/\gamma k_B) \ , \tag{2.22}$$

where ER_j is the rate and $\Delta \mathrm{E}_j$ the energy threshold of the electron-impact reaction *j*. $EELR_j$ and HR_j will be later used to describe the contribution of different classes of reactions to the electron energy deposition onto distinct processes, and to the gas heating, respectively.

2.2.6 Estimation of the reduced electric field (E/N)

The E/N is an essential parameter to define the energy transfers between electrons and heavy species in discharges where the dynamics is dominated by electron impact processes, whose rate coefficients depend on E/N. The balance between electron creation by ionization and loss by electron attachment, volume recombination and diffusion to the walls determines the sustaining E/N. In particular, under the conditions studied here, dissociative electron attachment ($e^- + CO_2 \rightarrow O^- + CO$) constitutes the main electron loss channel, producing stable negative ions O^-, as well as CO_3^-, which are formed by $O^- + CO_2 + M \rightarrow CO_3^- + M$[168]. The inverse reactions, i.e. electron detachment (see Table A2 in Appendix A), are slower than attachment, determining a reduction in n_e, which needs to be replenished by additional ionization in order to sustain the discharge. Therefore, the E/N will be mainly defined by the balance between electron attachment and volume recombination and ionization.

Klarenaar *et al.*[50] estimated an E/N of 60 Td by measuring the potential difference over two metal rods pointing inside the positive column of the reactor, while maintaining a continuous discharge of 50 mA at 6.7 mbar. From this value, they calculated n_e as 10^{10} cm^{-3}, using the electron drift velocity estimated from Roznerski and Leja[169]. Later, Grofulović *et al.*[130] calculated an E/N of 55 Td for the same conditions, in good agreement with Klarenaar *et al.*[50]. In order to further confirm these calculations, we performed a self-consistent calculation of E/N and n_e using the current profile provided by Klarenaar *et al.*[50] and a fixed voltage of 1.5 kV. The E/N is computed as follows:

$$E/N = \frac{\sqrt{\frac{P}{V_R} / \frac{\mu_e}{N} \times n_e \times e}}{N} / 10^{-17}, \qquad (2.23)$$

where P = I × V is the power, calculated as the current multiplied by the voltage, V_R is the reactor volume and e is the elementary charge.

The electron density n_e is computed by ZDPlasKin and its magnitude is a result of a balance between electron-impact processes (i.e. ionization and attachment) and volume recombination reactions. The self-consistently calculated E/N, along with the corresponding T_e, and n_e are plotted in panels (a) and (b) of Figure 2.4, respectively, as a function of the discharge time.

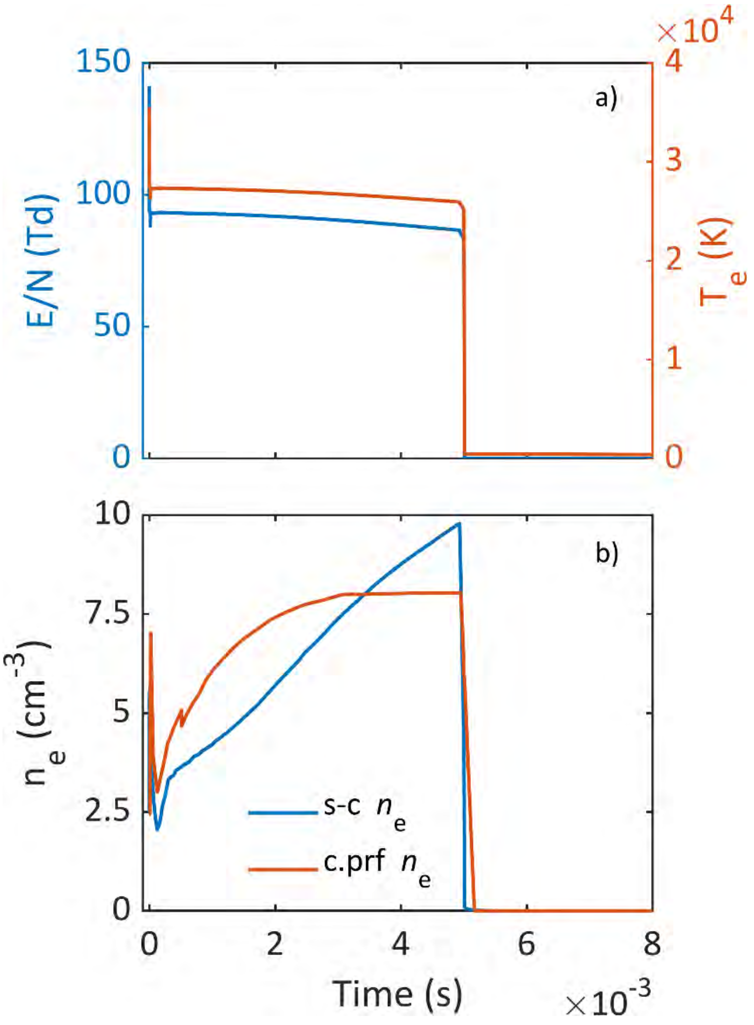

Figure 2.4. Time-evolution of (a) self-consistently calculated E/N and T_e and (b) n_e, self-consistently calculated (s-c) and estimated from the experimental current profile (c.prf) [50,130].

Our simulations suggest a larger E/N than the previous estimations (i.e. ca. 90 Td vs 60 Td[50] and 55 Td[130]), with a corresponding T_e of ca. 27000 K (or ca. 2.3 eV) (Figure 2.4(a)). The difference with E/N estimated from the experiments[50] can be ascribed to the fact that the measurements of the potential difference were performed in a continuous discharge and not in a pulsed regime. In the latter situation, ionizing conditions are needed to build up the electron density to sustain the discharge, at least at the beginning of the pulse. In other words, E/N is likely to be larger than 60 Td for a good part of the pulse. On the other hand, the differences in the calculated values of the self-consistent sustaining field between Grofulović *et al.*[130] and the present calculations are associated with the different discharge models used and still require further investigation. For instance, Grofulović *et al.*[130] only considered CO_2^+, whereas, in our chemistry set, additional positive and negative ions are also included. As pointed out at the beginning of this paragraph, the negative ions O^- and CO_3^- are important products of the dissociative electron attachment reactions, which reduce n_e and, consequently, increase E/N. In view of this, a detailed comparison of the different model formulations will be carried out in future work.

It is worth mentioning that the total length of the reactor tube, i.e. 23 cm, was used to calculate V_R and, therefore, the power density (P/V_R). This means that the power density may be larger than in our calculations if the plasma does not fill completely the entire volume, which in turns leads to higher E/N according to equation (2.23). On the other hand, the voltage evolution during the pulse is not known[50] and the assumption of a fixed value may be not accurate. Indeed, Damen *et al.*[170] displayed the voltage profiles for similar conditions in the same glow discharge reactor of Klarenaar *et al.*[50]. The authors showed that the voltage magnitude is not constant during the active phase of the discharge, dropping significantly during the first millisecond to maintain the current constant at 50 mA. The unsteadiness of the voltage directly affects the computation of the power density and leads unavoidably to inaccurate n_e, as shown in Figure 2.4(b), and to the E/N and T_e evolutions, displayed in Figure 2.4(a). Therefore, in our simulations, we kept the n_e profile estimated from the experimental current profile and we tested two values of E/N, i.e. 55 Td, for comparison with Grofulović *et al.*[130], and 90 Td, as an average value of the profile shown in Figure 2.4(a). Additional simulations that we performed with a range of E/N values also support the choice of 90 Td. More specifically, an E/N of 94 Td is needed to sustain the discharge and compensate for the electron losses to dissociative attachment during the onset of the discharge. After that, E/N should slowly decrease; otherwise, n_e exceeds the estimation based on the current profile. Hence, we believe that 55 and 90 Td represent two extreme situations that can describe the end and the beginning of the discharge pulse, respectively. In Chapter 4, we present the simulation outcomes for both E/N values, first without and then with self-consistent calculation of T_g. The effect of E/N on the gas heating dynamics is discussed in section 4.2.2.

As mentioned in section 1.3, vibrational excitation typically has little contribution to CO_2 dissociation in *warm* plasmas. Therefore, the vibrational kinetics can be assumed in a Boltzmann distribution with the gas temperature, and the kinetic scheme can be narrowed down to the relevant thermal reactions. Such an assumption will allow modeling of the discharge at multi-dimensional scale, since *warm* discharges are typically very inhomogeneous and therefore challenging to approach with 0D modeling. Thus, in the next section, we present a simple chemical kinetics model developed within this thesis to simultaneously study the gas-phase and surface reactivity in the post-discharge region of a CO_2 gliding arc plasma (as an example of *warm* discharge) with a carbon bed.

2.3 Description of the CO_2 + solid carbon model[3]

This kinetic model is developed to investigate the reactivity of a carbon bed interacting with a reactive mixture of CO_2 and its dissociation products. Due to the complexity of the system, in this thesis we only focus on the post-discharge region. Therefore, unlike the model described in section 2.2, the electron and vibrational kinetics are not included here. Nevertheless, this model is also solved using the ZDPlasKin[133] simulation tool, as previously described in section 2.2. The chemistry set used in this study is detailed in section 2.3.1, while the validation of the model with experimental results is described in section 2.3.2. The outcome of the validation step is then used in Chapter 5 to explain the trends observed in our experiments with a CO_2 gliding arc discharge with post-discharge carbon bed.

---

[3] This model was used in the following paper:
Carbon bed post-plasma to enhance the CO_2 conversion and remove O_2 from the product stream
O.Biondo*, F. Girard-Sahun*, G. Trenchev, G. van Rooij, A. Bogaerts
Chemical Engineering Journal 442, 136268 (2022)
https://doi.org/10.1016/j.cej.2022.136268
*Shared first author

2.3.1 Chemistry set

The gas-phase chemistry used in this study is reduced from the model described in section 2.2, down to the main thermal reactions. This is justified for warm plasmas, as explained above. The reduced chemistry was compared against the work of Vermeiren and Bogaerts[55], providing a very good overlap with the simulated temperature profiles. After this first step, the surface chemistry was added. The species included in the CO_2 + solid carbon model are listed in Table 2.3.

Table 2.3. Species described in the model.

Gas-phase ground state species
CO_2, CO, O_2, O, C
Surface species[a]
C(s), C(s)-O

[a] C(s) and C(s)-O represent an active carbon site and an oxygen atom chemisorbed at an active carbon site, respectively.

The investigation of gas-carbon reactions requires the introduction of active surface sites in the model. The concept of active surface site entails that heterogeneous reactions occur only at specific sites on which oxygen is adsorbed and forms complexes, which may ultimately lead to desorption of products, such as CO or CO_2. For carbonaceous materials, the active surface sites can be identified as structural features, such as defects in carbon layer planes and edge carbon atoms, disordered carbon atoms, heteroatoms (O, S, N) and mineral matter[171].

Prata *et al.*[172] applied the concept of active surface site to the modeling of the gas-surface reactions relevant for the ablative heat shield occurring during spacecraft atmospheric re-entry. We have chosen the chemical reaction set proposed by Prata amongst the other available sets[173–175], since it provides the most complete description for carbon oxidation reactions, along with a better agreement with experimental trends. The reaction set for the carbon oxidation is detailed in Table 2.4.

Table 2.4. Heterogeneous reactions and their rate coefficients taken from Prata et al.[172] *for solid carbon oxidation.*

Reaction	Rate constant	Units
O(g) + C(s) → C(s)-O (O chemisorption)	$\frac{1}{4B}\sqrt{\frac{8k_B\mathrm{T}}{\pi \mathrm{m_O}}}\frac{10^6}{N_A}$	$[\mathrm{cm^3\ s^{-1}}]$
C(s)-O → O(g) + C(s) (O desorption from mobile sites)	$\frac{2\pi \mathrm{m_o} k_B^2\mathrm{T}^2}{N_A B h^3} * \mathrm{e}^{-44277/\mathrm{T}}$	$[\mathrm{s^{-1}}]$
C(s)-O → O(g) + C(s) (O desorption from immobile sites)	$\frac{2\pi \mathrm{m_o} k_B^2\mathrm{T}^2}{N_A B h^3} * \mathrm{e}^{-96500/\mathrm{T}}$	$[\mathrm{s^{-1}}]$
C(s)-O + M → CO(g) + M M = O, O_2, CO, CO_2 (Collision-induced CO desorption)	$\frac{1}{4B}\sqrt{\frac{8k_B\mathrm{T}}{\pi \mathrm{m_M}}} * \mathrm{e}^{-6000/\mathrm{T}} * \frac{10^6}{N_A}$	$[\mathrm{cm^3\ s^{-1}}]^{a,b}$
O_2(g) + C(s) → O(g) + C(s)-O (O_2 partial chemisorption)	$\frac{1}{4B}\sqrt{\frac{8k_B\mathrm{T}}{\pi \mathrm{m_{O2}}}} * \mathrm{e}^{-14500/\mathrm{T}} * \frac{10^6}{N_A}$	$[\mathrm{cm^3\ s^{-1}}]^{c}$
O_2(g) + 2 C(s) → 2 C(s)-O (O_2 chemisorption)	$\frac{1}{4B^2}\sqrt{\frac{8k_B\mathrm{T}}{\pi \mathrm{m_{O2}}}} * \mathrm{e}^{-8000/\mathrm{T}} * \frac{V}{A} * \frac{10^{12}}{N_A{}^2}$	$[\mathrm{cm^6\ s^{-1}}]$
2 C(s)-O → O_2(g) + 2 C(s) (O_2 desorption from mobile sites)	$\sqrt{\frac{N_A\pi k_B\mathrm{T}}{B2\mathrm{m_{O2}}}} * 5 * 10^{-5} * \mathrm{e}^{-15000/\mathrm{T}} * \frac{V}{A} * \frac{10^6}{N_A}$	$[\mathrm{cm^3\ s^{-1}}]$
2 C(s)-O → O_2(g) + 2 C(s) (O_2 desorption from immobile sites)	$\sqrt{\frac{N_A\pi k_B\mathrm{T}}{B2\mathrm{m_{O2}}}} * 1 * 10^{-3} * \mathrm{e}^{-15000/\mathrm{T}} * \frac{V}{A} * \frac{10^6}{N_A}$	$[\mathrm{cm^3\ s^{-1}}]$
O(g) + C(s)-O → CO_2(g) (C(s)-O oxidation – only from mobile sites)	$\frac{1}{4B}\sqrt{\frac{8k_B\mathrm{T}}{\pi \mathrm{m_O}}} * \mathrm{e}^{-2000/\mathrm{T}} * \frac{10^6}{N_A}$	$[\mathrm{cm^3\ s^{-1}}]^{d}$
O_2(g) + C(s)-O → CO_2(g) + O(g) (CO_2 desorption – only from mobile sites)	$\frac{1}{4B}\sqrt{\frac{8k_B\mathrm{T}}{\pi \mathrm{m_{O2}}}} * \mathrm{e}^{-2000/\mathrm{T}} * \frac{10^6}{N_A}$	$[\mathrm{cm^3\ s^{-1}}]^{d}$

[a] activation energy increased from 4000 K[172] to 6000 K, pre-exponential factor lowered from 100[172] to 1 for the mobile sites and from 1000 to 1 for the immobile sites (see text).

[b] added also CO and CO_2 as collision partners, according to the Eley-Rideal model described in Prata *et al.*[172].

[c] added to the reaction set from the model by Zhluktov and Abe[174] (see text), not included in Prata *et al.*[172], for studying its effects in the model predictions.

[d] activation energy increased from 500 K (Prata) to 2000 K, as suggested by Zhluktov and Abe[174] (see text).

In this table, B is the active site density (in mole per square meter), k_B is the Boltzmann constant [J/K], h is the Planck constant [J·s], m_O, m_{O2}, m_{CO} and m_{CO2} are the O, O_2, CO and CO_2 mass in kg, respectively. Note that V/A is the ratio between the carbon bed volume and the carbon surface area and it is calculated according to the experimental conditions (hence: in our model here adopted from the data of Prata *et al.*[172]).

In our study we keep the assumption of two different types of oxygen chemisorption, namely mobile for weakly bonded oxygen (single-bond character C-O) and immobile for strongly bonded oxygen (double-bond character C=O). Zhluktov and Abe[174] already introduced this distinction between at least two different types of adsorption into a kinetic model. This is also justified by several studies demonstrating the heterogeneity of the active surface sites in carbon materials. Lussow *et al.*[176] determined the active site density on Graphon samples with O_2 chemisorption and found that, above 400°C, the oxygen saturation on the surface sharply increases, suggesting the presence of at least two types of active sites. Later on, Ahmed *et al.*[177] developed a kinetic model to describe the O_2 gasification of pyrolytic carbon, at low pressure (100 Pa) and in a narrow temperature range (748 – 898 K). The proposed mechanism involved the distinction between two types of active surface sites, and unveiled the importance of such distinction for an accurate description of CO_2 desorption. More recently, density functional theory (DFT) calculations demonstrated that the description of the heterogeneity of the surface of carbons through at least two types of active sites is needed to explain the desorption of CO_2[178,179].

As suggested by Prata *et al.*[172], we defined the distribution between sites giving mobile and immobile chemisorption to be 30% and 70%, respectively. The activation energy for the CO desorption stimulated by collisions with gas molecules (or atoms) is increased to 6000 K in order to match the experimental trends with our 0D kinetic model. For the same reason, we have lowered the pre-exponential factors to unity. The stimulated CO desorption is modeled as an Eley-Rideal reaction, where the pre-exponential factors typically take values between 0 and 1. Moreover, Prata *et al.*[172] determined the activation energy and pre-exponential factors by fitting with molecular beam experiments, under the assumptions that i) the desorption products are immediately removed from the surface and ii) the hyperthermal O and O_2 sent to the surface accommodate to the surface temperature. However, products may also interact with the surface and the O/O_2 beam might not be in equilibrium with the surface temperature, also mentioned by the author[172]. The choice of a larger activation energy is also supported by the value proposed by Yang and Yang[180] for the spontaneous CO desorption (see Table 2.5), by the values estimated by Tremblay *et al.*[181] and by the values computed by Montoya *et al.*[182]. Following the same reasoning, we increased the activation energy also for the CO_2 desorption, by choosing a value proposed by Zhluktov and Abe[174] in their model for carbon oxidation. The experimental evidences from Panerai *et al.*[183] corroborate our choice. In particular, the authors show that CO_2 is produced only at temperature higher than 700 K under O_2 atmosphere, whereas the use of the energy barrier proposed by Prata *et al.*[172] would lead to overestimation of CO_2 for lower temperatures. Moreover, we performed a thermogravimetric analysis coupled with mass spectrometry (TGA-MS) (see Figure 2.5) for one of the charcoals tested in the experiments described in Chapter 5, and the results are in good agreement with Panerai *et al.*[183] i.e. CO_2 desorption onsets only above 700 K. Finally, it is worth to remark that the activation energy of the surface reactions varies with the structure of the carbon material, the oxidation degree of the surface and the presence of catalytic impurities[58,61,182].

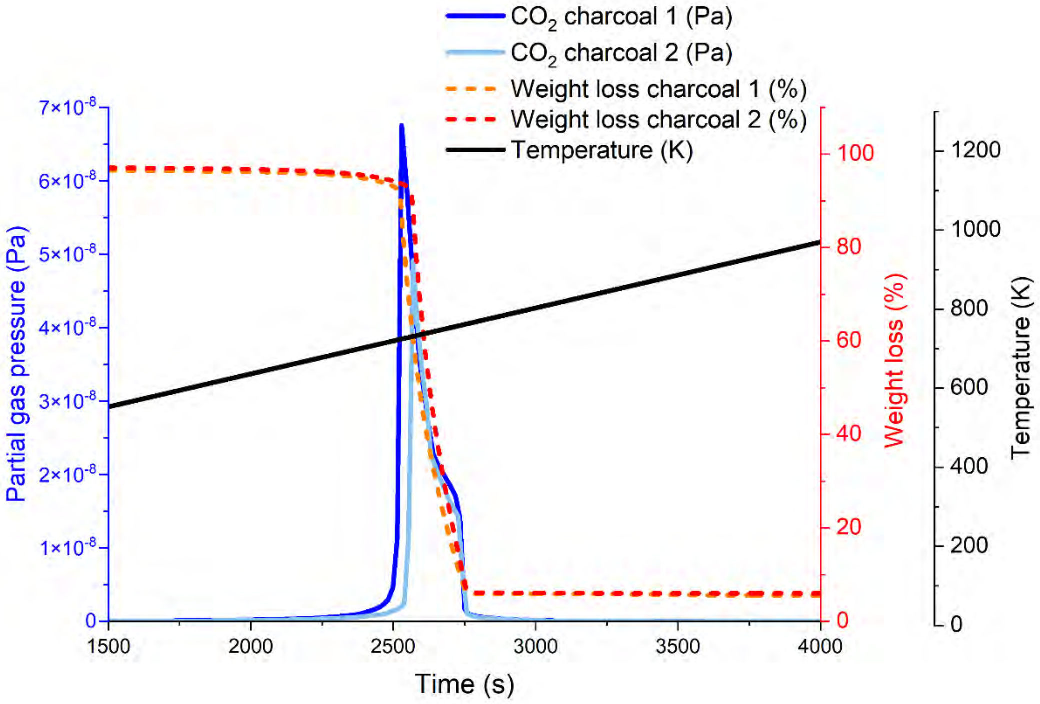

Figure 2.5. Partial pressure of CO_2 released from TGA-MS under O_2 atmosphere of charcoal 1 (dark blue) and charcoal 2 (light blue) and weight loss for charcoal 1 (orange dashed line) and charcoal 2 (red dashed line), as a function of the temperature and time. Heating rate 10 K/min and gas flow rate 40 mL/min.

Furthermore, to study the reactions occurring between CO_2 and the carbon active sites, we also implement the heterogeneous Boudouard reaction set proposed by Yang and Yang[180], reported in Table 2.5. The rate constants for the elementary steps were determined in a temperature range of 873-1173 K for graphite. In order to integrate it with the above carbon oxidation set, we assumed that the dissociation of CO_2 leads to formation of 30% mobile and 70% immobile oxygen chemisorption, as for atomic oxygen. The existence of at least two different types of oxygen adsorption is also documented for CO_2. For instance, Yang and Yang[180] found out that, after CO_2 gasification of graphite, the bond strength of the oxygen complexes formed on the monolayer edges is about 9 kcal mol^{-1} stronger than the complexes formed on the multilayer edges, and that they have an average bond character of two-thirds. Later, Calo and Perkins[61] stressed the need of accounting for the energetic heterogeneity of carbon surfaces in the kinetic analysis of the CO_2 gasification.

Table 2.5. Heterogeneous Boudouard reactions and their rate coefficients taken from Yang & Yang [180].

Reaction	Rate constant	Units
$CO(g) + C(s)\text{-}O \rightarrow CO_2(g) + C(s)$ (Forward Boudouard)	$2.14 * 10^{9} * e^{-16706.9/T} * \frac{10^{3}}{NA}$	[$cm^3\ s^{-1}$]
$CO_2(g) + C(s) \rightarrow CO(g) + C(s)\text{-}O$ (Reverse Boudouard)	$9.07 * 10^{10} * e^{-24346.6/T} * \frac{10^{3}}{NA}$	[$cm^3\ s^{-1}$]
$C(s)\text{-}O \rightarrow CO(g)$ (CO spontaneous desorption)	$\frac{2.14 * 10^{8} * e^{-19323.6/T}}{R * T}$	[s^{-1}]

Where R is the ideal gas constant [L atm K^{-1} mol^{-1}].

2.3.2 Experimental input parameters for model validation

The validation of a model is a crucial aspect and requires particular experimental conditions, in order to minimize the number of assumptions under which the predictions are valid. With this in mind, we have chosen to validate our model with the gasification experiments presented by Panerai *et al.*[183], under pure O_2 and CO_2 atmospheres, respectively, in order to get insights into the reaction pathways for carbon oxidation in the presence of O_2, CO_2 and CO and the deactivation of the carbon bed, with consequent decrease in selectivity towards the latter. This model greatly helps us to explain our experimental results, as will be described in detail in Chapter 5.

Indeed, their experimental setup has a simple design. It can be approximated as a plug flow reactor and allows isolating the effect of O_2 and CO_2 in the oxidation and consumption of solid carbon. Moreover, the absence of a plasma further reduces the complexity of the process, and therefore the number of experimental uncertainties, and it will enable us to investigate in a second stage the effect of plasma in the gasification mechanism, establishing solid foundations for future model developments.

The experiments carried out by Panerai *et al.*[183] provide a set of experimental data which can be implemented into our 0D kinetic model with relative ease. A cylindrical glass tube is placed inside a furnace, within which the temperature can be assumed homogeneous and constant. The carbon bed is fitted inside the glass tube, approximately at the center of the furnace. The feed gas, either pure O_2, CO_2 or CO, flows through the tube and reaches the carbon bed heated by the furnace. The products are then analyzed downstream by residual gas analysis mass spectrometry. This simple experimental configuration can be approximated to a plug flow reactor under a limited number of assumptions, the most important being that the fluid is perfectly mixed in the direction perpendicular to the axis. In addition, the high-temperature oxidation experiments were performed using FiberForm, a carbon fiber material which is thoroughly characterized[184–186] and therefore an excellent candidate for modelling purposes. Thus, this experimental set of data represents a good benchmark for the validation of our 0D kinetic model. The parameters taken by the experimental work of Panerai *et al.*[183] and used in our modelling study are listed in Table 2.6. Note that for the validation step with their experiments[183], the temperature is assumed constant and homogeneous throughout the reactor tube in the model. This assumption is needed since we had no information about the actual temperature at the carbon bed. We know from our experiments that the temperature increases locally where oxidation reactions take place, due to their exothermic nature. However, the use of a furnace, as in Panerai *et al.*[183], may help to maintain the temperature uniform in the carbon bed, and we believe that this supports our assumption. In our experiments, on the other hand, the carbon bed is partially heated by the plasma, and locally heated by oxidation reactions. Therefore, we measured the temperature variations in the carbon bed, as well as without, with the aim of linking our modelling results, for fixed T_g, to our experiments (see Chapter 5, section 5.2.6 below).

Table 2.6. Parameters used for the 0D simulations, taken from Panerai et al.[183]*, with* C_0 *mass being the carbon mass at the beginning of the each experimental test.*

Test	Feed gas	T_g [K]	p [Pa]	C_0 mass [g]	Carbon bed length [mm]	mass flow rate [g s^{-1}]
O_2_A	O_2	518	2172	1.366	20	2.36
O_2_E	O_2	1086	3668	1.357	20	2.34
O_2_H	O_2	1502	6180	1.372	20	2.34
O_2_H_{600}	O_2	1502	1900	0.372	7.18	2.34
CO_2_C	CO_2	983	2674	1.350	20	2.31
CO_2_H	CO_2	1413	4176	1.330	20	2.31
CO_C	CO	1508	3954	1.383	20	2.06

The notation for each individual test listed in Table 2.6 is taken from Panerai *et al.*[183]. The notation indicates the feed gas (O_2, CO_2 or CO), while the letters A, E, H and C were arbitrarily chosen by Panerai *et al.*[183] to enumerate the tests, but in fact they correspond to different temperatures (see Table 2.6). Note that only the tests for which the product concentrations were recorded over time and provided from the experiments have been used in this study. For test O2_H, we performed an additional simulation, named $O_2\_H_{600}$, with pressure, carbon mass and carbon bed length after 10 minutes of treatment. For each single test, the temperature is assumed constant and homogenous throughout the reactor tube inside the furnace. The experiments were carried out at controlled mass flow rate, with variable pressure. The initial mass of each carbon bed sample was weighted, allowing for a more accurate calculation of the absolute total surface area (TSA), in square meters, for each individual test. We estimated a specific surface area of 0.16 m^2/g for FiberForm, following the calculations presented by Gusarov *et al.*[187]. This estimation is in the same order of magnitude of other carbon fibers[188,189]. The TSA is a useful parameter to estimate the density of active sites C_{surf} (cm^{-3}), as described in formula 2.24:

$$C_{surf} = b * B * N_A * \mathrm{TSA}/V_{bed} * 10^{-6} \qquad (2.24)$$

where b is a fitting parameter, B is the active site density over the surface in mole m^{-2}, N_A is the Avogadro number and V_{bed} is the volume of the carbon bed in cubic meters. The choice of introducing the parameter b to calculate the active site density C_{surf} is justified by the influence of the experimental pressure on the reactivity of the carbon materials. Ismail[188] observed that at pressures above 2.67 kPa, a new type of active sites is activated. In molecular-beam studies, the pressure is typically near vacuum. Therefore, it is reasonable to assume that at higher pressures, such as in the experiments by Panerai *et al.*[183], the density of active sites is larger. This is consistent with the fact that without a fitting parameter to enhance the reactivity, the simulations predict a negligible effect of the carbon bed, in contrast with the experimental observations. We decided to keep b fixed at 30, as it provided the best agreement with the experiments. We do not expect b to vary significantly between one test and another, as the pressure is maintained within the same order of magnitude throughout the entire experimental study. We would like to point out that the chemistry set and the model developed for this study are only suitable to quantitatively simulate the performance of the gasification process under the conditions tested in the experiments by Panerai *et al.*[183]. With the aim of describing a different system (e.g. with different carbon materials or operational pressure), a tuning of the kinetic model may be required. Nevertheless, the model can still provide insights into the underlying mechanisms, even when the experimental conditions vary. The validation of the 0D model with the experiments of Panerai *et al.*[183] and the discussion of the experimental trends observed within the experiments described in Section 3.1 will be presented in Chapter 5.

Appendix A. Chemistry set

Table A1. List of the 101 CO_2 vibrational states considered in this study, with the corresponding energies and statistical weights. Details on the notation used, as well as on the calculation of the vibrational energies, can be found in Section 2.2.3.

Vibrational state	Energy (eV)	Statistical weight
$CO_2(00^001)$	0.000000	1
$CO_2(01^101)$	0.082793	2
$CO_2(02^201)$	0.165728	2
$CO_2(10^002)$	0.165742	2
$CO_2(11^102)$	0.248597	4
$CO_2(03^301)$	0.248807	2
$CO_2(00^011)$	0.291257	1
$CO_2(20^003)$	0.331312	3
$CO_2(12^202)$	0.331593	4
$CO_2(04^401)$	0.332032	2
$CO_2(01^111)$	0.372499	2
$CO_2(21^103)$	0.414216	6
$CO_2(13^302)$	0.414733	4
$CO_2(05^501)$	0.415403	2
$CO_2(02^211)$	0.453883	2
$CO_2(10^012)$	0.454254	2
$CO_2(30^004)$	0.496695	4
$CO_2(22^203)$	0.497261	6
$CO_2(14^402)$	0.498018	4
$CO_2(06^601)$	0.498924	2
$CO_2(03^311)$	0.535413	2
$CO_2(11^112)$	0.535558	4
$CO_2(00^021)$	0.579419	1
$CO_2(31^104)$	0.579636	8
$CO_2(23^303)$	0.580449	6
$CO_2(15^502)$	0.581450	4
$CO_2(07^701)$	0.582590	2
$CO_2(12^212)$	0.617004	4
$CO_2(20^013)$	0.617074	3
$CO_2(04^411)$	0.617089	2

$CO_2(01^121)$	0.659113	2
$CO_2(13^312)$	0.698596	4
$CO_2(05^511)$	0.698914	2
$CO_2(21^113)$	0.699517	6
$CO_2(02^221)$	0.738951	2
$CO_2(10^022)$	0.739683	2
$CO_2(30^014)$	0.779701	4
$CO_2(22^213)$	0.779923	6
$CO_2(14^412)$	0.780333	4
$CO_2(06^611)$	0.780889	2
$CO_2(03^321)$	0.818936	2
$CO_2(11^122)$	0.819440	4
$CO_2(00^031)$	0.864490	1
$CO_2(04^421)$	0.899069	2
$CO_2(12^222)$	0.899341	4
$CO_2(20^023)$	0.899764	3
$CO_2(01^131)$	0.942641	2
$CO_2(05^521)$	0.979351	2
$CO_2(13^322)$	0.979388	4
$CO_2(21^123)$	0.979571	6
$CO_2(02^231)$	1.020937	2
$CO_2(10^032)$	1.022033	2
$CO_2(22^223)$	1.059523	6
$CO_2(14^422)$	1.059583	4
$CO_2(30^024)$	1.059647	4
$CO_2(06^621)$	1.059786	2
$CO_2(03^331)$	1.099382	2
$CO_2(11^132)$	1.100247	4
$CO_2(00^041)$	1.146474	1
$CO_2(12^232)$	1.177932	4
$CO_2(04^431)$	1.177976	2
$CO_2(20^033)$	1.179387	3
$CO_2(01^141)$	1.223087	2
$CO_2(05^531)$	1.256721	2
$CO_2(13^332)$	1.257116	4
$CO_2(21^133)$	1.257653	6
$CO_2(02^241)$	1.299846	2
$CO_2(10^042)$	1.301308	2
$CO_2(06^631)$	1.335618	2
$CO_2(14^432)$	1.335773	4
$CO_2(22^233)$	1.336065	6
$CO_2(30^034)$	1.336539	4

$CO_2(03^{3}41)$	1.376755	2
$CO_2(11^{1}42)$	1.377985	4
$CO_2(00^{0}51)$	1.425377	1
$CO_2(04^{4}41)$	1.453814	2
$CO_2(12^{2}42)$	1.454809	4
$CO_2(20^{0}43)$	1.455948	3
$CO_2(01^{1}51)$	1.500456	2
$CO_2(05^{5}41)$	1.531026	2
$CO_2(13^{3}42)$	1.531782	4
$CO_2(21^{1}43)$	1.532678	6
$CO_2(02^{2}51)$	1.575683	2
$CO_2(10^{0}52)$	1.577514	2
$CO_2(06^{6}41)$	1.608392	2
$CO_2(14^{4}42)$	1.608906	4
$CO_2(22^{2}43)$	1.609554	6
$CO_2(30^{0}44)$	1.610381	4
$CO_2(03^{3}51)$	1.651060	2
$CO_2(11^{1}52)$	1.652658	4
$CO_2(04^{4}51)$	1.726590	2
$CO_2(12^{2}52)$	1.727951	4
$CO_2(20^{0}53)$	1.729453	3
$CO_2(05^{5}51)$	1.802273	2
$CO_2(13^{3}52)$	1.803393	4
$CO_2(21^{1}53)$	1.804650	6
$CO_2(06^{6}51)$	1.878112	2
$CO_2(14^{4}52)$	1.878988	4
$CO_2(22^{2}53)$	1.879995	6
$CO_2(30^{0}54)$	1.881178	4

Table A2. Chemistry set proposed in this work. Rate coefficients in cm^3 *s*$^{-1}$ *or cm*^{6} *s*$^{-1}$*, for two-body and three-body reactions, respectively, while* T_e *in eV and* T_g *in K. Note that* CO_2 *represents the sum of all the* CO_2 *vibrational states considered in this study and no scaling laws were applied to the rate coefficients to account for the vibrational energy of the reactants, unless specified differently (i.e. for electron-impact vibrational excitation and V-T, V-V-T and V-V reactions).*

Reaction	Rate coefficients	Reference
e^- impact ionization/excitation/dissociation		
$e + CO_2 \rightarrow e + e + CO_2^+$	EEDF	[135]
$e + CO_2 \rightarrow e + CO + O(^1D)$	EEDF	[160]
$e + CO_2 \rightarrow e + CO(a^3\Pi) + O$	EEDF	[160]
$e + CO_2 \rightarrow e + CO_2(E1)$	EEDF (see section 3.4)	

e + CO_2 → e + CO_2(E2)	EEDF (see section 3.4)	
e + CO_2 → e + $CO_2(v_1v_2v_3)$	EEDF (see section 3.2)	
e + CO → e + e + CO^+	EEDF	135
e + CO → e + C + O	EEDF	135
e + CO → e + CO($a^3\Pi$)	EEDF	135
e + O_2 → e + e + O_2^+	EEDF	135
e + CO → e + C + O	EEDF	135
e + CO → e + C + O(^{1}D)	EEDF	135
e + O → e + e + O^+	EEDF	135
e + O ↔ e + O(^{1}D)	EEDF	135
e^- impact recombination or attachment/detachment		
e + CO_2 → CO + O^-	EEDF	135
e + CO → C + O^-	EEDF	135
e + O_2 → O + O^-	EEDF	135
e + CO_2^+ → CO + O	$10^{-5} T_e^{0.5} T_g^{0.1}$	190,191
e + CO_2^+ → C + O_2	$1.07 \times 10^{-5} T_e^{0.5} T_g^{0.1}$	192
e + CO^+ → C + O	$3.46 \times 10^{-8} T_e^{0.48}$	193,194
e + O_2^+ + M → O_2 + M	1×10^{-26}	190
e + O_2^+ → O + O	$6.46 \times 10^{-5} T_e^{0.5} T_g^{0.5}$	193
e + O + M → O^- + M	1×10^{-31}	195
e + O^- → e + e + O	EEDF	135
Ion-neutral and ion-ion reactions		
CO_2^+ + O → CO_2 + O^+	9.62×10^{-11}	196
CO_3^- + O → CO_2 + O_2^-	8×10^{-11}	197
CO_4^- + O → CO_3^- + O_2	1.4×10^{-10}	198
O_2^- + O → O_2 + O^-	1.5×10^{-10}	198
O_2^+ + C → CO^+ + O	5.2×10^{-11}	196
CO_2^+ + O → O_2^+ + CO	1.64×10^{-10}	196
CO_2^+ + O_2 → CO_2 + O_2^+	5.3×10^{-11}	196
CO^+ + O_2 → CO + O_2^+	1.2×10^{-10}	196
O^+ + CO_2 → O + CO_2^+	4.5×10^{-10}	192
CO^+ + CO_2 → CO + CO_2^+	1×10^{-9}	198,199
O^+ + CO_2 → O_2^+ + CO	4.5×10^{-10}	192
O^+ + O^- → O + O	$4 \times 10^{-8} (300/T_g)^{0.43}$	200
O_2^+ + O^- → O_2 + O	1×10^{-7}	190
O_2^+ + O^- → O + O + O	2.6×10^{-8}	200
O_2^+ + O_2^- → O_2 + O_2	2×10^{-7}	200
O_2^+ + O_2^- → O_2 + O + O	4.2×10^{-7}	190
O_2^+ + O_2^- + M → O_2 + O_2 + M	2×10^{-25}	201
O_2^+ + CO_3^- → CO + O_2 + O	3×10^{-7}	190
O_2^+ + CO_4^- → CO + O_2 + O_2	3×10^{-7}	190
CO_2^+ + O_2^- → CO + O_2 + O	6×10^{-7}	195
CO_2^+ + CO_3^- → CO_2(10002) + CO_2(10002) + O	5×10^{-7}	195
CO_2^+ + CO_4^- → CO_2(10002) + CO_2(10002) + O_2	5×10^{-7}	195

$O^- + M \rightarrow O + e + M$	$2.3 \times 10^{-9} \exp(-26000/T_g)$	202–204
$O_2^- + M \rightarrow O_2 + e + M$	$2.7 \times 10^{-10}(300/T_g)^{0.5} \exp(-5590/T_g)$	205
$O^- + O \rightarrow O_2 + e$	2.3×10^{-10}	206
$O^- + CO \rightarrow CO_2 + e$	$5.8 \times 10^{-9} T_g^{-0.39}$	207
$O^- + CO_2 + CO_2 \rightarrow CO_3^- + CO_2$	1.5×10^{-28}	198,208
$O^- + CO_2 + CO \rightarrow CO_3^- + CO$	1.5×10^{-28}	198,208
$O^- + CO_2 + O_2 \rightarrow CO_3^- + O_2$	3×10^{-28}	198,208
$O_2^- + CO_2 + M \rightarrow CO_4^- + M$	4.7×10^{-29}	198,208
V-V, V-V-T and V-V reactions (see section 3.3)		
Neutral-neutral reactions		
$CO_2 + M \rightarrow CO + O + M$	$6.06 \times 10^{-10} \exp(-52525/T_g)$	209
$CO_2 + O \rightarrow CO + O_2$	$7.05 \times 10^{-12} \exp(-18161.22/T_g)$	210
$CO_2 + C \rightarrow CO + CO$	1×10^{-15}	211
$CO + M \rightarrow C + O + M$	$1.52 \times 10^{-4}(T_g/298)^{-3.1} \exp(-129000/T_g)$	212
$O_2 + M \rightarrow O + O + M$	$3 \times 10^{-6} T_g^{0.1} \exp(-59380/T_g)$	212
$O_2 + CO \rightarrow O + CO_2$	$3.99 \times 10^{-14} \exp(-15274.67/T_g)$	213
$CO + O + CO_2 \rightarrow CO_2 + CO_2$	$5.81 \times 10^{-33} \exp(-1510/T_g)$	212,214
$CO + O + CO \rightarrow CO_2 + CO$	$2.49 \times 10^{-33} \exp(-1510/T_g)$	212,214
$CO + O + O_2 \rightarrow CO_2 + O_2$	$9.96 \times 10^{-33} \exp(-1510/T_g)$	212,214
$O + C + M \rightarrow CO + M$	$2.14 \times 10^{-29}(T_g/300)^{-3.08} \exp(-2114/T_g)$	212
$O_2 + C + M \rightarrow CO + O + M$	$1.99 \times 10^{-10} \exp(-2010/T_g)$	215
$O + O + M \rightarrow O_2 + M$	$5.2 \times 10^{-35} \exp(900/T_g)$	212
$CO(a^3\Pi) + O_2 \rightarrow CO + O + O$	2.4×10^{-11}	216
$CO(a^3\Pi) + CO \rightarrow CO_2 + C$	9.12×10^{-13}	216
$CO(a^3\Pi) + CO_2 \rightarrow CO + CO + O$	5×10^{-12}	217
$CO + O(^1D) \rightarrow CO_2$	8×10^{-11}	218
Collisional quenching of electronic states		
$CO(a^3\Pi) + O \rightarrow CO + O$	1.9×10^{-10}	219
$CO(a^3\Pi) + O_2 \rightarrow CO + O_2$	2.4×10^{-11}	216
$CO(a^3\Pi) + CO \rightarrow CO + CO$	5.6088×10^{-11}	216
$CO(a^3\Pi) + CO_2 \rightarrow CO + CO_2$	5×10^{-12}	217
$O(^1D) + O \rightarrow O + O$	8×10^{-12}	220
$O(^1D) + O_2 \rightarrow O + O_2$	$3.12 \times 10^{-11} \exp(70/T_g)$	221
$O(^1D) + CO \rightarrow O + CO$	$4.7 \times 10^{-11} \exp(62.542/T_g)$	222
$O(^1D) + CO_2 \rightarrow O + CO_2$	$7.9 \times 10^{-11} \exp(133/T_g)$	221
$CO_2(E1) + M \rightarrow CO_2 + M$	1×10^{-11} (see section 3.4)	
$CO_2(E1) + M \rightarrow CO_2 + M$	1×10^{-11} (see section 3.4)	

Chapter 3 Experimental approach

3.1 CO_2 gliding arc plasmatron with post-discharge carbon bed[4]

3.1.1 Experimental setup

In this thesis, we investigate the conversion of CO_2 by a gliding arc plasmatron (GAP) in combination with a carbon bed after the plasma reactor, to promote O/O_2 removal and increase the CO fraction in the exhaust mixture, as detailed in Section 1.4.1. The GAP used here was originally developed by Nunnally *et al.*[223] and previously described in detail by our group[224]. We used pure CO_2 as reactant gas in the plasma reactor (Air Liquide, purity 99.995%; flow rate kept constant at 10 standard liters per minute (slm)). The flow rate was adjusted with a Bronkhorst volumetric flow controller. The cathode and anode (stainless steel) were connected to an AC current source-type power supply (AFS) and to the ground, respectively. Electrode degradation (e.g., due to ablation) was very limited at the conditions under study. Indeed, this AC power supply reduces the thermal stress on the developing cathode spots. Furthermore, we utilize a strongly turbulent internal gas flow, which efficiently cools down the electrodes. Voltage and current were measured by using a high-voltage probe (Cal Test Electronics CT4028) and a current sense resistor (2 Ω) connected to a two-channel digital oscilloscope (Keysight DSOX1102G). Based on the product of measured voltage and current, we calculated the power injected in the plasma. The plasma arc was formed between both electrodes, as previously described[224], and can also partly leave the reactor through the anode (reactor outlet)[31], forming an afterglow in contact with the carbon bed, placed at the anode exhaust.

The general scheme, including the GAP plasma reactor, the carbon bed and the silo, is illustrated in Figure 3.1A, and a picture is given in Figure 3.1B.

---

[4] The experiments were performed by Dr. Fanny Girard-Sahun at the PLASMANT lab, with my support, and are part of the following paper:
Carbon bed post-plasma to enhance the CO_2 conversion and remove O_2 from the product stream
O.Biondo*, F. Girard-Sahun*, G. Trenchev, G. van Rooij, A. Bogaerts
Chemical Engineering Journal 442, 136268 (2022)
https://doi.org/10.1016/j.cej.2022.136268
*Shared first author

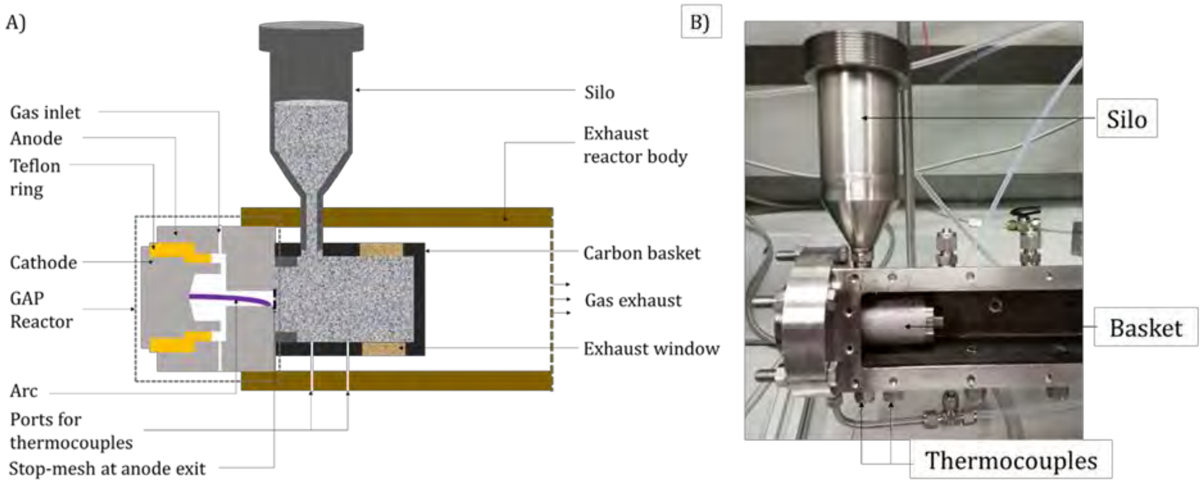

Figure 3.1. Scheme (A) and picture (B) of the GAP plasma reactor setup, including the carbon basket and silo. Note: The scheme is not at scale.

The carbon basket is directly attached to the anode. The silo containing spare carbon is attached to the basket through the exhaust reactor body. A metallic mesh is used at the anode exit to keep the carbon pellets out of the plasma reactor. Two dedicated ports allow measuring the temperature inside the carbon bed, at 15 and 35 mm from the anode exit; see Figure 3.2.

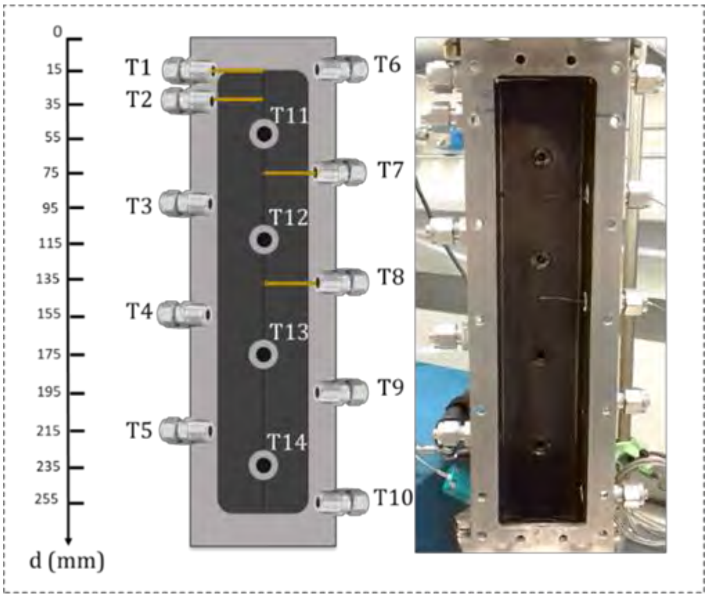

Figure 3.2. Scheme (left) and picture (right) of the post-plasma reactor tube with several ports for the K-type thermocouples (named Tx, with x = 1 to 14). The "zero" position corresponds to the reactor outlet (anode exit position). T1 and T2 (at 15 and 35 mm) measure the temperature inside the carbon bed; cf. Figure 3.1).

The reactor outlet (length 26 mm and inner diameter 7.07 mm, see Figure 3.3) was designed so that the contact of the plasma afterglow and the carbon bed is maximized: the aperture on the basket side is wider (Figure 3.3C), so that the carbon can get closer to the arc, which improves the contact between active plasma species and the carbon, and also takes benefit of the high temperature of the arc (3000 K according to computer simulations)[30].

Figure 3.3. A. and B. Side view and front view of the anode. C. Anode and basket assembled.

The basket was filled with ca. 5 g of carbon pellets for each plasma run. We used two different types of commercial carbon materials of different quality and particle size: activated charcoal Norit PK 1-3 (Sigma Aldrich, 1-3 mm typical pellet size, from peat, steam activated; named charcoal 1 in the figures below) and untreated activated charcoal C3014 (Sigma Aldrich, typical pellet size of 250-850 µm; named charcoal 2). Note that there is a very wide variety of commercial carbon samples available in the market. The particle size is usually the main (even sometimes the only one) parameter given by carbon suppliers. Therefore, the particle size of different carbon materials is an easy parameter to compare, but in future work, we also plan to compare carbon samples with the same particle size but different specific surface area and morphology, if available. The surface area of charcoal 1 and charcoal 2, as received, was estimated by N_2-Brunauer-Emmett-Teller (BET) measurements to be 705 ± 71 and 703 ± 70 m^2/g, respectively (see section 3.1.2. for details on the technique). The surface area of charcoal 1 was also measured after 7 minutes of treatment, in order to estimate the surface variation resulting from gasification reactions. The morphology of the charcoals as received, as well as after the gasification reactions, was investigated by scanning electron microscopy (SEM-see section 3.1.2.). The collected images are reported in Figure 3.4.

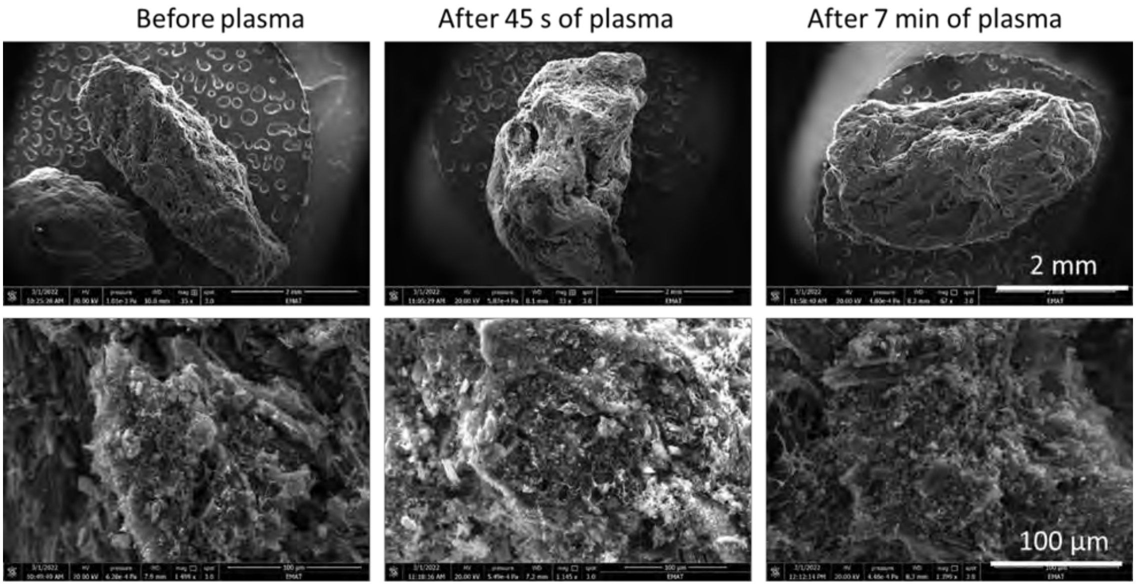

Figure 3.4. SEM images of charcoal 1, before and after the gasification reaction.

A silo (stainless steel) containing fresh carbon was inserted inside the basket through the post-plasma reactor tube, to provide a continuous source of carbon during the reaction and avoid carbon depletion upon reaction with O/O_2 (within the limits of the carbon volume contained in the silo, i.e., approx. 200 cm^3, see Figure 3.1A). It can be refilled with carbon through an opening on its top (Figure 3.1B). A mesh (stainless steel) was added at the anode exit to hold the carbon pellets inside the basket and avoid disturbing the arc inside the plasma reactor by creating a short circuit. In addition, the temperature in the carbon bed during operation was measured by means of two thermocouple ports along the basket (see Figure 3.1A-B).

Filters were placed on the exhaust line to make sure that the charcoal/ash particles did not enter the gas analytical equipment. The exhaust gas composition (CO_2, CO and O_2) was analysed online by NDIR (Non-Dispersive Infrared Spectroscopy, for CO_2 and CO) and by an optical oxygen sensor (for O_2). Besides, the exhaust gas mixture was also analysed by gas chromatography (GC); see next section.

The post-plasma reactor tube was designed specifically for the purpose of these experiments, i.e., (1) to accommodate the carbon basket combined with the silo, and (2) to measure the temperature in the post-plasma region as a function of distance from the reactor outlet, thanks to several ports for thermocouples. Indeed, to determine the best position of the carbon bed after the plasma at our operating conditions, we first measured the temperature profile in the post-plasma reactor tube with K-type thermocouples with four-channels type data loggers (Thermosense) in a free-reactor (i.e., without carbon bed; see Figure 3.2).

3.1.2 Characterization of the carbon materials

The carbon materials (namely charcoal 1 and 2) used in this study were characterized by BET analysis, scanning electron microscopy (SEM) and thermogravimetric analysis coupled with mass spectrometry (TGA-MS).

The specific surface area of charcoal 1 and 2 was calculated by the BET method. Prior to the measurements, the samples were degassed for 16 hours under vacuum at 200 °C. The sorption was then performed under N_2 atmosphere using a Quantachrome Quadrasorb SI.

For SEM analysis, an FEI Quanta 250 FEG scanning electron microscope was used. It was operated at 20 kV and the secondary electron detector was used to generate the images. The working distance (distance between the sample and the polepiece, i.e. the last lens of the imaging system; "WD") is given in the bar below every image and was always between 8 and 10 mm. To prepare the sample, a chuck of the charcoal was attached to the aluminium SEM stub using double-sided carbon tape. No further treatment of the sample was needed (like coating or crushing).

Thermogravimetric analysis (TGA) was used for studying the thermal properties of the activated charcoal, using a Mettler Toledo TGA-DSC 3+. The measurement was performed under a continuous flow of argon or oxygen i.e. 100 mL/min (80 mL/min protective gas to protect the balance + 20 mL/min purge gas). The sample was first flushed 45 min at 30 °C to remove all the air from the oven, and then heated up from 30 to 1000 °C with a heating rate of 10 °C/min. An alumina crucible of 150 µL was used. TGA was associated with a mass spectrometer to analyse the products from charcoal pyrolysis. The detection of the gaseous products was performed with a HPR-20 R&D (Hiden) mass spectrometer, controlled by EGAsoft software. The following settings were used: an electron voltage of 70 eV and an emission current of 400 mA. An electron multiplier (SEM) detector was used to scan m/z from 1 to 19, from 21 to 39 and from 42 to 120.

3.1.3 Gas analysis techniques

The exhaust gas mixture was analysed via various analytical techniques, to ensure the accuracy of the measurements. Non-dispersive infrared spectroscopy (NDIR) (X-STREAM enhanced general purpose process gas analyzer (XEGP) from Emerson) was used to analyse in real time the CO_2 and CO concentration profiles. Furthermore, we used a specific optical oxygen gas sensor (FDO_2, Pyroscience science technology) to measure the O_2 concentration continuously over time. We always started the measurements before plasma ignition, to first measure the blank composition, needed for the conversion calculation (i.e., 100 % CO_2). All measurements were performed in triplicate.

In addition, we also analysed the exhaust gas with a three-channel compact gas chromatograph from Interscience. Each channel leads to a different column and detector. Two channels were used for this study: (1) carboxen and molsieve columns (1010 PLOT and 5A, respectively) were used to separate the permanent gases, such as O_2, N_2 and CO, further detected with a thermal conductivity detector (TCD); and (2) two RT Q-bond columns (3 m and 10 m length, respectively) were used for the pre-separation and separation of CO_2 from the permanent gases, leading to a second TCD. The concentrations of the different products were calculated based on prior calibration of the GC in the concentration ranges of interest. As the GC analyses a sample immediately after sampling, a waiting time of about 6 minutes (time to get the chromatogram) was needed between one measurement and another. Moreover, this technique does not allow on-time measurements. Therefore, we compared the optical measurements (NDIR and optical O_2 sensor) with the GC measurements, to ensure their accuracy and to eventually use them for calculating the performance of the GAP with carbon bed in terms of CO_2 conversion and CO and O_2 concentrations. The methods agreed well within a 1% error margin and the comparison is shown later in Chapter 5, figure 5.3C.

3.1.4 Performance calculations

The conversion of CO_2 is usually defined as:

$$X_{CO_2}\,(\%) = ([CO_2]_{blank} - [CO_2]_{plasma})/[CO_2]_{blank} * 100\%, \quad (3.1)$$

with $[CO_2]_{blank}$ and $[CO_2]_{plasma}$ the CO_2 concentrations in the blank (without plasma) and during plasma, respectively (in %).

However, pure CO_2 splitting results in the expansion of the gas ($CO_2 \rightarrow CO + 1/2O_2$) i.e., 1 molecule of CO_2 produces 1.5 molecules after (complete) reaction. In presence of a carbon bed, possible heterogeneous reactions between CO_2/O_2/O/CO and solid carbon might also occur, contributing even more to the gas expansion effect[70]. Consequently, the exhaust, gas flow rate is higher than the initial flow rate and all species are diluted in a higher volume than the initial one, i.e., the CO_2 concentration in the final volume appears lower than it would be in the initial volume without expansion, resulting in an apparent higher conversion. Therefore, we need to know the exhaust flow rate, to correct the conversion from gas expansion. For this purpose, we used the method by Huang *et al.*[70]:

$$X_{corr,CO_2}(\%) = (Q_{in} - Q_{out} * [CO_2]_{out}/100\%)/Q_{in} * 100\%, \tag{3.2}$$

with Q_{in} and Q_{out} the total flow rates at the inlet and outlet, respectively (mol/min).

Q_{out} is determined based on the oxygen balance of the gas mixtures in the inlet and outlet[70]:

$$Q_{out}\ (mol/min) = 2*Q_{in}/(2*([CO_2]_{out}/100\%+[O_2]_{out}/100\%)+[CO]_{out}/100\%). \tag{3.3}$$

Besides the CO_2 conversion and the CO and O_2 concentrations in the exhaust mixture, we also calculated the energy efficiency and energy cost for our experiments. For this purpose, we need to know the specific energy input (SEI). The latter is the ratio of power over flow rate, and is defined as:

$$SEI\ (kJ/mol) = (P*60/Q_{CO_2,in}) * V_m, \tag{3.4}$$

with P the power delivered into the plasma (kW), $Q_{CO_2,in}$ the inlet CO_2 flow rate in slm, 60 is the number of seconds per minute (s/min) and V_m the molar volume at atmospheric pressure and room temperature (24.5 L/mol).

The energy efficiency is defined as:

$$\eta\ (\%) = \Delta H_R^{\circ} * (X_{corr,CO_2})/SEI\ (kJ/mol). \tag{3.5}$$

Based on our modelling insights, we expect the RBR to play only a minor role in the chemistry at the conditions under study. Therefore, the ΔH_R° used in the calculation refers to pure CO_2 splitting, i.e., ΔH_R° = 283 kJ/mol (cf. Equation (1.1)).

Finally, the energy cost of the CO_2 conversion process is defined as:

$$\text{EC (kJ/L)} = \text{SEI (kJ/L)}/(X_{\text{corr,CO}_2}/100\%) = (\text{SEI (kJ/mol)}/\ V_m)/(X_{\text{corr,CO}_2}/100\%). \qquad (3.6)$$

3.2 Laser scattering setup[5]

In this section, the main characteristics of the plasma setup and applied diagnostics, used in Chapter 6 and 7, are illustrated. First, the experimental setup is presented, followed by the different types of laser scattering applied within this thesis. In the last section, the gas chromatography measurements, performed separately from the laser scattering measurements, are introduced.

3.2.1 Experimental setup

The reactor configuration used in our experiments was already applied to CO_2 conversion in earlier studies conducted at the Dutch Institute for Fundamental Energy Research (DIFFER), and thoroughly described elsewhere[25,225]. Following the same method as van de Steeg *et al.*[51], we make use of combined Thomson-Raman scattering to obtain spatially resolved values of T_e and n_e, as well as rotational temperature, assumed to be in equilibrium with T_g. We couple this laser scattering to a MW plasma setup as schematically illustrated in Figure 3.5.

---

[5] The description of these diagnostics is part of the following papers:
Power concentration determined by thermodynamic properties in complex gas mixtures: the case of plasma based dry reforming of methane
O.Biondo, A. Hughes, A. van de Steeg, S. Maerivoet, B. Loenders, G. van Rooij, A. Bogaerts
Plasma Sources Sci. Technol. 32, 045001 (2023)
https://doi.org/10.1088/1361-6595/acc6ec

Flow pattern control avoids solid carbon deposition in plasma-based dry reforming of methane
O.Biondo, C. F. A. M. van Deursen, A. Hughes, A. van de Steeg, W. Bongers, M. C. M van de Sanden, G. van Rooij, A. Bogaerts
In preparation for submission to Chemical Engineering Journal

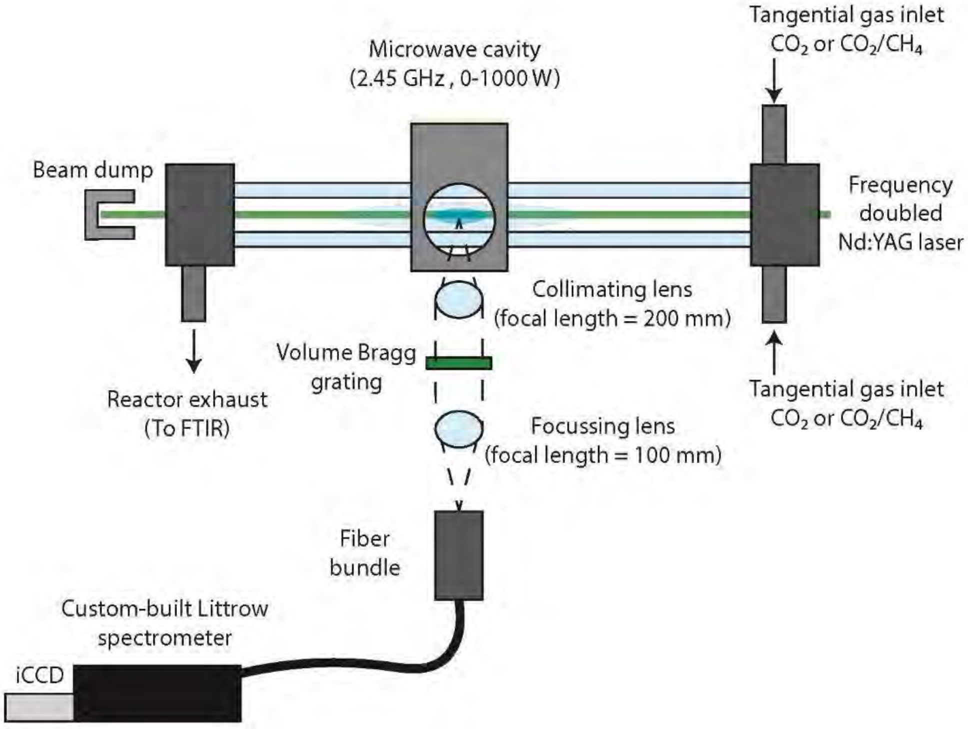

Figure 3.5. Schematic of the combined plasma-laser scattering setup.

A 2.45 GHz magnetron of 1 kW input power provides microwaves to the plasma, ignited in a quartz tube of 27 mm inner diameter. The quartz tube is positioned at a 90° angle from the long side of a WR340 waveguide. Optimal power transfer to the plasma is achieved by the combination of an adjustable short and EH tuner. More details are available in the doctoral thesis of van de Steeg[225], where the reactor setup was fully characterized. CO_2 (99.995 % purity) and CH_4 (4.5 grade) are premixed and tangentially injected into the reactor by two nozzles, located 100 mm upstream of the waveguide center. The tangential injection is used to create a swirl flow in the tube, protecting the walls from overheating and eventually melting, and the volumetric flow rate is fixed at 10 or 17 slm. All the experiments presented in Chapter 6 are conducted in a forward vortex (FV) flow configuration, whereas FV and reverse vortex (RV) flow configuration[226] are compared in Chapter 7.

A frequency-doubled Nd:YAG laser (SpectraPhysics GCR-230, 30 Hz, 400 mJ per 10 ns pulse, 532 nm) is focused into the reactor along the axial direction and the scattered light is collimated and focused into a Littrow spectrometer. Attenuation of the intense Rayleigh scattered light and stray light is necessary to resolve Thomson and Raman signals. Therefore, a volume Bragg grating filter is placed before the entrance of the fiber array.

The resulting spectrally resolved image is captured by an intensified camera (Princeton Instruments PI-MAX, 40 ns gate-width). Additionally, all measured images are corrected for the sensitivity of most optical components (camera, fibers, spectrometer), as calibrated with an integrating sphere. More details regarding the laser scattering setup, along with a discussion of the improvements introduced to the diagnostics, are available elsewhere[51,225].

In Chapter 6, we characterize the optical emission distribution and its evolution as a function of pressure (in the range of 75-500 mbar) for small additions of CH_4 (up to 30% of total volumetric flow rate) to CO_2 with an image intensified CCD high-speed camera. After ignition of the plasma in pure CO_2, CH_4 is gradually added to the feed gas in steps of 0.5 slm to ensure stability of the discharge and prevent carbon deposition inside the reactor, which may lead to operational issues. Severe carbon deposition inside the quartz tube is observed after ca. 5 minutes of operation with 30% CH_4 in the feed gas. Imaging of the plasma by OES is widely used in the context of CO_2 discharges[51,227–231]. In particular, the O 777 nm emission line intensity is often followed to reconstruct the shape of the plasma and, sometimes even the power density distribution[232]. Of course, this technique is only suitable when the optical emission arises from electron-impact excitation to the upper excited state involved, as is the case for the 777 nm $O(3s^5S^0 \leftarrow 3p^5P)$ transition[232]. An example of the plasma geometry obtained through OES imaging, along with the radial resolution of the laser scattering measurements, is displayed in Figure 3.6. The radial resolution is obtained by taking multiple spectra at different positions of the plasma relative to the laser and has a typical step size of 0.5 mm. The required motion is provided by an automated translation stage on which the entire plasma setup is mounted. Individual spectra contain a fine axial resolution of 8 mm along the laser propagation direction, as the linear fiber array images ca. 20 fibers (400 μm fiber diameter) simultaneously on the camera. The radial resolution is obtained by taking multiple spectra at different positions of the plasma relative to the laser and has a typical step size of 0.5 mm. The required motion is provided by an automated translation stage on which the entire plasma setup is mounted. Individual spectra contain a fine axial resolution of 8 mm along the laser propagation direction, as the linear fiber array images ca. 20 fibers (400 μm fiber diameter) simultaneously on the camera. As integrated optical emission is generally not linear with power density but a complicated function of species densities and temperatures, a correction factor is used to estimate the plasma volume from the radial and axial decays of the 777 nm line emission. Viegas *et al.*[228] proposed to calculate the correction factor as the ratio of (Λ_{n_e}) over the FWHM of the 777 nm line emission distribution (Λ_{777}). Later, in Section 6.3.4, we provide an estimation of the $\Lambda_{n_e}/\Lambda_{777}$ ratio from our experimental results and compare them with

Viegas *et al.*[228]. More details on the derivation of the plasma dimensions are available in Wolf *et al.*[232].

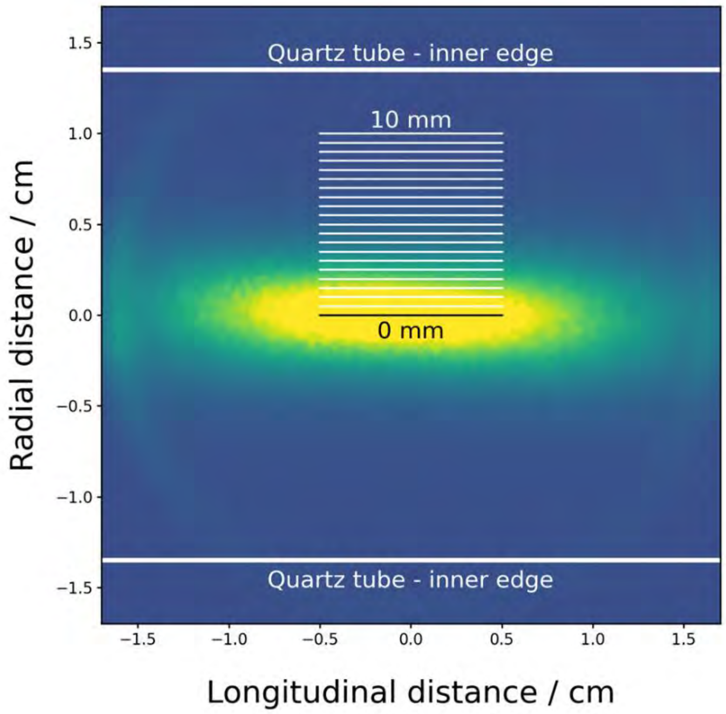

Figure 3.6. Plasma photograph (120 mbar, 1000 W, 10 slm CO_2). The black line represents the laser chord that is covered by the fiber array to yield axial profiles in a single experiment. The white lines represent the scanning of the entire reactor with respect to the laser to yield radial profiles.

3.2.2 Laser scattering

Laser scattering is used for the characterization of the CO_2 and DRM MW plasma in Chapter 6 and 7 of this thesis. The use of laser scattering enables good spatial resolution, excellent temporal resolution and non-intrusiveness for measurements of vibrational and rotational temperatures, electron properties and the heavy-particle composition. Within this thesis, two types of laser scattering are used: inelastic scattering on molecules (Raman scattering) and elastic scattering on free plasma electrons (Thomson scattering). A third type of laser scattering, namely elastic scattering on molecules (Rayleigh scattering), is often applied to measure T_g[25,233,234], gas density (pressure)[235] and composition (assuming local chemical equilibrium)[25]. However, in this study T_g is measured by rotational Raman scattering. Thus, Rayleigh scattering is not used. Figure 3.7 contains an overview of the different types of laser scattering, their spectral shape (specifically for CO_2 in the case of Raman scattering) and the type of information obtained.

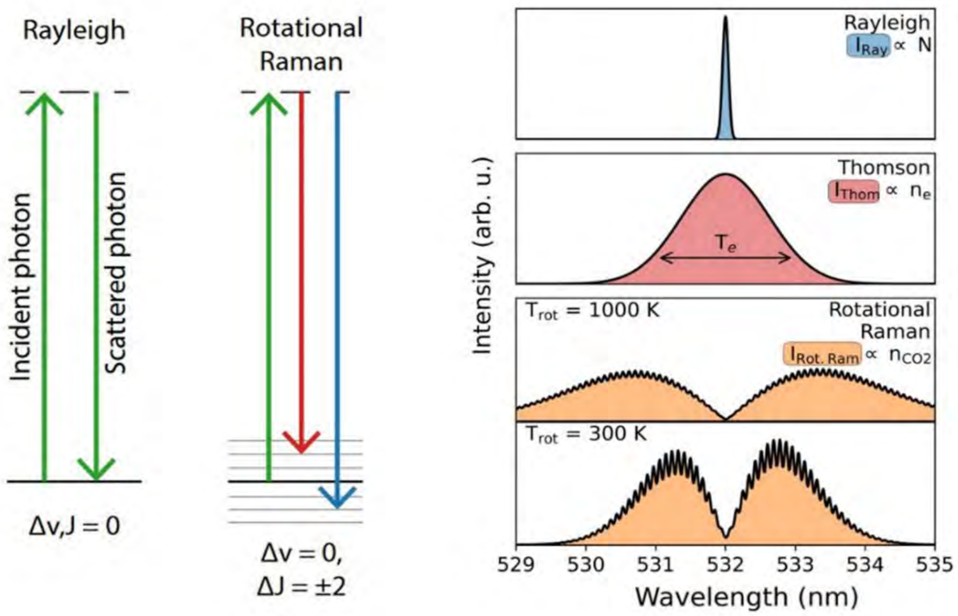

Figure 3.7. Overview of laser scattering types. Left: The Rayleigh and Raman processes illustrated with rovibrational energy levels. Right: Spectral signature of different scattering types: Rayleigh scattering, Thomson scattering and rotational Raman scattering. The effect of increasing temperatures on the Raman spectra is indicated. This figure is adapted from the doctoral thesis of van de Steeg[225]*.*

3.2.2 (a) Raman scattering

Raman scattering is a robust technique to infer the populations of rotational and vibrational states of the present molecules by inducing a change in quantum number of the scattering species. In rotational Raman scattering, the change in quantum number, usually $\Delta J = \pm 2$, is spectrally close to the laser fundamental due to the small energy separation of rotational states (Figure 3.7)[236]. In addition, spontaneous Raman scattering on O atoms is used for quantitative oxygen detection[237]. The wavelength of the scattered photon changes depending on the type of scattering particle and amount of excitation, enabling the fingerprinting of the rotational and vibrational distribution functions of the target species. In our study, we use rotational Raman scattering in pure CO_2 and CO_2/CH_4 plasmas to spatially resolve the rotational temperature T_{rot}, which can be assumed equilibrated with T_g. Moreover, this powerful technique can be applied to detect and quantify the number densities of multiple Raman active molecules in the spectral range of a single measurement, as previously demonstrated[56,234,238,239]. However, the addition of CH_4 poses extra complications to the *in-situ* characterization of the plasma-activated gas mixture. The detection of CH_4 dissociation products, such as CH_3 and CH radicals, requires more sophisticated laser techniques (e.g. laser-induced fluorescence (LIF)[240], coherent anti-Stokes Raman scattering (CARS)[241–243] and photo-fragmentation LIF[244]), which are currently not suitable for our setup. Therefore, the quantification of the species formed in the plasma upon the addition of CH_4 and the full characterization of the gas mixture are delegated to future studies.

3.2.2 (b) Thomson scattering

Thomson scattering originates from the elastic scattering of the laser photons on the free plasma electrons and takes the shape of a single peak around the laser wavelength (Figure 3.7). However, this peak is much wider than the Rayleigh peak due to an increased Doppler width, caused by the smaller mass and generally higher temperature of the electrons[245]. The cross-section of Thomson scattering is high, but because of the typically low ionization degree of CO_2 plasma[232], the absolute strength of Thomson scattering remains low. That is the reason why we use a Bragg grating filter to attenuate the Rayleigh signal, which otherwise would completely hide the Thomson feature. The total scattering intensity is proportional to n_e, while the width of the Thomson feature is proportional to T_e[245], providing spatially resolved measurements of these two important macroscopic descriptors of electrons. Thomson scattering in pure molecular discharges is complicated by spectral overlap of rotational Raman scattering. However, recent developments[51,246–248] enabled the disentangling of the Raman and Thomson features. We apply the technique to follow the radial decay and the evolution with pressure of n_e and T_e in Chapter 6, as well as, to estimate the variations with the reactor geometry in Chapter 7. For all experiments, the Thomson spectra are fitted as a single Gaussian centered on the laser fundamental. The absolute values of n_e follow from calibration with the rotational Raman spectrum of N_2 at room temperature and fixed pressure, while T_e is calculated from the fitted width of the Gaussian. For more details on the spectral analysis, we refer to the work of Carbone and Nijdam[245].

3.3 Gas chromatography[6]

In Chapter 7, the reactor performance is evaluated for two different flow geometries, namely FV and RV configurations. The exhaust composition is measured with a gas chromatograph (GC) (CompactGC 4.0 model), positioned about 2 m downstream from the microwave cavity. N_2 is added after the reactor outlet as internal standard to account for the flow rate changes between the reactor in- and outlet arising from e.g., formation of dissociation products and removal of liquids, as detailed by Wanten *et al.*[86] and reported in Section 3.3.1. The gas flow going into the GC is dried using a MD-70-24 nafion filter to prevent overflow of the liner and ensure peak separation, which could be compromised due to poor stationary phase wetting. Three injection loops are used for the detection of all components in the gas mixture. The first loop consists of an Rt-Q-Bond pre-column (4 m length, 0.32 mm ID) followed by a TC-Molsieve 5A (10 m length, 0.53 mm ID) column and a TCD detector for the detection of CO, N_2 and O_2. The second loop consists of an Rt-Q-Bond pre-column (2 m length, 0.32 mm ID) followed by a CP-PoraBOND Q column (20 m length, 0.32 mm ID) and a TCD detector for the detection of CO_2 and C_2H_2. The third loop consists of an Rt-Q-Bond column (3 m length, 0.32 mm ID) followed by a Molsieve 5A (10 m length, 0.53 mm ID) column and a TCD for detection of H_2. The molar composition of the gas is then obtained from the chromatograms using linear regression after calibrating the system.

3.3.1 Correction factors α and β

Most plasma reactors are plug-flow type reactors where the reactions, taking place in quasi-isobaric conditions, determine a change in the total number of particles, the gas volume and the volumetric flow rate, along the reactor. Particularly in DRM, the change in concentration of the gas mixture components can be significant and the process parameters depending on the volumetric flow rate are affected. Therefore, neglecting the effect of reactions on concentrations and on the gas flux introduces a systematic error in the computation of process[249]. Furthermore, H_2O is removed prior to injecting the gas in

---

[6] The measurements were performed by Cas van Deursen at DIFFER (Eindhoven), with my support, and are included in the following paper:
Flow pattern control avoids solid carbon deposition in plasma-based dry reforming of methane
O.Biondo, C. F. A. M. van Deursen, A. Hughes, A. van de Steeg, W. Bongers, M. C. M van de Sanden, G. van Rooij, A. Bogaerts
In preparation for submission to Chemical Engineering Journal

the GC, and some products may be removed from the gas mixture along with H_2O, thus leading to a change in concentration of the remaining components. If not taken into account, these effects can lead to significant errors regarding conversion, selectivity, etc. To correct for these effects, N_2 is used as an internal standard and added to the gas mixture after the reactor outlet. In this way, two correction factors can be defined:

$$\alpha = \frac{\phi_{\text{plasma}}}{\phi_{\text{blanc}}} = \frac{A_{\text{IS}}^{\text{blanc}}}{A_{\text{IS}}^{\text{plasma}}}(1+\beta)-\beta \tag{3.7}$$

with ϕ_{blanc} and ϕ_{plasma} being the volumetric flow rate before and after the plasma, respectively, and $A_{\text{IS}}^{\text{blanc}}$ and $A_{\text{IS}}^{\text{plasma}}$ being the integrated area of the peak detected at the GC of CO_2 or CH_4 with plasma off and on, respectively, and

$$\beta = \frac{\phi_{\text{IS}}}{\phi_{\text{blanc}}}, \tag{3.8}$$

defined as the flow rate of the internal standard ϕ_{IS} with respect to the flow rate at the reactor inlet. The factor α corrects for the overall change in flow rate when comparing a blank to a plasma measurement, and can be expressed as a function of β and the peak areas of the internal standard for a blank and plasma measurement. These factors are derived from the work of Pinhão *et al.*[249] by Wanten *et al.*[86].

3.3.2 Performance parameters

The concentrations for each reactant *i* and product *j*, corrected for the dilution by the addition of an internal standard, can be defined for a blank and plasma measurement as:

$$c_i^{\text{blanc}} = c_{i,m}^{\text{blanc}}\left(1+\frac{\phi_{\text{IS}}}{\phi_{\text{blanc}}}\right) = c_{i,m}^{\text{blanc}}(1+\beta) \tag{3.9}$$

$$c_i^{\text{plasma}} = c_{i,m}^{\text{plasma}}\left(1+\frac{\phi_{\text{IS}}}{\phi_{\text{plasma}}}\right) = c_{i,m}^{\text{plasma}}\left(1+\frac{\beta}{\alpha}\right) \tag{3.10}$$

$$c_j^{\text{plasma}} = c_{j,m}^{\text{plasma}}\left(1+\frac{\phi_{\text{IS}}}{\phi_{\text{plasma}}}\right) = c_{j,m}^{\text{plasma}}\left(1+\frac{\beta}{\alpha}\right) \tag{3.11}$$

with c_m being for the concentration measured at the GC.

The conversion of a single reactant is expressed in terms of the concentrations, defined in equation (3.9) and (3.10), and the correction factor α defined in equation (3.7):

$$X_i = \frac{c_i^{\text{blanc}} - \alpha \cdot c_i^{\text{plasma}}}{c_i^{\text{blanc}}} = 1 - \frac{\alpha \cdot c_i^{\text{plasma}}}{c_i^{\text{blanc}}}. \tag{3.12}$$

The total conversion is defined as the weighted average of the conversion for each reactant, weighted over their concentration in the inlet gas mixture:

$$X^{\text{tot}} = \sum_i c_i^{\text{blanc}} \cdot X_i. \tag{3.13}$$

The SEI and the energy cost are calculated according to equations 3.4 and 3.6 in Section 3.1.4. The selectivity is defined as the amount of atoms *a* that end up in product *j*, with respect to the amount of atoms *a* that are available through conversion of the reactant(s) *i*. In equation form, this becomes:

$$S_{j,a} = \frac{\mu_{j,a} \cdot \alpha \cdot c_j^{\text{out}}}{\sum_i \mu_{i,a} \cdot \left(c_i^{\text{in}} - \alpha \cdot c_i^{\text{out}}\right)}. \tag{3.14}$$

3.3.3 Estimation of the H_2O concentration

H_2O is removed from the gas mixture before injection in the GC to ensure accurate measurements of the other gas components. Therefore, the concentration of H_2O in the plasma mixture is obtained from oxygen balance equation, whose formula is written as:

$$b_O = \frac{\alpha \cdot \left(\sum_i \mu_{i,O} \cdot c_i^{\text{plasma}} + \sum_j \mu_{j,O} \cdot c_j^{\text{plasma}}\right)}{\sum_i \mu_{i,O} \cdot c_i^{\text{blanc}}} \cdot 100 = 100\%, \tag{3.15}$$

assuming that the liquid fraction removed is composed of 100% H_2O, as explained in Wanten *et al.*[86]. Equation (3.15) can be rewritten as:

$$c_{H_2O} = \sum_i \mu_{i,O} \cdot c_i^{\text{blanc}} - \left(\alpha \cdot \sum_i \mu_{i,O} \cdot c_i^{\text{plasma}} + \sum_j \mu_{j,O} \cdot c_j^{\text{plasma}}\right). \tag{3.16}$$

Chapter 4 Insights into the limitations to vibrational excitation of CO_2[7]

Abstract

In this chapter, the viability of vibrational excitation is investigated in low-pressure pulsed discharges, with the intention of selectively exciting the asymmetric stretching mode, leading to stepwise excitation up to the dissociation limit of the molecule. Gas heating is crucial for the attainability of this process, since the efficiency of V-T relaxation strongly depends on temperature, creating a feedback mechanism that can ultimately thermalize the discharge. With the aim of backtracking the origin of gas heating in pure CO_2 plasma, we perform a kinetic study to describe the energy transfers under typical non-thermal plasma conditions, using the model described in Chapter 2 (section 2.2). The validation of our kinetic scheme with pulsed glow discharge experiments enables to depict the gas heating dynamics. In particular, we pinpoint the role of V-V-T relaxation in redistributing the energy from asymmetric to symmetric levels of CO_2, and the importance of collisional quenching of CO_2 electronic states in triggering the heating feedback mechanism in the sub-millisecond scale. This latter finding represents a novelty for the modelling of low-pressure pulsed discharges and we suggest that more attention should be paid to it in future studies. Additionally, O atoms convert vibrational energy into heat, speeding up the feedback loop. The efficiency of these heating pathways, even at relatively low gas temperature and pressure, underpins the lifetime of V-T non-equilibrium and suggests a redefinition of the optimal conditions to exploit the *ladder-climbing* mechanism in CO_2 discharges.

---

[7] This chapter is based on:
Insights into the limitations to vibrational excitation of CO_2: validation of a kinetic model with pulsed glow discharge experiments
O.Biondo, C. Fromentin, T. Silva, V. Guerra, G. van Rooij, A. Bogaerts
Plasma Sources Sci. Technol., 31, 074003 (2022)
https://doi.org/10.1088/1361-6595/ac8019

4.1 Introduction

Low-power glow discharges are typically grouped under the family of low-temperature plasmas (LTPs), which, by definition, are characterized by low T_g and a certain degree of vibration-translation (V-T) non-equilibrium. Therefore, this category represents a good candidate to explore the optimal conditions for a consistent vibrational excitation. Here, quenching of vibrational quanta to heat (V-T relaxation) constitutes an important pathway for vibrational energy loss and, consequently, gas heating[48]. The onset of V-T relaxation triggers a feedback loop between gas heating and vibrational deactivation because the rate coefficient of V-T relaxation increases with T_g. This eventually guides the discharge towards a V-T equilibrium, making the exploitation of the *ladder-climbing* mechanism very challenging[15,250]. In order to stop such a loop mechanism and limit T_g during the operations, power pulsing has been brought to attention as a convenient approach to attain high energy efficiency by modulating the pulse and inter-pulse duration[166]. Moreover, power pulsing enables the study of the plasma kinetics during the onset of the discharge, providing useful insights into the underlying mechanisms for vibrational excitation and relaxation and their role into the gas heating dynamics[50,119,129,130,246] and the recombination of O atoms to O_2 that can affect CO_2 conversion[251]. Therefore, pulsed low-power glow discharges form an ideal testbed for validation of kinetic models. In fact, glow discharges are an extremely useful instrument for studying the plasma kinetics, providing a simple geometry that can be safely approximated to a plug flow reactor[252] and allowing for the application of many *in-situ* diagnostics (e.g. Fourier transform infrared spectroscopy[50], Raman scattering[239], optical emission spectroscopy (OES)[253] and actinometry[254]).

With this in mind, we chose to verify our kinetic scheme for vibrational excitation and heating dynamics in CO_2 low-temperature plasmas, detailed in Chapter 2, with the experiments presented by Klarenaar *et al.*[50]. This set of experiments was already applied to unveil the relevant reactions for vibrational excitation, during the active phase of the discharge[130], and relaxation, in the afterglow[129]. These two contributions opened the possibility of using a state-to-state approach to benchmark the validity of a multi-temperature description of CO_2 plasmas for capturing some essential features of non-equilibrium phenomena, as previously done for N_2[255], with reduced computational effort. For instance, Kosareva *et al.*[256] demonstrated that the state-to-state approach can be substituted by the multi-temperature approach for the problem of spatially homogeneous relaxation in non-equilibrium CO_2 flows, without sacrificing the accuracy of the results. The multi-temperature description consisted of up to 4 different temperatures, namely T_g, and the vibrational temperatures of the symmetric stretching (T_1), bending (T_2) and asymmetric (T_3) levels[256]. Alternatively, symmetric and bending modes can be described by T_{12} thanks to the Fermi resonance between their levels (as described in section 2.1), reducing the description to a three-temperature model.

Despite T_g is a key parameter determining the efficiency of vibrational energy exchanges and, more in general, a macroscopic descriptor of plasmas, only a few modelling studies featured its self-consistent calculation for CO_2 discharges. This means that in most cases we can only estimate the degree of vibrational excitation when we know T_g from the experiments. The possibility of calculating T_g from the discharge parameters (i.e. power and volume) enables an appropriate understanding of the gas heating and, ultimately, a better definition of the optimal discharge conditions to harness vibration-translation non-equilibrium. In the context of N_2 and N_2-O_2 mixtures, Pintassilgo and Guerra[257] studied the energy transfer to gas heating with a 0D model. In particular, the authors showed that the energy transferred to heat increases with O_2 addition to N_2, with a maximum at 20%, in line with experimental observations. More recently, Kelly *et al.*[258] inferred the plasma dynamics in a N_2 pulsed MW discharge by a combination of 0D modelling and experiments. Specifically, their study elucidated the role of gas heating in inducing thermal-ionization instabilities, which are believed to drive the discharge volume contraction with rising gas pressure. Other contributions on the modelling of these mixtures can be found in the review by Popov and Starikovskaia[259]. For CO_2 plasma discharges, Silva *et al.*[164] modelled the afterglow of a pulsed glow discharge with a self-consistent calculation of T_g, providing a very good agreement with the experimental T_g evolution. Their work proved that the gas heating dynamics in the post-discharge region can be accurately described by V-T and V-V relaxation. Their observation finds additional confirmation in our calculations. However, the energy transfer scheme depicted by their heating analysis may not be sufficiently descriptive for the active part of the discharge.

Recently, Pokrovskiy *et al.*[157] studied the relevant mechanisms underlying the onset of gas heating in a nanosecond capillary discharge at 19-20 mbar. These types of discharges feature E/N typically larger than pulsed glow discharges (i.e. 150-250 Td), promoting the direct electron-impact dissociation over the *ladder-climbing* mechanism. Under these conditions, the well-known phenomenon of the fast gas heating[158] dominates the heating dynamics during the pulse on-time[157]. This mechanism can consume an important fraction of the energy deposited by the electrons onto molecules, limiting the performance and efficiency of the reactor. The mechanism of fast gas heating, which occurs at the sub-microsecond timescale, was traced back to the quenching reactions of $CO(a^3\Pi)$, $O(^1S)$ and $O(^1D)$ excited species, which are products of the direct electron-impact dissociation of CO_2[157]. This heating channel is faster than typical V-T and V-V relaxation[259], which cannot fully describe the heating dynamics. Indeed, van de Steeg *et al.*[246] showed that V-T relaxation makes up only ca. 50% of the total heating rate in a pulsed MW discharge (pulse time = 200 µs, p = 25 mbar). Under these conditions, the characteristic V-T relaxation time can be estimated to be about 0.15 ms at 300 K[260], thus other heating pathways need to be taken into account to explain the T_g evolution. Similar conclusions can be drawn for the pulsed glow discharge case, i.e. gas heating onsets at $t < 0.1$ ms, before the maximum vibrational excitation is reached ($t \cong 0.9$ ms)[50].

In this perspective, we developed a 0D kinetic model (see Section 2.2) to reproduce the temperature (T_g, T_{12} and T_3) evolution measured by[50] and to verify our new kinetic scheme, which includes a detailed description of the vibrational chemistry of CO_2, along with the electronic excitation and relaxation of different species. We constructed the kinetic scheme starting from the preceding modelling efforts of both the research groups (N-PRiME[119,129,130] and PLASMANT[48,52,261,262]), following a procedure established within the framework of this collaboration. In this work, we focused on the modelling of the *single-pulse* measurements[50], where the dissociation degree throughout the pulse is negligible and no dissociation products are left in the subsequent pulse. In this way, we could study the CO_2 vibrational and electronic kinetics and their role into the gas heating dynamics, decoupling it from the influence of dissociation products. The inclusion of the collisional quenching of CO_2 electronic states represents a novelty in the modelling of low-pressure pulsed discharges that deserves more attention in the study of the energy transfers in CO_2 plasmas. Upon the verification of the kinetic scheme proposed, here we demonstrate the importance of the relaxation of electronically excited molecules besides vibrational deactivation, which we could bring to light via a self-consistent calculation of T_g.

4.2 Results and discussion

4.2.1 Validation of the vibrational kinetics

The investigation of the vibrational kinetics by means of a kinetic model must first be based on a confirmation of the kinetic scheme with experiments. To this end, the *single-pulse* measurement performed by Klarenaar *et al.*[50] in a pure CO_2 glow discharge represents an ideal benchmark for the validation of a 0D kinetic model. Indeed, this measurement was already used for this purpose by Grofulović *et al.*[130]. The authors demonstrated that their model was able to predict in good approximation the evolution of T_3 while introducing the experimental T_g evolution, the n_e profile estimation and a E/N of 55 Td as input parameters. The very good agreement between the model predictions and the experimental results verified the description of the kinetics of v_3. As a follow-up to their work, we started our modelling study from the simulations performed by Grofulović *et al.*[130] and we replicated the comparison with the experimental temperature profiles to validate the changes we have implemented since then. The comparison is illustrated in Figure 4.1.

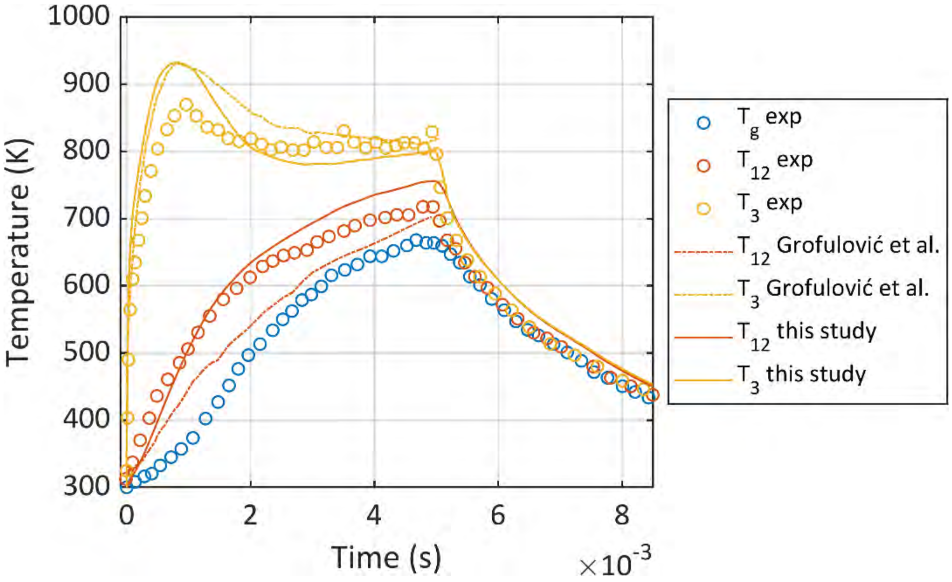

Figure 4.1. Time-evolution of T_{12} and T_3, measured and digitalized from Klarenaar et al.[50] *(circles), simulated and digitalized from Grofulović et al.*[130] *(dash-dotted lines), and simulated in this study (solid lines). The experimental T_g profile, used for the simulations, is also plotted.*

The new chemistry set refines the agreement with the experimental vibrational temperature profiles when compared to the previous effort[130]. In particular, T_3 and T_{12} show similar evolutions during the first millisecond in the pulse, until the peak in T_3 is reached. After that, a deviation in the model predictions arises: our T_{12} more or less follows the experimental trend whereas T_{12} calculated in Grofulović *et al.*[130] relaxes to T_g. Our reaction analysis indicates that the $CO_2(10^002)$ level, from which T_{12} is derived, is mostly populated by e-V, V-V and V-V-T reactions at 1 ms. and T_g is still too low to have an important contribution from V-T reactions. To explain the discrepancy of the results, note that in Grofulović *et al.*[130] while considering the complete vibrational kinetics of Blauer and Nickerson[124], the repeated reaction $CO_2(11^102) + CO_2(01^101) \leftrightarrow CO_2(10^002) + CO_2(10^002)$ was badly adjusted to $CO_2(11^102) + CO2(00^001) \leftrightarrow CO_2(10^002) + CO_2(10^002)$. The latter reaction, not considered in this study, leads to an underestimation of the higher bending and symmetric levels ($v_2 > 2$ and $v_1 > 1$) at short-time scales ($t < 5$ ms) of the plasma pulse. Notwithstanding this correction, the temperature of the symmetric levels was still underestimated compared to the experiments. Therefore, the reason for the different T_{12} is to be sought elsewhere.

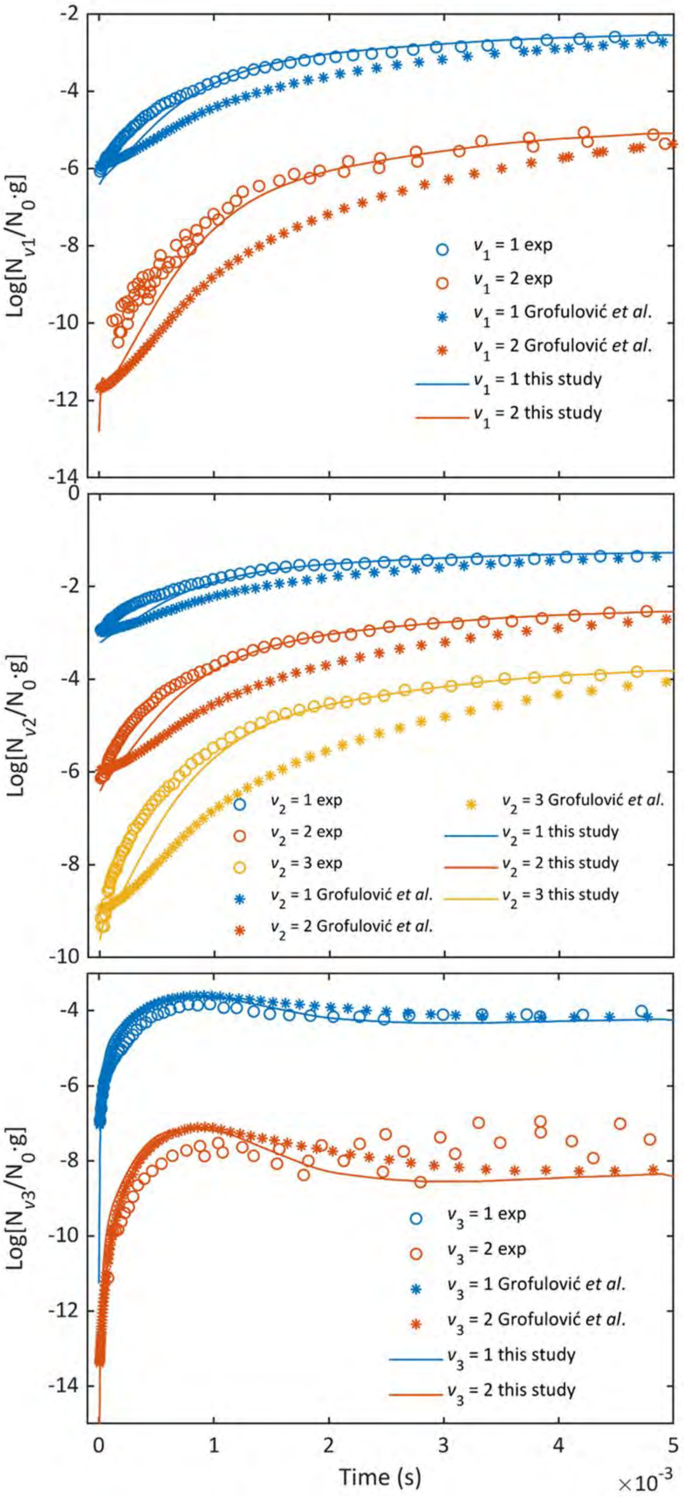

Figure 4.2. Normalized density of several states (a) in the symmetric stretching mode, (b) in the bending mode and (c) in the asymmetric stretching mode of vibration as a function of the discharge time. The circles corresponds to the experimental data[50] *(digitalized from*[130]*), the asterisks to the calculations of Grofulović et al* [130] *(digitalized) and the solid lines to our calculations.*

Specifically, $CO_2(00^011) + CO_2(00^001) \leftrightarrow CO_2(02^201) + CO_2(01^101)$ was only introduced in this study; analogously to reaction (2.12), this V-V-T reaction populates v_{12} at the expense of v_3. The close coupling via efficient V-V exchanges of $CO_2(02^201)$ and $CO_2(10^002)$ causes an increase in T_{12}, explaining the improved agreement with the experiments. These results confirm the importance of the additional V-V-T process to describe the vibrational kinetics of both v_3 and v_{12}, whose evolutions are closely related. Moreover, Grofulović *et al.*[130] found that the populations of some v_{12} states were underestimated by their model compared to the experiments. The temporal evolution of the calculated and measured normalized populations of $CO_2(v_10^00f)$, $CO_2(0v_2^{v2}01)$, and, in addition, $CO_2(00^0v_31)$ are presented in panels (a), (b) and (c) of Figure 4.2, respectively.

For v_{12}, our model results are in very good agreement with the experimental data (Figure 4.2(a,b)), displaying a growth of the vibrational populations closer to the experiments than the predictions of Grofulović *et al.*[130]. In fact, the additional V-V-T transfer considered in this study speeds up the redistribution of the energy from v_3 to v_{12}. Figure 4.3 shows that the characteristic relaxation rate coefficient of V-V-T transfers is right in between typical V-V and V-T transfer rate coefficients.

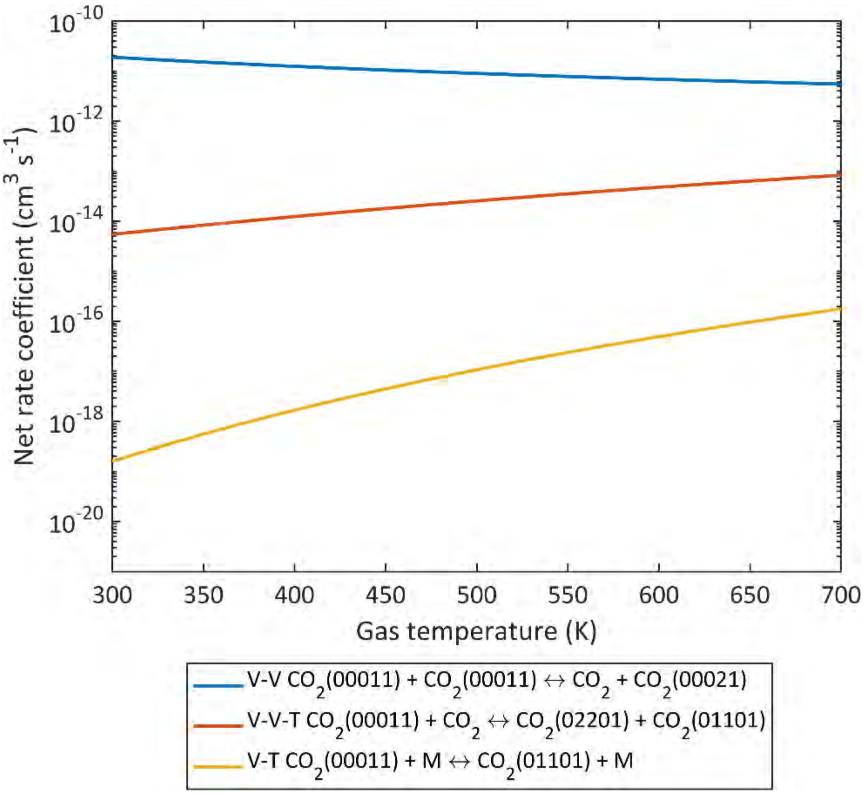

Figure 4.3. Net (forward minus reverse) rate coefficients of the main relaxation reactions of the first asymmetric level of CO_2 as a function of the gas temperature.

Despite V-V is a faster transfer, V-V-T and V-T reactions represent a nearly irreversible loss of energy for v_3 to v_{12}, since V-T from v_{12} is a very efficient channel of loss of vibrational quanta and, consequently, heating, as demonstrated in the next section and pointed out in Armenise and Kustova[263]. Therefore, V-V-T relaxation can be identified as a relevant mechanism determining the timeframe for a significant T_3-T_g non-equilibrium.

Nevertheless, some underestimation of the growth of the v_{12} populations, along with a slight overestimation of the v_3 population, is still present during the onset of the discharge (cf. Figure 4.2). This discrepancy indicates that fast energy transfer mechanisms from v_3 to v_{12} may still lack in our model. As suggested by Grofulović *et al.*[130], collisions with O_2 molecules or excited atoms may play a role here, even though the CO_2 dissociation degree is typically very low at the beginning of the pulse. Alternatively, V-V-T relaxation may be faster than dictated by the rate coefficient proposed by Blauer and Nickerson[124] at the beginning of the pulse, at 300 K, as highlighted by the comparison with Lepoutre *et al.*[149] in Figure 2.2 (in section 2.2.3) above.

As explained in section 2.2.6, our self-consistent calculation of E/N suggested that at least 94 Td is needed to sustain the discharge during the onset phase and that E/N > 55 Td is likely to persist throughout the pulse duration. This considered, we tested an E/N of 90 Td, as averaged from Figure 2.4(a), to investigate the effect into vibrational excitation. The comparison between the vibrational temperature evolutions for a fixed E/N of 55 and 90 Td is shown in panel (a) of Figure 4.4, while in panel (b), the electron energy deposition rate into different excitation processes as a function of time is depicted for the same conditions. The choice of the E/N significantly affects the way the energy is transferred from the electrons to the different degrees of freedom and excitation channels. Indeed, at 90 Td, clearly more electron energy (ca. 5 eV s^{-1} more) is transferred to the asymmetric stretching and symmetric vibrational levels, as well as to the electronically excited levels (increase of up to 45 eV s^{-1}), and to direct dissociation (ca. 10 eV s^{-1} more). However, the increase in energy deposited into vibrational levels, highlighted by the arrows in panel (b) of Figure 4.4, does not determine a substantial increment in vibrational temperature, in panel (a). Indeed, the extra energy deposited is promptly distributed over the entire array of levels through V-V-T and V-T relaxation, whose efficiency increases with T_g. Hence, we consider the vibrational kinetics description proposed in this study validated for the interval of E/N relevant for the pulsed glow discharge experiments. Notwithstanding this, an E/N of 90 Td means a larger amount of energy relocated from the electrons to the heavy species compared to 55 Td, triggering different excitation and heating channels. In this connection, a deeper discussion is given in the next section.

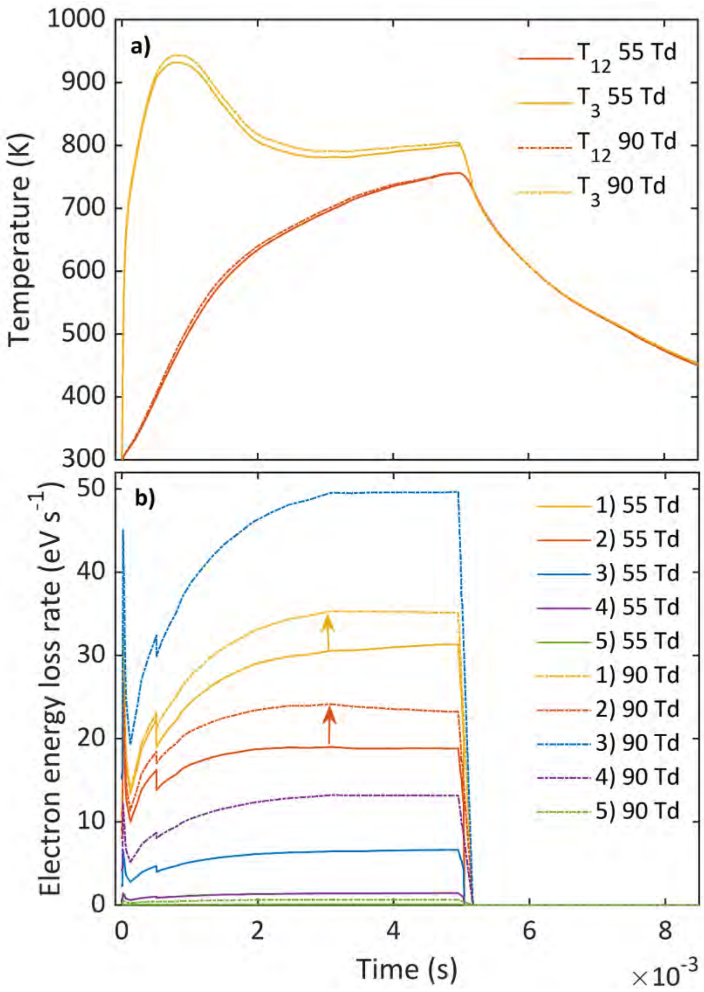

Figure 4.4. (a) Simulated time-evolution of T_{12} and T_3 for a fixed E/N of 55 Td (solid lines) and 90 Td (dash-dotted lines); (b) electron energy loss rate to (1) asymmetric stretching, (2) symmetric levels, (3) electronic excitation, (4) direct dissociation and (5) other processes (namely ionization, attachment and elastic scattering).

4.2.2 Gas heating dynamics

While the validation of the vibrational kinetics can be conducted by imposing a T_g profile as input parameter for the model, as demonstrated in the previous section, the same cannot apply for the study of the gas heating dynamics. In fact, panel (b) of Figure 4.4 shows that the selection of the E/N determines the excitation routes that are activated, among which vibrational excitation is only one of the possible pathways, and to which extent they are energized. To verify the impact of E/N on the gas heating dynamics, we performed simulations with self-consistent calculation of T_g. The outcome for E/N = 55 and 90 Td, compared against the experiments, is reported in Figure 4.5.

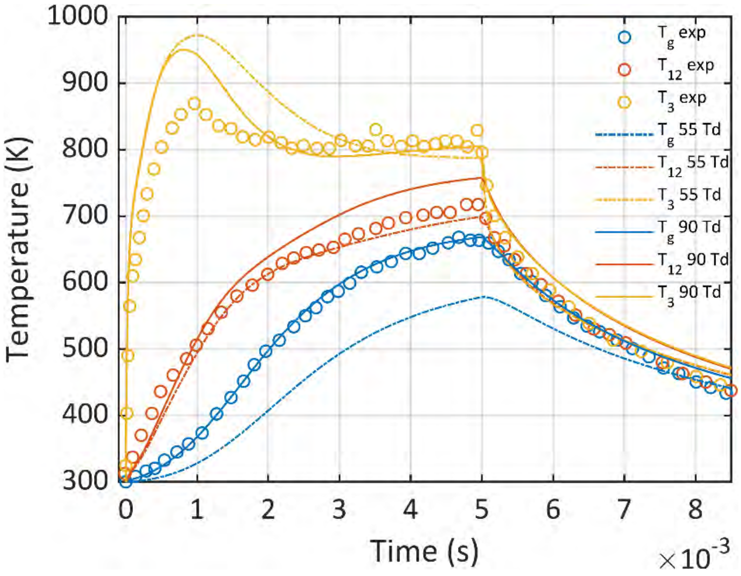

Figure 4.5. Experimental (circles) and simulated (dash-dotted lines E/N = 55 Td; solid lines E/N = 90 Td) temperature profiles as a function of the discharge time.

Interestingly, the choice of the E/N within the range of interest for this study does affect the vibrational excitation of CO_2. In accordance to Figure 4.4(b), the T_g profile in Figure 4.5 is now dependent on the chemistry that is activated by the electrons. Therefore, an overall lower excitation regime determines a diminished heating rate. In general, E/N = 90 Td provides a better agreement with the experiments, confirming our hypothesis that E/N > 55 Td endures throughout the pulse length.

With attention paid to the afterglow in Figure 4.5, i.e. t > 5 ms, it is visible that both simulated T_{12} and T_3 lie slightly above the experimental values for long time, without fully relaxing to T_g. The experimental profiles instead indicate that thermalization between vibrational and translational degrees of freedom is reached in 1 ms after the pulse on-time. A comparison with Silva *et al.*[164] for the same experimental conditions suggests that wall deactivation of vibrationally-excited CO_2 molecules, which is not included in our study, may help in further refining the agreement with the experiments in the post-plasma region. Nevertheless, under the conditions tested, we expect the contribution of this deactivation mechanism into the gas heating to be very small compared to V-T relaxation.

Thus, in order to investigate the relevant heating sources at 55 and 90 Td, and to picture the heating dynamics, we plotted in Figure 4.6 the contributions of the most relevant reactions, expressed as heating rates, as a function of the discharge time.

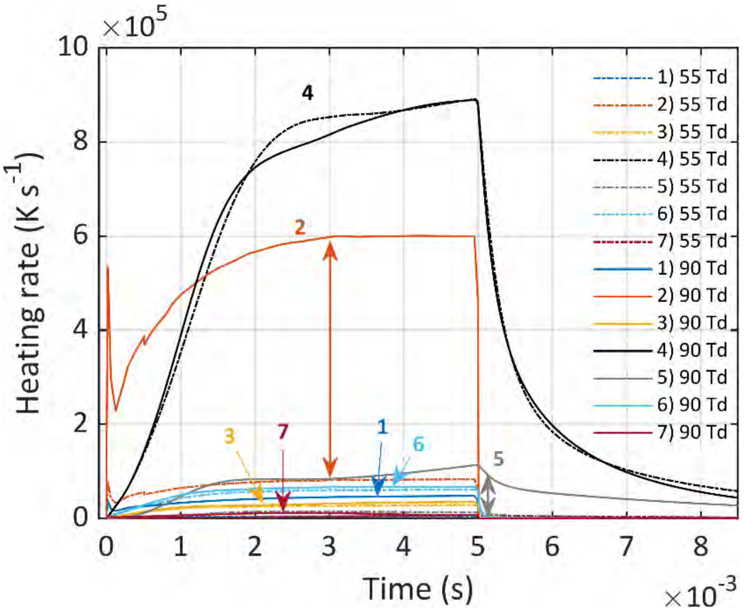

Figure 4.6. Calculated evolution of the heating rate from: (1) relaxation of CO($a^3\Pi$) and O(^1D); (2) relaxation of CO_2(E1) and CO_2(E2) electronic states; (3) V-T relaxation from v_3 to v_{12}; (4) V-T relaxation of v_{12}; (5) V-T deactivation by collisions with O atoms; (6) V-V-T relaxation; (7) other reactions (namely electron-ion recombination, ion-neutral, V-V relaxation, thermal reactions and electron-neutral elastic scattering).

This comparison indicates that V-T and V-V-T relaxation contributions are barely changed between 55 and 90 Td, suggesting that the underestimation of the gas heating, at 55 Td, comes from elsewhere. Indeed, the double arrows in Figure 4.6 evidence the most relevant differences between the two cases. Of particular interest is the striking increase in vibration-translation deactivation by O atoms and in electronic relaxation. While the former becomes important towards the end of the pulse, the latter strictly follows the current profile and is a result of a larger fraction of energy deposited into CO_2(E1) and CO_2(E2) by electrons at 90 Td (Figure 4.4(b)). In fact, turning off this process would reflect into overpopulation of v_3, resulting in a T_3 peak value of nearly 1000 K. During the same timeframe (i.e. 1 ms), T_g would be underestimated to a bigger extent than setting E/N = 55 Td, confirming the necessity of including this relaxation process into the description of the heating dynamics. In particular, the relaxation of CO_2 electronic states is a source of fast gas heating (i.e. with characteristic relaxation times smaller than V-T and V-V-T processes[259]) which smooths out the T_3 peak and reduces the duration of the T_3-T_g non-equilibrium. Note that its fast kinetics is highlighted by the spike at the very beginning of the pulse (see solid curve (2) in Figure 4.6). Indeed, the production of electronic states strongly depends on n_e and the consequent quenching happens at the sub-microsecond scale, depending on the pressure. Thus, excitation and de-excitation are nearly simultaneous and, therefore, the corresponding heating mechanism accurately resembles the current profile. On the other hand, the vibrational excitation is faster than the relaxation at low temperatures, which is the basis for vibration-translation non-equilibrium. Hence, the V-T profile (curves (4) in Figure 4.6) is shifted in time, eventually crossing over into the afterglow, where the electron kinetics is fully quenched. The existence of fast gas heating in pure CO_2 was already brought to light by Pokrovskiy *et al.*[157], although their study covered a range of E/N 150-250 Td. On the other hand, van de Steeg *et al.*[246] demonstrated that in pure CO_2 pulsed MW plasma, for a similar interval of E/N, V-T relaxation is responsible for up to 50% of the total heating rate, suggesting that the remaining part most likely comes from electronic relaxation. Their observations are in good agreement with our calculations.

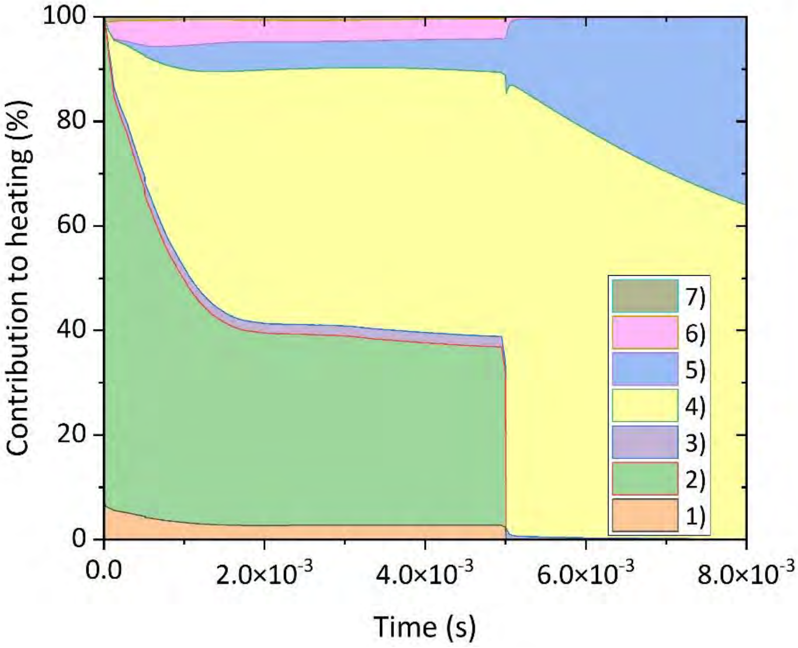

Figure 4.7. Percentage contribution to the gas heating rate from: (1) relaxation of $CO(a^3\Pi)$ and $O(^1D)$; (2) relaxation of $CO_2(E1)$ and $CO_2(E2)$ electronic states; (3) V-T relaxation from v_3 to v_{12}; (4) V-T relaxation of v_{12}; (5) V-T deactivation by collisions with O atoms; (6) V-V-T relaxation; (7) other reactions (namely electron-ion recombination, ion-neutral, V-V relaxation and thermal reactions and electron-neutral elastic scattering). Note that the contributions are stacked in order from (1) to (7).

Specifically, Figure 4.7 shows that after ca. 1.5 ms, the contribution of CO_2(E1) and CO_2(E2) collisional quenching stabilizes around 35% of the global heating rate, while V-T from v_{12} contributes for ca. 50%. During the first millisecond in the pulse, however, electronic relaxation is the leading heating pathway, whereas the afterglow is dominated by V-T relaxation from v_{12} and V-T deactivation upon collision with O atoms. In fact, in the afterglow the electronically excited states are quickly quenched and the thermal balance is ruled by V-V, V-T and thermal conductivity, in agreement with Silva *et al.*[164]. This last finding highlights the relevance of O atom kinetics to describe the vibrational kinetics of CO_2, as pointed out by Morillo-Candas *et al.*[154]. Indeed, at the end of the pulse, the CO_2 conversion is only 0.7%, corresponding to an O atom fraction of 0.6% and, yet, it is responsible for ca. 5% of the heating during the pulse and up to 35% in the afterglow. However, we would like to stress that the effects of the dissociation products on vibrational excitation and gas heating will be more accurately addressed in a future study, and this observation further motivates us to prosecute it.

With the information collected in this modelling work, we are now able to propose a gas-heating scheme for a pure CO_2 pulsed low-pressure plasma, which is depicted in Figure 4.8.

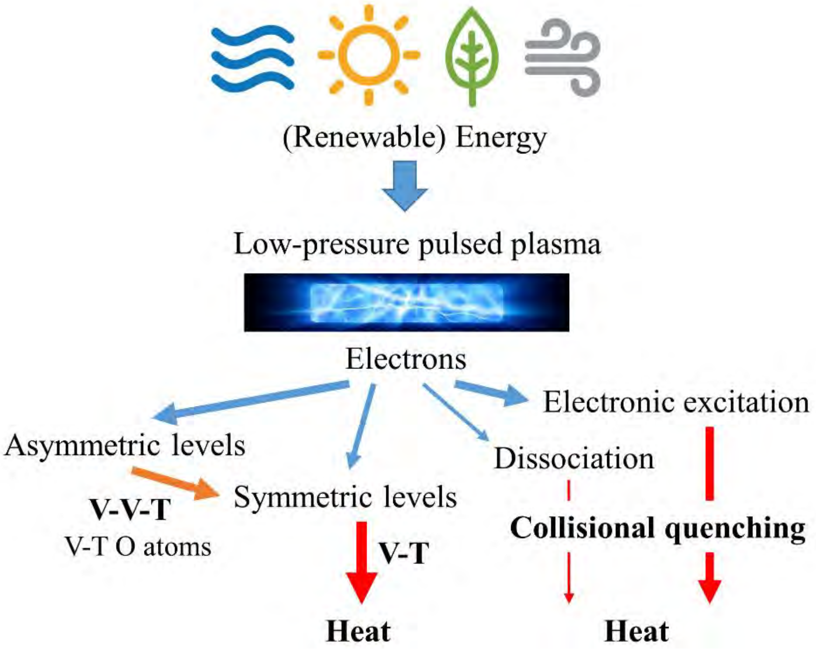

Figure 4.8. Schematic overview of the flow of energy in a pure CO_2 low-pressure pulsed plasma. The red arrows stand for the main heating mechanisms involved: vibration-vibration-translation (V-V-T) relaxation, vibration-translation (V-T) relaxation and V-T deactivation by collisions with oxygen atoms (V-T O atoms) and collisional quenching of electronic states coming from direct excitation or electron-impact dissociation of CO_2.

In a typical implementation of plasma technology for CO_2 recycling, the energy from renewable sources is supplied as electricity to the system. Thus, the plasma source is turned on and a plasma is ignited in the gas. The electrons collide with CO_2 molecules and a fraction of their energy is transferred into dissociation. The excited dissociation products, CO($a^3\Pi$) and O(^1D), contribute to the gas heating through collisional quenching with heavy species. Besides that, an important fraction of the electron energy is spent into excitation of electronic states of CO_2, which promptly relax to heat. The rest of the electron energy goes into vibrational excitation; of this, more than half is deposited into v_3 and the rest into v_{12}. The energy stored in v_3 is then distributed over v_{12} by V-V-T relaxation and partially by V-T deactivation upon collision with O atoms (V-T O atoms). Finally, the energy is transferred efficiently to translational degrees of freedom due to fast relaxation of low-lying v_{12}, accounting for a large part of the total heat.

The presence of these multiple channels for gas heating reduces the extent and the timeframe to exploit V-T non-equilibrium in CO_2 plasmas. E/N < 90 Td would be required to limit the dispersion of electron energy into electronic excitation and, consequently, heat. On the other hand, high E/N are necessary to ionize the gas and sustain the discharge in CO_2, due to n_e depletion through efficient electron attachment. This means that, at the beginning of the discharge pulse, electron energy is unavoidably lost to other excitation processes than vibrational excitation. Therefore, the redefinition of the conditions suitable for a consistent and exploitable vibrational excitation, as well as its possible role into dissociation, is highly desirable. In this regard, we aim to provide more insights in a future study, where we will focus on the dissociation of CO_2 and its effects on the heating dynamics.

4.3 Conclusions

In this chapter, the attainability of a prominent vibrational excitation to promote energy-efficient CO_2 conversion is investigated. Experimentally, evidences for very energy-efficient conversion (up to 90%) were provided in the past. Nevertheless, the hypothesis that vibrational excitation is at the basis of these successful results found increasingly less support since it is practically difficult to realize. With this purpose, pulsed discharges have been proposed. Theoretically, the pulse and inter-pulse time modulation can help to selectively excite v_3 while maintaining T_g low, which is a pre-condition to sustain a consistent V-T non-equilibrium and drive the stepwise excitation up to the dissociation limit of CO_2. On the other hand, experiments have not yet evidenced any prominent vibrational excitation in pulsed discharges, and T_3-T_g non-equilibrium seems limited to $t < 1$ ms and $T_g < 500$ K.

In this thesis, we focus on the validation of chemistry and gas heating dynamics in the ideal case of pure CO_2 using the single-pulse measurements performed by Klarenaar *et al.*[50]. In a multi-pulse situation, reaction products build up. Our present model needs to be expanded with an accurate description of CO, O and O_2 in order to assess their effect on chemistry and gas heating. Nevertheless, this study sets the stage for an in-depth and self-consistent investigation of the mechanisms underlying the energy exchanges in CO_2 low-temperature plasmas.

Thus far, modelling investigations focused on the study of the vibrational kinetics, identifying V-T relaxation as central mechanism for vibrational depopulation and gas heating. However, the energy transfer between different vibrational modes still lacks a clear interpretation. In particular, here we pinpoint the key role of V-V-T relaxation in coupling the kinetics of v_3 and v_{12}. The validation of our new kinetic scheme with experiments provides evidence of the essential contribution of v_{12} in promoting the gas heating in pure CO_2 discharges.

In addition, V-T relaxation alone cannot fully describe the heating dynamics under typical experimental conditions. This hypothesis was recently supported by some experimental and theoretical investigations[157,246], and finds confirmation in our study. In particular, our 0D simulations with self-consistent calculation of T_g predict a contribution of ca. 35% to gas heating from electronic relaxation, and even up to nearly 100% during the onset of the discharge. Despite the uncertainties related to the characterization of the electronic states of CO_2 and the lack of accurate relaxation rates, our work strongly suggests the importance of electronic collisional quenching to portray the underlying heating mechanism in CO_2 plasmas. Finally, it is worth mentioning that the O atom kinetics plays an important role in the heating dynamics as well, becoming essential to describe the energy transfers in the afterglow, where the electron kinetics is quenched. This observation confirms the insights provided by previous studies on CO_2 low-pressure plasmas and will be subject of more in-depth investigation in future work. Indeed, we expect the role of V-T relaxation by O atoms in the heating dynamics to become even more important in discharges with higher dissociation degrees, i.e. in discharges in continuous regime.

This modelling effort establishes the basis for the redefinition of the operational parameter space for sustaining a consistent vibrational excitation and its potential contribution into CO_2 dissociation. The polyatomic nature of CO_2 and, therefore, the existence of low-lying symmetric stretching and bending levels besides the asymmetric levels is a major constraint to a strong V-T non-equilibrium. Additional limitation is posed by the fast loss of energy into electronic states and, subsequently, heat, which seems to be unavoidable in pulsed regimes. Moreover, the presence of dissociation products (e.g. O atoms, as demonstrated in this study) can alter the vibrational distribution and the heating dynamics during the active phase of the discharge and in the afterglow. Therefore, in our future work we will prosecute the investigation and expand the study to experimental conditions where a non-negligible dissociation degree exists in the plasma.

Chapter 5 Carbon bed post-plasma to enhance the CO_2 conversion and remove O_2 from the product stream[8]

Abstract

As demonstrated in the previous chapter, gas heating is detrimental for vibrational excitation. Therefore, its role in promoting CO_2 dissociation in plasmas close to thermal equilibrium is minimal. Under such conditions, quenching of recombination reactions becomes crucial to improve the conversion. Hence, in this chapter, we present a carbon (charcoal) bed placed after a *warm* plasma, to remove O/O_2, quenching recombination reactions and, therefore, enhancing the CO_2 conversion and increasing the CO fraction in the exhaust mixture. Thanks to the carbon bed, the energy efficiency of the conversion process drastically increases from 27.9 to 45.4%, and the energy cost significantly drops from 41.9 to 25.4 kJ/L. We also present time-resolved measurements of the temperature in the carbon bed, as well as the CO_2, CO and O_2 concentrations, revealing that the initial enhancements in CO_2 conversion and in CO concentration are not maintained in our current setup. Therefore, we present a model, as described in Chapter 2, section 2.3, to study the gasification of carbon with different feed gases (i.e., O_2, CO and CO_2 separately), from which we can conclude that the oxygen coverage at the surface plays a key role in determining the product composition and the rate of carbon consumption. Indeed, our model insights indicate that the drop in CO_2 conversion and in CO concentration after a few minutes is attributed to deactivation of the carbon bed, due to rapid formation of oxygen complexes at the surface.

---

[8] This chapter is based on:
Carbon bed post-plasma to enhance the CO_2 conversion and remove O_2 from the product stream
O.Biondo*, F. Girard-Sahun*, G. Trenchev, G. van Rooij, A. Bogaerts
Chemical Engineering Journal 442, 136268 (2022)
https://doi.org/10.1016/j.cej.2022.136268
*Shared first author

5.1 Introduction

The modeling study presented and discussed in Chapter 4 demonstrates the crucial role of gas heating in determining the timeframe of V-T non-equilibrium. Under the specific conditions simulated (i.e. 6.7 mbar and low dissociation degree), V-T equilibrium is reached within the millisecond scale. Previous research demonstrated that at higher pressure (100 mbar), the lifetime of V-T non-equilibrium is further reduced to the microsecond scale[246]. Therefore, operations at atmospheric pressure, desirable for industrial applications, imply that the timeframe to exploit vibrational excitation to enhance CO_2 dissociation might be too short to affect the performance of the reactor. Continuous discharges at atmospheric pressure indeed typically feature a high-degree of equilibrium between vibrational and translational degrees of freedom[15,55]. Moreover, the heavy-particle kinetics tends towards the equilibrium with the electron kinetics, as demonstrated by van de Steeg *et al.*[51] for a MW discharge in pure CO_2 and by this thesis in CO_2/CH_4 mixtures in Chapter 6. For these reasons, these types of discharges are classified as *warm* plasmas. In such plasmas, CO_2 can be fully dissociated in the hot core of the discharge. Hence, quenching of the dissociation products becomes essential to improve the performance of the reactor.

Thus, in this chapter, we investigate the conversion of CO_2 by a gliding arc plasmatron (GAP), as a representative of *warm* plasmas, in combination with a carbon bed after the plasma reactor, to promote O/O_2 removal and increase the CO fraction in the exhaust mixture. The GAP reactor used in this study provided already promising CO_2 conversion performance[224] and is described in Section 3.1. However, the combination with a post-plasma carbon bed will further improve the performance. We present an innovative design (Figure 3.1), in which the carbon is constantly supplied over time by a silo system, to avoid carbon depletion upon reaction with O/O_2. The carbon bed is put in direct contact with the afterglow of the gliding arc plasma produced in pure CO_2 at atmospheric pressure, for maximum effect. During the process, the temperature is recorded as a function of time directly in the carbon bed, providing useful information for a better understanding of the underlying mechanisms. Furthermore, the exhaust gas composition is analysed by a combination of gas chromatography and optical sensors (Section 3.1.3). The performance of the GAP with carbon bed is determined and compared with the benchmark (i.e without carbon bed) (cf. Section 3.1.4).

Although it has been experimentally proven that carbonaceous materials are effective options to increase the selectivity towards CO in the CO_2 splitting process, more insight is needed to demonstrate its full potential and identify the relevant underlying mechanisms. In this respect, modelling is a very useful tool to unravel chemical pathways especially when these are inaccessible experimentally. 0D models, also referred to as global models, are the method of choice to study the contributions of different chemical reactions occurring in plasma ignited in complex gas mixtures[264]. Therefore, in addition to the experimental work[9], we examine here the gasification process occurring when a reactive gas mixture produced by a plasma comes in contact with a carbon bed. This analysis involves the construction (detailed in Section 2.3) and the validation of a 0D chemical kinetics model against experiments. The validation of a model is a crucial aspect and requires particular experimental conditions, in order to minimize the number of assumptions under which the predictions are valid. With this in mind, we have chosen to validate our model with the gasification experiments presented by Panerai *et al.*[183], under pure O_2 and CO_2 atmospheres, respectively, in order to get insights into the reaction pathways for carbon oxidation in the presence of O_2, CO_2 and CO and the deactivation of the carbon bed, with consequent decrease in selectivity towards the latter. This model greatly helps us to explain our experimental results, as will be described in detail in this Chapter. To resume, the innovations of this work, compared to previous research on the topic[68–70], are: i) the use of a silo system, to avoid carbon depletion due to gasification; ii) time-resolved temperature measurements in the carbon bed; iii) a combination of gas chromatography and optical sensors to determine the exhaust composition as a function of time; iv) and especially coupling our experiments with detailed kinetic modelling, to provide detailed insights into the underlying chemistry and the deactivation of the carbon bed.

5.2 Results and discussion

5.2.1 Performance comparison: with and without carbon bed

Figure 5.1 presents the maximum CO_2 conversion, and the corresponding energy efficiency and energy cost, without carbon bed (benchmark) and for two different carbon materials with different particle size, namely active charcoal 1 and 2 (see previous section). The obtained maximum CO and O_2 concentrations are also depicted in Figure 5.1.

---

[9] The experiments were performed by Dr. Fanny Girard-Sahun at the PLASMANT lab, with my support.

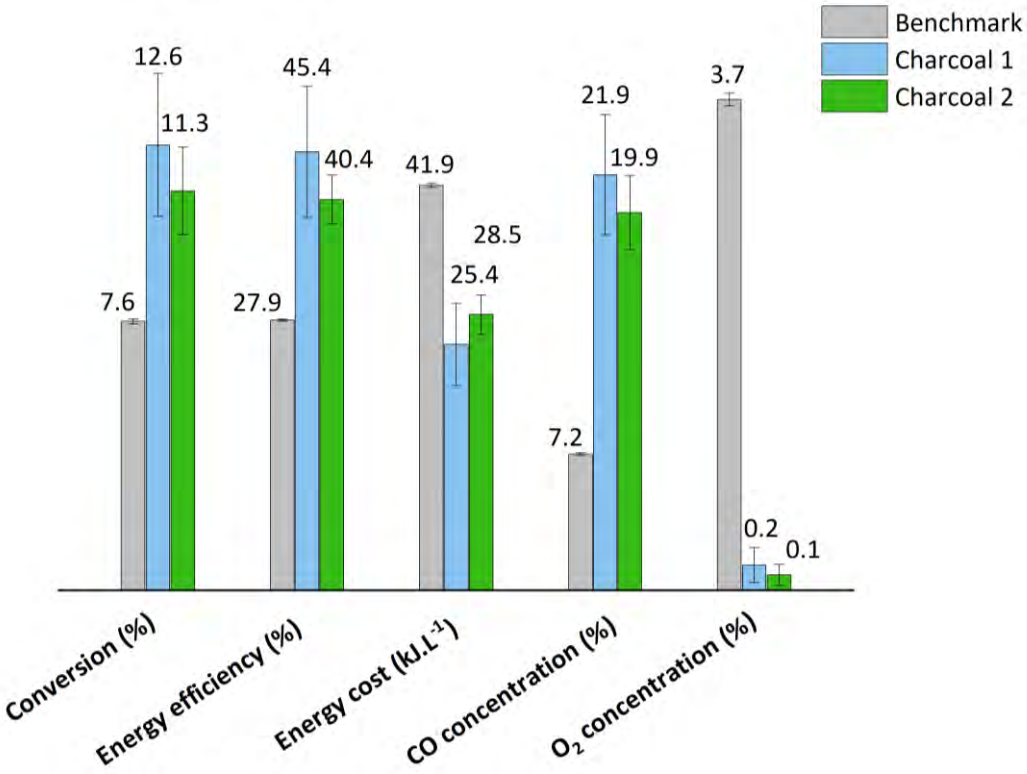

Figure 5.1. Conversion, energy efficiency, energy cost, and CO and O_2 concentrations (obtained at the maximum conversion, after 1 min of operation; see below), without carbon bed (benchmark), and with carbon bed (charcoal 1 and charcoal 2). 10 L/min CO_2. The SEI was about 3.2 kJ/L^{-1} in all cases.

It is known that the physicochemical properties of the carbon material and the particle size can seriously affect the carbon reactivity towards CO_2 during gasification[59,265]. More specifically, the concentration of active sites where the heterogeneous reactions between CO_2, O/O_2 (from gas) and carbon (from solid) occur is a critical parameter. However, we do not observe any significant difference between the charcoal 1 and 2, with small deviations within the error margin.

Nevertheless, whatever the type of charcoal (1 or 2), the conversion is significantly enhanced with the carbon bed, almost by a factor of two (from 7.6 ± 0.1 to 12.6 ± 2.0% and 11.3 ± 1.2% for charcoal 1 and 2, respectively), for the same SEI (about 3.2 kJ/L). Consequently, the energy efficiency is increased from 27.9 ± 0.1 % to 45.4 ± 6.8% and 40.4 ± 2.5% for charcoal 1 and 2, respectively, whereas the energy cost is much lower (from 41.9 ± 0.2 kJ/L for the benchmark to 25.4 ± 4.2 kJ/L and 28.5 ± 2.0 kJ/L for charcoal 1 and 2, respectively). The exact contribution of the RBR in the chemical process is not known, and, as mentioned in section 2.3.1, we expect it to play a minor role at the conditions under study (i.e., temperature in the carbon bed is only at the limit for the RBR to occur for fresh carbon, which is higher than 1000 K[59]), so we calculated the energy efficiency based on ΔH_R° for pure CO_2 splitting. This must however be kept in mind for the values obtained with the carbon bed. Finally, Figure 5.1 also shows that the CO concentration is about three times higher upon addition of the carbon bed, while the amount of O_2 is negligible when the carbon bed is present.

Therefore, adding a carbon bed not only favourably improves the CO_2 conversion and increases the CO concentration, but also gives much better energy efficiency and a much lower energy cost. In addition, the exhaust can be kept low in oxygen, which is very beneficial, as it reduces separation costs of CO from O_2. Indeed, besides removal and recycling of unconverted CO_2, CO purification is a technical challenge in case of scaled-up facilities, and thus an expensive process[11]. A CO_2/CO mixture obtained in the presence of a charcoal bed, low in O_2, could be directly recycled, by recirculating the gas in the plasma reactor, increasing the CO_2 conversion and eventually (ideally) leading to a pure CO stream. Note that recycling the exhaust in the plasma reactor again would reduce the overall energy efficiency, because energy is again needed for the second pass through the plasma. In real-life application, however, especially featuring near-zero cost renewable energy sources, there will be a trade-off between CAPEX (more reactors) and OPEX (recycling, hence more energy needed).

A similar improvement of the CO_2 conversion in the presence of a carbon bed was obtained with an atmospheric GAP studied by Huang *et al.*[70] (conversion up to 21.3% with carbon bed), but with a rather low associated energy efficiency (24.0%) due to a relatively high SEI (≈ 7 kJ/L) compared with our conditions (where the SEI is 3.2 kJ/L). In a thermal plasma, the CO_2 conversion was even more increased (up to 95%) at a very high energy efficiency (70%), as studied by Li *et al.*[69]. However, these experiments were performed in CO_2/Ar mixtures, and Ar helps to enhance the CO_2 conversion and energy efficiency[21], but in reality, Ar also consumes part of the plasma energy, which was not accounted for when calculating both the conversion and energy efficiency. For a fair comparison, the fraction of CO_2 in the mixture should be accounted for[21,266]. Therefore, we cannot compare the absolute values. Moreover, because of the thermal plasma, the temperature was considerably higher (more than 1000 °C at 6 cm from the initial carbon surface) and therefore more beneficial for the RBR. A very high power (up to 16 kW) was necessary to drive this thermal plasma, which is far from our operating conditions (power around 0.5 kW). The authors proposed the following mechanism: CO_2 is first decomposed in a $CO/O/O_2$ mixture that reaches the carbon bed with a high temperature, favouring carbon oxidation by oxygen atoms and molecules; Second, the unconverted CO_2 is able to react with the carbon bed via the RBR thanks to the elevated temperature from exothermic oxidation reactions[69].

In the next sections, we present the measured temperature profile after the plasma reactor, as well as the time-evolution of the CO_2, CO and O_2 concentrations, to explain the influence of the carbon bed on the CO_2 chemistry after the plasma in our conditions. Furthermore, we will also present modelling results, to validate our hypotheses.

5.2.2 Temperature profile after the plasma reactor, without carbon bed

We measure the temperature profile after the plasma reactor, without carbon bed, to gain more insight in the chemical reactivity of the carbon towards CO_2, CO, O and O_2[183] (also needed to interpret the modelling results presented in section 5.2.6 below) and to determine the most suitable position of the carbon bed in the post-plasma reactor tube. The results are presented in Figure 5.2 (red curve). Note that the post-plasma reactor tube was designed so that the temperature could be measured over the entire length (i.e. up to 255 mm), if necessary. However, we were most interested in measuring the temperature close to the reactor outlet, so we only measured up to 140 mm, because at further distances, the temperature is not so elevated anymore (see Figure 5.2).

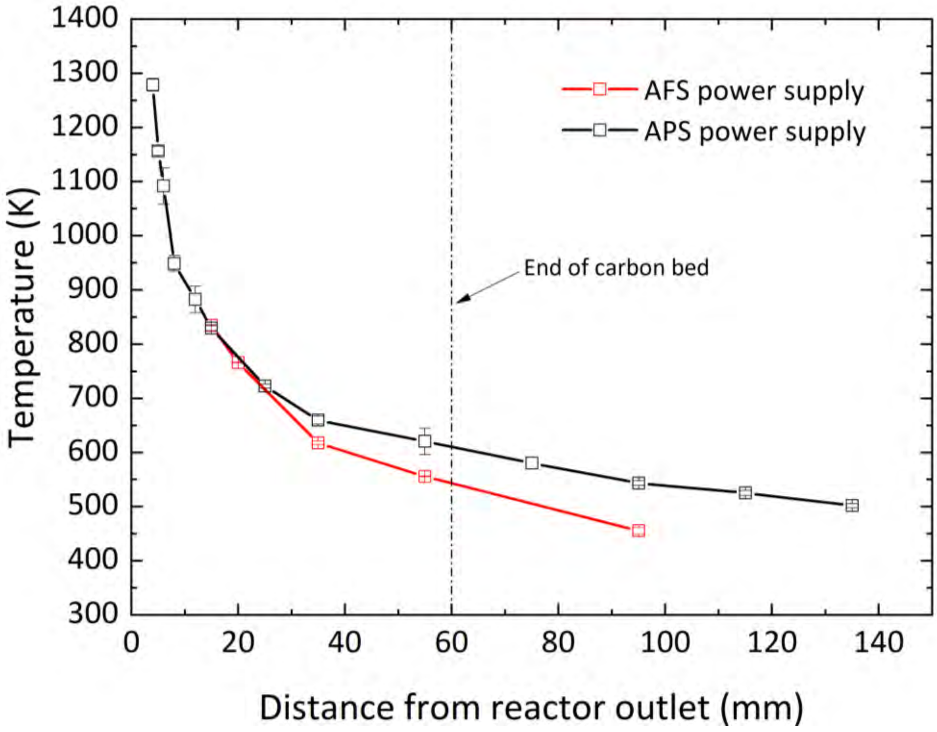

Figure 5.2. Measured temperature profile in the post-plasma region without carbon bed (basket removed), with two different power supplies. Flow rate: 10 L/min CO_2, SEI = 2.9 kJ/L.

Note that the error bars, based on three independent measurements, are too small to be visible. Moreover, when the carbon bed is present, it starts at 0 mm (right at the reactor outlet) and extends until 60 mm (see vertical dashed line). In absence of the carbon bed, the temperature profile exhibits an exponential decrease with increasing distance from the reactor outlet (red curve). At 15 mm distance, the temperature reaches about 850 K and it drops to about 450 K at 95 mm distance. Note that for positions < 15 mm, the thermocouple tip was molten, as it was most likely in direct contact with the arc extending out of the plasma reactor, which made the measurements not possible. Based on previous modelling results, the arc temperature in the GAP is around 3000 K[30], so we can expect the temperature to be much higher than 850 K closer to the reactor outlet. Earlier, we had performed similar measurements for the same setup but with another power supply (APS; Advanced Plasma Solutions). However, the latter power supply later got broken, so it could not be used for our plasma conversion experiments. Nevertheless, we plot these temperature measurements in the same figure (black curve). They show a similar profile, and because the plasma arc behaviour is different due to a different operational mode (attributed to the power supply), measurements closer to the reactor outlet are possible in this case, without melting the thermocouple tip. Particularly, we can measure up to 1300 K at 4 mm distance from the reactor outlet. Although the temperature profile is slightly different for a distance > 35 mm, the trend indicates a very similar behaviour for positions < 25 mm and therefore similar temperatures are expected close to the reactor outlet with the actual power source (red curve). Thus, positioning the carbon bed as close as possible to the reactor outlet (hence: to the plasma) allows the carbon bed not only to be in contact with the reactive O atoms from the plasma (providing quenching, so that they do not contribute to the back-reactions; see Section 1.4.1), but also to take benefit from the high temperature to enhance possible reactions between the exhaust gas and the solid carbon. This temperature profile will be used to explain the underlying chemical reactions, described in the model, in section 5.2.6 below.

5.2.3 Time-evolution of CO_2, CO and O_2 concentrations, and associated CO_2 conversion

To better understand the chemical reactions occurring at the carbon bed and explain the results from Figure 5.1, we plot in Figure 5.3 the concentrations of CO_2, CO and O_2 in the exhaust gas mixture as a function of time during plasma exposure, both without and with carbon bed (Figure 5.3A and 5.3B) by using NDIR/O_2 optical sensors, and we also compare with GC measurements, to ensure a good accuracy of the optical sensors (Figure 5.3C). Note, however, that the GC measurements only allow a few time points; hence the advantage of the optical sensors. We only present the results for charcoal 1, but the data for charcoal 2 are very similar.

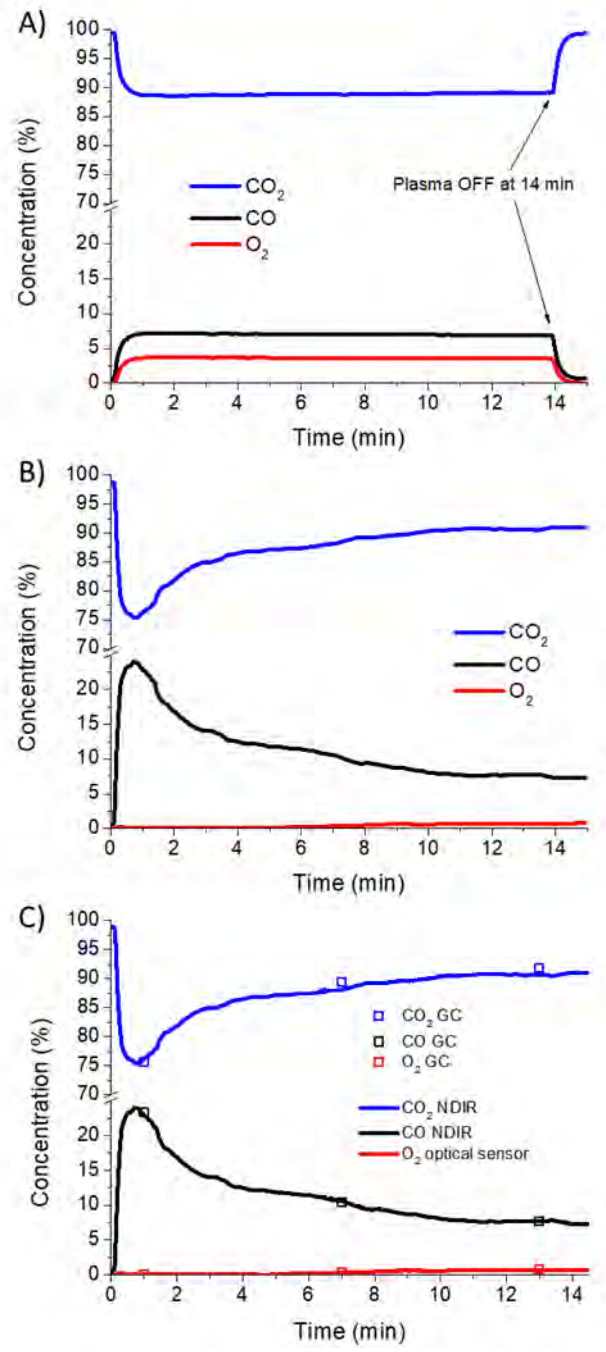

Figure 5.3. CO_2, CO and O_2 concentrations measured in real time, without carbon bed (A) and with carbon bed filled with charcoal 1 (B); C. Comparison of the optical sensors with GC measurements which only allow a few time points. Charcoal 1, 10 L/min CO_2, SEI = 3.2 kJ/L. The plasma is turned ON at time 0.

Without carbon bed (Figure 5.3A), when the plasma is turned ON, the CO_2 concentration immediately drops to about 88%, whereas the CO and O_2 concentrations rise to 7.2% and 3.6%, respectively. In less than one minute, the three concentrations stabilize and stay constant over time, meaning that the plasma reaches an equilibrium, in line with previous studies with this plasma reactor[31,224]. Once the plasma is turned OFF, i.e., at 14 min, the chemical reactions stop and the concentrations return to their original values. The only reaction occurring here is CO_2 splitting, producing CO and O_2, as described in Equation 1.1 in Section 1.1.

Upon addition of a carbon bed (Figure 5.3B), the concentrations feature a quite different evolution over time. The CO_2 concentration immediately drops after plasma ignition and reaches a minimum value (ca. 75%) within 30-40 sec, and then gradually increases to ca. 90% at 14 min. The CO concentration reaches up to 24% when the CO_2 concentration is minimal, and then decreases again, similarly to the CO_2 increase. In contrast, the O_2 concentration depicts a very small transient rise right after plasma ignition (≈ 0.2%, see Figure 5.4) before dropping to a negligible amount for about 5 minutes, followed by a very slow increase, but it stays below 0.8% as final value. A similar evolution was observed by Huang *et al.* with an atmospheric non-thermal plasmatron[70]. Therefore, the comparison between (A) and (B) shows that the carbon bed is deactivated after some time, for the production of CO (which relaxes to the benchmark value) but not for the O_2 consumption. The underlying mechanisms will be discussed later in sections 5.2.5 and 5.2.6.

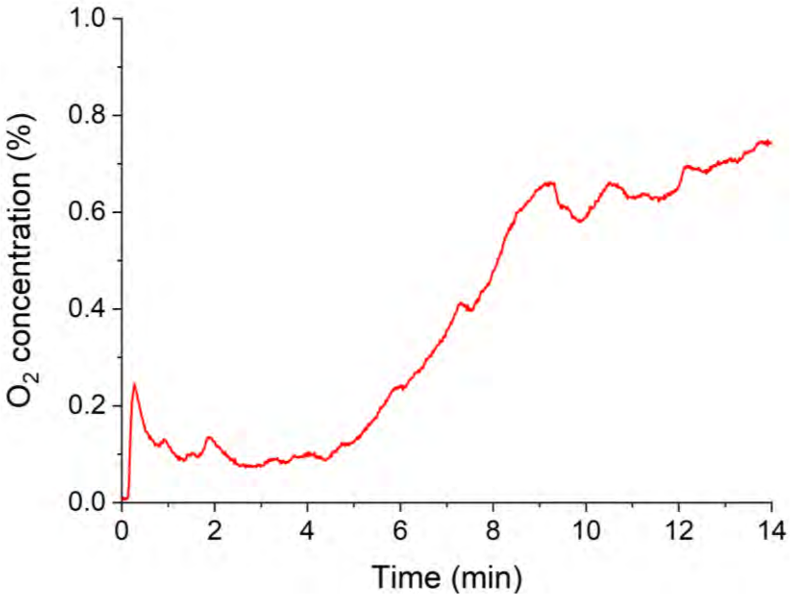

Figure 5.4. O_2 concentration measured in real time with carbon bed, charcoal 1 (zoom in from Figure 5.3B in the main paper). 10L/min CO_2, SEI = 3.2 kJ/L.

To verify the accuracy of our NDIR and O_2 optical sensor measurements, we compare them with GC analysis, performed at the same time in parallel. GC is a very common technique for analysing gas mixtures and known to be very efficient and reliable; however, in the context of these experiments, on-time measurement is more useful to understand the complex chemistry. The results are presented in Figure 5.3C and indicate a very good agreement between both techniques. Therefore, we can consider the on-time data reliable to calculate the conversion and the performance of the carbon bed.

From the time-profile of the CO_2 concentration (Figure 5.3), we calculated the CO_2 conversion (Eq. 3.1 and 3.2 in Section 3.1.4) for both the benchmark and the carbon bed addition, and the results are plotted in Figure 5.5. In the first 1-2 minutes, the conversion upon carbon bed addition is much higher than without carbon bed, but it drops to lower values after ca. 3 minutes. In the next section, we discuss the results of the characterization study of the charcoals, before and after the gasification reaction.

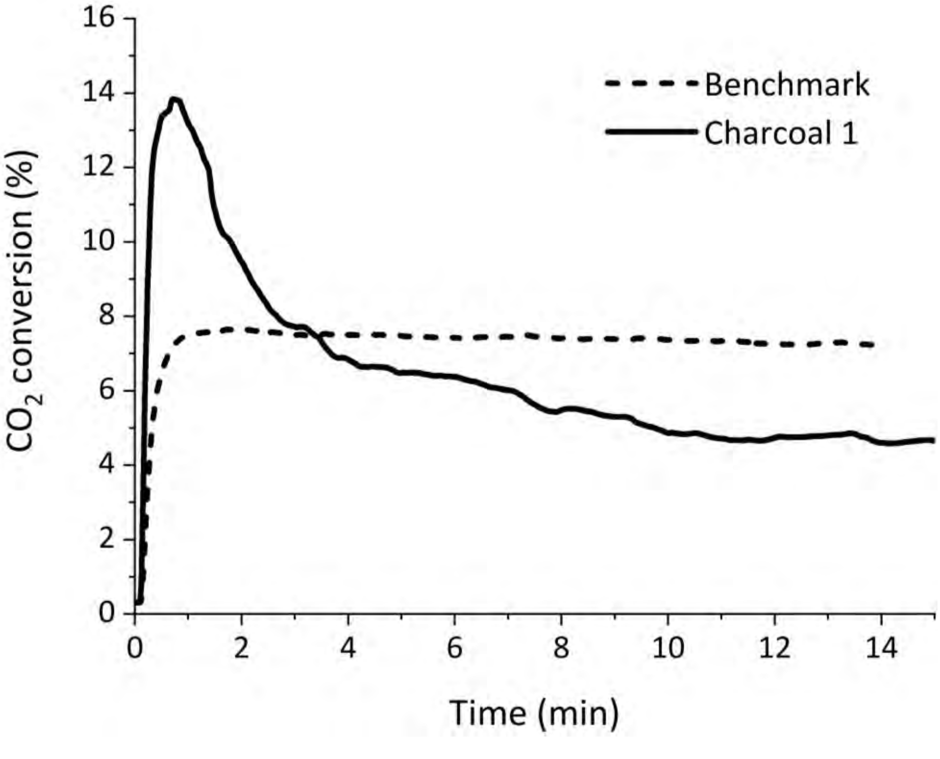

Figure 5.5. CO_2 conversion as a function of time without (dash line) and with (solid line) carbon bed. Charcoal 1, 10 L/min CO_2, SEI = 3.2 kJ/L.

5.2.4 Characterization of charcoal before and after the gasification reaction

The gasification of solid carbon is governed by interdependent factors such as the micro- and macrostructure of the material, the total and the active surface area, the degree of oxidation, the presence of catalytic impurities and the gas-phase composition. Any modification of one of these factors may alter the others. Therefore, the study of the underlying mechanisms for the gasification process, and their variations with time, cannot be separated from the screening of the modifications occurring during the reaction. For this purpose, we analysed the alterations of the surface exposed to the plasma-treated gas mixture, using SEM, N_2-BET and TGA-MS. The SEM images were collected for charcoal 1 as received and after 45 s and 7 minutes of reaction (see Figure 3.3 in Section 3.1.1). From the images, we cannot identify any visible morphology change during the gasification reaction, except for the formation and deposition of ashes over the surface, which look more intense after 45 s rather than after 7 minutes of reaction. The BET measurements were performed on charcoal 1 and 2, as received, and after the gasification reaction for charcoal 1. The results are given in Table 5.1.

Table 5.1. BET measurements of the surface area.

Sample	BET surface area [m^2 g^{-1}]
Charcoal 1	705 ± 71
Charcoal 2	703 ± 70
Charcoal 1, after 45 s, top layer	767 ± 77
Charcoal 1, after 45 s, bottom layer	732 ± 73
Charcoal, after 7 minutes	787 ± 79

The BET measurements reveal that charcoal 1 and 2 have the same initial surface area. For this reason, we perform the measurements after the reaction only for charcoal 1. After 45 s, the CO_2 conversion spikes (see Figure 5.5) and the temperature is higher than 1300 K at 15 mm in the carbon bed, in the top layer, and still lower than 500 K at 35 mm, in the bottom layer (see Figure 5.6, below). Therefore, it is reasonable to deduce that the gasification reactions are mainly occurring in the top layer of the bed. However, the surface area is barely affected, with a bigger effect on the top layer, most likely because of desorption of volatile species (e.g. water) from the surface during the first seconds of reaction, freeing up more pores. After 7 minutes, the temperature in the top and bottom layer is nearly the same (see Figure 5.6). At this point, Figure 5.5 shows that the carbon bed is deactivated and the CO_2 conversion is lower than the benchmark value. Regardless of this, the surface area is further increased compared to 45 s. In view of the above, we cannot clearly link the drop in performance of the carbon bed with a change in morphology or surface area. To investigate the presence of adsorbed species and thermolabile functional groups at the charcoal surface, before and after the gasification reaction, we carry out a TGA-MS study, described in Section 3.1.2. The analysis highlights that H_2O is the main species desorbed by charcoal, already at room temperature (see Figure B1 in the Appendix B). This is an indication that H_2O is mainly adsorbed over the surface and not coming from the decomposition of surface functional groups. Only at about 850 K, CO_2, CO and H_2 are also detected. We would like to point out that the analysis is not quantitative. Indeed, a quantitative analysis of the desorbed compounds goes beyond the purpose of this thesis, as the experiments were performed by a postdoc in our group, and they were only included in this chapter as they formed part of the joint paper (of this chapter) and to give the context of the model that I developed to explain the experimental results. Therefore, we need to be careful when comparing different products in terms of magnitude, because the mass spectrometer was not calibrated. However, at this point, H_2O desorption drops, and we hypothesize that a fraction of the other species detected are products of the reaction between water and charcoal, also called steam gasification[267,268]:

$$H_2O(g) + C(s) \leftrightarrow H_2(g) + CO(g), \text{ with } \Delta H^{\circ}_{R} = 131 \text{ kJ/mol.} \qquad (5.1)$$

The presence of CO_2 could be explained by either the water-gas shift reaction[268]:

$$CO(g) + H_2O(g) \leftrightarrow CO_2(g) + H_2(g), \text{ with } \Delta H^{\circ}_{R} = -41 \text{ kJ/mol,} \qquad (5.2)$$

or by the decomposition of oxygen complexes or surface functional groups i.e. carboxyl groups[269], naturally found in charcoals. However, the TGA-MS of charcoal 1, after 45 s and 7 minutes of reaction (see Figure B2 and B3, respectively in the Appendix B), shows that H_2O is still the main species desorbed from the surface, despite charcoal was certainly exposed to high temperatures during the gasification reactions. Such an observation indicates that H_2O is probably re-adsorbed from the moisture in the atmosphere after the reaction, as charcoal is a hygroscopic material[270]. For this reason, it is not possible to draw clear conclusions from this analysis. However, the weight loss during the TGA (see Figure B4 in the Appendix B) shows that the charcoal tends to release less gaseous products with increasing gasification time, indicating that the surface may undergo a physico-chemical transformation that reduces the hygroscopicity of charcoal and/or modifies the nature or the amount of complexes and functional groups at the surface, favouring more stable interactions. With the results presented above, we hypothesize the underlying mechanisms in the next section.

5.2.5 Hypothesis of the underlying mechanisms

Based on the conversion and concentrations as a function of time, plotted in Figures 5.3 and 5.5, we hypothesize that the following mechanisms take place:

First, the conversion increases abruptly up to 14% (corresponding to the minimal CO_2 concentration observed in Figure 5.3B). We can reasonably assume that, when the converted mixture (containing CO_2, CO and O/O_2) is flowing through the carbon bed, O and/or O_2 are immediately adsorbed (either chemically or physically) on the carbon surface, as depicted in Figure 5.3B and Figure 5.4.

Hence, recombination reactions (CO + O/O_2 forming again CO_2) are suppressed and the net conversion increases, producing at the same time more CO compared with the benchmark (cf. Figure 5.3A,B). The most likely mechanism occurring here is the partial oxidation of carbon by O/O_2, following equations 5.3 and 5.5[172,183,271]:

$$C(s) + O(g) \rightarrow C(s)\text{-}O, \qquad (5.3a)$$

$$C(s) + C(s) + O_2(g) \rightarrow C(s)\text{-}O + C(s)\text{-}O, \qquad (5.3b)$$

$$C(s)\text{-}O + M \rightarrow CO(g) + M, \qquad (5.4)$$

with C(s) a solid carbon active site. In Equations (5.3A,B), O and O_2 are immediately adsorbed by the carbon bed, followed by the release of a CO molecule promoted by collisions with gas molecules and high temperature (Equation 5.4).

Note that for CO_2 splitting without carbon bed, the CO_2 conversion is usually equal to the CO concentration in the exhaust. Indeed, for the benchmark, both CO_2 conversion and CO concentration are about 7-7.5% in this case (Figure 5.3A and Figure 5.5). With carbon bed, the maximum conversion is 14 % (Figure 5.5), whereas the associated CO concentration is 1.5 times higher, i.e., 22%. Therefore, we can reasonably assume that part of the measured CO is released from the carbon surface, as described in Equation 5.4, in addition to CO coming from initial CO_2 splitting, which is most likely unreactive toward solid carbon[183]. A second hypothesis is that the RBR takes place as well (Equation 1.3 in Section 1.3.1), but only if high enough temperature can be achieved (above ca. 973 K[59]) to activate the reaction towards the formation of CO. This will be further discussed in section 5.2.6 below.

After this peak, the conversion decreases until reaching the benchmark value in around 3 minutes, whereas the CO concentration decreases and the O_2 concentration starts rising. Even more, from then on, the conversion continues dropping until being about 2% lower than the benchmark value, meaning that the positive effect previously observed does not last over time. We hypothesize that the carbon surface reaches saturation of oxygen: gas-phase O/O_2 is still being consumed by the remaining pellets that are not yet saturated (as seen in Figure 5.3B and Figure 5.7) but it now leads to full oxidation and the release of CO_2 molecules (Equation 5.5). The role of the formation of oxygen complexes at the surface, most likely epoxy and peroxy complexes, on the CO_2 evolution during the carbon oxidation reactions, is also underlined by DFT calculations[272]. Moreover, the forward Boudouard reaction takes place (as demonstrated by our computer simulations; see section 5.2.6 below), explaining why the performance in terms of conversion becomes lower than the benchmark.

$$C(s)\text{-}O + O(g) \rightarrow CO_2(g) \qquad (5.5a)$$

$$C(s)\text{-}O + O_2(g) \rightarrow CO_2(g) + O(g) \qquad (5.5b)$$

Moreover, as the oxidation reactions (sum of the elementary reactions 5.3 and 5.5) are exothermic[183,273,274], heat will be released and thus we expect an increase of the carbon bed temperature compared to the benchmark. In order to check this, we measured the temperature in the carbon bed (cf. Figure 3.1) and compared it with the benchmark (in this case, the temperature is also measured in the basket, but free of carbon). The results are presented in Figure 5.6, measured at 15 mm from the reactor outlet (dark blue line).

The temperature in the carbon bed reaches a maximum almost immediately after plasma ignition (ca. 1700 K), then decreases to finally stabilize around 1200 K after 2 minutes. Note that the temperature at 35 mm from the reactor outlet (light blue line in Figure 5.6) is lower than at 15 mm during the first 4 minutes. This shows that the temperature profile is not uniform along the carbon bed and depends on the distance from the plasma. Moreover, we can assume that the carbon pellets at the end section of the basket are not yet saturated, as O atoms and O_2 are being consumed by the top layer. However, after 4 minutes the temperature at 35 mm increases and becomes equal to that at 15 mm, strengthening our hypothesis of full oxidation ($O_2(g) + C(s)\text{-}O \rightarrow CO_2(g) + O(g)$) occurring at a later stage on the pellets placed further away from the anode exit (35 mm vs 15 mm) when they are saturated with oxygen (Equation 5.5).

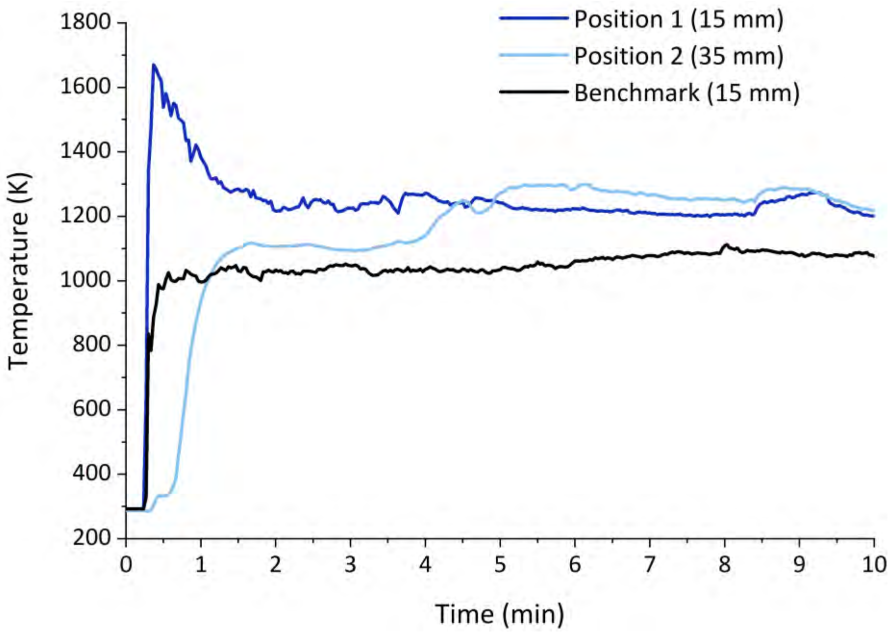

Figure 5.6. Measured temperature at 15 mm and 35 mm from the reactor outlet, with carbon bed (dark and light blue lines, respectively), and without carbon bed (black line). Charcoal 1, 10 L/min CO_2, SEI = 3.2 kJ/L.

As mentioned above, we believe that the initial rise in temperature at 15 mm, observed in Figure 5.6, is due to exothermic reactions, most likely partial carbon oxidation (Equations 5.3-5.4)[275]. When the temperature is around 1200 K, CO_2 is most likely released from the surface, at the expense of CO[183], and this is what we actually observe in Figure 5.3B.

Moreover, it is very likely that the RBR occurs at such high temperature (1700 K)[69,70]. This is a highly endothermic reaction (see eq. 1.3 in Section 1.3.1), so we can expect the temperature to be even higher than the measured one, but probably in a short period of time. Its contribution is however not straightforward to evaluate compared with carbon oxidation, which is more obvious from our experimental results. In any case, the presence of the carbon bed strongly influences the temperature, especially during the first minutes. Furthermore, the presence of the carbon bed might also affect the flow dynamics (physical effect), and consequently, this may affect the temperature. Hence, to discriminate between this physical effect and the chemical effects, we have replaced the carbon bed with an unreactive material (i.e., ceramic beads) that can withstand high temperatures. The temperature in the *dummy bed* did not exceed 1000 K, with associated CO_2 conversion and CO/O_2 concentrations similar to the benchmark values. Therefore, the main reason for the elevated temperature with the carbon bed is indeed most likely due to the exothermic reactions (5.3) and (5.5), as previously explained.

In comparison, the temperature in the basket without carbon (black line in Figure 5.6) is lower and rather constant in the range of 1000 - 1050 K. This temperature is higher than at the same position without basket (about 850 K; see Figure 5.2 above). This could be explained by the limited gas circulation inside the basket: its thick walls are heated up and they keep on releasing heat to the gas during the process.

In addition, the carbon bed may also represent a physical constraint to the flow, increasing the pressure upstream and causing a pressure drop throughout the bed. Panerai *et al.*[183] reported a pressure drop of up to ca. 90% under their conditions. Such a drop can be ascribed to the use of a roots pump to evacuate the system downstream their carbon bed. However, they did not discuss the effects of the pressure drop to the performance of their reactor. In our experiments, we could only estimate the drop by measuring the overpressure built upstream the carbon bed and assuming that the pressure downstream the bed is equal to atmospheric pressure. This is a good approximation since the exhaust flow is evacuated to open air, under the fume hood, without any pump. From our pressure measurements, we estimated the pressure drop to be lower than 0.4% for charcoal 1 and ca. 2% for charcoal 2. Therefore, we do not expect the pressure drop to play any significant role in the performance of the process under our operational conditions.

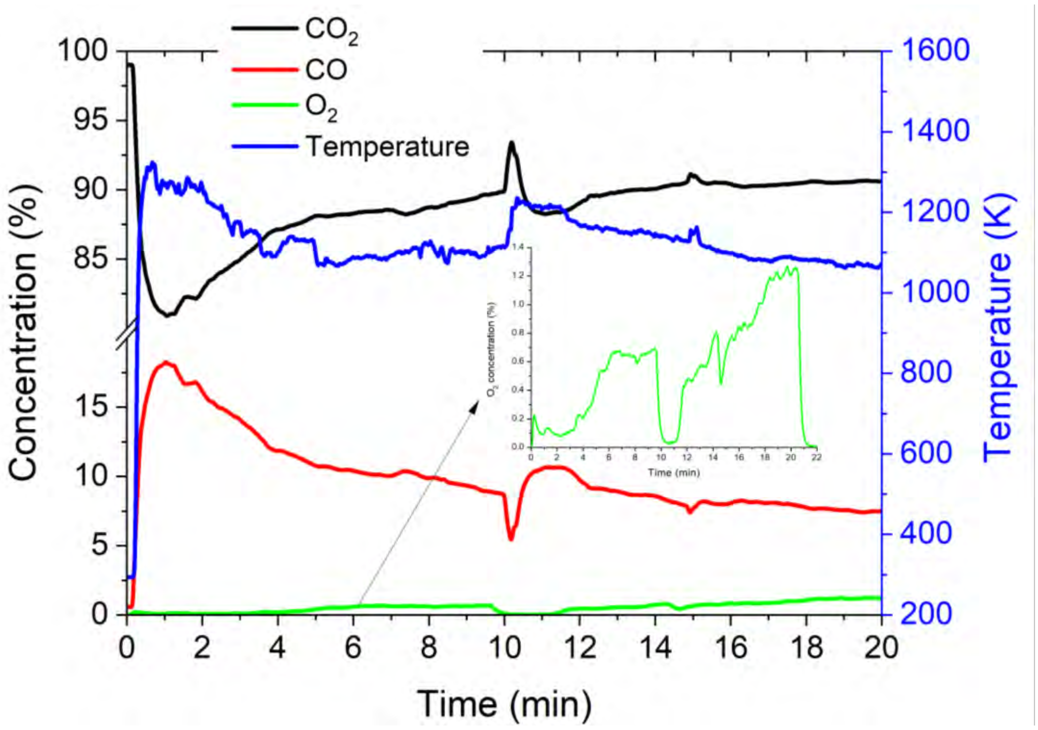

Figure 5.7. CO_2, CO and O_2 concentration profiles compared with the temperature profile obtained in the presence of the carbon bed. Charcoal 1, 10 L/min CO_2, SEI = 3.2 kJ/L.

Finally, as shown in Figure 3.1, the silo should provide fresh carbon once depleted in the basket and thus prolong the positive effect observed during the first minutes. Hence, the question arises whether the silo is not working properly. However, in another experiment in similar conditions (see Figure 5.7), we observe a sudden rise in temperature of about 100 K after ca. 10 minutes, followed again by a decrease.

At the same time, the O_2 concentration drops to zero again, but for a very short period. This phenomenon is most likely due to fresh carbon supplied by the silo in the basket, leading to a drop in O_2 concentration and a small bump in CO_2 and CO concentration profiles (see Figure 5.7), following equations 5.3 and 5.4. However, the amount of fresh carbon seems insufficient to quench all the O/O_2, as observed in Figure 5.7 (the O_2 concentration rises again almost immediately, see inset figure), and therefore the positive effect remains limited. In any case, the temperature in the carbon bed seems very much linked to the CO_2, CO and O_2 behaviour in the mixture, but the cause and effect is not straightforward to understand and requires more in-depth analysis based on chemical kinetics modelling. Therefore, in the next section, we provide results of our model for the carbon gasification with different feed gases and we link the outcome to our experimental observations. This helps us indeed to better understand our experimental results.

5.2.6 Testing the hypothesis by means of modelling

Aiming to validate the set of reactions included in our model (Section 2.3), we simulate the experimental tests listed in Table 2.6 in section 2.3.2 of Chapter 2 above, with the corresponding input parameters. The simulated product compositions, compared against the experimental values of Panerai *et al.*[183], are depicted in Figure 5.8. Note that the product concentrations are taken at steady state, which is reached within 200 s of treatment at all the conditions tested, except for O_2_H_{600}, for which the comparison refers to the product concentrations after 600 s of treatment.

Figure 5.8 shows that the model is able to capture the experimental trends and predict the product composition reasonably well. In particular, both our simulations and the experiments highlight no reactivity of solid carbon towards O_2 at 518 K (O_2_A), i.e., the only "product" is unreacted feed gas (O_2). Furthermore, they also agree on the total consumption of O_2 at higher temperature i.e. 1086 K (O_2_E) and 1502 K (O_2_H), producing 20-25 % CO and 75-80 % CO_2 at 1086 K, and pure CO at 1502 K. The reaction analysis for O_2_E and O_2_H (see Figure C1 and C2 in the Appendix C, respectively) indicates that O_2

promptly chemisorbs at the carbon surface, forming oxygen complexes. However, CO desorption is kinetically limited at 1086 K, therefore the oxygen complexes accumulate at the surface and can only undergo total oxidation (low activation energy), releasing CO_2 and consuming all the O_2. As a result, CO_2 is the main oxidation product in this case (O_2_E).

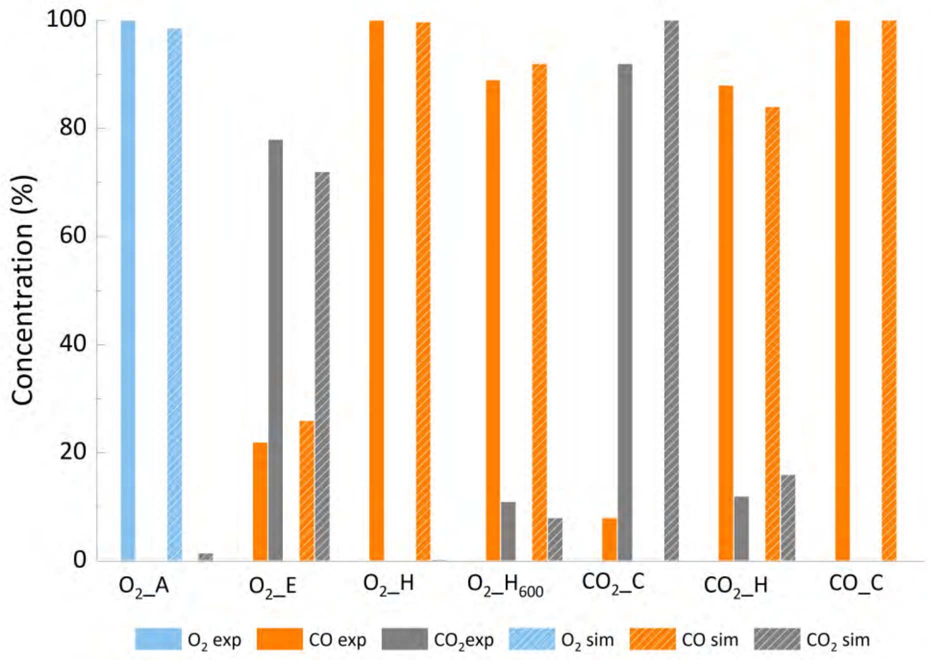

Figure 5.8. Comparison between experimental (solid)[183] *and simulated (diagonal pattern) product concentrations (see section 2.3.2 and Table 2.6) for the notation and the experimental conditions). The uncertainty on the concentration of the oxidation products was reported to be ± 12%*[183].

At 1502 K, CO desorption is kinetically favoured and competes with C(s)-O oxidation ($O_2(g) + C(s)\text{-}O \rightarrow CO_2(g) + O(g)$). Interestingly, the Boudouard equilibrium favours the CO_2 production until 1 cm in the carbon bed (see Figure C2 in the Appendix C). At that point, most of the active sites are free (see Figure 5.9), as CO has been desorbed, and the RBR can proceed and convert CO_2 back to CO. Consequently, O_2 is fully converted into CO, while CO_2 is not detectable as a product in this case (O_2_H). Therefore, we can divide the carbon bed in two zones: zone 1 where O_2 is depleted and carbon is primarily oxidized to CO_2, and zone 2 where CO_2 is consumed via the RBR. The length of the two zones depends on the temperature and the oxygen coverage (C(s)-O/C(s)) of the carbon surface. Indeed, despite the fact that the oxidation reactions typically occur within a few millimetres in the carbon bed (see Figure C1 and C2 in the Appendix C), the deactivation may start earlier than the substantial depletion of the pellets.

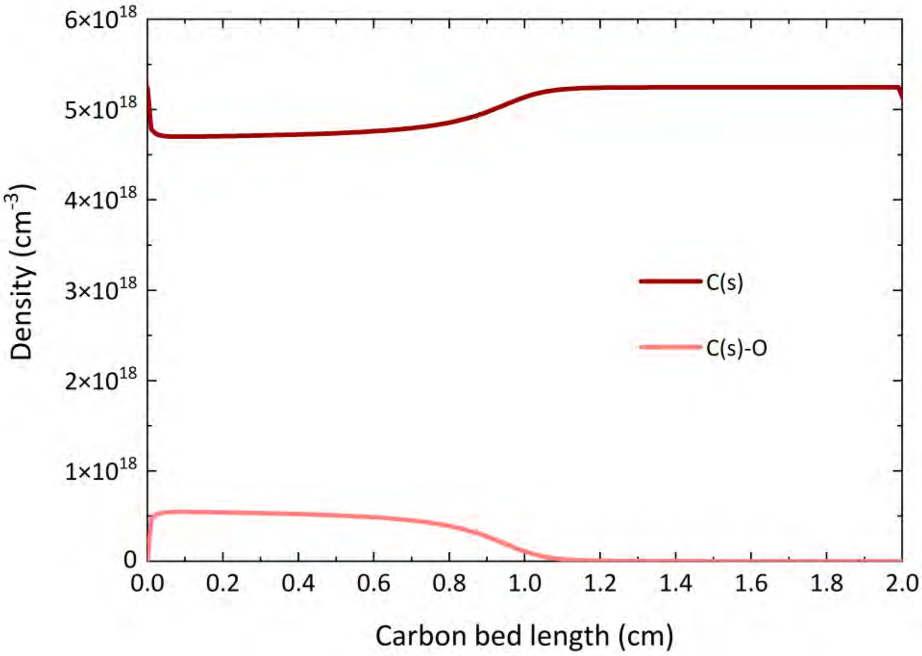

Figure 5.9. Densities of free C(s) and occupied C(s)-O active sites as a function of the carbon bed length for the O_2_H test.

In order to get more insights into the deactivation mechanism, we simulate the gasification process after 10 minutes of treatment (O_2_H_{600}). The experiments display that the carbon bed is no longer able to completely convert the CO_2 produced by the oxidation reactions through the RBR, due to both the reduced length of the bed (0.718 cm) and the saturation in oxygen of the surface. Indeed, in order to predict simultaneously a quantitative conversion of O_2 and the presence of CO_2 in the products, 11% of oxygen coverage at the surface is added in the model. Without such addition, O_2 is not fully consumed by the oxidation of the oxygen complexes and only CO is produced. According to Figure 5.9, we can reasonably assume that oxygen coverage builds up. The reaction analysis for O_2_H_{600} (see Figure C3 in the Appendix C) indicates that O_2 chemisorption rapidly slows down until O_2 is released instead, due to oxygen coverage at the surface. The onset of oxygen coverage with consequent release of O_2 favours the formation of CO_2. The Boudouard equilibrium is also shifted towards CO_2 production.

Thus, the deactivation of the carbon bed, as observed in our experiments after a few minutes (see Figures 5.3 and 5.5 above) can be ascribed to the rapid formation of oxygen complexes at the surface, which undergo both fast oxidation to CO_2 and decomposition to CO. Both reactions efficiently consume solid carbon, reducing the bed size and the zone where CO_2 can react with the active sites. However, O_2 chemisorption is so fast that C(s)-O oxidation and decomposition are the limiting steps, leaving the surface partially saturated in oxygen. On top of that, the oxygen coverage hinders the sites for O_2 chemisorption, favouring oxidation, which promotes the forward over the reverse Boudouard reaction, producing additional CO_2 at the expense of CO. This explains the drop in CO_2 conversion and in CO concentration after a few minutes in our experiments (see Figures 5.3 and 5.5 above).

Figure 5.8 also shows that when pure CO_2 is introduced as input gas into the reactor tube, the performance of the carbon bed is constant over time. In contrast to O_2, CO_2 is unreactive towards solid carbon at temperature lower than about 1000 K[59]. In fact, at 983 K (CO_2_C) the production of CO is very small, resulting from the RBR. For similar conditions (O_2_E, 1086 K), O_2 is promptly removed from the gas phase.

On the other hand, at 1413 K (CO_2_H), the RBR slowly consumes CO_2, producing CO and oxygen complexes (see Figure C2 in the Appendix C). Such complexes release a second CO molecule upon collisions with gas molecules (or O atoms). Since the reaction, $CO_2(g) + C(s) \rightarrow CO(g) + C(s)\text{-}O$, proceeds much slower than the O_2 dissociative chemisorption, the RBR is never hindered by oxygen coverage at the surface. Such a slower kinetics is also highlighted by the carbon consumption rates described in Panerai *et al.*[183]. As a result, at this condition more than 80% CO is produced, both in the experiments and predicted by our model (CO_2_H).

Finally, CO is tested as feed gas and the experiments confirmed its inertness toward solid carbon, even at high temperature (CO_C, 1508 K). Indeed, in absence of O/O_2 in the gas phase, oxygen complexes cannot be formed over the surface and CO cannot be oxidized through the forward Boudouard reaction. At the same time, CO does not present any reactivity towards the free active sites.

At this point, we have validated our 0D kinetic model for the gasification of carbon under different atmospheres (O_2, CO_2, CO, separately) in a wide range of operating conditions. The insights achieved by this set of simulations, performed to reproduce the experimental results from Panerai *et al.*[183], help us to explain the underlying pathways for O/O_2 removal and CO formation, as well as for subsequent carbon bed consumption and deactivation occurring in our experiments. These mechanisms are schematically illustrated in Figure 5.10, and can be summarized as follows.

When we turn on the plasma, a part of CO_2 undergoes splitting into CO and O. Subsequently, the O atoms will recombine into O_2 and/or react back with CO to form again

CO_2. Therefore, the reactive mixture reaching the carbon pellets will be composed of a combination of CO_2, CO, O_2 and O. During the first millimetres of the carbon bed, O_2/O promptly chemisorb at the surface. The reaction is favoured both kinetically and thermodynamically, heating up the first layer of the pellets (see Figure 5.6). The temperature spikes up to ca. 1700 K and CO desorption can proceed. At such high temperature, CO_2 can also be consumed through the RBR, increasing its conversion and further enhancing the CO production (see Figures 5.3 and 5.5).

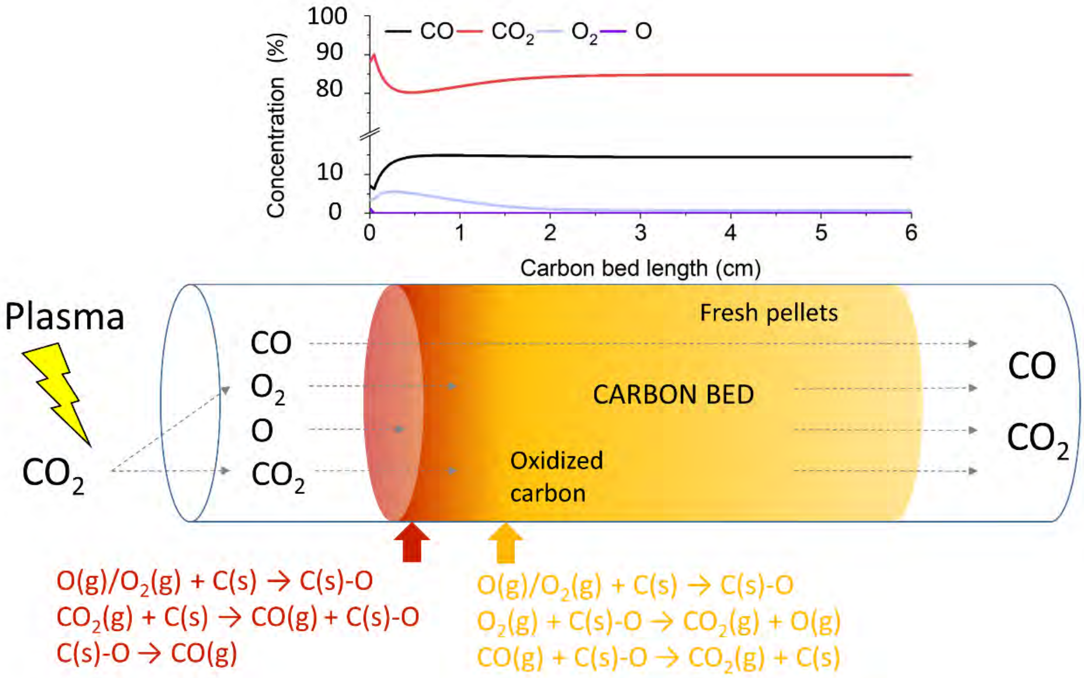

Figure 5.10. Schematic illustration of the underlying mechanism for O/O_2 removal and CO (and CO_2) formation in the presence of a carbon bed after a CO_2 plasma.

However, O_2/O chemisorption is faster than C(s)-O oxidation (O_2(g) + C(s)-O $\rightarrow$ CO_2(g) + O(g)) and CO desorption (C(s)-O $\rightarrow$ CO(g)) and the oxygen coverage at the surface starts to rise. Consequently, oxidation slows down, lowering the temperature, and O_2/O can reach the bulk of the carbon bed, explaining the increase in temperature further away from the plasma (see Figure 5.6). The oxygen coverage deactivates the entire bed and CO_2 production is promoted by the full oxidation of the surface (O_2(g) + C(s)-O $\rightarrow$ CO_2(g) + O(g)) and the forward Boudouard reaction (CO(g) + C(s)-O $\rightarrow$ CO_2(g) + C(s)). At this point, the CO_2 concentration is higher than the benchmark, as well as the temperature, due to the exothermic oxidation reactions. Eventually, the oxygen coverage is so important that the carbon bed no longer quenches O_2, which can be found in the product composition. As mentioned, the overall mechanism for O/O_2 removal and CO (as well as CO_2) formation is summarized in Figure 5.10.

Thus, the underlying mechanisms hypothesised based on our experimental observations are in line with the interpretation of our modelling results. In particular, the proposed mechanism demonstrates that the fast drop in performance of our experimental setup is not caused by a malfunctioning of the silo supplying fresh pellets. Instead, the operating temperature represents a crucial parameter, defining the composition of the gas-phase products and the rate of consumption of the pellets. Following these observations, we believe that providing additional heating to the carbon bed could help reducing the oxygen coverage and promoting the CO desorption. In this respect, an additional burner, most likely powered by gas, can purge periodically the amount of spent pellets left in the reactor, favouring the descent of fresh carbon from the silo. Another option can be the use of a thermal plasma, which can provide higher dissociation in the plasma region and, therefore, a more reactive mixture entering the carbon bed, with higher gas temperature, thus increasing conversion and energy efficiency[68,69]. However, as a drawback, argon had to be added to CO_2 in the feed mixture, in order to maintain the discharge and protect the cathode from carbon contamination[73]. The removal of argon from the product mixture would require additional energy thereby reducing the energy efficiency.

The above-mentioned studies on the combination of plasma and a carbon bed reported that O/O_2 is rapidly quenched by the carbon bed as well, although different carbon materials were used. We must point out that our experimental setup features a mesh between the plasma and carbon bed, not in use in previous studies[68,69]. This mesh may prevent the plasma from getting in contact with the carbon bed. However, in one of our experiments, the mesh was molten in its center, indicating that the plasma was in contact with the mesh, being attracted towards the center of the mesh, as the latter is conductive. Moreover, if the mesh would cause an obstruction, leading to a lower peak temperature, we would observe it from the very beginning of the measurement, while this is not the case (see the experimental temperature profile in Figure 5.6). Finally, Huang *et al.*[70] used an atmospheric non-thermal plasmatron with a stop-mesh on top of the carbon bed, to split the plasma into numerous micro-plasma jets after passing through the mesh. Therefore, adding a mesh at the anode exit is a way to attract the arc toward the outlet, directly towards the carbon bed. Huang *et al.*[70] were able to observe a transient peak in the O_2 online-concentration profile 20 seconds after plasma ignition, that rapidly drops to zero, while Li *et al.*[69] did not detect any oxygen in their experiments. This is indeed very beneficial in terms of separation costs, as mentioned in section 5.2.1, in addition to the higher CO concentration obtained at these conditions. Hence, the key parameter to reach higher conversion appears to be the temperature, that depends not only on the type of plasma but also on the reactivity of the carbon bed toward O/O_2, and subsequently the ability of the carbon bed to release heat that can be directly reused to drive the RBR. Thus, future work should focus on searching the ideal combination of these parameters (type and size of carbon material, and operating conditions).

5.3 Conclusions

In *warm* plasmas such as the GAP tested in this thesis, conversion and energy efficiency of the process can be increased by quenching the recombination reactions that form CO_2 again downstream the discharge zone. Thus, in this work, we place a carbon bed after the plasma, promoting O/O_2 removal and increasing the CO fraction in the exhaust mixture. This carbon bed allows to significantly enhance the CO_2 conversion, by almost a factor two (from 7.6 % to 12.6 %), while the energy efficiency rises from 27.9 % to 45.4 %, corresponding to a drop in energy cost from 41.9 kJ/L (without) to 25.4 kJ/L (with carbon bed). In addition, the CO concentration is about three times higher upon addition of the carbon bed, while the O_2 is nearly completely removed from the exhaust mixture, which is very beneficial, as it simplifies separation costs.

To understand the underlying mechanisms, we measure the temperature as a function of distance from the reactor outlet, and we monitor the CO_2, CO and O_2 concentrations, as well as the temperature in the carbon bed, as a function of time. The time-resolved measurements reveal that the CO_2 conversion and CO concentration are only enhanced in the first minutes, followed by a drop to values below the benchmark (i.e., without carbon bed). To better understand this behaviour, we develop a model for the gasification of carbon under the effect of different gases (O_2, CO and CO_2 separately), which is successfully validated with published experimental results.

Both our measurements and modelling results reveal that the onset of oxygen coverage at the carbon surface is of crucial importance to define the performance of the conversion process. In particular, the presence of oxygen complexes increases the selectivity towards CO_2 through the C(s)-O oxidation and the forward Boudouard reactions. In other words, the drop in CO_2 conversion and in CO concentration after a few minutes is attributed to the deactivation of the carbon bed, due to rapid formation of oxygen complexes at the surface.

This oxygen coverage can be limited by increasing the temperature in the carbon bed, i.e., by providing additional heating, leading to a complete consumption of the bed, followed by supplying fresh pellets from the silo. Hence, in our future work, we plan to apply additional heating, to further improve the performance. This additional heating will increase the energy cost of the process, linearly with the additional power supplied for the heating. This may lower the overall energy efficiency. However, the latter is not necessarily the case, if the rise in conversion due to the additional heating (promoting the specific chemical reactions) is higher than the increase in energy consumption. We aim to find conditions under which the beneficial effect of additional heating is larger than the additional energy cost. Nevertheless, our present results are already very promising, and clearly demonstrate the large potential of adding a carbon bed after a plasma reactor. In addition, our model provides very useful insights that explain our experimental observations and that are also useful for other experimental groups.

Appendix B. TGA-MS

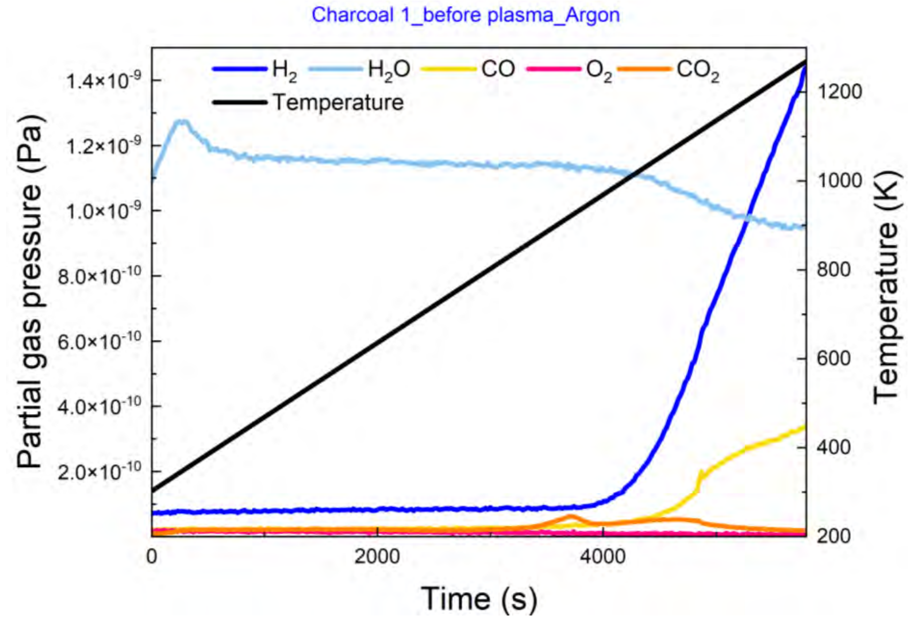

Figure B1. TGA-MS under argon atmosphere of charcoal 1 as received. Heating rate 10 K/min and gas flow rate 40 mL/min.

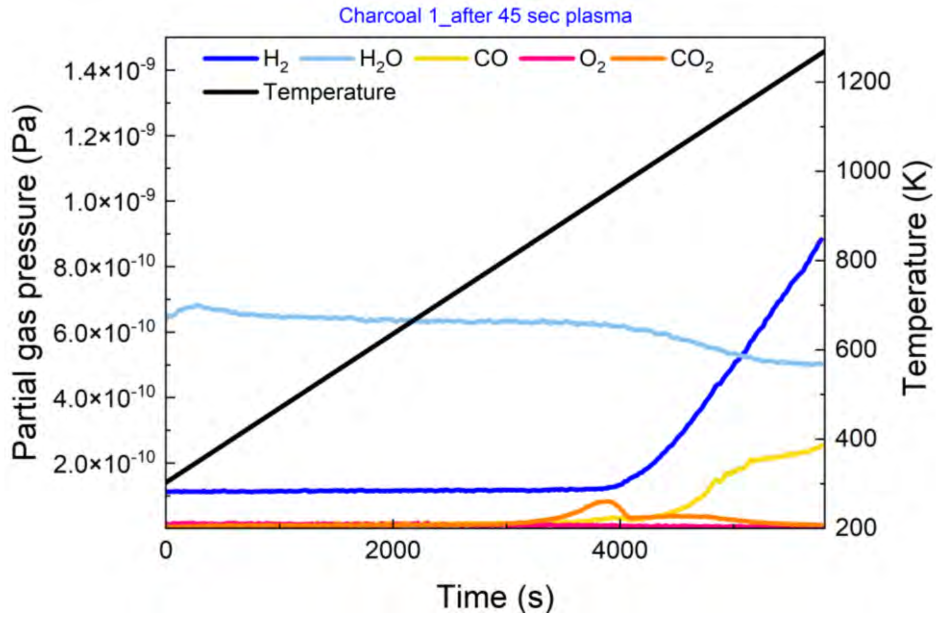

Figure B2. TGA-MS of charcoal 1, top layer, after 45 s of reaction. Heating rate 10 K/min and gas flow rate 40 mL/min.

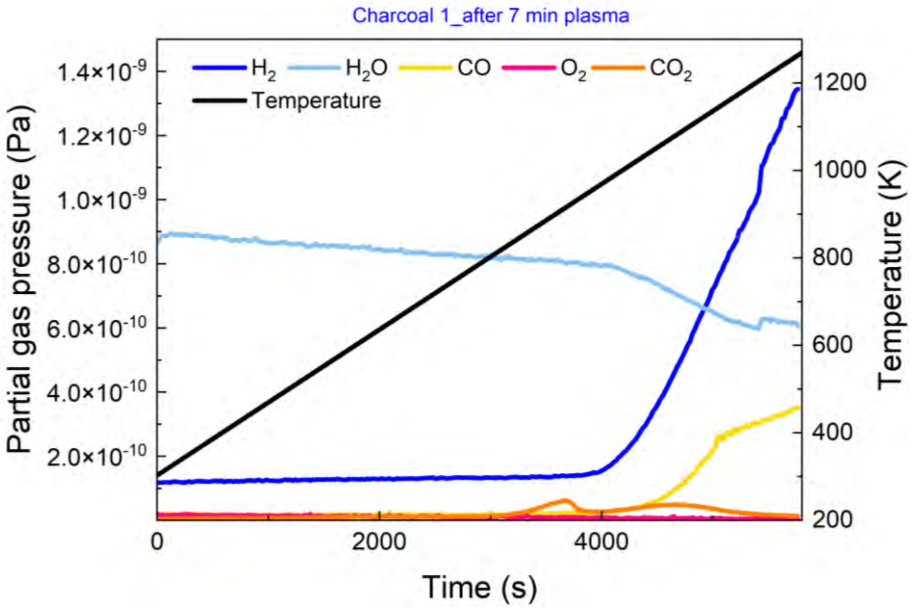

Figure B3. TGA-MS of charcoal 1, after 7 minutes of reaction. Heating rate 10 K/min and gas flow rate 40 mL/min.

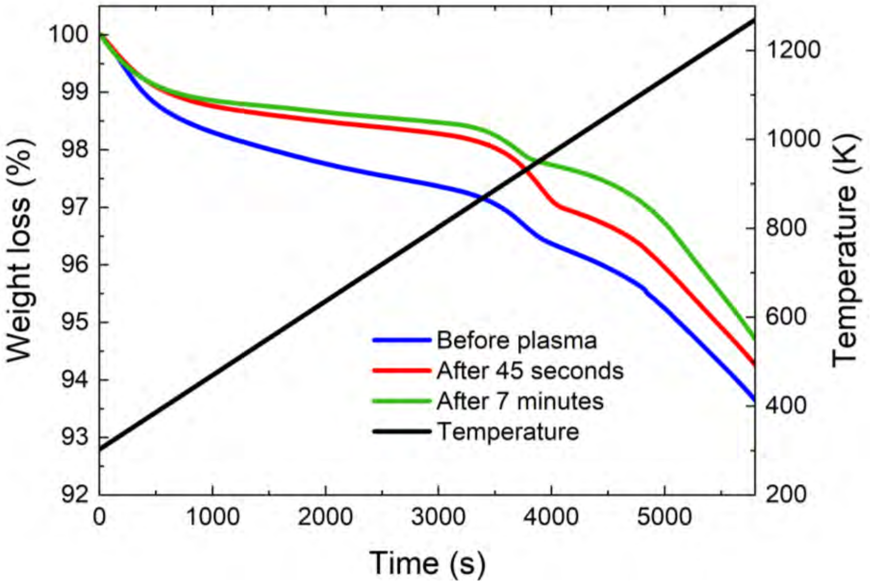

Figure B4. TGA of charcoal 1, as received and after 45 s and 7 minutes of reaction. Heating rate 10 K/min and gas flow rate 40 mL/min

Appendix C. Reaction analysis

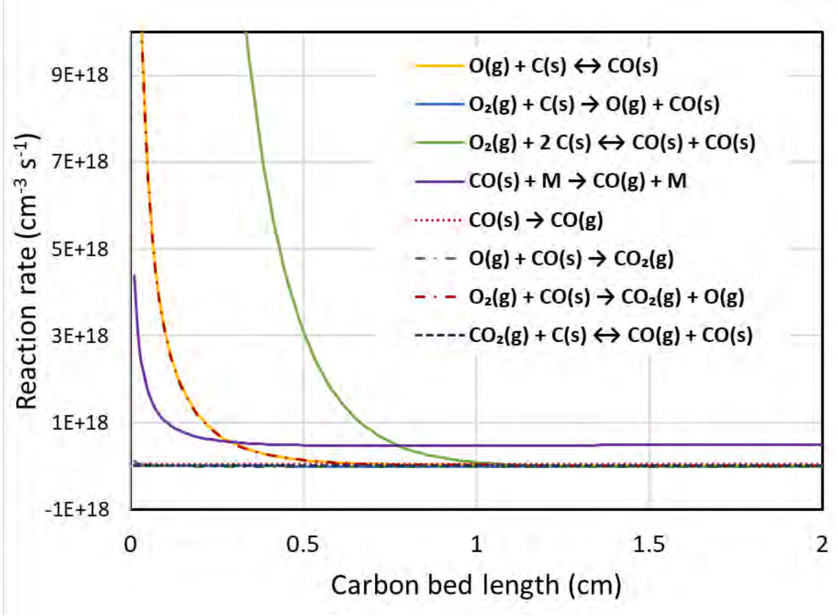

Figure C1. Rate of the main heterogeneous reactions triggered by the carbon bed at 1086 K, with O_2 as feed gas (O_2_E).

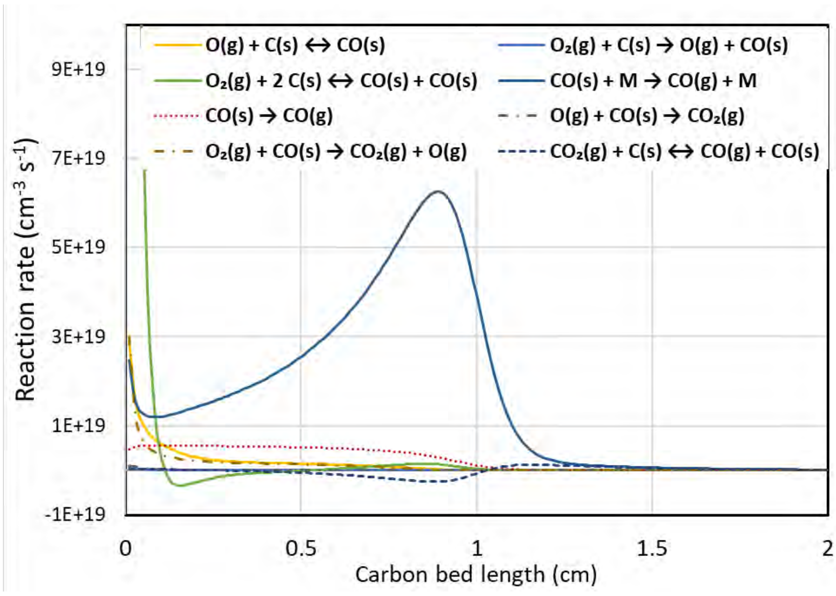

Figure C2. Rate of the main heterogeneous reactions triggered by the carbon bed at 1502 K, with O_2 as feed gas (O_2_H).

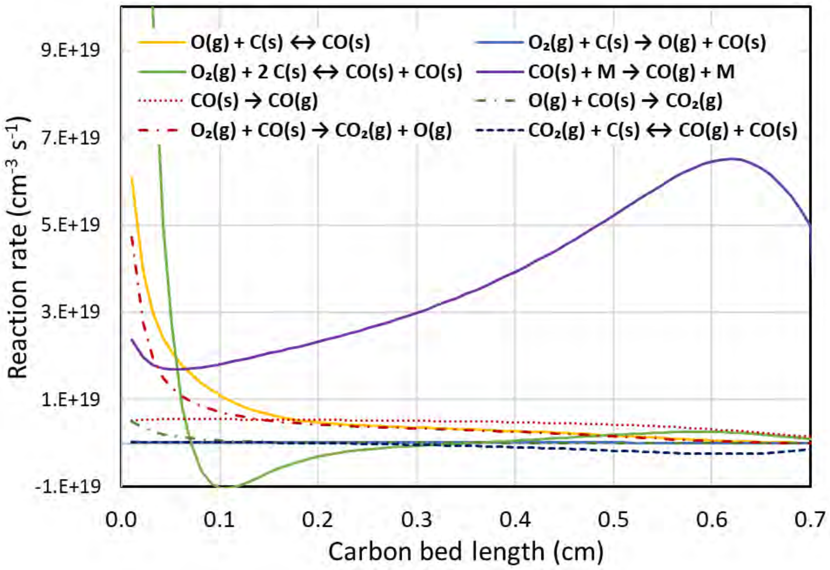

Figure C3. Rate of the main heterogeneous reactions triggered by the carbon bed at 1502 K, with O_2 as feed gas, after 10 minutes of treatment ($O_2\_H_{600}$).

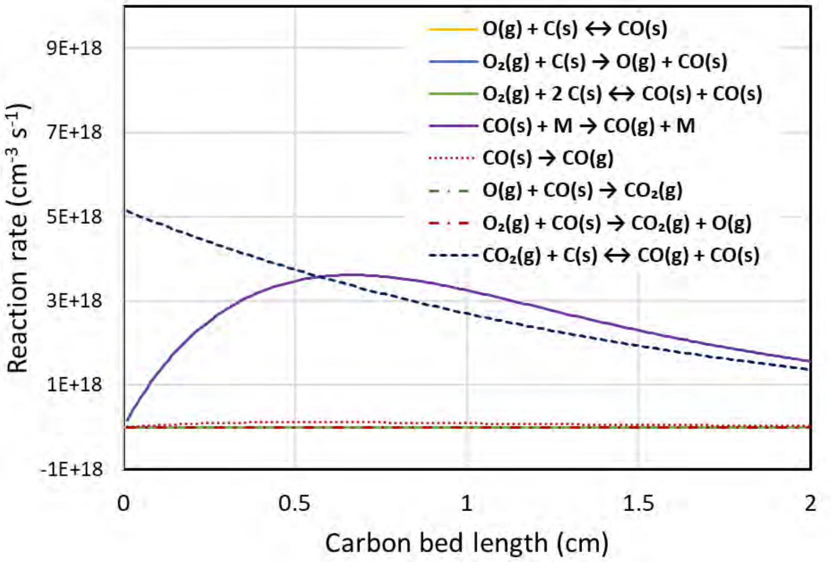

Figure C4. Rate of the main heterogeneous reactions triggered by the carbon bed at 1413 K, with CO_2 as feed gas (CO_2_H)

Chapter 6 Power concentration determined by thermodynamic properties in complex gas mixtures[10]

Abstract

In this chapter, we return the focus on the active zone of the discharge, which is subject to substantial variations with the operating conditions (e.g., pressure), affecting the reactor performance. Here, we investigate discharge contraction in a microwave plasma at sub-atmospheric pressure, operating in CO_2 and CO_2/CH_4 mixtures. The rise of the electron number density with plasma contraction intensifies the gas heating in the core of the plasma. This, in turn, initiates fast core-periphery transport and defines the rate of thermal chemistry over plasma chemistry. In this context, power concentration describes the overall mechanism including plasma contraction and chemical kinetics. In a complex chemistry such as dry reforming of methane, transport of reactive species is essential to define the performance of the reactor and achieve the desired outputs. Thus, we couple experimental observations and thermodynamic calculations for model validation and understanding of reactor performance. Adding CH_4 alters the thermodynamic properties of the mixture, especially the reactive component of the heat conductivity. The increase in reactive heat conductivity increases the pressure at which plasma contraction occurs, because higher rates of gas heating are required to reach the same temperature. In addition, we suggest that the predominance of heat conduction over convection is a key condition to observe the effect of heat conductivity on gas temperature.

---

[10] This chapter is based on:
Power concentration determined by thermodynamic properties in complex gas mixtures: the case of plasma based dry reforming of methane
O.Biondo, A. Hughes, A. van de Steeg, S. Maerivoet, B. Loenders, G. van Rooij, A. Bogaerts
Plasma Sources Sci. Technol. 32, 045001 (2023)
https://doi.org/10.1088/1361-6595/acc6ec

6.1 Introduction

In Chapter 5, we prove that a post-discharge carbon bed can effectively increase the energy efficiency of the conversion process, even without interacting with the plasma. In effect, in *warm* plasmas like the gliding arc discharge investigated in the previous chapter, and the MW discharge studied in this chapter, the conversion performance is controlled outside the plasma core, where the feed gas is fully dissociated. Another characteristic of these discharges is the high degree of inhomogeneity, compared to e.g., the pulsed glow discharge studied in Chapter 4. This means that *warm* plasmas are typically challenging to approach with a 0D kinetic model, requiring a substantial degree of approximation. Hence, in this chapter, we get back to the investigation of the active zone of a CO_2 discharge, upon the addition of CH_4. The choice falls to a MW discharge, as it displays promising conversion performance for CO_2 splitting (see Chapter 1, section 1.3) and there is a substantial literature gap for DRM (see Chapter 1, section 1.4.2).

Due to the high degree of inhomogeneity of *warm* plasmas, reactor engineering is important towards energy-efficient gas conversion and improved performance. For instance, van de Steeg and co-authors[56] suggested that the theoretical efficiency limit (~52%) of thermal CO_2 splitting may be increased to ca. 70% by improving the reactor engineering. Specific for CO_2, controlling the transport of atomic oxygen produced by CO_2 splitting can reduce back-reactions (i.e., recombination of CO + O into CO_2) and further enhance the conversion to CO (by the reaction CO_2 + O into CO + O_2)[55,56]. In the same study[56], the authors found that the enhanced performance of their MW plasma reactor is a result of thermal chemistry in the chemical non-equilibrium in the plasma core and lowered reaction barriers due to a vibrational non-equilibrium in close proximity, making super-ideal quenching possible (i.e., the above reaction of CO_2 + O into CO + O_2)[55]. A chemical non-equilibrium results from a balance between transport and chemical kinetics, with the former being a consequence of the steep gradients established between the hot plasma core and the cooler periphery[56].

In the case of DRM, such correlation was thus far not elucidated, but we expect the transport of O atoms to also play an important role in determining the conversion rate and efficiency of the dissociation process. For instance, O atoms may react with cold CH_4 molecules (e.g. through $CH_4 + O \rightleftarrows CH_3 + OH$[276,277]) in the proximity of the hot plasma core and determine an increase in conversion of both CH_4 and CO_2 (because the O atoms will not recombine anymore with CO) compared to configurations with limited mixing between hot plasma zone and cold outer gas. Hence, reactor modelling is highly needed to tune plasma parameters and thermal chemistry and couple them through efficient transport.

Nevertheless, multi-dimensional modelling is very sensitive to the input parameters and can become extremely time-consuming for complex chemistries such as DRM. Thus, identifying the key parameters that determine the dynamics underlying plasma contraction is of great importance.

In plasmas, T_g determines thermal reactions on top of electron processes, which are determined by the electron temperature (T_e). For instance, a characteristic T_g of 3000 – 5000 K can be detected in the hot core of MW plasmas at sub-atmospheric pressure, with a sudden rise to $T_g > 6000$ K when approaching atmospheric pressure[51,278]. Such an abrupt increase in temperature is accompanied by a volume reduction of the plasma, often characterized by a contraction of the optical emission profile[25,51,227,232,258,278,279]. However, the latter presents a non-monotonic dependence on the electron density (n_e) in moderate pressure regimes[280]. This phenomenon is known as optical contraction[228,280,281], with non-trivial implications on the accuracy of the measurements of the plasma volume (cf. Section 6.3.4). Concurrently, power deposition concentrates with n_e in the center of the reactor tube. We define this phenomenon as power concentration, but it is also known as plasma contraction[25,46,227,232] or constriction[25,282–284], to emphasize that it implies more than just a shrinkage of the plasma parameters. Indeed, the phenomenon involves changes in heavy-particle properties within the reaction zone and, therefore, it affects the productivity of the reactor. This term was recently adopted by van de Steeg *et al.*[51] and never used before, although power concentration, in the form of volume contraction, was observed in thermal plasmas (e.g. MW plasma torches (MPT)[227,285] and thermal arcs[286–288]), *warm* plasmas (e.g. MW[51,278,289] and gliding arc (GA)[290,291] discharges) and low-temperature plasmas (e.g. glow discharges[280,284,292,293] and radiofrequency (RF) jets[294,295]).

The mechanisms underlying discharge contraction have been extensively investigated for plasmas in atomic gases (i.e. He[280,289,296,297], Ne[280,289,296–298], Ar[280,289,294–297,299–301], Kr[289,296,297] and Xe[289,296,297]). It was concluded that the kinetics of molecular ions plays a dominant role in the contraction behavior[302], except for He where the effect of non-homogeneous heating prevails[280]. Generally, the contraction of the plasma column arises from a feedback mechanism between inhomogeneous gas heating and the creation and loss of molecular ions, leading to thermal-ionization instability[303–305]. In atomic gases, the inhomogeneous heating of the discharge in the radial direction, which is a result of the finite heat conductivity (κ) of the gas[299], causes a rise of T_g in the core of the plasma. In atomic gases, molecular ions are formed upon atomic-ion association[302]:

$$X^+ + X + X \rightarrow X_2^+ + X, \tag{6.1}$$

with X representing a ground state atom of a noble gas. With increasing T_g, the thermal dissociation of molecular ions dominates over the production, leading to higher atomic ion density and lowering the loss of charged particles through dissociative recombination:

$$X_2^+ + e^- \rightarrow X^m + X, \quad (6.2)$$

where X^m represents a metastable atom of a noble gas. As a consequence, n_e increases. Its increase is further enhanced by the loss of molecular ions through either electron-impact dissociation:

$$X_2^+ + e^- \rightarrow X^+ + X + e^- \quad (6.3)$$

or by collisions with atoms:

$$X_2^+ + X \rightarrow X^+ + X + X \quad (6.4)$$

with simultaneous increasing contribution of stepwise ionization

$$X^m + e^- \rightarrow X^+ + e^- + e^- \quad (6.5)$$

to the electron production rate in the hot plasma core. In the periphery, the radial T_g decay from the discharge axis to the wall favors dissociative recombination (6.2), leading to a net loss of n_e and, thus, driving the discharge contraction[302].

In the case of molecular gases, discharge contraction at increasing pressure has been investigated in a number of publications. During the last decade, multiple efforts have been devoted to the modelling of the contraction behavior in N_2[293,306,307], air[308], CO_2[309,310] and $H_2/O_2/N_2$ mixtures[311,312]. In particular, Zhong *et al.*[312] found computationally that both the heat release/absorption and the chemical kinetics affected the critical plasma current for the transition between the homogeneous and the contracted discharge regime in $H_2/O_2/N_2$ mixtures. This new concept was subsequently taken up by Wolf *et al.*[278] and Viegas *et al.*[310], who proved that the classical thermal-ionization instability is coupled to thermally-driven endothermic CO_2 dissociation reactions, highlighting the impact of chemical kinetics on the contraction phenomena of reactive molecular gas plasmas[311]. Furthermore, van de Steeg *et al.*[51] and Vialetto *et al.*[309] investigated the main physical and chemical mechanisms associated with diffuse and contracted CO_2 MW plasmas. In particular, a change in the dominant ionization mechanism (from electron impact to associative ionization) with pressure was proposed by comparing experimental measurements with model results.

As mentioned earlier, in the context of plasma-based CO_2 conversion, power concentration determines an intensification of the gas heating in the discharge zone, which, in turn, defines the dissociation rate of the molecule. In effect, experimental studies on MW plasmas[25,227] indicated that the optimal conditions for CO_2 conversion with respect to energy efficiency and CO yield are obtained concurrently with the transition from a diffuse to a contracted discharge. As mentioned earlier, the improved performance under these specific conditions may arise from optimized transport of O atoms (and their role in reacting with CO_2, producing more CO, vs recombining with CO into CO_2 again) from the hot plasma to the cold edges[56]. However, modelling efforts have thus far included a limited description of the flow dynamics[309–311] and, therefore, transport effects are not yet fully understood. In addition, it was found that the onset of contraction affects the product distribution in the CH_4 coupling to C_2 hydrocarbons, indicating that power concentration can help in complex chemical systems to steer the desired outputs[313].

In the present work, we study the relation of power concentration and the thermodynamic properties of the gas upon admixing CH_4 to CO_2 in a vortex-stabilized MW plasma, by a combination of optical emission imaging, laser scattering and thermodynamic calculations. To the best of our knowledge, this relation has never been characterized for DRM in the literature. Hence, this study provides new insight into the role of chemical kinetics and transport in the performance of the DRM plasma system, in view of the knowledge acquired from experiments and modelling efforts for other molecular plasmas. We interpret the evolution of the discharge parameters with power concentration in terms of the thermodynamic properties of the reactive mixtures resulting from the plasma activation of different initial CO_2/CH_4 mixtures. A deeper grasp of the plasma volume and power density evolutions with gas pressure will enable us to isolate the dominant factors determining the power concentration. The outcome will be valuable to model the mechanisms at more dimensions (2D or 3D) and pave the way towards the optimization of the reactor design for efficient conversion and tuned selectivity towards desired products.

6.2 Thermodynamic calculations

Recent work published by Wolf *et al.*[278] demonstrated the important role of thermodynamic properties of the plasma medium, especially heat capacity, as a result of its reactive nature. More specifically, the effects of composition and associated changes in reactive heat capacity were for the first time investigated in the context of CO_2 MW plasmas. As an outcome, the authors found that the endothermic nature of thermally driven CO_2 and CO dissociation reactions could explain why the diffuse and contracted regimes are characterized by a specific T_g range. Hence, motivated by these useful findings, we extend the characterization of thermodynamic properties to CO_2/CH_4 mixtures and compare them with the pure CO_2 case. In Appendix D, we describe the calculations of the equilibrium gas composition, which is essential for the computation of thermodynamic properties, such as heat capacity and heat conductivity, elucidated in Section 6.2.1 and based on the work of Magin *et al*.[314].desired products.

6.2.1 Thermodynamic model[11]

The thermodynamic model is solved within COMSOL Multiphysics® 6.0 software, and calculates the specific heat capacity at constant pressure C_p, the heat conductivity κ, as well as the specific enthalpy of the reaction, all at thermal equilibrium and as a function of T_g. In particular, C_p consists of a nonreactive fraction and a reactive fraction. The reactive fraction acts as a stand-in for the reaction enthalpy between reactions of different mixtures[315]:

$$C_{p,\mathrm{tot}} = C_{p,\mathrm{nonreactive}} + C_{p,\mathrm{reactive}} \tag{6.6}$$

where, $C_{p,\mathrm{nonreactive}}$ is defined as:

$$C_{p,\mathrm{nonreactive}} = \sum_i w_i \times \frac{C_{p,i}}{M_i} \tag{6.7}$$

The first factor, w_i, is the weight fraction of species *i*. The second factor uses the species' molar heat capacity, $C_{p,i}$, which is calculated using the NASA polynomials[315,316]:

$$C_{p,i} = R_\mathrm{g}(a_1 T_\mathrm{g}^{-2} + a_2 T_\mathrm{g}^{-1} + a_3 + a_4 T_\mathrm{g} + a_5 T_\mathrm{g}^{2} + a_6 T_\mathrm{g}^{3} + a_7 T_\mathrm{g}^{4}), \tag{6.8}$$

where R_g is the gas constant and a_i are the NASA constants, adopted for each species from the NASA Glenn Polynomials[317].

---

[11] This model was developed and tested by Stein Maerivoet at PLASMANT

Heat changes by endothermic and exothermic reactions can be restructured into reactive heat capacity, as reaction enthalpies. These are obtained from the formation enthalpies. Heat capacity and formation enthalpies are interdependent via:

$$h = \int_0^{T_g} C_{p,\mathrm{reactive}} \mathrm{d}T_g + h(0) \tag{6.9}$$

rewritten as:

$$\frac{\mathrm{d}h}{\mathrm{d}T_g} = C_{p,\mathrm{reactive}} \tag{6.10}$$

with $h(0)$ being the species' enthalpy of formation at 0 K[315]. The specific enthalpy of a gas mixture, h, can be expressed using the specific enthalpies of its components, h_i, using[315]:

$$h = \sum_i \frac{h_i w_i}{M_i}. \tag{6.11}$$

This formula uses the mass fraction of species i, w_i, and the molar mass of species i, M_i. The specific enthalpy of species i can be defined using its NASA polynomial via[317]:

$$h_\mathrm{i} = R_g T_g \left(-a_1 T_g{}^{-2} + a_2 \frac{\ln T_g}{T_g} + a_3 + \frac{a_4}{2} T_g + \frac{a_5}{3} T_g{}^2 + \frac{a_6}{4} T_g{}^3 + \frac{a_7}{5} T_g{}^4 + b_1 T_g{}^{-1} \right), \tag{6.12}$$

where a_i and b_1 are again the NASA constants, adopted for each species from NASA Glenn Polynomials [317].

Fourier's law for heat conductivity describes the relationship between local heat flux density q, heat conductivity κ, and temperature gradient ∇T_g:

$$q = -\kappa \cdot \nabla T_g. \tag{6.13}$$

In an isotropic medium, Fourier's law combined with the heat balance equation without an external heat source:

$$\rho C_p \cdot \frac{\partial T_g}{\partial t} = -\nabla \boldsymbol{q}, \tag{6.14}$$

results in:

$$\frac{\partial T_g}{\partial t} = \alpha \left(\frac{\partial^2 T_g}{\partial x^2} + \frac{\partial^2 T_g}{\partial y^2} + \frac{\partial^2 T_g}{\partial z^2} \right). \tag{6.15}$$

In this equation, α is the heat diffusivity, described using:

$$\alpha = \frac{\kappa}{\rho C_p}, \tag{6.16}$$

where ρ is the mass density. We describe the heat diffusivity, i.e., the rate of heat transfer of a material from the hot end to the cold end, as constant for the reactive and non-reactive part of the gas. This means that we have to calculate a reactive part of the heat conductivity to include in the total heat conductivity.

$$\kappa_{\text{reactive}} = \kappa_{\text{nonreactive}} \frac{C_{\text{p,reactive}}}{C_{\text{p,nonreactive}}} \tag{6.17}$$

Consequentially, κ_{reactive} will dominate over $\kappa_{\text{nonreactive}}$ when the heat released or removed by reactions results in domination of $C_{\text{p,reactive}}$ over $C_{\text{p,nonreactive}}$.

It should be noted that $C_{\text{p,reactive}}$ is not a physical heat capacity; it is just a mathematical expression for the exothermic and endothermic reactions of our system. Hence, κ_{reactive} is also not a real (physical) heat conductivity. The addition of κ_{reactive} is necessary to account for the heat flux that chemical reactions create. As the equilibrium gas composition fluctuates with temperature, diffusion of species over temperature gradients increases the heat flux. For instance, species absorb heat by an endothermic reaction at a high temperature, and, after diffusing towards a low temperature region, the reverse exothermic reaction takes place to sustain the equilibrium, releasing heat in the process. This system has effectively transported heat from a high temperature region towards a low temperature region via chemical reactions, which is expressed as κ_{reactive}. This is described by equation 17 in Butler and Brokaw[318], of which equation 6.17, in this thesis, is a reformatting for the estimation of the order of magnitude of κ_{reactive}.

The total heat conductivity is thus composed of reactive and nonreactive terms[315]:

$$\kappa_{\text{tot}} = \kappa_{\text{nonreactive}} + \kappa_{\text{reactive}}, \tag{6.18}$$

where $\kappa_{\text{nonreactive}}$ can be expressed as:

$$\kappa_{\mathrm{nonreactive}} = 0.5\left(\sum_i x_i \kappa_i + \frac{1}{\sum_i {x_i}/{\kappa_i}}\right). \tag{6.19}$$

In eq. 6.19, x_i is the molar fraction of species i in the gas mixture and κ_i is the heat conductivity of species i, which is calculated using[315,319–321]:

$$\kappa_i = 2.669 \times 10^{-6}\,\frac{\sqrt{T_{\mathrm{g}} M_i \times 10^3}}{\sigma_i^2 \Omega_k} \times \frac{1.15 C_{p,i} + 0.88 R_{\mathrm{g}}}{M_i}, \tag{6.20}$$

where σ_i is the characteristic length of the Lennard-Jones potential, and Ω_k is the dimensionless collision integral given by[315,320,321]:

$$\Omega_k = \frac{b_1}{\left(T^*\right)^{b_2}} + \frac{b_3}{\exp\left(b_4 T^*\right)} + \frac{b_5}{\exp\left(b_6 T^*\right)} + \frac{4.998 \times 10^{-40} \mu_{D,i}^4}{k_{\mathrm{b}}^2 T^* \sigma_{\mathrm{i}}^6}, \quad T^* = T_{\mathrm{g}} \frac{\varepsilon_i}{k_{\mathrm{b}}}, \tag{6.21}$$

with b_x being empirical constants, $\mu_{D,i}$ the dipole constant of species i, ε_i the potential energy minimum value and k_{b} the Boltzmann constant. These values are tabulated data taken from the literature[315].

These calculations provide the evolution of the thermodynamic properties as a function of T_{g}, which are used to put the experimental observations in perspective in Section 6.3.4 and to gain a deeper understanding of the mechanism, as discussed in Section 6.3.7.

6.3 Results and discussion

6.3.1 Plasma imaging

Imaging of the O 777 nm emission line intensity is used as proxy for the plasma volume and its evolution in response to operational parameters. This is justified as the 777 nm O($3s^5S^0$ ← $3p^5P$) spectral line emission is mostly a result of direct electron impact excitation from the ground state, since the excitation energy of the upper state is 10.74 eV, far above $k_{\mathrm{B}}T_{\mathrm{g}}$[232]. The acquired discharge images are presented in Figure 6.1, for different CH_4 percentages added to CO_2 (0, 5, 10, 20 and 30%) as a function of pressure.

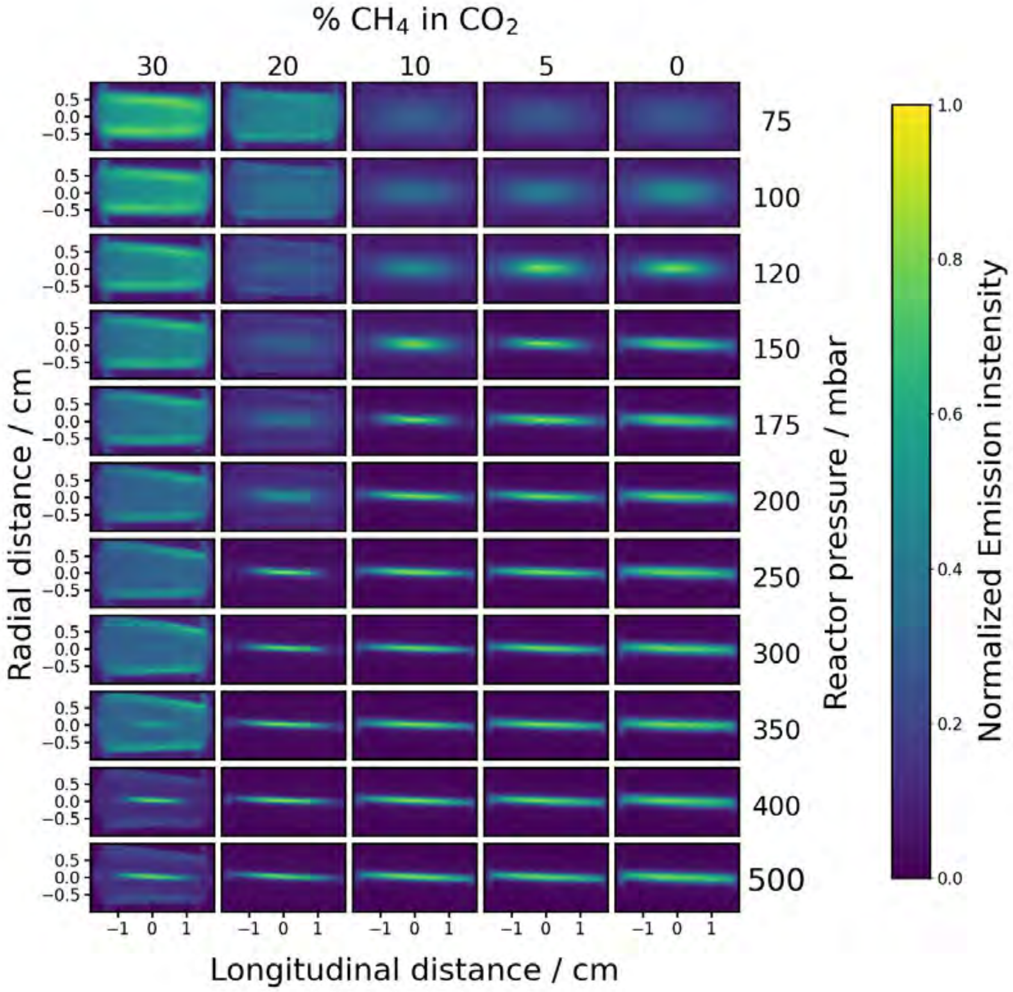

Figure 6.1. Discharge images for different CO_2/CH_4 mixtures as a function of pressure (1000 W, 10 slm), with subtraction of the background emission and normalized central emission profiles.

In pure CO_2, the plasma filament appears at 120 mbar at the center of the tube, which is in agreement with the previous work of Wolf *et al*.[278] for a similar CO_2 vortex-stabilized MW plasma. The contraction is nearly complete at 150 mbar. Indeed, for higher pressures, the radial size of the plasma is barely changed (see Figure 6.6, below). The addition of CH_4 to CO_2 has the effect of shifting the emergence of the plasma filament towards higher pressures. For instance, an addition of 5% leads to a shift of ca. 30 mbar, while the admixture of 30% CH_4 moves the transition to a contracted plasma to 400 mbar, i.e., a shift of nearly 300 mbar (Figure 6.1). Furthermore, the width of the recorded emission in the contracted regime decreases upon rising fraction of CH_4. This may arise from quenching of excited O atoms through reactions with CH_x species to produce CH_{x-1} and OH radicals[276,277,322,323] or by transfer of their energy into the dissociation of the collision partner[323]. Due to the lack of studies on the kinetics of the upper state of the $O(3s^5S^0 \leftarrow 3p^5P)$ transition in the complex CO_2/CH_4 environment, no straightforward conclusions can be drawn at this stage. In addition, optical interference due to broadband emission (ca. 500-1100 nm, with a maximum at 800-900 nm[324–326]) from hot carbon nanoparticles may alter the plasma shape. Concurrently, carbon deposition is observed inside the reactor tube (particularly intense for the CO_2/CH_4 70/30 mixture), confirming that the condensation of nanoparticles occurs at the boundaries between the hot inner region and the cold outer vortex[324,325]. In this regard, Thomson scattering is an alternative tool to spatially resolve n_e and define the size of the plasma. Therefore, we apply this technique to reveal the effect of CH_4 addition on the plasma properties, as shown in the next section. After that, we verify OES imaging against Thomson measurements and we provide more insights in the intrinsic limitations of OES imaging in section 6.3.4.

6.3.2 Determination of electron density and temperature

Thomson scattering enables the capture of electron properties with good spatial (sub-mm[225]) resolution. In our study, we follow the procedure for the derivation of the plasma properties (n_e and T_e) as reported by van de Steeg *et al.*[246]. The main plasma parameters (n_e and T_e), measured at the plasma center, with a volumetric flow rate of 10 slm, are plotted in Figure 6.2 as a function of pressure.

In pure CO_2 plasma, n_e sharply rises between 120 and 150 mbar and then tends to a plateau at about 3×10^{19} m^{-3} (Figure 6.2(a)). Concurrently, T_e drops from ca. 25000 K (or ca. 2.15 eV) at 100 mbar down to ca. 7500 K (or ca. 0.65 eV) at 400 mbar (Figure 6.2(b)). These results are in line with the measurements by van de Steeg *et al.*[51] for the same reactor and identical experimental conditions, proving the reproducibility of these measurements. The pressure interval within which the abrupt increase in n_e occurs (i.e. 120-150 mbar) is consistent with the appearance of the plasma filament (Figure 6.1), emphasizing the strong connection between volume contraction and electron properties through power concentration.

Small additions of CH_4 (5-10 %) slightly increase the threshold pressure for the onset of contraction. While this is appreciable from the n_e evolution (Figure 6.2(a)), no effect on T_e within error bars is observed during the transitioning phase of the plasma (Figure 6.2(b)). The origin of these uncertainties can be twofold. First, an overall lower n_e is observed compared to the pure CO_2 case and, at low pressure, n_e is very close to the detection limit of the Thomson feature with our laser setup. Therefore, T_e is hard to estimate with sufficient accuracy for $n_e \leq 2 \times 10^{18}$ m^{-3} without the use of magnification techniques[327]. Second, the C_2 Swan ($d^3\pi_g \rightarrow a^3\pi_u$) bands blend the Thomson signal. The latter is fitted with a Gaussian, and the error is calculated as the standard deviations of the residuals. Unlike the cross sections for light scattering on CO_2, CO, O_2 and O atoms, cross sections for C_2 Swan band LIF[328,329] are not included in the fitting script. Thus, the C_2 Swan band peaks contribute to increase the residual signal and, therefore, the error on n_e and T_e determination.

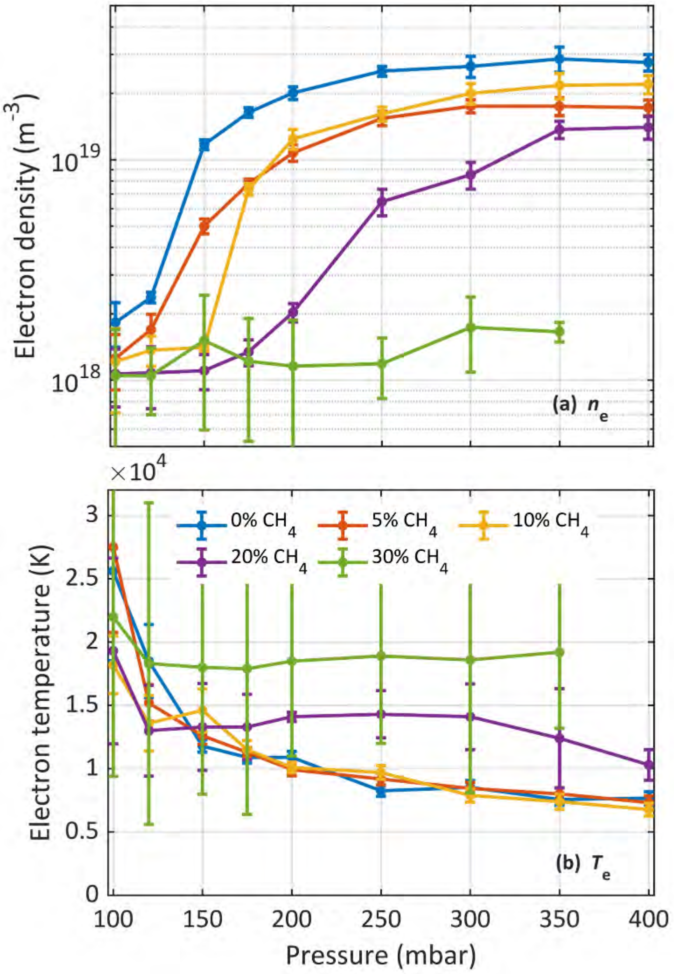

Figure 6.2. Measured electron density (n_e, a) and temperature (T_e, b) as a function of pressure for different CO_2/CH_4 mixtures, measured at the center of the plasma. Note that the measurements were not possible at 400 mbar for 30% CH_4 because of the high instability of the discharge.

Additions of 20 and 30% CH_4 have a prominent effect on the plasma parameters. The pressure threshold to observe a substantial n_e increase is further shifted towards higher values. Consistently, T_e stays above 1 eV, although it is difficult to retrieve due to the low n_e. As a result, the volume contraction appears to be prevented by the admixture of CH_4. In the next section, T_{rot} measurements are presented and compared with the electron properties.

6.3.3 Thermalization of the discharge

Additional Rotational Raman scattering is applied to measure the heavy gas particle properties, namely T_{rot} and number densities[239]. In our study, we determine T_{rot} following a procedure described by van den Bekerom and co-workers[54,330], and its evolution, along with T_e, is shown as a function of the pressure in Figure 6.3.

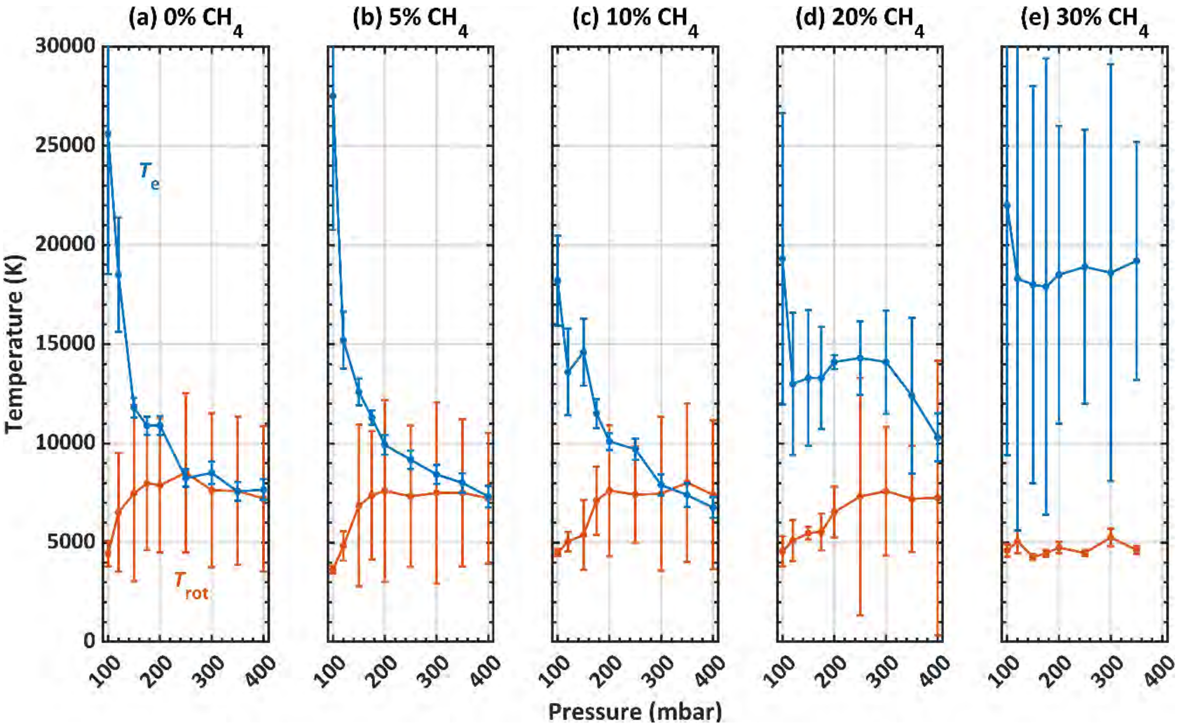

Figure 6.3. Evolution of the rotational (T_{rot}) and electron (T_e) temperature as a function of pressure for (a) pure CO_2, (b) 5%, (c) 10%, (d) 20% and (e) 30% CH_4 addition, measured at the center of the plasma.

T_e equilibrates to T_{rot} at ca. 250 – 300 mbar for all the CO_2/CH_4 mixtures, except for 20% and 30% CH_4. Specifically, with 20% CH_4, full thermalization is reached only at $p > 350$ mbar, whereas it is not observed for 30% CH_4. Recently, van de Steeg *et al.*[51] and Vialetto *et al.*[309] demonstrated the fundamental role played by associative ionization reactions (mostly $C + O \rightarrow CO^+ + e^-$) in determining the discharge thermalization, linking T_g to T_e. However, the threshold pressure for a substantial volume reduction and the concomitant appearance of the plasma filament is lower than the pressure at which thermalization is observed. In order to obtain a deeper understanding on the phenomenon, we evaluate in the next section the applicability of OES imaging to determine the plasma size and, eventually, estimate the average power density in the discharge zone.

6.3.4 Validation of OES with Thomson scattering

Our MW setup features radial laser scattering measurements (cf. Figure 3.4), allowing for the estimation of n_e decay as a function of distance from the reactor tube axis. Such measurements enable the assessment of the plasma width, which can also be determined by OES imaging. A comparison between both techniques is shown in Figure 6.4.

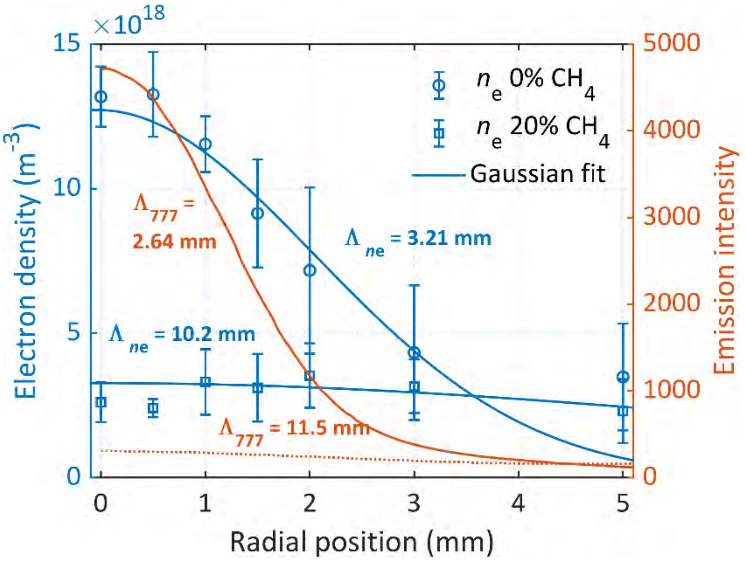

Figure 6.4. Radial electron density profile (blue) and O 777 emission intensity (red) for pure CO_2 (solid) and 20% CH_4 in CO_2 (dashed) MW plasma (1000 W, 10 slm, 150 mbar). The Gaussian fit of the electron density profile is also plotted, from which the full width at half maximum (FWHM) is calculated (Λ_{n_e}). Note that for the readability of the figure, the Gaussian fit of the O 777 line emission is not plotted, but it closely resembles the experimental profile. The corresponding FWHM (Λ_{777}) is reported in red. The radial position = 0 mm corresponds to the reactor tube axis (cf. Figure 3.4).

In pure CO_2 plasmas, the O 777 line emission intensity can be used as a proxy for the n_e distribution[232]. However, for accurate quantification of n_e and the plasma size, correction factors accounting for the non-monotonic dependence of the O 777 line distribution on n_e must be taken into account[228]. As a result, the radial distribution of the line emission appears to be more compressed than the n_e profile e.g., comparing the red and blue lines for 0% CH_4 in Figure 6. The corresponding $\Lambda_{n_e}/\Lambda_{777}$ ratio of 1.22 is somewhat lower than 1.5, calculated by Viegas *et al.*[228] for a CO_2 MW discharge in contracted regime. The difference may arise either from the experimental error, which increases with the radial position due to overlapping of the strong rotational Raman signal with the Thomson signal, or from the different methods used to estimate the n_e distribution, i.e. Thomson scattering in this study and a 1D numerical model including an O atom collisional-radiative model in Viegas *et al*.[228]. Nevertheless, we observe a good overlap of the O 777 line distribution with the n_e measured by radial Thomson scattering within the plasma core (up to 1 mm from the tube axis). Outside the plasma core (> 1 mm), a rapid drop of T_g (see Figure 6.9, below) leads to an increasing rotational Raman signal, progressively hiding the Thomson feature and making the determination of n_e less accurate. At the same time, this favors recombination of O atoms (see Figure 6.5), therefore lowering the OES intensity. Nevertheless, both OES imaging and Thomson scattering outline substantially similar n_e radial distributions, indicating that they both are suitable tools for the estimation of the plasma width, with the necessary corrections taken into account. A validation of the estimated n_e profiles with numerical models is highly desirable, especially for conditions where the sensitivity of Thomson scattering is low.

When CH_4 is added to CO_2, the ratio between the OES and Thomson scattering profiles deviates and the overlap at the center is lost. The dependence of the intensity of O 777 line emission on the n_e distribution is determined by T_e, the density of O atoms and their origin (i.e. formed upon thermal or electron-impact dissociation)[228,232]. In this study, we lack accurate spatially resolved measurements of O atom density. Thus, at the status of development, we cannot apply a scaling factor to match the peak O 777 line intensity with the peak n_e in CO_2/CH_4 mixtures. Notwithstanding this, both techniques agree well in the trends and can be used to retrieve the plasma width in a good approximation.

The underestimation of n_e upon the use of OES imaging when CH_4 is added to CO_2 may be explained by a lower O atom density compared to pure CO_2. At the status of development, absolute O-atom density cannot be easily quantified in CO_2/CH_4 mixtures by Raman scattering due to a variety of H-containing species not included in the fitting procedure. Notwithstanding this, the technique can still provide an insight into the quenching of O atoms, as displayed in Figure 6.5.

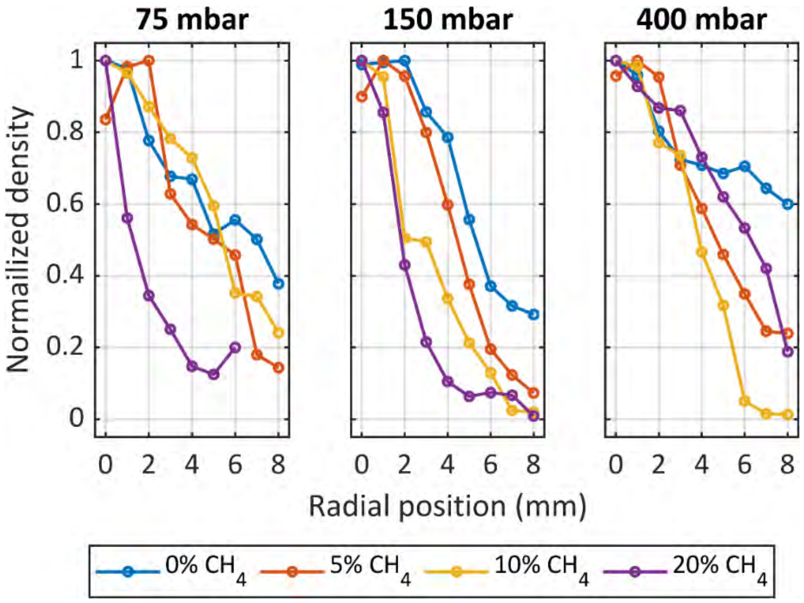

Figure 6.5. Radial evolution of the O atom density normalized at its highest value, for different CO_2/CH_4 ratios at 75, 150 and 400 mbar (1000 W, 10 slm). 30% CH_4 is not shown due to overlap of C_2 Swan ($d^3\pi_g \rightarrow a^3\pi_u$) with the O atom Raman peaks.

A faster radial decay of the O atom density is generally observed with increasing CH_4 content. This can be explained by a more efficient quenching by CH_x species and may suggest that $CH_4 + O \rightleftarrows CH_3 + OH$ is occurring at the edges of the plasma volume. Such hypothesis can have interesting implications for the performance of the reactor. For instance, a higher conversion of both CH_4 and CO_2 is expected. In this perspective, power concentration at the center of the tube is advantageous as it provides extra insulation of the plasma from the walls and prevents carbon deposition compared to a more diffuse regime with lower power density. At the same time, the predominance of diffusion over convection in the inner region of the vortex, where the plasma is located, favors fast core-periphery transport of hot O atoms, enhancing the collisions between the latter and cold CH_4 molecules. Such process can potentially increase the energy efficiency up to a higher thermal limit, analogously to the O-CO_2 association in pure CO_2 MW plasmas[56]. As the authors suggested, reactor engineering plays here an essential role to find the pathways to fully exploit the features of vortex-stabilized discharges. In this sense, knowing where the power is absorbed by the electrons and transferred to the gas is crucial. In the next section, OES imaging is used to determine the plasma dimensions and estimate the power density.

6.3.5 Estimation of the power density

lasma width and length are calculated upon the fitting of the O 777 line intensity with a Gaussian as described in Wolf *et al.*[232] and are plotted as a function of pressure in Figure 6.6(a) and (b), rspectively.

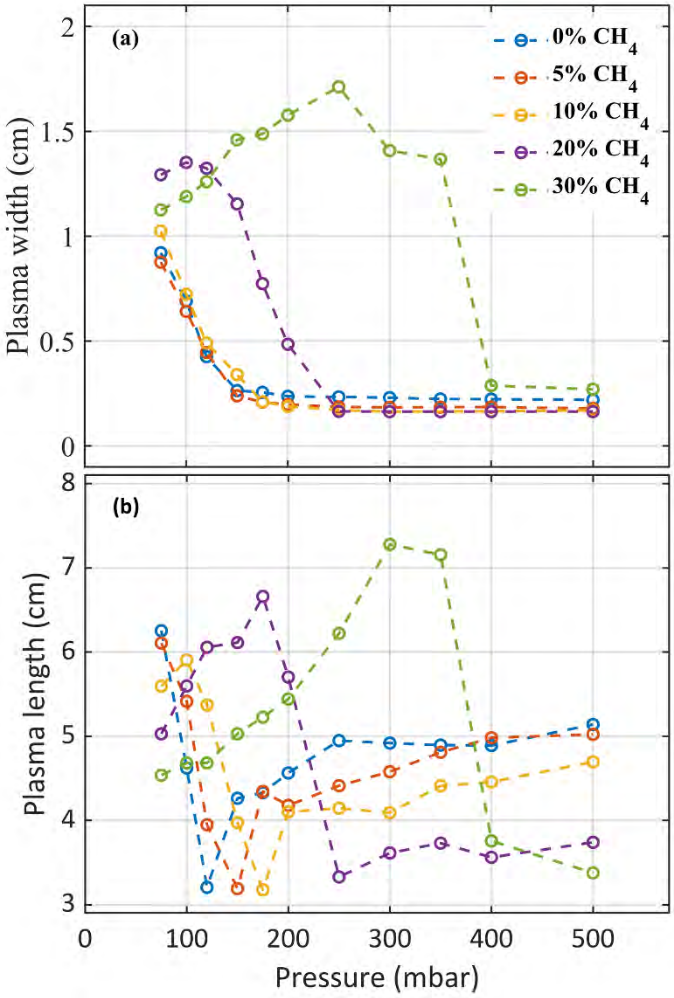

Figure 6.6. Plasma width (a) and length (b) estimated from the fitting of the radial profile of the O 777 line intensity with a Gaussian, as a function of pressure for different CO_2/CH_4 mixtures (1000 W, 10 slm).

Interestingly, the width and the length exhibit a different behavior with increasing pressure. The former progressively decreases and approaches a plateau at high pressure. The latter sharply decreases when the filament appears, reaches a minimum value and then increases again. Such behavior was captured by Wolf *et al.*[278] in a CO_2 MW discharge, who ascribed the elongation to the onset of surface waves, promoted by the increase in ionization degree during the transition from diffuse to contracted regime. This mechanism may explain why the power concentration is mainly a radial phenomenon in MW discharges. Moreover, the plasma seems to expand in both dimensions before the onset of power concentration. This is evident for high CH_4 percentage (20 and 30%) but the effect of the optical interference from carbon nanoparticles cannot be easily ruled out. Particularly, the blackbody radiation may lead to a deviation from a Gaussian distribution, especially in the radial direction, where local maxima in emission intensity are observed (Figure 6.1). In order to reduce the resulting overestimation of the plasma dimensions, we cropped the OES images excluding the local maxima and fitting only the inner region. Furthermore, we would like to point out that, due to optical contraction, the width and the length of the plasma may be underestimated in absolute values by a factor of 0.6-0.8 compared to the n_e distribution estimated by 1D modeling[228] or by Thomson scattering (Figure 6.4). Thus, a deeper investigation is needed to validate the estimated dimensions in absolute values.

From the width and the length, the plasma volume V is calculated assuming an ellipsoid shape:

$$V = \frac{4}{3}\pi\frac{l}{2}r^2, \tag{6.22}$$

with l being the length and r being half of the width of the plasma. Subsequently, the power density is estimated as the input power (1000 W) divided by the plasma volume, shown in Figure 6.7(a). The resulting power density is plotted as function of pressure in Figure 6.7(b).

In contrast to the thermalization of the discharge, the power density shows an abrupt increase at intermediate pressure, exactly in the region where the plasma filament appears in the OES images (cf. Figure 6.1). The increase is of about 2 orders of magnitude, consistent with the square dependence of the volume on the discharge radius (Eq. 6.22), which decreases by one order (see Figure 6.6(a)). However, the increase in n_e (Figure 6.2(a)) and T_{rot} (Figure 6.3) is not monotonically dependent on the average power density (Figure 6.7(b)), especially upon the addition of CH_4. Particularly, the power density in the contracted regime increases with increasing CH_4 content, except for 30% CH_4 where other effects may come into play, i.e. strong emission from carbon nanoparticles and discharge instability. At the same time, n_e decreases (cf Figure 6.2(a)), suggesting that the presence of CH_4 may alter the production/destruction balance of charged particles, while T_{rot} is barely changed (Figure 6.3), likely due to variations in thermodynamic properties of the gas with CH_4 admixing.

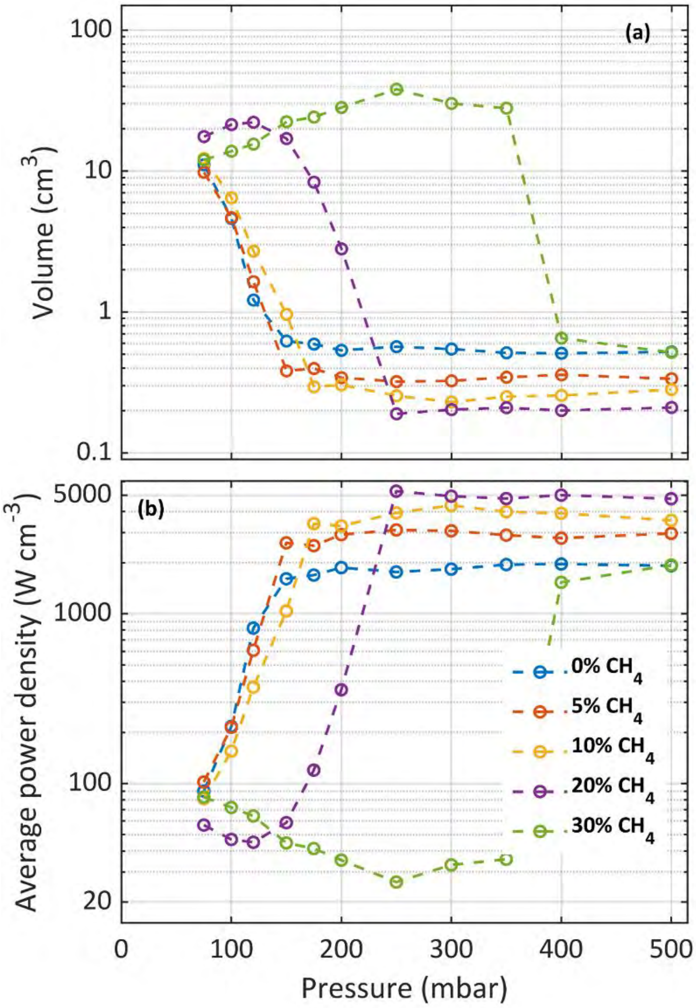

Figure 6.7. Estimated (a) plasma volume and (b) power density as a function of pressure for different CO_2/CH_4 mixtures (1000 W, 10 slm). Note that the underestimation of the plasma width and length, due to the phenomenon of the optical contraction[228]*, may result in the underestimation of the plasma volume (up to a factor of 4), and a corresponding overestimation of the power density.*

According to the general hypothesis on the mechanisms underlying the discharge contraction, the plasma radius is set by an equilibrium between ionization and dissociative electron-ion recombination[302]. Such equilibrium is determined by T_g, which defines the lifetime of molecular ions. Thus, the effect of CH_4 is to be sought either in the thermodynamic properties of the mixture or in the different chemistry. More likely, an interplay between both thermodynamics and chemistry underpins this behavior. In the next section, we address this question and discuss this connection more in-depth, based on to our thermodynamic calculations.

6.3.6 Thermodynamic properties of CO_2/CH_4 mixtures

Previous experimental and modelling efforts demonstrated that there is a strong link between the thermodynamic properties of the gas and the contraction of the discharge[278,288,289,293,301,302]. Recently, Wolf *et al.*[278] found that a MW discharge in pure CO_2 is stabilized in the diffuse regime at ca. 3000 K by the high reaction enthalpy of CO_2 dissociation. Above 3000 K, the discharge stability is lost and a new equilibrium is found at ca. 6000 K, where CO dissociation takes place. Thus, the discharge stability indicates that at certain T_g, C_p is higher than for other temperatures. This can be explained by the enthalpy change due to dissociation reactions. This concept is better visualized by the introduction of the specific energy input in thermodynamic equilibrium, $q_{te}(p, T_g)$[278]. This quantity identifies the amount of energy required per initial CO_2/CH_4 molecule to reach a state of thermodynamic equilibrium by isobaric heating trajectory from $T_{g,0}$ to $T_{g,1}$, obtained by integration over $C_{p,\mathrm{tot}}$ as follows:

$$q_{te} = (xM_{CO_2} + yM_{CH_4})/(eN_A)\int_{T_{g,0}}^{T_{g,1}} C_{p,\mathrm{tot}}\left(T_g\right)\mathrm{d}T_g, \tag{6.23}$$

where M_{CO_2} and M_{CH_4} are the molar masses of CO_2 and CH_4, respectively, in kg mol^{-1}, x and y are the fractions of CO_2 and CH_4, respectively, in the mixture, e is the elementary charge and N_A is Avogadro's number. The evolution of T_g in response to q_{te} is shown in Figure 6.8.

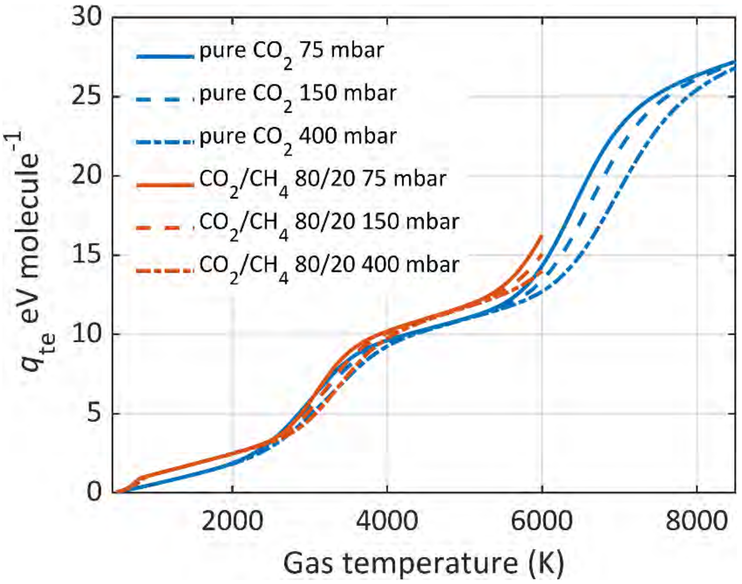

Figure 6.8. Specific energy input q_{te} per molecule of reactant in relation to the mixture temperature, relative to 300 K, for three different pressures, and for pure CO_2 and the CO_2/CH_4 80/20 mixture.

As pointed out by Wolf *et al.*[278], we notice that the span in q_{te} associated with the stable T_{g} regions (namely ca. 3000 and 6000 K) corresponds well to the bond energies of the CO-O bond (5.51 eV) and C-O bond (11.16 eV). However, Raman T_{rot} measured in the diffuse and contracted regimes are typically 1500 K higher, indicating that the gas is not in a thermodynamic chemical equilibrium. Indeed, non-dissociated CO_2 can still be detected in the core of the plasma, even at $T_{\mathrm{g}} > 4500$ K[56]. As a result of the thermal non-equilibrium identified in this study (cf Figure 5) and fast transport, the admixture of CH_4 may introduce additional chemical non-equilibrium. Such complexity was already observed in the context of CH_4 MW plasmas[331]. It follows that the corresponding thermodynamic properties may be affected by uncertainties in the composition mixtures. Notwithstanding this, we believe that the thermodynamic calculations are still valid in a good approximation and that they can provide useful information to understand power concentration.

The evolution of the T_{g} response with q_{te} of the pure CO_2 case closely resembles the behaviour in CO_2/CH_4 80/20 mixture. Hence, T_{g} corresponding to the plasma contraction regimes seems to coincide with regions of high $C_{p,\mathrm{tot}}$, where q_{te} steeply increases because more energy is required to obtain a rise in T_{g}. Nonetheless, while this may explain the stabilization of the plasma in certain T_{g} intervals, it cannot justify the pressure shift (see Figure 6.1) and the substantial increase in power density (see Figure 6.7(b)) observed upon the addition of CH_4.

It has often been found that κ defines the radial T_{g} gradient, which in turn determines the degree of inhomogeneity of the gas heating[288,289,299,302,332]. In order to find further verification of this mechanism, we plot $\kappa_{\mathrm{nonreactive}}$ and κ_{tot} (sum of nonreactive and reactive components) as a function of T_{g} in panels (a) and (b) of Figure 6.9, respectively. We would like to point out that $\kappa_{\mathrm{nonreactive}}$ is here the sum of the translation of heavy species and the contribution from internal energy changes, while the translation of electrons is neglected. Notwithstanding this, our results are in good agreement with the work of Niu *et al.*[333] (and other contributions concerning only the pure CO_2 case[334,335]). In addition, $\kappa_{\mathrm{reactive}}$, which is included in κ_{tot} (Figure 6.9(b)), only includes the contributions of chemical reactions between heavy neutral species and disregards possible contributions from ions and electrons, which are, however, not relevant under the conditions studied here[333].

Analogously to C_p, κ is mainly defined by its reactive component, $\kappa_{\mathrm{reactive}}$, which accounts for the heat flux caused by chemical reactions. The sharp peaks in κ_{tot} are, therefore, a result of the chemistry activated by T_{g}, exactly as it happens for $C_{p,tot}$[333]. Unlike q_{te} (which is derived from $C_{p,tot}$), k_{tot} exhibits important deviations upon addition of CH_4, being about twice as high for $T_{\mathrm{g}} > 3000$ K compared to pure CO_2.

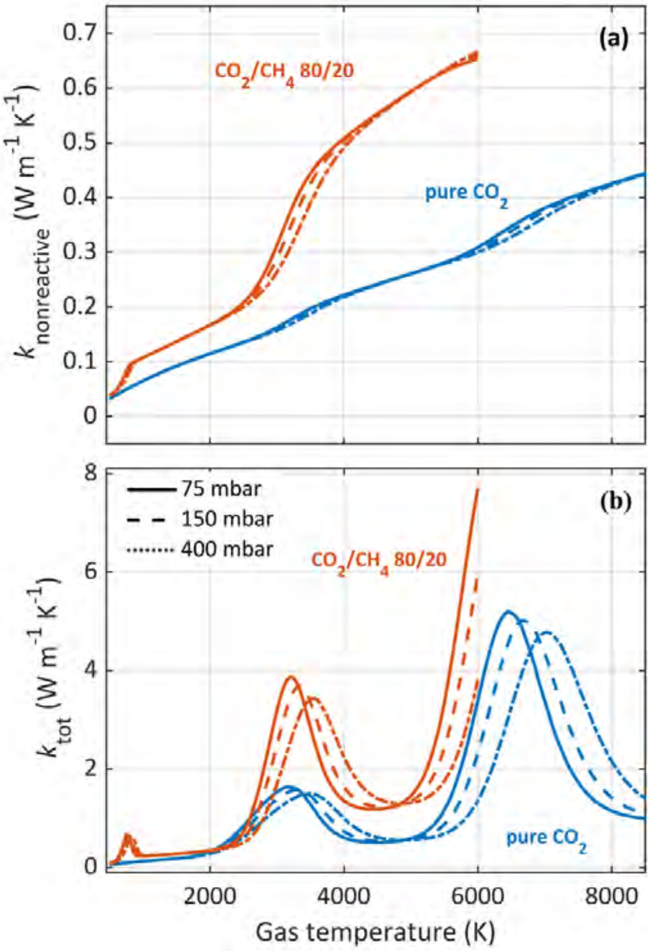

Figure 6.9. (a) Nonreactive component $\kappa_{\mathrm{nonreactive}}$, and (b) total heat conductivity (including equilibrium reactions) κ_{tot}, as a function of the gas temperature, for three different pressures, and for pure CO_2 and the CO_2/CH_4 80/20 mixture.

Interestingly, the critical power density to observe the plasma filament is also increased by a factor of two, moving from ca. 800 up to ca. 2500 W cm^{-3} (Figure 6.7(b)). This indicates that a twofold intensification of the power concentration is necessary to shift the production/destruction balance of charged particles and establish a significant radial and axial volume reduction. The increase in $\kappa_{\mathrm{reactive}}$ is ascribed to the lower thermal stability of H-containing products (bond energies in the order of 4-5 eV[336]) compared to CO (bond breaking energy of 9.6 eV[337]) at $T_g > 3000$ K, making the CO_2/CH_4 80/20 mixture more reactive than pure CO_2. Thus, we believe that κ may explain the pressure shift in the contraction of the plasma with the admixture of CH_4, highlighted by the plasma images (see Figure 6.1).

Our observations are in good agreement with Wolf *et al.*[278] for pure CO_2 and demonstrate that the relationship between power concentration and T_g is governed by C_p even in CO_2/CH_4 mixtures. In addition, we suggest that κ is of fundamental importance to study the power concentration in different chemical environments. For instance, Kabouzi *et al.*[289] demonstrated that the high κ of He prevents a non-uniform radial distribution of T_g that is required for plasma radial contraction. These findings were also reported by Moisan and Pelletier[302].

At this point, we are able to formulate a hypothesis on the inherent dynamics, incorporating the findings from previous efforts and the new insights achieved within our work. The proposed mechanisms underlying power concentration in CO_2/CH_4 mixtures, which we believe can be generalized to molecular discharges, are illustrated in the next section.

6.3.7 Underlying mechanisms

A comparison between the evolution of plasma parameters against C_p and κ highlights the importance of the thermodynamic properties of the gas in determining T_g characteristic for the diffuse and contracted regimes. Furthermore, we demonstrate that changes in κ can explain the different contraction behaviour upon modifications of the chemical kinetics in the plasma (e.g. by adding CH_4 to CO_2). However, to fully describe the mechanism leading to power concentration in a plasma, we need to take a step back and look at the evolution of the heavy-particle temperature with pressure once more. Specifically, the importance of κ for the onset of discharge constriction is evidenced in the T_{rot} radial profiles displayed in Figure 6.10, especially in the central panel where the results for 150 mbar are presented, corresponding to the transition from diffuse to contracted discharge mode.

In the reaction zone, κ transports the energy radially outwards from the hot core, where the electrons deposit their energy into the molecules, until a balance between conduction and convective heat losses is reached[293]. In a forward vortex flow configuration, the discharge is stabilized in a recirculation cell where heat diffusion dominates over convection. Therefore, an equilibrium between conduction and convection is only found at the boundary between the hot inner region and the cold outer vortex. Indeed, the latter functions as an effective wall in vortex-stabilized discharges. Under these conditions, the radial T_g gradient is determined by κ. This effect is more pronounced at 150 mbar (Figure 6.10). Particularly, higher κ (e.g., for increasing CH_4 fractions in the feed gas) leads to lower

T_g gradients for the same heat flux and faster heat losses from the core of the plasma outwards, thus cooling down the discharge region and preventing the establishment of strong radial T_g gradients and non-homogeneous heating. In the diffuse regime, T_g ranges within ca. 3000 – 4500 K in the region inside the vortex, whose boundaries are located at a radial position of approximately 10 mm (see the cylindrical shape of the 20% and 30% CH_4 experiments in Figure 6.1). The high κ in this T_g region (Figure 6.9(b)) facilitates the heat conduction from the core to the outer vortex, where heat is lost by convection. Thus, heat conduction stabilizes the diffuse plasma in the 3000 – 4500 K regime. Under these conditions, electron losses over the whole discharge cross section are mainly determined by dissociative recombination of electrons with molecular ions through reaction $X_2^+ + e^- \rightarrow X^+ + X$ (2). Hence, the diffuse discharge regime is governed by a local balance of charged particles[293,306].

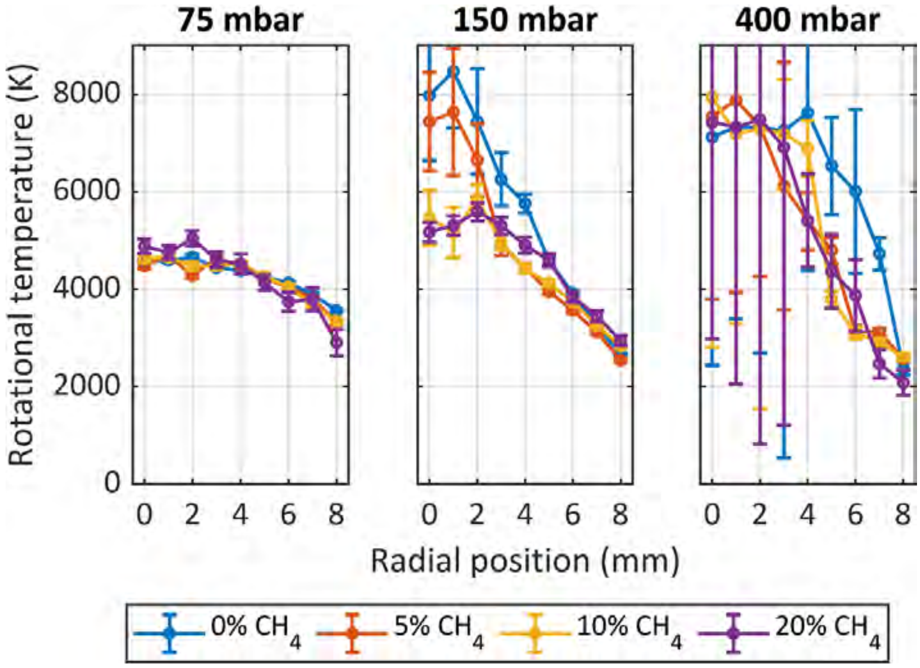

Figure 6.10. Radial profiles of rotational temperature (T_{rot}) for different $CO_2 + CH_4$ mixtures at 75 mbar (diffuse discharge mode), 150 mbar (transitioning discharge mode) and 400 mbar (contracted discharge mode), with input power of 1000 W and flow rate of 10 slm. 30% CH_4 is not shown due to overlap of C_2 Swan ($d^3\pi_g \rightarrow a^3\pi_u$) with the rotational Raman signal.

With increasing pressure, the number of collisions between electrons and heavy particles increases and so does T_g. However, above 4500 K, κ finds a new minimum (Figure 6.9(b)) and heat conduction between the core of the plasma and the outer vortex is reduced. This promotes the establishment of non-homogeneous heating within the discharge cross section, increasing the core T_g until a new maximum of κ is reached (T_g > 6000 K, see Figure

6.9(b)). At this point, thermally driven, associative ionization reactions of radicals (e.g., C + O → $CO^+ + e^-$) contribute to the intensification of radial contraction and provide extra ionization without requiring higher power density and eventually leading to thermalization of the discharge (Figure 6.3)[51]. On the other hand, the plasma is now insulated inside a region of low κ (T_g ~ 4500 – 6000 K), limiting heat conduction and thus determining stronger T_g gradients. As a consequence of the high T_g, molecular ions dissociate into atomic species, thus reducing the role of electron-ion recombination (owing to the very low recombination rates for atomic ions[338]) in the core, where radial ambipolar diffusion becomes the dominant electron loss pathway[293,306]. Once atomic species recombine at the edges of the hot core, molecular ions are formed and volume recombination dominates (6.2). Note that associative ionization is a source of molecular ions (reverse of electron-ion recombination). Therefore, it may further contribute to an increase of radial electron losses and, therefore, power concentration. In other words, ionization and electron-ion recombination are separated in space[293]. Hence, the contracted discharge regime is governed by non-local balance of charged particles. The conditions, under which a deviation from a local to a non-local balance and, therefore, power concentration is observed, are set by κ.

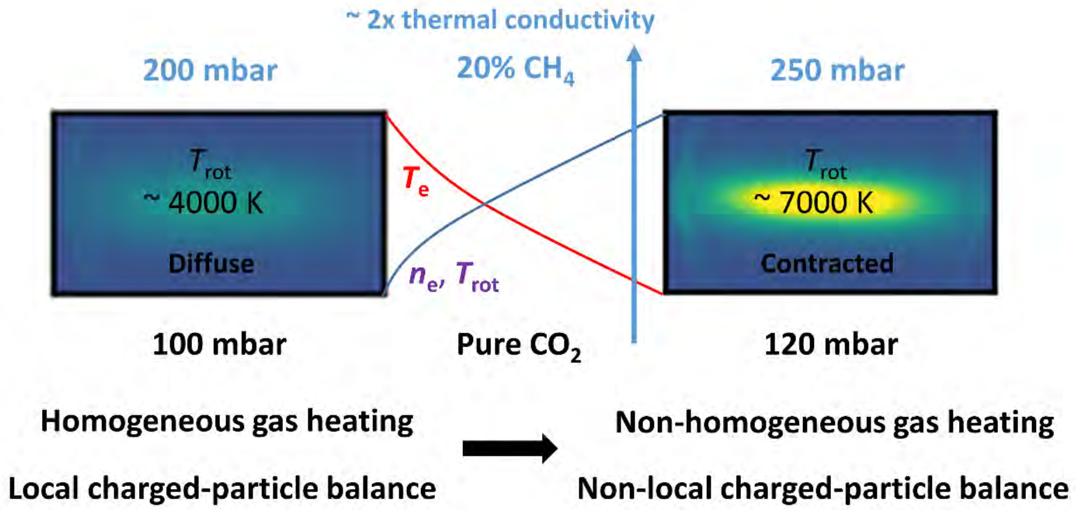

Figure 6.11. Schematics of the mechanism underlying power concentration in CO_2/CH_4 vortex-stabilized microwave discharges. For the same experimental conditions, the addition of 20% CH_4 in the feed gas corresponds to a twofold increase in heat conductivity, resulting in a shift towards higher pressure to create non-homogeneous gas heating and power concentration along the axis.

Hence, our observations confirm that power concentration in CO_2/CH_4 MW plasmas can be explained by non-uniform gas heating, and the relationship between power concentration and T_g is governed by the thermodynamic properties of the gas mixture. Once power concentration onsets, associative ionization reactions may further intensify a self-reinforcing mechanism between n_e and gas heating in the core (in agreement with previous results[51,309] for pure CO_2) and promote radial electron losses at the edges of the hot core due to the formation of molecular ions, yielding a separation between ionization and volume recombination (non-local charged-particle balance[293]). The effect of CH_4 addition to a CO_2 MW discharge is summarized in Figure 6.11.

Nevertheless, chemical modelling of the plasma is sought-after to verify the aforementioned hypotheses on the main reaction mechanisms that are associated with diffuse and contracted discharges. For instance, deviations from chemical non-equilibrium established by fast transport of atoms from the hot core outwards[56] are not captured in our thermodynamic calculations, and the role of associative ionization of radicals (e.g., between excited H radicals[283]) in the presence of CH_4 is not yet understood. Thus, the mechanism proposed in this study is yet to be fully established, and further computational and experimental efforts are highly desirable, also for verifying the mechanism in other complex gas mixtures. At the same time, this study represents a step forward in the understanding of the power concentration dynamics in vortex-stabilized discharges, and these insights can be used to optimize reactor design and verify numerical models.

With a view towards multi-dimensional modelling, the selection of the chemical reactions and physical parameters to describe the discharge behavior becomes critical. Computational time is highly dependent on the model input and the latter is expected to grow heavily due to the complexity of the DRM chemistry. Our results agree well with the number of parameters required to characterize the power density and T_g distributions as suggested in previous work[309,310] for pure CO_2 MW plasmas. Namely, these parameters are the pressure, the reactor geometry, C_p, κ, the flow dynamics and the chemistry. Particularly, the latter calls for special attention. An accurate description of electron, ion and neutral particle kinetics has to be included with a maximum number of ca. 100 reactions. Thus, a kinetic scheme descriptive of the gas heating dynamics should be first validated with a 0D model, as done in this thesis (Chapter 4) for pure CO_2. After that, the 0D model can be used to perform a drastic reduction of the scheme that can still describe the underlying mechanism in a good approximation.

6.4 Conclusions

In this chapter, we study a MW plasma used for the conversion of CO_2 and we extend the characterization of the contraction dynamics to mixtures with CH_4. In particular, optical emission imaging indicates that the constriction of the discharge into a filament, axially centered in the reactor tube, is progressively shifted towards higher pressures upon increasing fraction of CH_4. This observation is confirmed by combined Thomson-Raman measurements, demonstrating that the plasma emission pattern mostly follows the rising trend of n_e, except for conditions where carbon nanoparticles are formed. Simultaneously, an abrupt increase of the average power density in the discharge volume is estimated from the fitting of the O 777 line emission.

The comparison between experimental parameters and calculated thermodynamic properties demonstrates that the relationship between power concentration and T_g is governed by C_p and κ. Specifically, their reactive components determine the core T_g of the diffuse and contracted discharge regimes. Moreover, the addition of CH_4 evidences the essential role of κ in defining the radial T_g gradients. Compared to CO_2 alone, a larger number of endothermic reactions is activated at ca. 3000 K, leading to a twofold increase of κ. The enhanced heat conduction lowers the core T_g and smoothens the radial gradients, favoring a local balance between electron-ion recombination and electron production, thus, preventing contraction and lowering the power concentration. In this mechanism, associative ionization reactions play the role of providing an increase of the core n_e and thermalize the discharge in the contracted regime. These reactions are highly T_g dependent. Therefore, the inhibition of the gas heating has the effect of increasing the degree of non-equilibrium between electron and heavy particle kinetics. For this reason, the underlying mechanism becomes inherently difficult to model in more dimensions and we suggest that a step back to 0D kinetic modelling is necessary to expand the description of the dynamics underlying power concentration to CO_2/CH_4 mixtures. Upon the reduction of the chemical kinetics to the essential reaction pathways, flow modelling will enable to identify the key parameters to improve the performance of the DRM process.

Appendix D. Equilibrium gas composition[12]

The thermodynamic equilibria are calculated using a python code, which operates as described hereafter. First, the temperature-dependent molar enthalpy $H°(T_g)$ and entropy $S°(T_g)$ are calculated for the included species, using the NASA Glenn Polynomials[317]. From this, we calculate the Gibbs free energies of formation $G°(T_g)$ for each species:

$$G°\left(T_g\right) = H°\left(T_g\right) - T_g \cdot S°(T_g). \tag{D.1}$$

We then calculate the Gibbs free energies of formation $\Delta G_{CxHyOz}(T_g)$ for every species $C_xH_yO_z$ with respect to three molecules that contain H, O or C, namely H_2, O_2 and CH_4 for the calculations with CO_2/CH_4 mixtures. For the calculations with pure CO_2, we calculate the Gibbs free energies of formation relative to O_2 and CO. In other words, for CO_2/CH_4 mixtures we calculate the reaction energies of:

$$\mathrm{xCH_4} + \frac{\mathrm{y}}{2}\,\mathrm{H_2} + \frac{\mathrm{z}}{2}\mathrm{O_2} \rightarrow \mathrm{C_xH_yO_z} + 2\mathrm{xH_2} \tag{D.2}$$

$$\Delta G°_{\mathrm{C_xH_yO_z}}\left(T_g\right) = G°_{\mathrm{C_xH_yO_z}}\left(T_g\right) + 2\mathrm{x}G°_{\mathrm{H_2}}\left(T_g\right) - \mathrm{x}G°_{\mathrm{CH_4}}\left(T_g\right) - \frac{\mathrm{y}}{2}G°_{\mathrm{H_2}}\left(T_g\right) - \frac{\mathrm{z}}{2}G°_{\mathrm{O_2}}\left(T_g\right) \tag{D.3}$$

On the other hand, for pure CO_2, we calculate the reaction energies of:

$$\mathrm{xCO} + \frac{\mathrm{y}}{2}\mathrm{O_2} \rightarrow \mathrm{C_xO_y} + \frac{\mathrm{x}}{2}\mathrm{O_2} \tag{D.4}$$

$$\Delta G°_{\mathrm{C_xO_y}}\left(T_g\right) = \mathrm{G}°_{\mathrm{C_xO_y}}\left(T_g\right) + \frac{\mathrm{x}}{2}G°_{\mathrm{O_2}}\left(T_g\right) - \mathrm{x}G°_{\mathrm{CO}}\left(T_g\right) - \frac{\mathrm{y}}{2}G°_{\mathrm{O_2}}\left(T_g\right). \tag{D.5}$$

From the Gibbs free reaction energies, we calculate the equilibrium constants:

$$K_{\mathrm{eq,\ C_xH_yO_z}}\left(T_g\right) = \exp\left(-\frac{\Delta G°_{\mathrm{C_xH_yO_z}}\left(T_g\right)}{RT_g}\right), \tag{D.6}$$

---

[12] This model was developed and tested by Björn Loenders at PLASMANT

where R is the ideal gas constant. At thermal equilibrium, the equilibrium constants can be expressed as a function of the activities (partial pressures) of the gasses:

$$K_{\mathrm{eq},\ C_xH_yO_z}\left(T_g\right) = \frac{p_{C_xH_yO_z}\cdot\left(p_{H_2}\right)^{2x}}{\left(p_{CH_4}\right)^{x}\cdot\left(p_{H_2}\right)^{\frac{y}{2}}\cdot\left(p_{O_2}\right)^{\frac{z}{2}}} = \exp\left(-\frac{\Delta G^{\circ}{}_{C_xH_yO_z}\left(T_g\right)}{RT_g}\right), \tag{D.7}$$

or, for the case with pure CO_2:

$$K_{\mathrm{eq},\ C_xO_y}\left(T_g\right) = \frac{p_{C_xO_y}\cdot\left(p_{O_2}\right)^{\frac{x}{2}}}{\left(p_{CO}\right)^{x}\cdot\left(p_{O_2}\right)^{\frac{y}{2}}} = \exp\left(-\frac{\Delta G^{\circ}{}_{C_xO_y}\left(T_g\right)}{RT_g}\right). \tag{D.8}$$

This way, we can get n-3 independent equations for the CO_2/CH_4 mixture or n-2 equations for pure CO_2, with n equal to the number of species included in the calculations. More specifically, we have one expression (like eq. (D.6)) for each species with the exception of CH_4, H_2 and O_2 for the CO_2/CH_4 mixture, or with the exception of CO and O_2 for pure CO_2.

Since we calculate the equilibria at constant pressure, for each temperature, the sum of all partial pressures must remain equal to this constant total pressure.

$$p_{\mathrm{tot,cst}} = \sum_{i=1}^{n} p_{\mathrm{i},\ C_xH_yO_z} \tag{D.9}$$

Additionally, the ratio of C atom vs. O atoms and the ratio of C atom vs. H atoms must remain constant to keep the atom balances the same.

$$\frac{p_{CH_4,\mathrm{init}} + p_{CO_2,\mathrm{init}}}{2p_{CO_2,\ \mathrm{init}}} = \frac{\sum_{i=1}^{n} x\cdot p_{\mathrm{i},C_xH_yO_z}}{\sum_{i=1}^{n} z\cdot p_{\mathrm{i},C_xH_yO_z}} \tag{D.10}$$

$$\frac{p_{CH_4,\mathrm{init}} + p_{CO_2,\mathrm{init}}}{4p_{CH_4,\ \mathrm{init}}} = \frac{\sum_{i=1}^{n} x\cdot p_{\mathrm{i},C_xH_yO_z}}{\sum_{i=1}^{n} y\cdot p_{\mathrm{i},C_xH_yO_z}} \tag{D.11}$$

where $p_{CH4,\mathrm{init}}$ and $p_{CO2,\mathrm{init}}$ are the initial partial pressures of CH_4 and CO_2, respectively. Of course, the equation for the C vs. H ratio is not applicable, nor required for the calculations of the pure CO_2 plasma.

These three (or two, for the pure CO_2 plasma) extra equations give us a system of n equations, which is solved using a root-finding algorithm to get the equilibrium partial pressures of the n gas species at temperature T_g. The gas species included in the equilibrium calculations are listed in Table D1 for both mixtures.

Table D1. List of gas species included in the equilibrium calculations.

Gas mixture	**Species included in the calculations**
CO_2 / CH_4	O, O_2, C, C_2, CO, CO_2, OH, H_2O, H, H_2, CH, CH_2, CH_3, CH_4, C_2H, C_2H_2, C_2H_4, C_2H_6, HCO, HCOOH, HCHO, CH_3OH, CH_3CH_2OH, CH_3CHO
CO_2	O, O_2, C, C_2, CO, CO_2

Chapter 7 Flow pattern control avoids solid carbon deposition in plasma-based dry reforming of methane[13]

Abstract

In Chapter 6 we show that a CO_2/CH_4 microwave plasma can reach very high core temperatures. A direct consequence of these high temperatures is solid carbon deposition, which hampers the development and commercialization of dry reforming of methane (DRM), causing plasma instabilities and catalyst deactivation. In this work, we use a microwave plasma in reverse vortex flow configuration to overcome this issue in CO_2/CH_4 plasmas. For the first time, we observe almost no carbon deposition inside the reactor, allowing operations even in pure CH_4 feed gas, along with very good reactor performance (33% and 44% CO_2 and CH_4 conversion and an energy cost of 14 kJ/L at CO_2:CH_4 ratio of 1:1). The reverse vortex configuration features a lower characteristic gas residence time in the discharge compared to the more frequently studied forward vortex configuration. Laser scattering and optical emission imaging demonstrate that the shorter residence time lowers the gas temperature in the discharge and allows switching from full to partial pyrolysis. The difference in gas residence time is determined by the characteristic flow field of the vortex configuration. This highlights the key role of the flow configuration in controlling the process selectivity towards gaseous products vs solid, which is of fundamental importance in complex chemistries such as CO_2/CH_4 mixtures. Thus, the reverse vortex configuration enables full exploitation of the DRM chemistry, opening up the implementation of plasma-based technology to a wider scale.

---

[13] This chapter is based on:
Flow pattern control avoids solid carbon deposition in plasma-based dry reforming of methane
O.Biondo, C. F. A. M. van Deursen, A. Hughes, A. van de Steeg, W. Bongers, M. C. M van de Sanden, G. van Rooij, A. Bogaerts
In preparation for submission to Chemical Engineering Journal

7.1 Introduction

In Chapter 6, we mention the formation of solid carbon deposition inside our MW reactor, limiting our analysis at 30% CH_4 in the feed gas. As explained in Chapter 1 (section 1.4.2), plasma-based dry reforming of methane (DRM)[15,86], i.e., the combined conversion of CO_2 and CH_4, is an attractive solution to electrify the energy-intensive production of syngas (H_2 + CO), as essential building block for the synthesis of hydrocarbons through Fischer-Tropsch[339] or oxygenates (e.g. methanol[340]). However, as also discussed in Chapter 1 (section 1.4.2(b)), its full exploitation is hampered by solid carbon deposition inside the reactor, leading to unstable operations (e.g., due to microwave absorption in microwave discharges[341,342] (see also Chapter 6) or by creating conductive layers inside the reactor body[343]) and limiting the CO_2/CH_4 ratio to ≥ 1 under most experimental conditions[15,84,86]. In DRM, solid carbon is primarily formed as a consequence of gas-phase, homogeneous pyrolytic reactions, especially C_2 hydrocarbon pyrolysis[108], enhanced by O and OH radicals[113,344]. Hydrocarbon pyrolysis is endothermic and, therefore, promoted by the gas temperature (T_g) and gas residence time (t_{res}) in the reaction zone[108]. Previous research on plasma-based DRM suggested that solid carbon formation rises with the specific energy input (SEI = input power/feed flow rate)[105,343,345], and thus also with the residence time and/or the power, which affects T_g. Power pulsing limits gas heating and, therefore, the onset of pyrolytic reactions. Indeed, plasma-based DRM studies with power pulsing reported little[346] to no carbon deposition[347,348], although the carbon balance was not explicitly evaluated. Recently, Mei *et al.*[349] applied nanosecond power pulsing to a DRM dielectric barrier discharge, seemingly without operational issues due to carbon deposition, even at CO_2/CH_4 ratio < 1. However, their carbon balance was lower than 100% for all tested conditions.

Alternatively, microwave plasmas are expected to provide very good performance for DRM, with high selectivity towards syngas and high treatment capacity compared to other plasma sources, without compromising on energy efficiency[15]. Chun *et al.*[91] achieved nearly solid carbon-free syngas production in a CO_2:CH_4 1:1 atmospheric microwave (MW) plasma torch, with a power input of 6 kW and a gas flow rate of 30 standard liters per minute (slm). These values are much larger than any other plasma-based DRM experiment thus far, although the resulting SEI (12 kJ/L) is comparable with most studies. The authors estimated a T_g of 6760 K in the plasma by fitting the C_2-Swan band region of the recorded optical emission spectra. Despite the very high temperature and conversion (68% and 97% for CO_2 and CH_4, respectively), no solid deposition was visible inside the reactor. Nevertheless, the authors observed the release of solid carbon from the reactor body and did not report the carbon balance for their measurements. Thus, we hypothesize that carbon deposition inside the reactor was prevented by the high flow rate, thus displacing the deposition of solids further downstream. Subsequently, Sun *et al.*[92] tested a microwave reactor at lower power (2 kW) and flow rate (10 slm), but the same SEI (12 kJ/L), achieving very high conversion (91% and 96% for CO_2 and CH_4, respectively). However, unlike Chun *et al.*[91], the authors reported the presence of solid carbon on the inner wall of the reactor tube[92], suggesting that the flow rate magnitude determines whether solid carbon can be found inside the reactor or not. However, the mechanism underlying solid carbon reduction is not yet understood, and the literature on CO_2/CH_4 microwave discharges is still very limited.

Compared to microwave plasmas, arc discharges have been more often investigated for DRM[15]. In this class of plasma sources, the performance depends strongly on the reactor geometry. For instance, Dinh *et al.*[96] compared the performance of a conventional rotating arc reactor with a nozzle-type rotating arc reactor for N_2-assisted DRM (CO_2:CH_4:N_2 2:6:8), reporting that the latter enhances both conversion and energy efficiency, thanks to improved heat transfer from the arc into gas activation and reduced heat losses to the walls. In the context of gliding arc discharges, optimization of the gas flow dynamics may enable improved performance along with reduced carbon losses to solid products[350]. Liu *et al.*[351] could operate their forward vortex, gliding arc reactor at a $CO_2/CH_4 = 1.5$ ratio for nearly 2 h, with an SEI of 1.38 kJ/L and without severe carbon deposition. More recently, Van Alphen *et al.*[352] were able to lower the CO_2/CH_4 ratio to 1 in a reverse vortex, gliding arc reactor, while operating at a SEI of 3 kJ/L, with no operational issues reported. The ability of increasing the SEI while lowering the CO_2/CH_4 ratio suggests that the type of vortex stabilization affects carbon deposition at the reactor walls.

Up to now, the effect of the gas flow dynamics has never been studied in CO_2/CH_4 microwave discharges, despite the promising results mentioned earlier. In vortex-stabilized microwave plasmas, the cold outer vortex surrounding the hot plasma core facilitates rapid quenching of products, increasing the energy efficiency of the process[353]. In the commonly studied forward vortex flow configuration, quenching of products from the hot core is mainly provided by radial transport, as a result of temperature gradients as large as 5000 K/cm[56,353]. Nevertheless, the performance of a microwave plasma in forward vortex configuration suffers from weak control of the plasma core characteristics, due to suppression of convective core-periphery transport[225,353,354].

In contrast, in reverse vortex flow configuration, a second inner vortex is forced through the plasma zone, establishing convective core-periphery transport[354]. In this configuration, the tangential gas inlets and outlet are located on the same side of the plasma (Figure 7.1). This results in an outer vortex flow along the reactor walls, and an inner vortex aimed at the opposite direction[355]. The plasma is confined in the inner vortex, while the outer vortex provides near perfect heat insulation[354–356]. Bongers *et al.*[37] were the first to study both the forward and reverse vortex configurations in a CO_2 microwave plasma at sub-atmospheric pressure and reported slightly higher energy efficiency in reverse vortex at increasing pressure, with a maximum at ca. 500 mbar. In addition, they observed that the energy efficiency decreases less with increasing pressure than in forward vortex configuration, suggesting that the reverse vortex configuration may provide a more energy-efficient CO_2 conversion at atmospheric pressure. Nevertheless, this has not yet been demonstrated thus far. A first *in-situ* characterization of the reverse vortex CO_2 microwave plasma was provided by van de Steeg[225], showing that control over the residence time and T_g can be achieved through convective core-periphery transport by varying the inlet gas flow rate. In systems with more complex chemistry and where product selectivity is important, such as DRM, control over the residence time is expected to be even more beneficial.

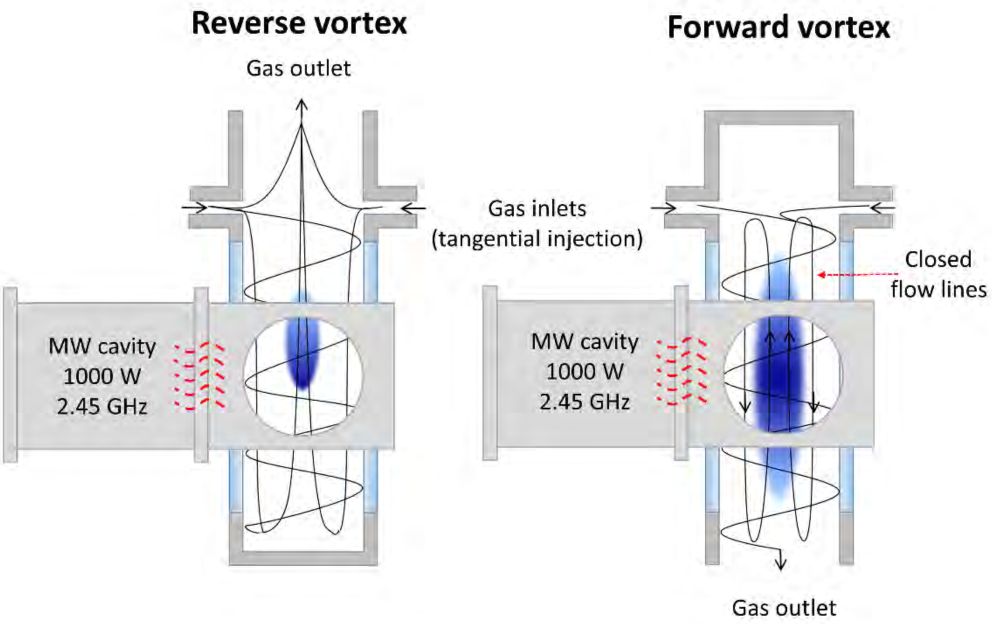

Figure 7.1. Schematics of the reverse vortex (RV) and forward vortex (FV) flow configurations, with illustrations of flowlines based on Gutsol and Bakken [354].

In this work, we report for the first time on the inhibition of solid carbon deposition in a DRM microwave plasma in reverse vortex flow configuration, even in pure CH_4 feed gas. For the same experimental conditions, we observe that the more widely used, forward vortex configuration achieves syngas production along with severe carbon deposition, eventually leading to discharge shutdown for CH_4 fractions larger than 75% in the feed gas.

7.2 Results and discussion

7.2.1 Combined Raman-Thomson scattering

In order to gain a deeper insight in the effect of the flow configuration on carbon deposition, and thus plasma stability, we perform for the first time an *in-situ* characterization of the reverse vortex, microwave plasma using a combination of rotational Raman and Thomson scattering, providing quantitative measurements of the rotational (gas) temperature (assumed in equilibrium with T_g), and electron density and temperature, respectively. For more details on the methodology, we refer to previous work of van de Steeg *et al*[51]. For a more detailed description of this microwave reactor equipped with a laser scattering device, we direct the reader to previous work[225,357]. The results for the reverse and forward vortex configuration are compared in Figure 7.2, with the purpose of unravelling the transport phenomena, lying at the basis of solid carbon inhibition. The *in-situ* characterization of the plasma for CH_4 fractions > 20% in CO_2 is not yet possible due to the complexity of the chemical environment and the increase in C_2-Swan laser induced fluorescence[329], which blends the Raman spectra.

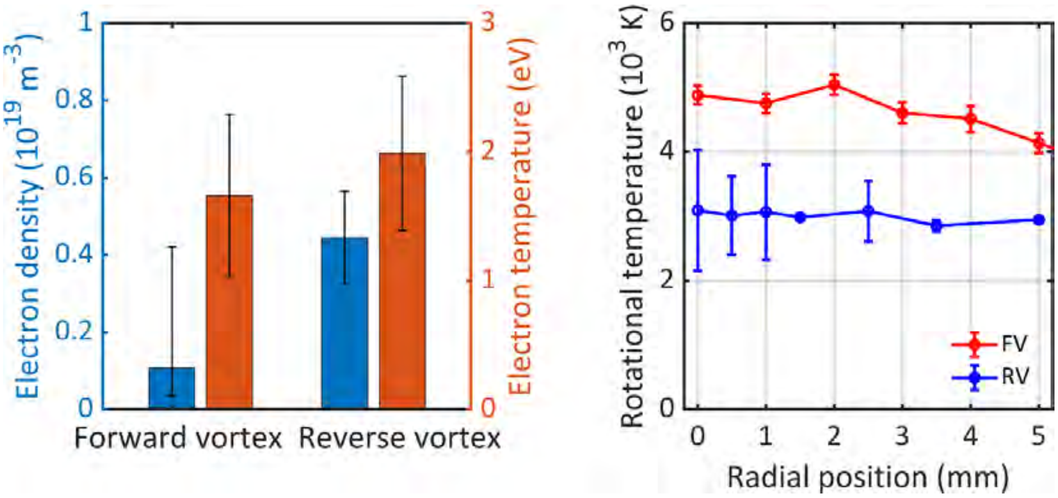

Figure 7.2. Electron density and temperature (left) measured at the core of the plasma (averaged over 1 mm) and radial profiles of rotational temperature (right), for 20% CH_4 in the feed gas, in forward and reverse vortex flow configurations (1000 W, 100 mbar, total flow rate of 17 slm).

Figure 7.2 shows that T_g is ca. 1500 K lower in reverse than in forward vortex configuration, leading to a larger difference between T_e and T_g, and thus a more pronounced non-equilibrium plasma in the reverse vortex configuration. On the other hand, the electron number density (n_e) and temperature (T_e) are in the same order of magnitude for both forward and reverse vortex configurations. The large error bars are ascribed to the overlap with the Rayleigh peak and the stray light that are cut from the spectra with a notch filter[358,359].

The lower T_g of the reverse vortex flow configuration indicates that it enhances the heat removal from the core of the discharge, compared to the forward vortex configuration. This cooling effect is provided by a prominent convective flow established in the reverse vortex configuration, being absent in forward vortex configuration[353,354].

7.2.2 The effect of the flow topology

Additional evidence of the reduction of solid-carbon precursors in the reverse vortex configuration is provided by optical emission imaging, presented in Figure 7.3.

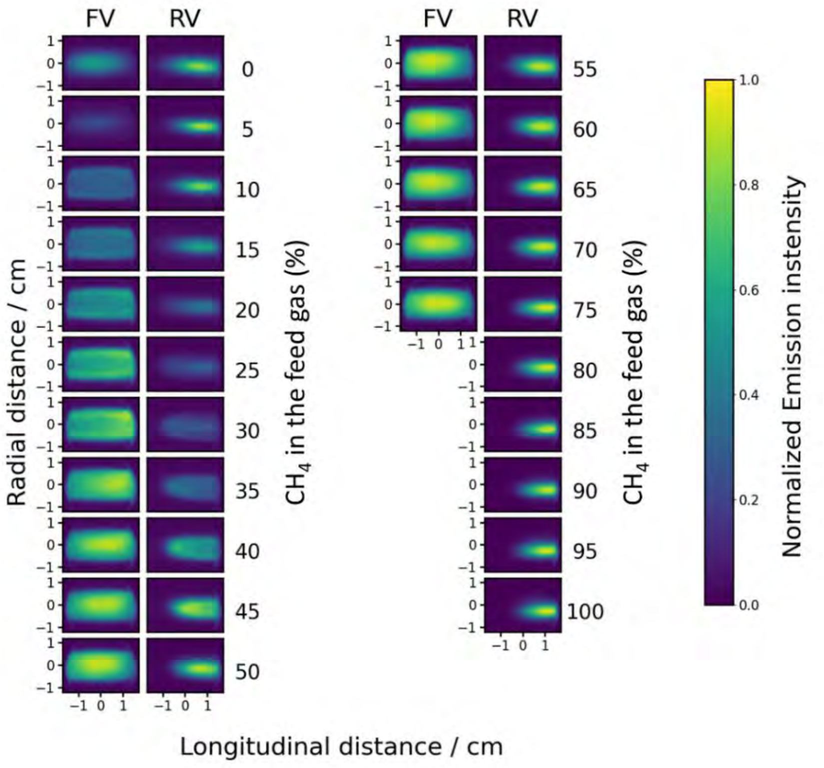

Figure 7.3. Optical emission images of the plasma in forward and reverse vortex configurations as a function of the CH_4 fraction in the feed gas, with emission intensity normalized at the maximum value in each image (1000 W, 17 slm, 100 mbar).

These images are taken with a bandpass filter with a central wavelength of ca. 780 nm, aiming to simultaneously isolate the 777 nm $O(3s^5S^0 \leftarrow 3p^5P)$ spectral line emission, often used to reconstruct the plasma shape[228,232], and to capture the onset of the broadband emission (ca. 500 – 1100 nm, with a maximum at 800 – 900 nm) from hot carbon particles[324–326]. In this manner, optical emission imaging becomes a useful tool to trace the formation of carbon particles as precursors for carbon deposition in DRM, while keeping track of the change in emission distribution. Figure 7.3 shows a sudden change in emission shape from 5% to 10% CH_4 in the feed gas in forward vortex configuration. Particularly, the emission zone exhibits a cylindrical, hollow shape, as a result of the particle formation at the interface between the hot core and the cold outer vortex[325]. The last step of the Kassel mechanism[109,114] (i.e. the full dehydrogenation to solid carbon) is an inherently kinetically limited process, composed of a nucleation step followed by mass growth[115]. The recirculation cell created in forward vortex configuration (represented by the closed flow lines in Figure 7.1) traps the hot gas inside, which can only leave by slow radial diffusion promoted by the onset of strong temperature gradients. This causes an increase in $t_{res,}$ creating the conditions to form a considerable number of nucleation sites and therefore carbon particles through H-abstraction and C_2H_2 addition (HACA mechanism)[115,360] and/or coagulation[361]. Since particle sizes are significantly larger than the sizes of gas molecules, thermophoresis affects their motion to a lesser extent[362], further increasing their t_{res} compared to that of the gas in the recirculation cell. Here, carbon particles tend to accumulate and aggregate in larger structures, until they achieve sufficient momentum to leave the closed flow lines and attach to the reactor walls as a result of inertial impaction[363]. A similar behavior was observed for soot particles in C_2H_4 fueled flames, where recirculation zones were created with the aim of trapping the carbon particles and tracking their trajectories inside a vortex flow[364]. Their broadband emission, visible to the naked eye as an orange halo[325,365], corresponds to the shape of the recirculation cell in our case. The part that is protruding outside the waveguide is not included in the images in Figure 7.3. Once the particles are sufficiently heavy and can leave the recirculation cell, they are only ca. 6 mm separated from the reactor walls. Under these conditions, solid deposition is thus facilitated.

In reverse vortex configuration, the transition from O 777 nm to carbon-dominated emission, with a clear change in shape, appears at ca. 30% CH_4 in the feed gas. Nevertheless, the emission zone is limited within a few millimeters in the core of the reactor tube, where the plasma is confined. For reverse vortex, the images in Figure 7.3 locate the convective flow in the space, pointing towards the right-hand side, where the gas outlet is located (cf. Figure 7.1). Unlike in the forward vortex configuration, no broadening of the emission in the radial or axial direction is observed. The lower core T_g

and reduced T_g gradients (cf. Figure 7.2), as a consequence of strong convective cooling, reduces the formation of particles outside the plasma zone.

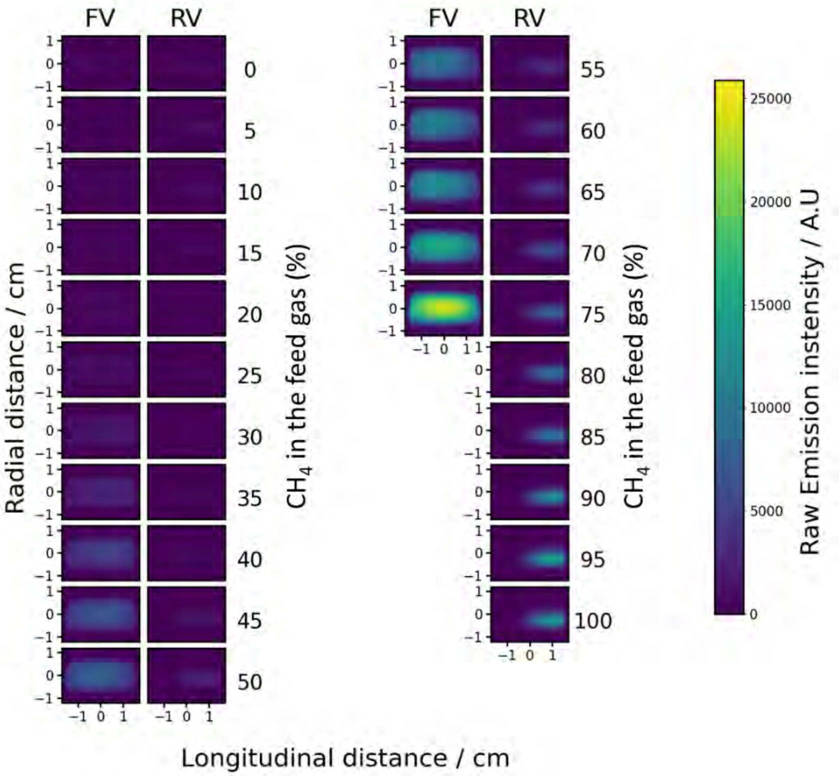

Figure 7.4. Optical emission images of the plasma in forward and reverse vortex flow configurations as a function of the CH$_4$ fraction in the feed gas. The images are recorded with an image intensified CCD high speed camera, with a bandpass filter with a central wavelength of ca. 780 nm.

However, broadband emission is still visible, although with much lower intensity compared to the forward vortex configuration for the same CH$_4$ fraction in the feed gas (Figure 7.4), indicating that primary carbon particles are still formed. In effect, the emission intensity increases with the fraction of CH$_4$, and the maximum intensity is achieved at 75% CH$_4$ in the feed gas in forward vortex flow configuration, right before severe carbon deposition is observed inside the reactor walls and the plasma shuts off. This clearly links the observed emission with carbon particles. Interestingly, broadband emission is observed also in reverse vortex flow configuration, where carbon deposition does not occur. However, its intensity is much lower than in the forward vortex configuration for the same conditions, suggesting that the amount (and likely also the size) of carbon particles is substantially reduced. Notwithstanding this, the absence of a recirculation zone in reverse vortex limits the formation of larger and stable carbon aggregates, explaining the lower emission intensity from blackbody radiation, together with nearly absent carbon deposition at the walls. Moreover, the hot gas removed from the plasma zone is quickly quenched by the input gas in reverse vortex configuration (cf. flow lines in Figure 7.1 and Bongers *et al*.[37]). If the cooling rate is sufficiently fast, mixing with the input gas may further reduce particle aggregation in stable structures downstream the plasma zone[115].

7.2.3 Reactor performance

With the aim of inferring the effect of the flow geometry on the chemistry, we evaluate the performance of DRM in a microwave plasma in both forward and reverse vortex configurations. The exhaust composition is measured with a gas chromatograph (GC) and reported in Figure 7.5 for a range of CO_2/CH_4 mixtures (from pure CO_2 up to pure CH_4). More details on the GC analysis are given in Section 3.3.

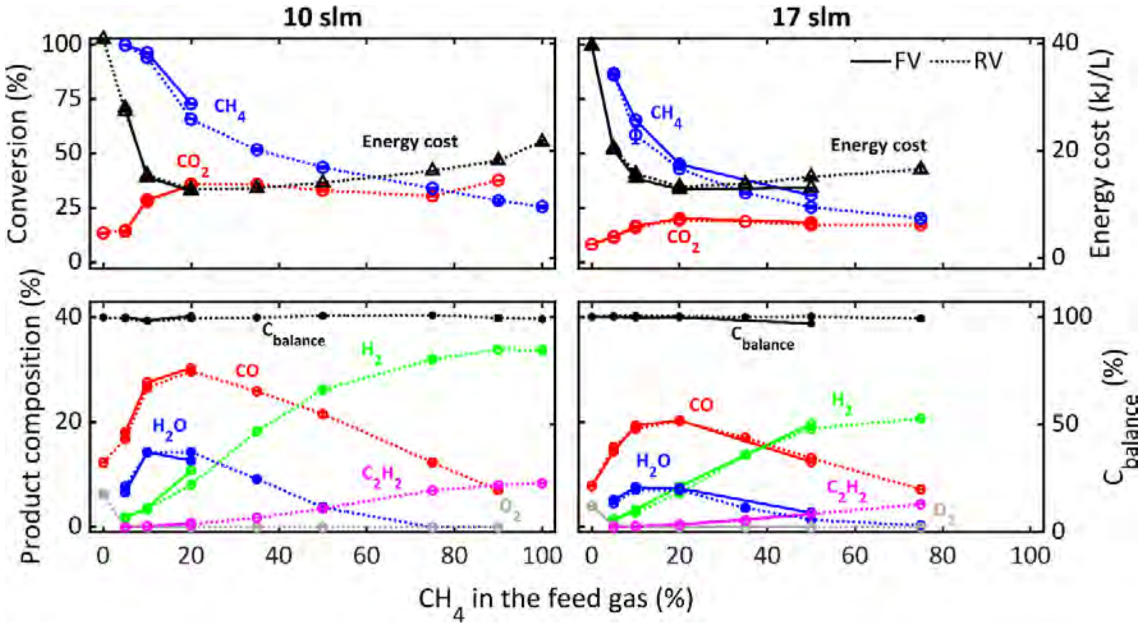

Figure 7.5. (Top) CO_2 and CH_4 conversion and energy cost; (Bottom) Product composition and carbon balance ($C_{balance}$) as a function of the CH_4 fraction in the feed gas, in forward and reverse vortex flow configuration, for 10 slm (left) and 17 slm (right) (1000 W, 100 mbar).

Figure 7.5 (top panel) shows that the flow rate has a stronger effect than the flow configuration on both CO_2 and CH_4 conversion at the experimental conditions under study. Despite the comparable conversion performance, more important is that operation in forward vortex is impossible by solid carbon formation for CO_2/CH_4 ratios < 4 at 10 slm, and < 1 at 17 slm (hence: the lack of data points for CH_4 fractions above 20% and 50%, respectively), with plasma instabilities arising at larger CH_4 fractions. Carbon particles are good microwave absorbers[342], causing a shielding of the microwave power to the plasma. For high fractions of CH_4 (i.e. at 50% and 75% at 10 and 17 slm, respectively), this eventually makes it impossible to maintain a stable discharge. On the contrary, the reverse vortex configuration enables stable and solid carbon-free operation up to pure CH_4 feed gas (the lack of data points for CO_2/CH_4 ratios < 0.33, or CH_4 fractions $> 75\%$, at 17 slm was due to inherent limitations of the volumetric flow controllers in use). This highlights that the flow stagnation in forward vortex leads to reduced mass and heat transfer, higher residence times and thus increased tendency to carbon deposition. Instead, reverse vortex is a method of increasing core transport, with great potential for DRM and perhaps even beyond that, for the chemical industry in the context of CH_4 non-oxidative coupling.

The minimum energy cost, calculated from the total conversion (i.e. the weighted average of CO_2 and CH_4 conversions), is achieved for 20% CH_4 fraction in the feed gas for all sets of measurements, with the lowest value being 12.6 kJ/L. At 50% CH_4, the lowest energy cost is 13.2 kJ/L in forward vortex configuration. In reverse vortex configuration, this increases to 14.1 kJ/L at 10 slm and to 15.1 kJ/L at 17 slm. For comparison, Chun *et al.*[91] and Sun *et al.*[92] achieved an energy cost of 14.5 kJ/L and 12.8 kJ/L, respectively, for CO_2/CH_4 50/50 microwave plasma. The product composition (Figure 7.5, bottom panel) mainly consists of syngas (H_2 and CO), along with H_2O (whose concentration is estimated from the O balance, as described by Wanten *et al.*[86]) and C_2H_2. The addition of 5% CH_4 in the feed gas removes O_2 from the output stream.

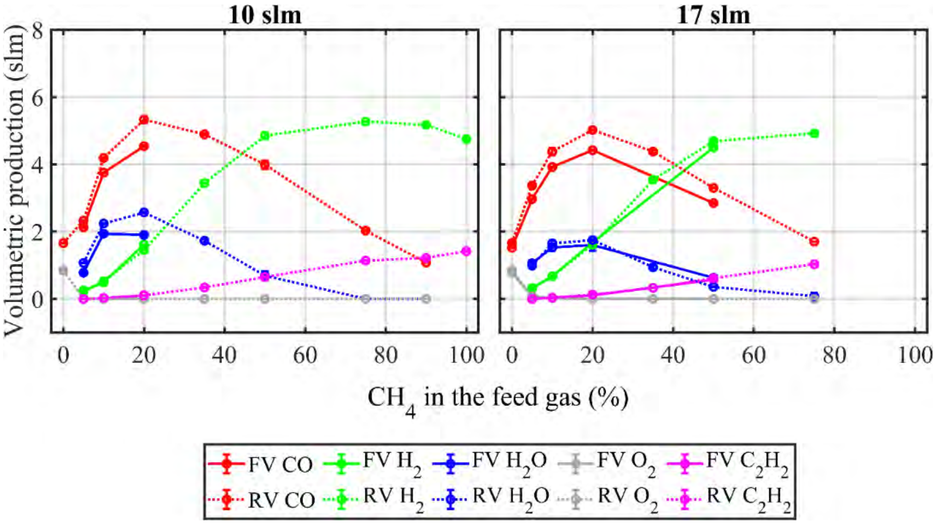

Figure 7.6. Volumetric production rate, in standard liters per minute (slm), calculated by multiplying the product fractions with the output flow rate, for forward vortex (FV) and reverse vortex (RV) flow configurations at 10 and 17 slm input flow rate (1000 W, 100 mbar).

Just like the conversions, the product distribution almost does not change with the flow configuration. The same is true for the volumetric production rates, presented in the Figure 7.6. Moreover, the carbon balance ($C_{balance}$) is close to 100% (within error margins).

A small deviation (ca. 96%) is seen only for 50% CH_4 in the feed gas in forward vortex at 17 slm, showing that carbon losses to solid deposits are small, even when deposition is clearly observable. For CH_4 fractions > 50% in forward vortex configuration, we observe strong deposition, along with unstable plasma, and, therefore, we expect larger deviations in carbon balance. Hence, despite no obvious differences are observed in gaseous product distributions, the reverse and forward vortex configurations clearly differ in the amount of solid carbon deposition.

7.2.4 Selectivity to C_2 hydrocarbons

The experimental, C-based selectivity (see Eq. 3.14 in Section 3.3.2) to C_2H_2 is plotted as a function of the SEI and compared against the literature (taken from the PIONEER database) in Figure 7.7. Note that only CO_2/CH_4 mixtures are considered, in a wide range of combinations. In our experiments, only C_2H_2 is quantifiable, whereas traces of C_2H_4 are detected by Fourier Transform Infrared spectroscopy for pure CH_4 plasma only, although below the limit of detection at the GC.

Figure 7.7 indicates that our microwave reactor exhibits high selectivity towards C_2H_2, especially for high fractions of CH_4 in the feed gas (max. of 69% at 90% CH_4 in the feed gas). Compared to the available literature, selectivities of ca. 25-28% can be achieved for CO_2/CH_4 50/50 mixtures at low SEI (hence, energy cost), analogously to gliding arc (GA) discharges. In effect, *warm* plasmas lead to higher conversion and more selective production of unsaturated hydrocarbons, especially C_2H_2, due to the characteristic higher T_g[107]. C_2H_4 is the most important feedstock for the chemical industry and, therefore, is more attractive than C_2H_2; however, the latter can be converted by post-discharge catalysis, as demonstrated by Delikostantis *et al.*[366] for a nanosecond repetively pulsed (NRP) discharge in pure CH_4. However, this is yet to be investigated in DRM post-discharge conditions. Alternatively, increasing the gas flow rate above 17 slm in reverse vortex flow configuration may further increase the cooling rate at the discharge zone, thus reducing T_g to a range where C_2H_4 formation is favored over C_2H_2 (i.e. 1000-1300 K)[107]. This would require adapting our microwave setup to withstand much higher gas flow rates and would be therefore desirable to first test this hypothesis with computational modeling. The insights gained in Chapter 6, together with the expertise of the PLASMANT group on this type of modeling, will be applied in the future to optimize the design of the reactor towards C_2H_4 production.

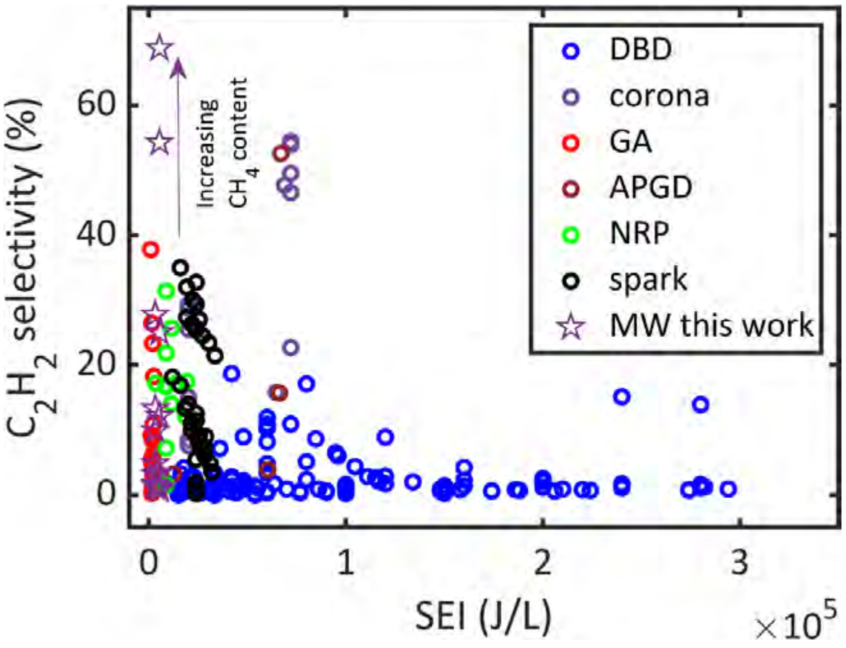

Figure 7.7. Selectivity to C_2H_2 as a function of the SEI for CO_2/CH_4 mixtures in different plasma sources (i.e. dielectric barrier discharges (DBD), corona, gliding arc (GA), atmospheric pressure glow discharge (APGD), nanosecond repetively pulsed (NRP) and spark discharges; taken from the PIONEER database), compared to the experimental results of this study for a microwave (MW) reactor.

7.2.5 Inhibition of carbon deposition

In DRM at high T_g, carbon deposition arises from the same mechanism as in pure CH_4 splitting, i.e. from (oxidative) hydrocarbon pyrolysis[108]. According to the Kassel mechanism[109,114], CH_3 radicals formed upon dissociation of CH_4 recombine to form C_2H_6. After that, a cascade of dehydrogenation reactions to C_2H_4 (within 10^{-6}-10^{-5} s), C_2H_2 (10^{-4}-10^{-3} s) and eventually to solid carbon takes place, depending on t_{res} in the reaction zone. The only C_2 hydrocarbon detected in our measurements is C_2H_2, indicating that t_{res} is likely in the millisecond range in both configurations. Van de Steeg[225] calculated convection velocities in the range of 150 m/s in reverse vortex flow configuration, and diffusion velocities of 5 m/s in forward vortex configuration, for pure CO_2 under similar conditions. In reverse vortex, the convective flow is oriented towards the gas outlet. If we take a plasma length of ca. 2 cm, as estimated from the plasma images (cf. Appendix E), the resulting t_{res}

is ca. 0.1 ms. In forward vortex, the diffusive flow goes mainly from the core towards the outer vortex. Hence, with a plasma radius of ca. 0.4 cm (see again Appendix E), the estimated t_{res} is ca. 0.8 ms, but if we consider the interface between the inner recirculation cell and the outer vortex, which is at ca. 0.7 cm from the core (cf. Figure 7.3), then t_{res} is ca. 1.4 ms i.e. 1 order of magnitude longer than in reverse vortex. In effect, in the forward vortex configuration, the gas is trapped inside a recirculation cell with closed flow lines (cf. Figure 7.1), in which the plasma is stabilized, and can only leave through radial transport, as demonstrated before[353,354]. This process is much slower than convection, which dominates core transport in reverse vortex, in line with previous work[225,354]. Hence, the difference in estimated t_{res}, arising from the characteristic flow topology, can explain the nearly absent carbon deposition in the reverse vortex configuration.

For the conditions tested during the GC campaign, i.e. CH_4 fractions $\leq$ 50% in forward vortex, only primary carbon particles are formed, with limited aggregation and thus with negligible contribution to the carbon balance. For high fractions of CH_4, the particles can form larger aggregates, carrying a larger momentum and eventually depositing at the inner walls of the quartz tube. In these conditions, losses to solid deposits may have a much larger contribution to the carbon balance. In effect, above 75% CH_4 in the feed gas, the plasma is not stable anymore and it quickly shuts off. This is ascribed to a prominent formation of carbon particles (as shown in Figure 7.4), which absorb the microwaves and shields the microwave power from the plasma.

Therefore, we hypothesize that the substantial inhibition of carbon deposition in the reverse vortex configuration arises from the specific flow topology, which determines the trajectory of the solid carbon precursors and their ability to aggregate and reach the reactor walls. Optical emission images show that carbon particles are formed in both flow configuration, although they have little contribution to the carbon balance until solid deposits are formed. The shorter t_{res} in the hot zone in reverse vortex configuration, together with the absence of a recirculation cell, determines the possibility to operate in a solid-carbon free regime even under conditions where solid carbon formation would be thermodynamically favorable[115]. Consequently, the flow topology affects the chemistry, determining a shift from a kinetics dominated by full (oxidative) hydrocarbon pyrolysis (e.g., $CH_4 \rightarrow C_s + 2H_2$) towards a larger contribution from partial pyrolysis (e.g., $2CH_4 \rightarrow C_2H_2 + 3H_2$), without any other parametric modification, as depicted in Figure 7.5.

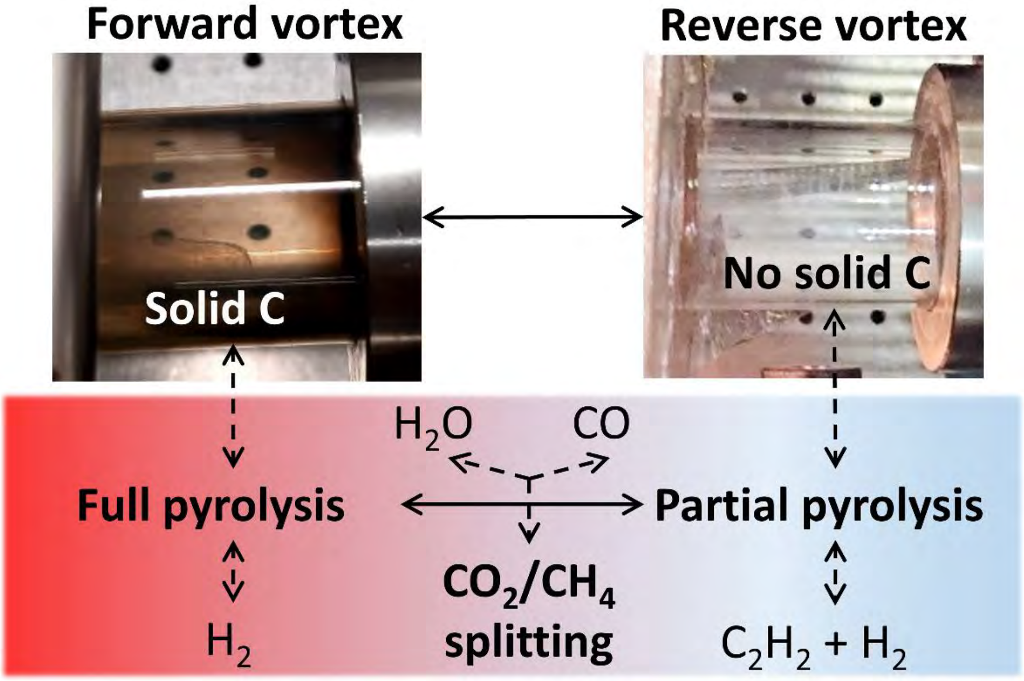

Figure 7.8. Schematic illustration of the effect of the reactor geometry on solid carbon deposition.

The shift is not captured by the GC analysis because conditions of severe carbon deposition are avoided to preserve the functionality of the diagnostics. However, the shift is observable from our experiments performed without the limitations imposed by the diagnostics, in which the plasma stability in forward vortex configuration is hampered by the large amount of solid carbon deposition. Hence, the insight provided by this work represents a step further in the understanding and, therefore, control of the process, from which future efforts in scaling up of plasma-based DRM (and CH_4 non-oxidative coupling) can benefit.

In effect, the reverse vortex configuration avoids carbon deposition and hence provides the opportunity of fully exploiting the DRM chemistry, from low fractions of CH_4 in the feed gas up to pure CH_4, and therefore achieving solid carbon-free syngas at the desired ratios, as shown in Figure 7.9. For instance, a H_2/CO ratio of 2 is desired for methanol and Fisher-Tropsch synthesis, which is potentially attainable with a CH_4 fraction of ca. 60% in reverse vortex flow configuration, without the use of a catalyst.

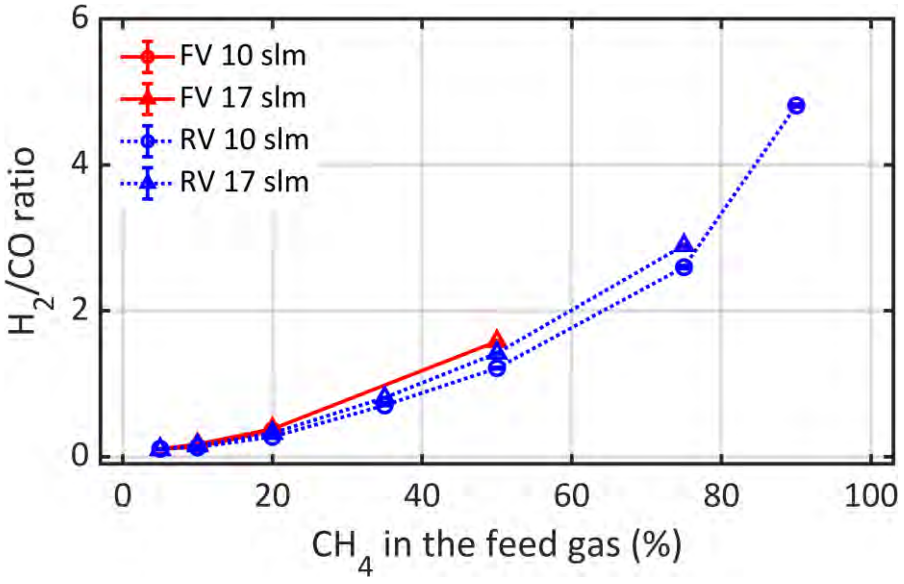

Figure 7.9. Syngas (H_2/CO) ratio as a function of the CH_4 fraction in the feed gas, in the FV and RV configuration, at 10 and 17 slm (100 mbar, 1000 W).

7.3 Conclusions

In conclusion, our work illustrates the essential role of the flow dynamics (reverse vs forward vortex) in determining the selectivity towards solid or gaseous products in complex mixtures such as CO_2/CH_4. With proper optimization of the reverse vortex configuration and exploration of a wider parameter space, especially higher flow rates and pressures in combination with varying power input, we hope to achieve steering of the selectivity towards higher-value hydrocarbons (e.g., C_2H_2 and C_2H_4), which seems to be not feasible in forward vortex configuration due to restricted control over the residence time in the hot plasma zone. Moreover, the reverse vortex configuration opens up the possibility to sustain a microwave plasma in non-thermal equilibrium (i.e. with $T_e > T_g$), thanks to the activation of intense core-periphery convection, cooling down the discharge zone. This can be beneficial for the production of C_2 hydrocarbons or heavier molecules, whose formation is limited by the high T_g in thermal plasmas.

Appendix E. Estimation of the plasma size

Optical emission imaging is used to reconstruct the shape of the plasma, following the O 777 nm emission line intensity[228,232] with an image intensified CCD high-speed camera. The O 777 nm line emission is isolated with a bandpass filter with a central wavelength of ca. 780 nm. The resulting axial and radial profiles for the pure CO_2 microwave discharge at 17 slm are shown in Figures E1 and E2, respectively. Pure CO_2 is chosen to avoid interference from broadband emission of carbon particles, which may alter the estimated plasma dimensions. An accurate estimation of the plasma size upon addition of CH_4 goes beyond the scope of this analysis, which is meant only to provide an estimate of the timescale of core-periphery transport in reverse and forward vortex flow configurations.

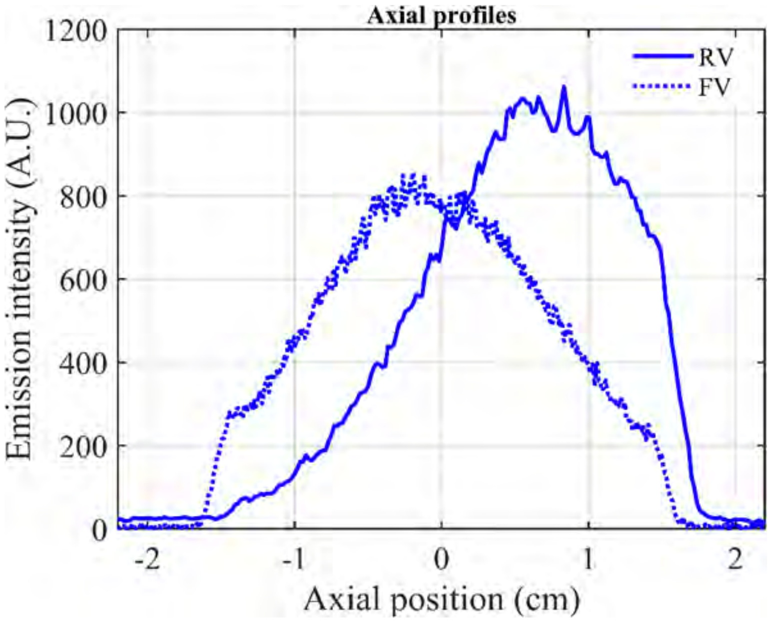

Figure E1. Axial profiles of the O 777 line emission intensity in reverse (RV) and forward vortex (FV) flow configurations (pure CO_2, 1000 W, 100 mbar, 17 slm).

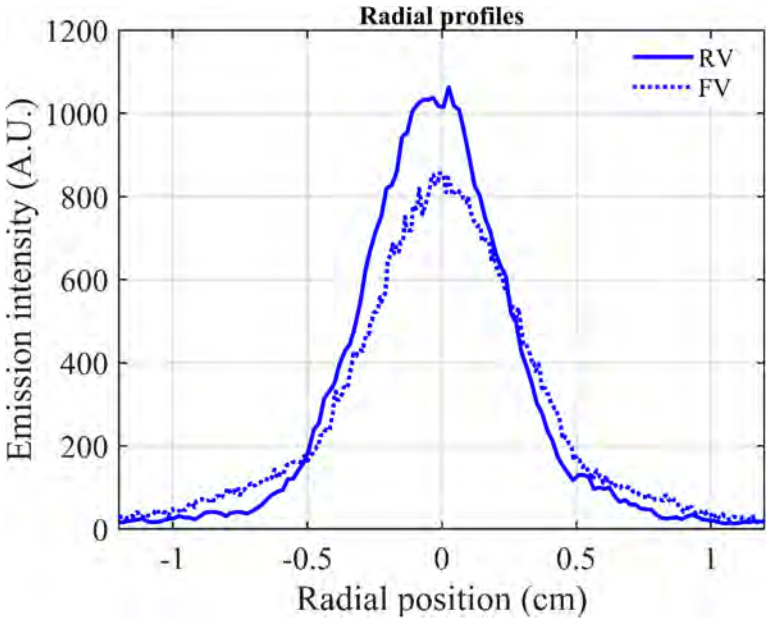

Figure E2. Radial profiles of the O 777 line emission intensity in reverse (RV) and forward vortex (FV) flow configurations (pure CO_2, 1000 W, 100 mbar, 17 slm).

Plasma length and width are calculated upon fitting of the O 777 line intensity (shown in Figure E1 and E2, respectively) with a Gaussian and defined as the full width at half maximum (FWHM) of the radial and axial profiles, respectively[232]. The resulting dimensions are reported in Table E1 and are used to estimate the characteristic gas residence time for the forward and reverse vortex flow configurations, reported in Section 7.2.5.

Table E1. Plasma length and width for pure CO_2, 1000 W, 100 mbar, 17 slm.

	Length (cm)	Width (cm)
Forward vortex	2.3	0.8
Reverse vortex	1.9	0.6

Chapter 8 Overall conclusions and outlook

Plasma-based CO_2 conversion is gaining increasing interest worldwide, but to improve its application, a better insight into the underlying mechanisms is desirable. This insight can be obtained by experiments, but also by modeling. Both plasma chemistry modeling and plasma reactor modeling are important for CO_2 conversion applications. Particularly, the latter can become extremely time-expensive due to the challenging nature of the plasma environment, especially in complex mixtures such as CO_2/CH_4. Nevertheless, being able to capture the underlying mechanisms paves the way to achieving control on them, which is key to bring plasma technology towards a wider scale of application.

Improving the energy efficiency of CO_2 conversion can be realized by a deeper understanding and improved control of the fundamental processes. A great deal of studies investigated the conversion performance in response to the variation of experimental parameters, yet a limited number focused on the fundamentals governing the performance. Plasma-based green chemistry is worldwide still mostly focused on trial-and-error experiments, making research time-consuming and expensive. This thesis aims to add to the state-of-the-art through detailed kinetic modelling and plasma diagnostics, addressing some essential questions:

- *What is the potential significance of vibrational excitation for CO_2 dissociation?*

Thus far, modelling investigations for CO_2 plasmas focused on the study of the vibrational kinetics, identifying V-T relaxation as central mechanism for vibrational depopulation and gas heating. However, Chapter 4 in this thesis pinpoints the key role of V-V-T relaxation in coupling the kinetics of v_3 and v_{12}, unveiling the essential contribution of v_{12} in promoting the gas heating in pure CO_2 discharges. Additional heating is caused by the fast transfer of energy into electronically excited states, followed by collisional quenching, which represents a fast and unavoidable heating mechanism in transient CO_2 discharges. Moreover, the presence of dissociation products (e.g. O atoms, as demonstrated in this study) can alter the vibrational distribution and the heating dynamics during the active phase of the discharge and in the afterglow. These limitations to the vibrational *ladder-climbing* process call for the redefinition of the operational parameter space for sustaining a consistent vibrational excitation and its potential contribution into CO_2 dissociation. At this point, it seems clear that discharges in pulsed regimes are not suitable for the selective excitation of vibrational quanta. On the other hand, *warm* discharges are too close to thermal equilibrium to promote the *ladder-climbing*. However, the microwave discharge in reverse vortex flow configuration, presented in Chapter 7, may still provide the optimal conditions to exploit non-equilibrium dissociation of CO_2, thanks to transport of dissociation products from the hot core to the cooler periphery and improved mixing with the cold feed gas. Particularly, increasing the feed gas flow rate may enhance the cooling of the discharge and therefore slow down vibration-translation relaxation reactions. This will require modifications of the reactor design to operate at high flow rates and should be accompanied by accurate reactor modeling, avoiding a *trial-and-error* approach. Hence, in future work, the detailed kinetic scheme developed within this thesis should be reduced in order to be coupled with multi-dimensional modeling. Coupling of computational fluid dynamics simulations with the reduced CO_2 chemistry should enable to define the key pathways for dissociation in discharges with high degree of inhomogeneity, such as microwave plasmas, but also gliding arc discharges.

- *Why is the beneficial effect of the carbon bed transient*?

Even if the vibrational *ladder-climbing* process cannot be realized in warm plasmas, there are other possibilities to improve the performance of CO_2 conversion in such plasmas. Indeed, both CO_2 conversion and energy efficiency, along with O_2-free CO production, can be achieved with a post-plasma carbon bed, as demonstrated in Chapter 5, but its beneficial effect is transient. To understand the underlying mechanisms, temperature measurements and detailed kinetic modelling (as described in Chapter 2) are applied. The combined results reveal that the onset of oxygen coverage at the carbon surface is of crucial importance to define the performance of the conversion process. In particular, the presence of oxygen complexes increases the selectivity towards CO_2 through the C(s)-O oxidation and the forward Boudouard reactions. According to the model developed, this oxygen coverage may be limited by increasing the temperature in the carbon bed, i.e., by providing additional heating, which should lead to a complete consumption of the bed, followed by supplying fresh pellets from the silo. Thus, in future work, external heating at the carbon bed should be tested by a combination of modeling and experiments. In particular, the detailed kinetic scheme developed in this thesis contains a limited number of reactions and is therefore well suited for coupling with (three-dimensional) computational fluid dynamics simulations of the post-discharge zone. For the active plasma zone, multi-dimensional modeling and chemistry should also be coupled, when the reduction of the CO_2 chemistry mentioned in the previous paragraph will be implemented. Microwave plasmas have a very high gas temperature, generally much higher than the gliding arc plasma tested in Chapter 5. Indeed, we demonstrate in Chapter 6 and 7 that the gas temperature is always higher than 3000 K in the core of the discharge. Thus, the addition of solid carbon in the post-discharge region of a microwave plasma can exploit this heat for the reactions at the carbon bed. Moreover, the high gas temperature of microwave plasmas may promote endothermic reactions such as the reverse Boudouard reaction, further enhancing the CO_2 conversion. Therefore, in future work we will implement a carbon basket downstream our microwave reactor, in order to verify our hypothesis. Computational fluid dynamics simulations will help drive the design process. Furthermore, in this thesis only two carbonaceous materials have been tested, while in the literature a wider range of materials can be found. However, most of them have been investigated for thermal gasification and not for plasma-assisted gasification. Thus, we will select materials with different characteristics than what we tested already, especially with larger surface area, which is thought to increase reactivity and the amount of oxygen that can be removed from the gas. Overall, the new insights from modeling and experiments will hopefully catalyse the adoption of the post-discharge carbon bed, which may also represent a model for other plasma-assisted waste gasification.

- *What is the effect of CH_4 concentration on the CH_4-CO_2 discharge parameters?*

In Chapter 5, we demonstrate that the energy efficiency of CO_2 conversion in a *warm* plasma can be improved by intervening in the post-discharge region. Indeed, in these plasmas the conversion performance is controlled by recombination rates outside the plasma core. In turns, recombination rates are controlled by the trajectories of the dissociation products, determined by the temperature gradients between the plasma core and the cooler periphery. In this regard, understanding how the discharge volume evolves with the operating conditions is crucial. In the last decades, the contraction dynamics has been thoroughly characterized for noble gases and little research has been recently conducted to molecular discharges such as CO_2. In this thesis, in Chapter 6, we characterize for the first time the evolution of the discharge volume with pressure in dry reforming of methane in a microwave discharge. The addition of CH_4 shifts the onset of power concentration towards higher pressures. A comparison between experiments and the calculated thermodynamic properties demonstrates that the relationship between power concentration and gas temperature is governed by the thermodynamic properties of the reactive gas mixture. The overall picture is further complicated by the role of the ion chemistry in intensifying the concentration mechanism and by the establishment of thermal non-equilibrium in CO_2/CH_4 discharges. For this reason, expanding the description of the dynamics underlying power concentration to these mixtures still requires detailed kinetic modelling. CO_2/CH_4 kinetic schemes are already available and ready to be tested at PLASMANT. However, a validation against experiments, especially to reproduce gas and electron temperatures, is still lacking. Hence, analogously to Chapter 4, in future work we plan to validate the available kinetic schemes with experiments, e.g., pulsed discharges, as they are good benchmarks to study the heating dynamics with 0D models, as indeed demonstrated in Chapter 4. After the reduction of the chemical kinetics to the essential reaction pathways, flow modelling will enable to identify the key parameters to improve the performance of DRM in microwave plasmas. The parameters collected in Chapter 6 (e.g., spatially resolved gas and electron temperature, electron number density, plasma dimensions) will serve as both input and validation parameters for the computational fluid dynamics simulations. In addition, new measurements should be taken, and the fitting scripts for the interpretation of the laser scattering spectra should be adapted to the complex chemical environment of CO_2/CH_4 plasmas. The combination of modeling and experimental efforts will hopefully pave the way towards the commercialization of plasma-based dry reforming of methane.

- *Can we avoid solid carbon deposition in low-ratio CO_2/CH_4 microwave discharges?*

Another effect of the addition of CH_4 to a CO_2 microwave plasma is the formation and deposition of solid carbon inside the reactor, as observed in Chapter 6. In effect, discharges with CO_2/CH_4 ratios < 1 are generally characterized by high carbon deposition, hampering stable operations and reducing the selectivity towards gaseous products. This thesis demonstrates for the first time, in Chapter 7, the essential role of the flow dynamics in determining the selectivity towards solid or gaseous products in complex mixtures such as CO_2/CH_4. Indeed, operations in reverse vortex flow configuration enable to inhibit the formation of carbon deposits, even in pure CH_4 experiments. This under-researched flow configuration offers a great potential to boost the adoption of plasma-based dry reforming of methane and, beyond that, of non-oxidative coupling of CH_4 in the chemical industry. However, the potential is yet to be fully demonstrated and more computational and experimental work is needed. As such, we plan to use the computational fluid dynamics simulations mentioned in the previous paragraphs to infer the effect of the increasing flow rate on the plasma parameters and the reactor performance. Based on the outcome of the simulations, we hope to adapt the microwave reactor design and verify the simulation predictions with the experiments. The little research thus far carried out has shown that the gas residence time is dependent on the gas flow rate in reverse vortex flow configuration, because of the strong core-periphery convection. Therefore, we expect that this configuration may enable to tune the process towards the desired products, without changing any other experimental parameters. If this will prove to be attainable, the reverse vortex flow configuration may represent the optimal design for implementation of plasma-based gas conversion at the industrial level.

Overall, this thesis aims to provide a deeper, fundamental understanding of plasma-based conversion of CO_2 and its mixtures with CH_4. A deep grasp of the underlying mechanisms will enable a better control of the conversion process, essential for optimization and commercialization. Therefore, this thesis will hopefully have impact for the application of plasma-based gas conversion at a wider scale, boosting the transition towards a more sustainable energy economy.

Bibliography

(1) Baker, H. S.; Millar, R. J.; Karoly, D. J.; Beyerle, U.; Guillod, B. P.; Mitchell, D.; Shiogama, H.; Sparrow, S.; Woollings, T.; Allen, M. R. Higher CO_2 Concentrations Increase Extreme Event Risk in a 1.5 °C World. *Nat. Clim. Change* **2018**, *8* (7), 604–608. https://doi.org/10.1038/s41558-018-0190-1.

(2) Steinacher, M.; Joos, F.; Stocker, T. F. Allowable Carbon Emissions Lowered by Multiple Climate Targets. *Nature* **2013**, *499* (7457), 197–201. https://doi.org/10.1038/nature12269.

(3) Seneviratne, S. I.; Donat, M. G.; Pitman, A. J.; Knutti, R.; Wilby, R. L. Allowable CO_2 Emissions Based on Regional and Impact-Related Climate Targets. *Nature* **2016**, *529* (7587), 477–483. https://doi.org/10.1038/nature16542.

(4) Tong, D.; Zhang, Q.; Zheng, Y.; Caldeira, K.; Shearer, C.; Hong, C.; Qin, Y.; Davis, S. J. Committed Emissions from Existing Energy Infrastructure Jeopardize 1.5 °C Climate Target. *Nature* **2019**, *572* (7769), 373–377. https://doi.org/10.1038/s41586-019-1364-3.

(5) Starace, F.; Lévy, J.-B.; Galán, I. S. *Energy prices, geopolitical crisis and net-zero goals: a brave new Europe towards energy independence*. Politico. https://www.politico.eu/sponsored-content/energy-prices-geopolitical-crisis-and-net-zero-goals-a-brave-new-europe-towards-energy-independence/ (accessed 2023-02-23).

(6) *Renovating and electrifying buildings strengthens Europe's economy and energy security*. European Climate Foundation. https://europeanclimate.org/resources/renovating-and-and-electrifying-buildings-strengthens-europes-economy-and-energy-security/ (accessed 2023-02-23).

(7) Communication From The Commission To The European Parliament, The European Council, The Council, The European Economic And Social Committee And The Committee Of The Regions: REPowerEU: Joint European Action for More Affordable, Secure and Sustainable Energy., 2022. https://eurlex. europa.eu/resource.html?uri=cellar:71767319-9f0a-11ec-83e1-01aa75ed71a1.0001.02/DOC_1&format=PDF (accessed 2023-02-23).

(8) Calanter, P.; Zisu, D. EU Policies to Combat the Energy Crisis. *Glob. Econ. Obs.* **2022**, *10* (1), 26–33.

(9) BP Statistical Review of World Energy. *BP Statistical Review of World Energy*. https://www.bp.com/content/dam/bp/business-sites/en/global/corporate/pdfs/energy-economics/statistical-review/bp-stats-review-2019-full-report.pdf (accessed 2022-03-21).

(10) OMV Group. *Renewable energy? Let's store it!* https://www.omv.com/en/blog/renewable-energy-lets-store-it (accessed 2023-02-22).

(11) van Rooij, G. J.; Akse, H. N.; Bongers, W. A.; van de Sanden, M. C. M. Plasma for Electrification of Chemical Industry: A Case Study on CO_2 Reduction. *Plasma Phys. Control. Fusion* **2018**, *60* (1), 014019. https://doi.org/10.1088/1361-6587/aa8f7d.

(12) Davis, S. J.; Lewis, N. S.; Shaner, M.; Aggarwal, S.; Arent, D.; Azevedo, I. L.; Benson, S. M.; Bradley, T.; Brouwer, J.; Chiang, Y.-M.; Clack, C. T. M.; Cohen, A.; Doig, S.; Edmonds, J.; Fennell, P.; Field, C. B.; Hannegan, B.; Hodge, B.-M.; Hoffert, M. I.; Ingersoll, E.; Jaramillo, P.; Lackner, K. S.; Mach, K. J.; Mastrandrea, M.; Ogden, J.; Peterson, P. F.; Sanchez, D. L.; Sperling, D.; Stagner, J.; Trancik, J. E.; Yang, C.-J.; Caldeira, K. Net-Zero Emissions Energy Systems. *Science* **2018**, *360* (6396), eaas9793. https://doi.org/10.1126/science.aas9793.

(13) Hassanpouryouzband, A.; Joonaki, E.; Edlmann, K.; Haszeldine, R. S. Offshore Geological Storage of Hydrogen: Is This Our Best Option to Achieve Net-Zero? *ACS Energy Lett.* **2021**, *6* (6), 2181–2186. https://doi.org/10.1021/acsenergylett.1c00845.

(14) Godin, J.; Liu, W.; Ren, S.; Xu, C. C. Advances in Recovery and Utilization of Carbon Dioxide: A Brief Review. *J. Environ. Chem. Eng.* **2021**, *9* (4), 105644. https://doi.org/10.1016/j.jece.2021.105644.

(15) Snoeckx, R.; Bogaerts, A. Plasma Technology – a Novel Solution for CO_2 Conversion? *Chem. Soc. Rev.* **2017**, *46* (19), 5805–5863. https://doi.org/10.1039/C6CS00066E.

(16) Dieterich, V.; Buttler, A.; Hanel, A.; Spliethoff, H.; Fendt, S. Power-to-Liquid *via* Synthesis of Methanol, DME or Fischer–Tropsch-Fuels: A Review. *Energy Environ. Sci.* **2020**, *13* (10), 3207–3252. https://doi.org/10.1039/D0EE01187H.

(17) Bogaerts, A.; Centi, G. Plasma Technology for CO_2 Conversion: A Personal Perspective on Prospects and Gaps. *Front. Energy Res.* **2020**, *8*, 111. https://doi.org/10.3389/fenrg.2020.00111.

(18) Bogaerts, A.; Tu, X.; Rooij, G. van; Sanden, R. van de. 28. Plasma-Based CO_2 Conversion. In *Transformations*; North, M., Styring, P., Eds.; De Gruyter: Berlin, Boston, 2019; pp 585–634. https://doi.org/10.1515/9783110665147-028.

(19) Aerts, R.; Snoeckx, R.; Bogaerts, A. In-Situ Chemical Trapping of Oxygen in the Splitting of Carbon Dioxide by Plasma: In-Situ Chemical Trapping of O_2 in CO_2 Splitting by DBD. *Plasma Process. Polym.* **2014**, *11* (10), 985–992. https://doi.org/10.1002/ppap.201400091.

(20) Aerts, R.; Somers, W.; Bogaerts, A. Carbon Dioxide Splitting in a Dielectric Barrier Discharge Plasma: A Combined Experimental and Computational Study. *ChemSusChem* **2015**, *8* (4), 702–716. https://doi.org/10.1002/cssc.201402818.

(21) Ramakers, M.; Michielsen, I.; Aerts, R.; Meynen, V.; Bogaerts, A. Effect of Argon or Helium on the CO_2 Conversion in a Dielectric Barrier Discharge. *Plasma Process. Polym.* **2015**, *12* (8), 755–763. https://doi.org/10.1002/ppap.201400213.

(22) Fridman, A.; Chirokov, A.; Gutsol, A. Non-Thermal Atmospheric Pressure Discharges. *J. Phys. Appl. Phys.* **2005**, *38* (2), R1–R24. https://doi.org/10.1088/0022-3727/38/2/R01.

(23) Pietanza, L. D.; Colonna, G.; Capitelli, M. Kinetics versus Thermodynamics on CO_2 Dissociation in High Temperature Microwave Discharges. *Plasma Sources Sci. Technol.* **2020**, *29* (3), 035022. https://doi.org/10.1088/1361-6595/ab6e5a.

(24) Silva, T.; Britun, N.; Godfroid, T.; Snyders, R. Understanding CO_2 Decomposition in Microwave Plasma by Means of Optical Diagnostics. *Plasma Process. Polym.* **2017**, *14* (6), 1600103. https://doi.org/10.1002/ppap.201600103.

(25) den Harder, N.; van den Bekerom, D. C. M.; Al, R. S.; Graswinckel, M. F.; Palomares, J. M.; Peeters, F. J. J.; Ponduri, S.; Minea, T.; Bongers, W. A.; van de Sanden, M. C. M.; van Rooij, G. J. Homogeneous CO_2 Conversion by Microwave Plasma: Wave Propagation and Diagnostics. *Plasma Process. Polym.* **2017**, *14* (6), 1600120. https://doi.org/10.1002/ppap.201600120.

(26) Spencer, L. F.; Gallimore, A. D. Efficiency of CO_2 Dissociation in a Radio-Frequency Discharge. *Plasma Chem. Plasma Process.* **2011**, *31* (1), 79–89. https://doi.org/10.1007/s11090-010-9273-0.

(27) Devid, E. J.; Ronda-Lloret, M.; Zhang, D.; Schuler, E.; Wang, D.; Liang, C.-H.; Huang, Q.; Rothenberg, G.; Shiju, N. R.; Kleyn, A. W. Enhancing CO_2 Plasma Conversion Using Metal Grid Catalysts. *J. Appl. Phys.* **2021**, *129* (5), 053306. https://doi.org/10.1063/5.0033212.

(28) Wang, W.; Mei, D.; Tu, X.; Bogaerts, A. Gliding Arc Plasma for CO_2 Conversion: Better Insights by a Combined Experimental and Modelling Approach. *Chem. Eng. J.* **2017**, *330*, 11–25. https://doi.org/10.1016/j.cej.2017.07.133.

(29) Paunska, Ts.; Trenchev, G.; Bogaerts, A.; Kolev, St. A 2D Model of a Gliding Arc Discharge for CO_2 Conversion; Sofia, Bulgaria, 2019; p 060008. https://doi.org/10.1063/1.5091186.

(30) Trenchev, G.; Kolev, St.; Wang, W.; Ramakers, M.; Bogaerts, A. CO_2 Conversion in a Gliding Arc Plasmatron: Multidimensional Modeling for Improved Efficiency. *J. Phys. Chem. C* **2017**, *121* (44), 24470–24479. https://doi.org/10.1021/acs.jpcc.7b08511.

(31) Ramakers, M.; Medrano, J. A.; Trenchev, G.; Gallucci, F.; Bogaerts, A. Revealing the Arc Dynamics in a Gliding Arc Plasmatron: A Better Insight to Improve CO_2 Conversion. *Plasma Sources Sci. Technol.* **2017**, *26* (12), 125002. https://doi.org/10.1088/1361-6595/aa9531.

(32) Trenchev, G.; Bogaerts, A. Dual-Vortex Plasmatron: A Novel Plasma Source for CO_2 Conversion. *J. CO2 Util.* **2020**, *39*, 101152. https://doi.org/10.1016/j.jcou.2020.03.002.

(33) Rusanov, V. D.; Fridman, A. A.; Sholin, G. V. The Physics of a Chemically Active Plasma with Nonequilibrium Vibrational Excitation of Molecules. *Sov. Phys. Uspekhi* **1981**, *24* (6), 447–474. https://doi.org/10.1070/PU1981v024n06ABEH004884.

(34) Butylkin, Iu. P.; Zhivotov, V. K.; Krasheninnikov, E. G.; Krotov, M. F.; Rusanov, V. D.; Tarasov, Iu. V.; Fridman, A. A. Plasma-Chemical Process of CO2 Dissociation in a Nonequilibrium Microwave Discharge. *Zhurnal Tekhnicheskoi Fiz.* **1981**, *51*, 925–931.

(35) Azizov, R. I.; Vakar, A. K.; Zhivotov, V. K.; Krotov, M. F.; Zinovev, O. A.; Potapkin, B. V.; Rusanov, A. A.; Rusanov, V. D.; Fridman, A. A. Non-Equilibrium Plasma- Chemical Process of CO_2 Decomposition in a Supersonic Microwave Discharge. *Proc USSR Acad Sci* **1983**, *271* (1), 94–98.

(36) van Rooij, G. J.; van den Bekerom, D. C. M.; den Harder, N.; Minea, T.; Berden, G.; Bongers, W. A.; Engeln, R.; Graswinckel, M. F.; Zoethout, E.; van de Sanden, M. C. M. Taming Microwave Plasma to Beat Thermodynamics in CO_2 Dissociation. *Faraday Discuss.* **2015**, *183*, 233–248. https://doi.org/10.1039/C5FD00045A.

(37) Bongers, W.; Bouwmeester, H.; Wolf, B.; Peeters, F.; Welzel, S.; van den Bekerom, D.; den Harder, N.; Goede, A.; Graswinckel, M.; Groen, P. W.; Kopecki, J.; Leins, M.; van Rooij, G.; Schulz, A.; Walker, M.; van de Sanden, R. Plasma-Driven Dissociation of CO_2 for Fuel Synthesis. *Plasma Process. Polym.* **2017**, *14* (6), 1600126. https://doi.org/10.1002/ppap.201600126.

(38) Spencer, L. F.; Gallimore, A. D. CO_2 Dissociation in an Atmospheric Pressure Plasma/Catalyst System: A Study of Efficiency. *Plasma Sources Sci. Technol.* **2012**, *22* (1), 015019. https://doi.org/10.1088/0963-0252/22/1/015019.

(39) Kim, H.; Song, S.; Tom, C. P.; Xie, F. Carbon Dioxide Conversion in an Atmospheric Pressure Microwave Plasma Reactor: Improving Efficiencies by Enhancing Afterglow Quenching. *J. CO2 Util.* **2020**, *37*, 240–247. https://doi.org/10.1016/j.jcou.2019.12.011.

(40) Mitsingas, C. M.; Rajasegar, R.; Hammack, S.; Do, H.; Lee, T. High Energy Efficiency Plasma Conversion of CO_2 at Atmospheric Pressure Using a Direct-Coupled Microwave Plasma System. *IEEE Trans. Plasma Sci.* **2016**, *44* (4), 651–656. https://doi.org/10.1109/TPS.2016.2531641.

(41) Ananthapadmanabhan, P. V.; Venkatramani, N. Chapter 6 Thermal Plasma Processing. In *Non-equilibrium Processing of Materials*; Suryanarayana, C., Ed.; Pergamon Materials Series; Pergamon, 1999; Vol. 2, pp 121–150. https://doi.org/10.1016/S1470-1804(99)80052-2.

(42) Bogaerts, A.; Neyts, E.; Gijbels, R.; van der Mullen, J. Gas Discharge Plasmas and Their Applications. *Spectrochim. Acta Part B At. Spectrosc.* **2002**, *57* (4), 609–658. https://doi.org/10.1016/S0584-8547(01)00406-2.

(43) Wang, B.; Song, Z.; Sun, L. A Review: Comparison of Multi-Air-Pollutant Removal by Advanced Oxidation Processes – Industrial Implementation for Catalytic Oxidation Processes. *Chem. Eng. J.* **2021**, *409*, 128136. https://doi.org/10.1016/j.cej.2020.128136.

(44) Rezaei, F.; Vanraes, P.; Nikiforov, A.; Morent, R.; De Geyter, N. Applications of Plasma-Liquid Systems: A Review. *Materials* **2019**, *12* (17). https://doi.org/10.3390/ma12172751.

(45) Babaeva, N. Y.; Naidis, G. V. On the Efficiency of CO_2 Conversion in Corona and Dielectric-Barrier Discharges. *Plasma Sources Sci. Technol.* **2021**, *30* (3), 03LT03. https://doi.org/10.1088/1361-6595/abe6e6.

(46) Fridman, A. *Plasma Chemistry*; Cambridge: Cambridge University Press, 2008.

(47) van den Bekerom, D. C. M.; van de Steeg, A.; van de Sanden, M. C. M.; van Rooij, G. J. Mode Resolved Heating Dynamics in Pulsed Microwave CO_2 Plasma from Laser Raman Scattering. *J. Phys. Appl. Phys.* **2020**, *53* (5), 054002. https://doi.org/10.1088/1361-6463/ab5311.

(48) Kozák, T.; Bogaerts, A. Splitting of CO_2 by Vibrational Excitation in Non-Equilibrium Plasmas: A Reaction Kinetics Model. *Plasma Sources Sci. Technol.* **2014**, *23* (4), 045004. https://doi.org/10.1088/0963-0252/23/4/045004.

(49) Diomede, P.; van de Sanden, M. C. M.; Longo, S. Insight into CO_2 Dissociation in Plasma from Numerical Solution of a Vibrational Diffusion Equation. *J. Phys. Chem. C* **2017**, *121* (36), 19568–19576. https://doi.org/10.1021/acs.jpcc.7b04896.

(50) Klarenaar, B. L. M.; Engeln, R.; van den Bekerom, D. C. M.; van de Sanden, M. C. M.; Morillo-Candas, A. S.; Guaitella, O. Time Evolution of Vibrational Temperatures in a CO_2 Glow Discharge Measured with Infrared Absorption Spectroscopy. *Plasma Sources Sci. Technol.* **2017**, *26* (11), 115008. https://doi.org/10.1088/1361-6595/aa902e.

(51) van de Steeg, A. W.; Vialetto, L.; Silva, A. F. S. da; Viegas, P.; Diomede, P.; van de Sanden, M. C. M.; van Rooij, G. J. The Chemical Origins of Plasma Contraction and Thermalization in CO_2 Microwave Discharges. *J. Phys. Chem. Lett.* **2022**, *13* (5), 1203–1208. https://doi.org/10.1021/acs.jpclett.1c03731.

(52) Berthelot, A.; Bogaerts, A. Modeling of CO_2 Splitting in a Microwave Plasma: How to Improve the Conversion and Energy Efficiency. *J. Phys. Chem. C* **2017**, *121* (15), 8236–8251. https://doi.org/10.1021/acs.jpcc.6b12840.

(53) Heijkers, S.; Bogaerts, A. CO_2 Conversion in a Gliding Arc Plasmatron: Elucidating the Chemistry through Kinetic Modeling. *J. Phys. Chem. C* **2017**, *121* (41), 22644–22655. https://doi.org/10.1021/acs.jpcc.7b06524.

(54) van den Bekerom, D. C. M.; Linares, J. M. P.; Verreycken, T.; van Veldhuizen, E. M.; Nijdam, S.; Berden, G.; Bongers, W. A.; van de Sanden, M. C. M.; van Rooij, G. J. The Importance of Thermal Dissociation in CO_2 Microwave Discharges Investigated by Power Pulsing and Rotational Raman Scattering. *Plasma Sources Sci. Technol.* **2019**, *28* (5), 055015. https://doi.org/10.1088/1361-6595/aaf519.

(55) Vermeiren, V.; Bogaerts, A. Plasma-Based CO_2 Conversion: To Quench or Not to Quench? *J. Phys. Chem. C* **2020**, *124* (34), 18401–18415. https://doi.org/10.1021/acs.jpcc.0c04257.

(56) van de Steeg, A.; Viegas, P.; Silva, A.; Butterworth, T.; van Bavel, A.; Smits, J.; Diomede, P.; van de Sanden, M.; van Rooij, G. Redefining the Microwave Plasma-Mediated CO_2 Reduction Efficiency Limit: The Role of O–CO_2 Association. *ACS Energy Lett.* **2021**, *6* (8), 2876–2881. https://doi.org/10.1021/acsenergylett.1c01206.

(57) Sun, S. R.; Wang, H. X.; Mei, D. H.; Tu, X.; Bogaerts, A. CO_2 Conversion in a Gliding Arc Plasma: Performance Improvement Based on Chemical Reaction Modeling. *J. CO2 Util.* **2017**, *17*, 220–234. https://doi.org/10.1016/j.jcou.2016.12.009.

(58) Irfan, M. F.; Usman, M. R.; Kusakabe, K. Coal Gasification in CO_2 Atmosphere and Its Kinetics since 1948: A Brief Review. *Energy* **2011**, *36* (1), 12–40. https://doi.org/10.1016/j.energy.2010.10.034.

(59) Lahijani, P.; Zainal, Z. A.; Mohammadi, M.; Mohamed, A. R. Conversion of the Greenhouse Gas CO_2 to the Fuel Gas CO via the Boudouard Reaction: A Review. *Renew. Sustain. Energy Rev.* **2015**, *41*, 615–632. https://doi.org/10.1016/j.rser.2014.08.034.

(60) Ascher, S.; Watson, I.; You, S. Machine Learning Methods for Modelling the Gasification and Pyrolysis of Biomass and Waste. *Renew. Sustain. Energy Rev.* **2022**, *155*, 111902. https://doi.org/10.1016/j.rser.2021.111902.

(61) Calo, J. M.; Perkins, M. T. A Heterogeneous Surface Model for the "Steady-State" Kinetics of the Boudouard Reaction. *Carbon* **1987**, *25* (3), 395–407. https://doi.org/10.1016/0008-6223(87)90011-X.

(62) Hunt, J.; Ferrari, A.; Lita, A.; Crosswhite, M.; Ashley, B.; Stiegman, A. E. Microwave-Specific Enhancement of the Carbon–Carbon Dioxide (Boudouard) Reaction. *J. Phys. Chem. C* **2013**, *117* (51), 26871–26880. https://doi.org/10.1021/jp4076965.

(63) Ono, H.; Yoshida, S.; Nezuka, M.; Sano, T.; Tsuji, M.; Tamaura, Y. Kinetics and Simulation on a High-Temperature Solar Thermochemical Energy Conversion Process on the Boudouard Reaction. *Energy Fuels* **1999**, *13* (3), 579–584. https://doi.org/10.1021/ef980140i.

(64) Gokon, N.; Ono, R.; Hatamachi, T.; Liuyun, L.; Kim, H.-J.; Kodama, T. CO_2 Gasification of Coal Cokes Using Internally Circulating Fluidized Bed Reactor by Concentrated Xe-Light Irradiation for Solar Gasification. *Int. J. Hydrog. Energy* **2012**, *37* (17), 12128–12137. https://doi.org/10.1016/j.ijhydene.2012.05.133.

(65) Menéndez, J. A.; Domínguez, A.; Fernández, Y.; Pis, J. J. Evidence of Self-Gasification during the Microwave-Induced Pyrolysis of Coffee Hulls. *Energy Fuels* **2007**, *21* (1), 373–378. https://doi.org/10.1021/ef060331i.

(66) Dai, H.; Zhao, H.; Chen, S.; Jiang, B. A Microwave-Assisted Boudouard Reaction: A Highly Effective Reduction of the Greenhouse Gas CO_2 to Useful CO Feedstock with Semi-Coke. *Molecules* **2021**, *26* (6), 1507. https://doi.org/10.3390/molecules26061507.

(67) Roncancio, R.; Gore, J. P. CO_2 Char Gasification: A Systematic Review from 2014 to 2020. *Energy Convers. Manag. X* **2021**, *10*, 100060. https://doi.org/10.1016/j.ecmx.2020.100060.

(68) Liu, P.; Liu, X.; Shen, J.; Yin, Y.; Yang, T.; Huang, Q.; Auerbach, D.; Kleiyn, A. W. CO_2 Conversion by Thermal Plasma with Carbon as Reducing Agent: High CO Yield and Energy Efficiency. *Plasma Sci. Technol.* **2019**, *21* (1), 012001. https://doi.org/10.1088/2058-6272/aadf30.

(69) Li, Z.; Yang, T.; Yuan, S.; Yin, Y.; Devid, E. J.; Huang, Q.; Auerbach, D.; Kleyn, A. W. Boudouard Reaction Driven by Thermal Plasma for Efficient CO_2 Conversion and Energy Storage. *J. Energy Chem.* **2020**, *45*, 128–134. https://doi.org/10.1016/j.jechem.2019.10.007.

(70) Huang, J.; Zhang, H.; Tan, Q.; Li, L.; Xu, R.; Xu, Z.; Li, X. Enhanced Conversion of CO_2 into O_2-Free Fuel Gas via the Boudouard Reaction with Biochar in an Atmospheric Plasmatron. *J. CO2 Util.* **2021**, *45*, 101429. https://doi.org/10.1016/j.jcou.2020.101429.

(71) Zhang, H.; Tan, Q.; Huang, Q.; Wang, K.; Tu, X.; Zhao, X.; Wu, C.; Yan, J.; Li, X. Boosting the Conversion of CO_2 with Biochar to Clean CO in an Atmospheric Plasmatron: A Synergy of Plasma Chemistry and Thermochemistry. *ACS Sustain. Chem. Eng.* **2022**, *10* (23), 7712–7725. https://doi.org/10.1021/acssuschemeng.2c01778.

(72) Wu, Y.; Li, S.-Z.; Niu, Y.-L.; Yan, H.-J.; Yang, D.; Zhang, J. Experimental Investigation of CO_2 Conversion in Boudouard Reaction Driven by an Atmospheric-Pressure Microwave Plasma Torch. *J. Phys. Appl. Phys.* **2023**, *56* (6), 065201. https://doi.org/10.1088/1361-6463/acaeda.

(73) Yin, Y.; Yang, T.; Li, Z.; Devid, E.; Auerbach, D.; Kleyn, A. W. CO_2 Conversion by Plasma: How to Get Efficient CO_2 Conversion and High Energy Efficiency. *Phys. Chem. Chem. Phys.* **2021**, *23* (13), 7974–7987. https://doi.org/10.1039/D0CP05275B.

(74) Snoeckx, R.; Ozkan, A.; Reniers, F.; Bogaerts, A. The Quest for Value-Added Products from Carbon Dioxide and Water in a Dielectric Barrier Discharge: A Chemical Kinetics Study. *ChemSusChem* **2017**, *10* (2), 409–424. https://doi.org/10.1002/cssc.201601234.

(75) Chen, G.; Buck, F.; Kistner, I.; Widenmeyer, M.; Schiestel, T.; Schulz, A.; Walker, M.; Weidenkaff, A. A Novel Plasma-Assisted Hollow Fiber Membrane Concept for Efficiently Separating Oxygen from CO in a CO_2 Plasma. *Chem. Eng. J.* **2020**, *392*, 123699. https://doi.org/10.1016/j.cej.2019.123699.

(76) Perez-Carbajo, J.; Matito-Martos, I.; Balestra, S. R. G.; Tsampas, M. N.; van de Sanden, M. C. M.; Delgado, J. A.; Águeda, V. I.; Merkling, P. J.; Calero, S. Zeolites for CO_2–CO–O_2 Separation to Obtain CO_2 -Neutral Fuels. *ACS Appl. Mater. Interfaces* **2018**, *10* (24), 20512–20520. https://doi.org/10.1021/acsami.8b04507.

(77) Luna-Triguero, A.; Vicent-Luna, J. M.; Jansman, M. J.; Zafeiropoulos, G.; Tsampas, M. N.; van de Sanden, M. C. M.; Akse, H. N.; Calero, S. Enhancing Separation Efficiency in European Syngas Industry by Using Zeolites. *Catal. Today* **2021**, *362*, 113–121. https://doi.org/10.1016/j.cattod.2020.03.061.

(78) Pandiyan, A.; Kyriakou, V.; Neagu, D.; Welzel, S.; Goede, A.; van de Sanden, M. C. M.; Tsampas, M. N. CO_2 Conversion via Coupled Plasma-Electrolysis Process. *J. CO2 Util.* **2022**, *57*, 101904. https://doi.org/10.1016/j.jcou.2022.101904.

(79) Arthur, J. R. Reactions between Carbon and Oxygen. *Trans. Faraday Soc.* **1951**, *47*, 164. https://doi.org/10.1039/tf9514700164.

(80) Walker, P. L.; Taylor, R. L.; Ranish, J. M. An Update on the Carbon-Oxygen Reaction. *Carbon* **1991**, *29* (3), 411–421. https://doi.org/10.1016/0008-6223(91)90210-A.

(81) Radovic, L. R.; Jiang, H.; Lizzio, A. A. A Transient Kinetics Study of Char Gasification in Carbon Dioxide and Oxygen. *Energy Fuels* **1991**, *5* (1), 68–74. https://doi.org/10.1021/ef00025a011.

(82) Islam, M. W. Effect of Different Gasifying Agents (Steam, H2O2, Oxygen, CO_2, and Air) on Gasification Parameters. *Int. J. Hydrog. Energy* **2020**, *45* (56), 31760–31774. https://doi.org/10.1016/j.ijhydene.2020.09.002.

(83) *Canadian Environmental Sustainability Indicators: Greenhouse Gas Concentrations*; Environment and Climate Change Canada = Environnement et changement climatique Canada: Gatineau, QC, 2021.

(84) Martin-del-Campo, J.; Coulombe, S.; Kopyscinski, J. Influence of Operating Parameters on Plasma-Assisted Dry Reforming of Methane in a Rotating Gliding Arc Reactor. *Plasma Chem. Plasma Process.* **2020**, *40* (4), 857–881. https://doi.org/10.1007/s11090-020-10074-2.

(85) Uytdenhouwen, Y.; Bal, K. M.; Neyts, E. C.; Meynen, V.; Cool, P.; Bogaerts, A. On the Kinetics and Equilibria of Plasma-Based Dry Reforming of Methane. *Chem. Eng. J.* **2021**, *405*, 126630. https://doi.org/10.1016/j.cej.2020.126630.

(86) Wanten, B.; Maerivoet, S.; Vantomme, C.; Slaets, J.; Trenchev, G.; Bogaerts, A. Dry Reforming of Methane in an Atmospheric Pressure Glow Discharge: Confining the Plasma to Expand the Performance. *J. CO2 Util.* **2022**, *56*, 101869. https://doi.org/10.1016/j.jcou.2021.101869.

(87) Lavoie, J.-M. Review on Dry Reforming of Methane, a Potentially More Environmentally-Friendly Approach to the Increasing Natural Gas Exploitation. *Front. Chem.* **2014**, *2*. https://doi.org/10.3389/fchem.2014.00081.

(88) Pakhare, D.; Spivey, J. A Review of Dry (CO_2) Reforming of Methane over Noble Metal Catalysts. *Chem Soc Rev* **2014**, *43* (22), 7813–7837. https://doi.org/10.1039/C3CS60395D.

(89) Bogaerts, A.; Tu, X.; Whitehead, J. C.; Centi, G.; Lefferts, L.; Guaitella, O.; Azzolina-Jury, F.; Kim, H.-H.; Murphy, A. B.; Schneider, W. F.; Nozaki, T.; Hicks, J. C.; Rousseau, A.; Thevenet, F.; Khacef, A.; Carreon, M. The 2020 Plasma Catalysis Roadmap. *J. Phys. Appl. Phys.* **2020**, *53* (44), 443001. https://doi.org/10.1088/1361-6463/ab9048.

(90) Li, D.; Li, X.; Bai, M.; Tao, X.; Shang, S.; Dai, X.; Yin, Y. CO_2 Reforming of CH4 by Atmospheric Pressure Glow Discharge Plasma: A High Conversion Ability☆. *Int. J. Hydrog. Energy* **2009**, *34* (1), 308–313. https://doi.org/10.1016/j.ijhydene.2008.10.053.

(91) Chun, S. M.; Hong, Y. C.; Choi, D. H. Reforming of Methane to Syngas in a Microwave Plasma Torch at Atmospheric Pressure. *J. CO2 Util.* **2017**, *19*, 221–229. https://doi.org/10.1016/j.jcou.2017.03.016.

(92) Sun, H.; Lee, J.; Bak, M. S. Experiments and Modeling of Atmospheric Pressure Microwave Plasma Reforming of a Methane-Carbon Dioxide Mixture. *J. CO2 Util.* **2021**, *46*, 101464. https://doi.org/10.1016/j.jcou.2021.101464.

(93) Uytdenhouwen, Y.; Hereijgers, J.; Breugelmans, T.; Cool, P.; Bogaerts, A. How Gas Flow Design Can Influence the Performance of a DBD Plasma Reactor for Dry Reforming of Methane. *Chem. Eng. J.* **2021**, *405*, 126618. https://doi.org/10.1016/j.cej.2020.126618.

(94) Gao, X.; Lin, Z.; Li, T.; Huang, L.; Zhang, J.; Askari, S.; Dewangan, N.; Jangam, A.; Kawi, S. Recent Developments in Dielectric Barrier Discharge Plasma-Assisted Catalytic Dry Reforming of Methane over Ni-Based Catalysts. *Catalysts* **2021**, *11* (4), 455. https://doi.org/10.3390/catal11040455.

(95) Mei, D.; Duan, G.; Fu, J.; Liu, S.; Zhou, R.; Zhou, R.; Fang, Z.; Cullen, P. J.; Ostrikov, K. (Ken). CO_2 Reforming of CH_4 in Single and Double Dielectric Barrier Discharge Reactors: Comparison of Discharge Characteristics and Product Distribution. *J. CO2 Util.* **2021**, *53*, 101703. https://doi.org/10.1016/j.jcou.2021.101703.

(96) Dinh, D. K.; Trenchev, G.; Lee, D. H.; Bogaerts, A. Arc Plasma Reactor Modification for Enhancing Performance of Dry Reforming of Methane. *J. CO2 Util.* **2020**, *42*, 101352. https://doi.org/10.1016/j.jcou.2020.101352.

(97) Lombardi, G.; Hassouni, K.; Stancu, G.-D.; Mechold, L.; Röpcke, J.; Gicquel, A. Modeling of Microwave Discharges of H2 Admixed with CH4 for Diamond Deposition. *J. Appl. Phys.* **2005**, *98* (5), 053303. https://doi.org/10.1063/1.2034646.

(98) Koldanov, V. A.; Gorbachev, A. M.; Vikharev, A. L.; Radishchev, D. B. Self-Consistent Simulation of Pulsed and Continuous Microwave Discharges in Hydrogen. *Plasma Phys. Rep.* **2005**, *31* (11), 965–977. https://doi.org/10.1134/1.2131133.

(99) Lobaev, M. A.; Bogdanov, S. A.; Radishev, D. B.; Vikharev, A. L.; Gorbachev, A. M. Method of Power Density Determination in Microwave Discharge, Sustained in Hydrogen–Methane Gas Mixture. *Diam. Relat. Mater.* **2016**, *66*, 177–182. https://doi.org/10.1016/j.diamond.2016.05.004.

(100) Wang, S.; Zhu, Z. H. Catalytic Conversion of Alkanes to Olefins by Carbon Dioxide Oxidative DehydrogenationA Review. *Energy Fuels* **2004**, *18* (4), 1126–1139. https://doi.org/10.1021/ef0340716.

(101) Arinaga, A. M.; Ziegelski, M. C.; Marks, T. J. Alternative Oxidants for the Catalytic Oxidative Coupling of Methane. *Angew. Chem. Int. Ed.* **2021**, *60* (19), 10502–10515. https://doi.org/10.1002/anie.202012862.

(102) Li, H.; Tan, Y.; Ditaranto, M.; Yan, J.; Yu, Z. Capturing CO_2 from Biogas Plants. *Energy Procedia* **2017**, *114*, 6030–6035. https://doi.org/10.1016/j.egypro.2017.03.1738.

(103) Galadima, A.; Muraza, O. Revisiting the Oxidative Coupling of Methane to Ethylene in the Golden Period of Shale Gas: A Review. *J. Ind. Eng. Chem.* **2016**, *37*, 1–13. https://doi.org/10.1016/j.jiec.2016.03.027.

(104) Centi, G.; Quadrelli, E. A.; Perathoner, S. Catalysis for CO_2 Conversion: A Key Technology for Rapid Introduction of Renewable Energy in the Value Chain of Chemical Industries. *Energy Environ. Sci.* **2013**, *6* (6), 1711. https://doi.org/10.1039/c3ee00056g.

(105) Scapinello, M.; Martini, L. M.; Dilecce, G.; Tosi, P. Conversion of CH_4/CO_2 by a Nanosecond Repetitively Pulsed Discharge. *J. Phys. Appl. Phys.* **2016**, *49* (7), 075602. https://doi.org/10.1088/0022-3727/49/7/075602.

(106) Heintze, M.; Magureanu, M. Methane Conversion into Acetylene in a Microwave Plasma: Optimization of the Operating Parameters. *J. Appl. Phys.* **2002**, *92* (5), 2276–2283. https://doi.org/10.1063/1.1497457.

(107) Heijkers, S.; Aghaei, M.; Bogaerts, A. Plasma-Based CH_4 Conversion into Higher Hydrocarbons and H_2 : Modeling to Reveal the Reaction Mechanisms of Different Plasma Sources. *J. Phys. Chem. C* **2020**, *124* (13), 7016–7030. https://doi.org/10.1021/acs.jpcc.0c00082.

(108) Kahle, L. C. S.; Roussière, T.; Maier, L.; Herrera Delgado, K.; Wasserschaff, G.; Schunk, S. A.; Deutschmann, O. Methane Dry Reforming at High Temperature and Elevated Pressure: Impact of Gas-Phase Reactions. *Ind. Eng. Chem. Res.* **2013**, *52* (34), 11920–11930. https://doi.org/10.1021/ie401048w.

(109) Scapinello, M.; Delikonstantis, E.; Stefanidis, G. D. The Panorama of Plasma-Assisted Non-Oxidative Methane Reforming. *Chem. Eng. Process. Process Intensif.* **2017**, *117*, 120–140. https://doi.org/10.1016/j.cep.2017.03.024.

(110) Migone, R. A.; Agarwal, S. K.; Marcelin, G. Differences in Catalytic and Gas-Phase Reactions in Methane Coupling. *J. Chem. Soc. Chem. Commun.* **1990**, No. 3, 223. https://doi.org/10.1039/c39900000223.

(111) Holmen, A.; Olsvik, O.; Rokstad, O. A. Pyrolysis of Natural Gas: Chemistry and Process Concepts. *Fuel Process. Technol.* **1995**, *42* (2–3), 249–267. https://doi.org/10.1016/0378-3820(94)00109-7.

(112) Zanthoff, H.; Baerns, M. Oxidative Coupling of Methane in the Gas Phase. Kinetic Simulation and Experimental Verification. *Ind. Eng. Chem. Res.* **1990**, *29* (1), 2–10. https://doi.org/10.1021/ie00097a001.

(113) Chen, Q.; Hoebink, J. H. B. J.; Marin, G. B. Kinetics of the Oxidative Coupling of Methane at Atmospheric Pressure in the Absence of Catalyst. *Ind. Eng. Chem. Res.* **1991**, *30* (9), 2088–2097. https://doi.org/10.1021/ie00057a006.

(114) Kassel, L. S. THE THERMAL DECOMPOSITION OF METHANE [1]. *J. Am. Chem. Soc.* **1932**, *54* (10), 3949–3961. https://doi.org/10.1021/ja01349a019.

(115) Fincke, J. R.; Anderson, R. P.; Hyde, T. A.; Detering, B. A. Plasma Pyrolysis of Methane to Hydrogen and Carbon Black. *Ind. Eng. Chem. Res.* **2002**, *41* (6), 1425–1435. https://doi.org/10.1021/ie010722e.

(116) Herzberg, G. *Molecular Spectra and Molecular Structure. 2 Infrared and Raman Spectra of Polyatomic Molecules*; London: Van Nostrand, 1960.

(117) Suzuki, I. General Anharmonic Force Constants of Carbon Dioxide. *J. Mol. Spectrosc.* **1968**, *25* (4), 479–500. https://doi.org/10.1016/S0022-2852(68)80018-9.

(118) Chedin, A. The Carbon Dioxide Molecule. *J. Mol. Spectrosc.* **1979**, *76* (1–3), 430–491. https://doi.org/10.1016/0022-2852(79)90236-4.

(119) Silva, T.; Grofulović, M.; Terraz, L.; Pintassilgo, C. D.; Guerra, V. Modelling the Input and Relaxation of Vibrational Energy in CO_2 Plasmas. *J. Phys. Appl. Phys.* **2018**, *51* (46), 464001. https://doi.org/10.1088/1361-6463/aadbd7.

(120) Csaszar, A. G. Anharmonic Force Field of Carbon Dioxide. *J. Phys. Chem.* **1992**, *96* (20), 7898–7904. https://doi.org/10.1021/j100199a015.

(121) Martin, J. M. L.; Taylor, P. R.; Lee, T. J. Accurate Ab Initio Quartic Force Fields for the N_2O and CO_2 Molecules. *Chem. Phys. Lett.* **1993**, *205* (6), 535–542. https://doi.org/10.1016/0009-2614(93)80009-E.

(122) Courtoy, C.-P. SPECTRES DE VIBRATION-ROTATION DE MOLECULES SIMPLES DIATOMIQUES OU POLYATOMIQUES AVEC LONG PARCOURS D’ABSORPTION: XII. LE SPECTRE DE $C^{12}O^{16}_2$ ENTRE 3500 ET 8000 CM^{-1} ET LES CONSTANTES MOLECULAIRES DE CETTE MOLECULE. *Can. J. Phys.* **1957**, *35* (5), 608–648. https://doi.org/10.1139/p57-068.

(123) Herzberg, G. *Molecular Spectra and Molecular Structure. 2 Infrared and Raman Spectra of Polyatomic Molecules*; New York: D Van Nostrand, 1945.

(124) Blauer, J.; Nickerson, G. A Survey of Vibrational Relaxation Rate Data for Processes Importantto CO_2-N_2-H_2O Infrared Plume Radiation. In *7th Fluid and PlasmaDynamics Conference*; American Institute of Aeronautics and Astronautics: Palo Alto,CA,U.S.A., 1974. https://doi.org/10.2514/6.1974-536.

(125) Atkins, P. W.; Friedman, R. *Molecular Quantum Mechanics*; New York: Oxford University Press, 2005.

(126) Joly, V.; Roblin, A. Vibrational Relaxation of CO_2(m, Nl, p) in a CO_2-N_2 Mixture. Part 1: Survey of Available Data. *Aerosp. Sci. Technol.* **1999**, *3* (4), 229–238. https://doi.org/10.1016/S1270-9638(99)80045-5.
(127) Dennison, D. M. The Infra-Red Spectra of Polyatomic Molecules. Part II. *Rev. Mod. Phys.* **1940**, *12* (3), 175–214. https://doi.org/10.1103/RevModPhys.12.175.
(128) Amat, G.; Pimbert, M. On Fermi Resonance in Carbon Dioxide. *J. Mol. Spectrosc.* **1965**, *16* (2), 278–290. https://doi.org/10.1016/0022-2852(65)90123-2.
(129) Silva, T.; Grofulović, M.; Klarenaar, B. L. M.; Morillo-Candas, A. S.; Guaitella, O.; Engeln, R.; Pintassilgo, C. D.; Guerra, V. Kinetic Study of Low-Temperature CO_2 Plasmas under Non-Equilibrium Conditions. I. Relaxation of Vibrational Energy. *Plasma Sources Sci. Technol.* **2018**, *27* (1), 015019. https://doi.org/10.1088/1361-6595/aaa56a.
(130) Grofulović, M.; Silva, T.; Klarenaar, B. L. M.; Morillo-Candas, A. S.; Guaitella, O.; Engeln, R.; Pintassilgo, C. D.; Guerra, V. Kinetic Study of CO_2 Plasmas under Non-Equilibrium Conditions. II. Input of Vibrational Energy. *Plasma Sources Sci. Technol.* **2018**, *27* (11), 115009. https://doi.org/10.1088/1361-6595/aadb60.
(131) Tejero-del-Caz, A.; Guerra, V.; Gonçalves, D.; da Silva, M. L.; Marques, L.; Pinhão, N.; Pintassilgo, C. D.; Alves, L. L. The LisbOn KInetics Boltzmann Solver. *Plasma Sources Sci. Technol.* **2019**, *28* (4), 043001. https://doi.org/10.1088/1361-6595/ab0537.
(132) *The LisbOn KInetics (LoKI) 2020 http://plasmakit.tecnico. ulisboa.pt*.
(133) Pancheshnyi, S.; Eismann, B.; Hagelaar, G. J. M.; Pitchford, L. C. *ZDPlasKin*. http://www.zdplaskin.laplace.univ-tlse.fr.
(134) Hagelaar, G. J. M.; Pitchford, L. C. Solving the Boltzmann Equation to Obtain Electron Transport Coefficients and Rate Coefficients for Fluid Models. *Plasma Sources Sci. Technol.* **2005**, *14* (4), 722–733. https://doi.org/10.1088/0963-0252/14/4/011.
(135) Grofulović, M.; Alves, L. L.; Guerra, V. Electron-Neutral Scattering Cross Sections for CO_2: A Complete and Consistent Set and an Assessment of Dissociation. *J. Phys. Appl. Phys.* **2016**, *49* (39), 395207. https://doi.org/10.1088/0022-3727/49/39/395207.
(136) *Plasma Kinetics in Atmospheric Gases*; Capitelli, M., Ed.; Springer series on atomic, optical, and plasma physics; Springer: Berlin ; New York, 2000.
(137) Billing, G. D. Vibration-Vibration and Vibration-Translation Energy Transfer, Including Multiquantum Transitions in Atom-Diatom and Diatom-Diatom Collisions. In *Nonequilibrium Vibrational Kinetics*; Capitelli, M., Ed.; Topics in Current Physics; Springer Berlin Heidelberg: Berlin, Heidelberg, 1986; Vol. 39, pp 85–112. https://doi.org/10.1007/978-3-642-48615-9_4.
(138) Schwartz, R. N.; Slawsky, Z. I.; Herzfeld, K. F. Calculation of Vibrational Relaxation Times in Gases. *J. Chem. Phys.* **1952**, *20* (10), 1591–1599. https://doi.org/10.1063/1.1700221.
(139) Rapp, D.; Englander-Golden, P. Resonant and Near-Resonant Vibrational—Vibrational Energy Transfer between Molecules in Collisions. *J. Chem. Phys.* **1964**, *40* (2), 573–575. https://doi.org/10.1063/1.1725158.

(140) Sharma, R. D.; Brau, C. A. Energy Transfer in Near-Resonant Molecular Collisions Due to Long-Range Forces with Application to Transfer of Vibrational Energy from ν_3 Mode of CO_2 to N_2. *J. Chem. Phys.* **1969**, *50* (2), 924–930. https://doi.org/10.1063/1.1671145.

(141) Treanor, C. E. Vibrational Energy Transfer in High-Energy Collisions. *J. Chem. Phys.* **1965**, *43* (2), 532–538. https://doi.org/10.1063/1.1696777.

(142) Zelechow, A.; Rapp, D.; Sharp, T. E. Vibrational–Vibrational–Translational Energy Transfer between Two Diatomic Molecules. *J. Chem. Phys.* **1968**, *49* (1), 286–299. https://doi.org/10.1063/1.1669823.

(143) Adamovich, I. V.; Macheret, S. O.; Rich, J. W.; Treanor, C. E. Vibrational Energy Transfer Rates Using a Forced Harmonic Oscillator Model. *J. Thermophys. Heat Transf.* **1998**, *12* (1), 57–65. https://doi.org/10.2514/2.6302.

(144) Pietanza, L. D.; Guaitella, O.; Aquilanti, V.; Armenise, I.; Bogaerts, A.; Capitelli, M.; Colonna, G.; Guerra, V.; Engeln, R.; Kustova, E.; Lombardi, A.; Palazzetti, F.; Silva, T. Advances in Non-Equilibrium CO_2 Plasma Kinetics: A Theoretical and Experimental Review. *Eur. Phys. J. D* **2021**, *75* (9), 237. https://doi.org/10.1140/epjd/s10053-021-00226-0.

(145) Lagan, A.; Lombardi, A.; Pirani, F.; Gamallo, P.; Say s, R.; Armenise, I.; Cacciatore, M.; Esposito, F.; Rutigliano, M. Molecular Physics of Elementary Processes Relevant to Hypersonics: Atom-Molecule, Molecule-Molecule and Atoms-Surface Processes. *Open Plasma Phys. J.* **2014**, *7* (1), 48–59. https://doi.org/10.2174/1876534301407010048.

(146) Lombardi, A.; Faginas-Lago, N.; Pacifici, L.; Grossi, G. Energy Transfer upon Collision of Selectively Excited CO_2 Molecules: State-to-State Cross Sections and Probabilities for Modeling of Atmospheres and Gaseous Flows. *J. Chem. Phys.* **2015**, *143* (3), 034307. https://doi.org/10.1063/1.4926880.

(147) Jeffers, W. Q.; Kelley, J. D. Calculations of V–V Transfer Probabilities in CO–CO Collisions. *J. Chem. Phys.* **1971**, *55* (9), 4433–4437. https://doi.org/10.1063/1.1676770.

(148) Pack, R. T. Analytic Estimation of Almost Resonant Molecular Energy Transfer Due to Multipolar Potentials. *V V* Processes Involving CO_2. *J. Chem. Phys.* **1980**, *72* (11), 6140–6152. https://doi.org/10.1063/1.439071.

(149) Lepoutre, F.; Louis, G.; Manceau, H. Collisional Relaxation in CO_2 between 180 K and 400 K Measured by the Spectrophone Method. *Chem. Phys. Lett.* **1977**, *48* (3), 509–514. https://doi.org/10.1016/0009-2614(77)85082-3.

(150) López-Puertas, M.; Rodrigo, R.; Molina, A.; Taylor, F. W. A Non-LTE Radiative Transfer Model for Infrared Bands in the Middle Atmosphere. I. Theoretical Basis and Application to CO_2 15 mm Bands. *J. Atmospheric Terr. Phys.* **1986**, *48* (8), 729–748. https://doi.org/10.1016/0021-9169(86)90022-X.

(151) Huetz-Aubert, M.; Lepoutre, F. An Optic-Acoustic Study of Thermal Vibrational Relaxation in CO_2 and in Mixtures of CO_2 with Monoatomic Gases. *Physica* **1974**, *78* (3), 435–456. https://doi.org/10.1016/0031-8914(74)90373-5.

(152) Lopez-puertas, M.; Taylor, F. W. *Non-Lte Radiative Transfer In The Atmosphere*; World Scientific Publishing Company, 2001.

(153) Terraz, L.; Silva, T.; Morillo-Candas, A.; Guaitella, O.; Tejero-del-Caz, A.; Alves, L. L.; Guerra, V. Influence of N_2 on the CO_2 Vibrational Distribution Function and Dissociation Yield in Non-Equilibrium Plasmas. *J. Phys. Appl. Phys.* **2019**, *53* (9), 094002. https://doi.org/10.1088/1361-6463/ab55fb.

(154) Morillo-Candas, A. S.; Klarenaar, B. L. M.; Amoedo, C.; Guerra, V.; Guaitella, O. Effect of Oxygen Atoms on the Vibrational Kinetics of CO_2 and CO Revealed by the Use of a Large Surface Area Material. *J. Phys. Appl. Phys.* **2021**, *54* (9), 095208. https://doi.org/10.1088/1361-6463/abc992.

(155) Popov, N. A. Pulsed Nanosecond Discharge in Air at High Specific Deposited Energy: Fast Gas Heating and Active Particle Production. *Plasma Sources Sci. Technol.* **2016**, *25* (4), 044003. https://doi.org/10.1088/0963-0252/25/4/044003.

(156) Zhu, Y.; Starikovskaia, S. Fast Gas Heating of Nanosecond Pulsed Surface Dielectric Barrier Discharge: Spatial Distribution and Fractional Contribution from Kinetics. *Plasma Sources Sci. Technol.* **2018**, *27* (12), 124007. https://doi.org/10.1088/1361-6595/aaf40d.

(157) Pokrovskiy, G. V.; Popov, N. A.; Starikovskaia, S. M. Fast Gas Heating and Kinetics of Electronically Excited States in a Nanosecond Capillary Discharge in CO_2. *Plasma Sources Sci. Technol.* **2022**, *31* (3), 035010. https://doi.org/10.1088/1361-6595/ac5102.

(158) Popov, N. A. Investigation of the Mechanism for Rapid Heating of Nitrogen and Air in Gas Discharges. *Plasma Phys. Rep.* **2001**, *27* (10), 886–896. https://doi.org/10.1134/1.1409722.

(159) Lowke, J. J.; Phelps, A. V.; Irwin, B. W. Predicted Electron Transport Coefficients and Operating Characteristics of CO_2–N_2–He Laser Mixtures. *J. Appl. Phys.* **1973**, *44* (10), 4664–4671. https://doi.org/10.1063/1.1662017.

(160) Polak, L. S.; Slovetsky, D. I. Electron Impact Induced Electronic Excitation and Molecular Dissociation. *Int. J. Radiat. Phys. Chem.* **1976**, *8* (1–2), 257–282. https://doi.org/10.1016/0020-7055(76)90070-X.

(161) Bogaerts, A.; Wang, W.; Berthelot, A.; Guerra, V. Modeling Plasma-Based CO_2 Conversion: Crucial Role of the Dissociation Cross Section. *Plasma Sources Sci. Technol.* **2016**, *25* (5), 055016. https://doi.org/10.1088/0963-0252/25/5/055016.

(162) Morillo-Candas, A. S.; Silva, T.; Klarenaar, B. L. M.; Grofulović, M.; Guerra, V.; Guaitella, O. Electron Impact Dissociation of CO_2. *Plasma Sources Sci. Technol.* **2020**, *29* (1), 01LT01. https://doi.org/10.1088/1361-6595/ab6075.

(163) Silva, A. F.; Morillo-Candás, A. S.; Tejero-del-Caz, A.; Alves, L. L.; Guaitella, O.; Guerra, V. A Reaction Mechanism for Vibrationally-Cold Low-Pressure CO_2 Plasmas. *Plasma Sources Sci. Technol.* **2020**, *29* (12), 125020. https://doi.org/10.1088/1361-6595/abc818.

(164) Silva, T.; Grofulović, M.; Terraz, L.; Pintassilgo, C. D.; Guerra, V. Dynamics of Gas Heating in the Afterglow of Pulsed CO_2 and CO_2–N_2 Glow Discharges at Low Pressure. *Plasma Chem. Plasma Process.* **2020**, *40* (3), 713–725. https://doi.org/10.1007/s11090-020-10061-7.

(165) Vesovic, V.; Wakeham, W. A.; Olchowy, G. A.; Sengers, J. V.; Watson, J. T. R.; Millat, J. The Transport Properties of Carbon Dioxide. *J. Phys. Chem. Ref. Data* **1990**, *19* (3), 763–808. https://doi.org/10.1063/1.555875.

(166) Vermeiren, V.; Bogaerts, A. Improving the Energy Efficiency of CO_2 Conversion in Nonequilibrium Plasmas through Pulsing. *J. Phys. Chem. C* **2019**, *123* (29), 17650–17665. https://doi.org/10.1021/acs.jpcc.9b02362.

(167) *NIST-JANAF Thermochemical Tables*, 4th ed.; Chase, M. W., National Institute of Standards and Technology (U.S.), Eds.; American Chemical Society ; American Institute of Physics for the National Institute of Standards and Technology: Washington, DC : New York, 1998.

(168) Moruzzi, J. L.; Price, D. A. Ionization, Attachment and Detachment in Air and Air-CO_2 Mixtures. *J. Phys. Appl. Phys.* **1974**, *7* (10), 1434–1440. https://doi.org/10.1088/0022-3727/7/10/317.

(169) Roznerski, W.; Leja, K. Electron Drift Velocity in Hydrogen, Nitrogen, Oxygen, Carbon Monoxide, Carbon Dioxide and Air at Moderate E/N. *J. Phys. Appl. Phys.* **1984**, *17* (2), 279–285. https://doi.org/10.1088/0022-3727/17/2/012.

(170) Damen, M. A.; Martini, L. M.; Engeln, R. Temperature Evolution in a Pulsed CO_2–N_2 Glow Discharge Measured Using Quantum Cascade Laser Absorption Spectroscopy. *Plasma Sources Sci. Technol.* **2020**, *29* (6), 065016. https://doi.org/10.1088/1361-6595/ab8e50.

(171) McEnaney, B. Active Sites in Relation to Gasification of Coal Chars. In *Fundamental Issues in Control of Carbon Gasification Reactivity*; Lahaye, J., Ehrburger, P., Eds.; Springer Netherlands: Dordrecht, 1991; pp 175–203. https://doi.org/10.1007/978-94-011-3310-4_10.

(172) Prata, K. S.; Schwartzentruber, T. E.; Minton, T. K. Air–Carbon Ablation Model for Hypersonic Flight from Molecular-Beam Data. *AIAA J.* **2022**, *60* (2), 627–640. https://doi.org/10.2514/1.J060516.

(173) Park, C. Effects of Atomic Oxygen on Graphite Ablation. *AIAA J.* **1976**, *14* (11), 1640–1642. https://doi.org/10.2514/3.7267.

(174) Zhluktov, S. V.; Abe, T. Viscous Shock-Layer Simulation of Airflow Past Ablating Blunt Body with Carbon Surface. *J. Thermophys. Heat Transf.* **1999**, *13* (1), 50–59. https://doi.org/10.2514/2.6400.

(175) Poovathingal, S.; Schwartzentruber, T. E.; Murray, V. J.; Minton, T. K.; Candler, G. V. Finite-Rate Oxidation Model for Carbon Surfaces from Molecular Beam Experiments. *AIAA J.* **2017**, *55* (5), 1644–1658. https://doi.org/10.2514/1.J055371.

(176) Lussow, R. O.; Vastola, F. J.; Walker, P. L. Kinetics of Oxygen Interaction with Graphon between 450 and 675°C. *Carbon* **1967**, *5* (6), 591–602. https://doi.org/10.1016/0008-6223(67)90039-5.

(177) Ahmed, S.; Back, M. H.; Roscoe, J. M. A Kinetic Model for the Low Temperature Oxidation of Carbon: I. *Combust. Flame* **1987**, *70* (1), 1–16. https://doi.org/10.1016/0010-2180(87)90155-6.

(178) Radovic, L. R. Active Sites in Graphene and the Mechanism of CO_2 Formation in Carbon Oxidation. *J. Am. Chem. Soc.* **2009**, *131* (47), 17166–17175. https://doi.org/10.1021/ja904731q.

(179) Radovic, L. R.; Suarez, A.; Vallejos-Burgos, F.; Sofo, J. O. Oxygen Migration on the Graphene Surface. 2. Thermochemistry of Basal-Plane Diffusion (Hopping). *Carbon* **2011**, *49* (13), 4226–4238. https://doi.org/10.1016/j.carbon.2011.05.037.

(180) Yang, K. L.; Yang, R. T. Absolute Rates of the Carbon-Carbon Dioxide Reaction. *AIChE J.* **1985**, *31* (8), 1313–1321. https://doi.org/10.1002/aic.690310810.

(181) Tremblay, G.; Vastola, F. J.; Walker, P. L. Thermal Desorption Analysis of Oxygen Surface Complexes on Carbon. *Carbon* **1978**, *16* (1), 35–39. https://doi.org/10.1016/0008-6223(78)90113-6.

(182) Montoya, A.; Truong, T.-T. T.; Mondragón, F.; Truong, T. N. CO Desorption from Oxygen Species on Carbonaceous Surface: 1. Effects of the Local Structure of the Active Site and the Surface Coverage. *J. Phys. Chem. A* **2001**, *105* (27), 6757–6764. https://doi.org/10.1021/jp010572l.

(183) Panerai, F.; Cochell, T.; Martin, A.; White, J. D. Experimental Measurements of the High-Temperature Oxidation of Carbon Fibers. *Int. J. Heat Mass Transf.* **2019**, *136*, 972–986. https://doi.org/10.1016/j.ijheatmasstransfer.2019.03.018.

(184) Panerai, F.; Ferguson, J. C.; Lachaud, J.; Martin, A.; Gasch, M. J.; Mansour, N. N. Micro-Tomography Based Analysis of Thermal Conductivity, Diffusivity and Oxidation Behavior of Rigid and Flexible Fibrous Insulators. *Int. J. Heat Mass Transf.* **2017**, *108*, 801–811. https://doi.org/10.1016/j.ijheatmasstransfer.2016.12.048.

(185) Jambunathan, R.; Levin, D. A.; Borner, A.; Ferguson, J. C.; Panerai, F. Prediction of Gas Transport Properties through Fibrous Carbon Preform Microstructures Using Direct Simulation Monte Carlo. *Int. J. Heat Mass Transf.* **2019**, *130*, 923–937. https://doi.org/10.1016/j.ijheatmasstransfer.2018.11.006.

(186) Nouri, N.; Panerai, F.; Tagavi, K. A.; Mansour, N. N.; Martin, A. Evaluation of the Anisotropic Radiative Conductivity of a Low-Density Carbon Fiber Material from Realistic Microscale Imaging. *Int. J. Heat Mass Transf.* **2016**, *95*, 535–539. https://doi.org/10.1016/j.ijheatmasstransfer.2015.12.004.

(187) Gusarov, A. V.; Poloni, E.; Shklover, V.; Sologubenko, A.; Leuthold, J.; White, S.; Lawson, J. Radiative Transfer in Porous Carbon-Fiber Materials for Thermal Protection Systems. *Int. J. Heat Mass Transf.* **2019**, *144*, 118582. https://doi.org/10.1016/j.ijheatmasstransfer.2019.118582.

(188) Ismail, I. M. K. Structure and Active Surface Area of Carbon Fibers. *Carbon* **1987**, *25* (5), 653–662. https://doi.org/10.1016/0008-6223(87)90219-3.

(189) Fukunaga, A.; Komami, T.; Ueda, S.; Nagumo, M. Plasma Treatment of Pitch-Based Ultra High Modulus Carbon Fibers. *Carbon* **1999**, *37* (7), 1087–1091. https://doi.org/10.1016/S0008-6223(98)00308-X.

(190) Hokazono, H.; Fujimoto, H. Theoretical Analysis of the CO_2 Molecule Decomposition and Contaminants Yield in Transversely Excited Atmospheric CO_2 Laser Discharge. *J. Appl. Phys.* **1987**, *62* (5), 1585–1594. https://doi.org/10.1063/1.339606.

(191) Beverly, R. E. Ion Aging Effects on the Dissociative-Attachment Instability in CO_2 Lasers. *Opt. Quantum Electron.* **1982**, *14* (6), 501–513. https://doi.org/10.1007/BF00610306.

(192) Beuthe, T. G.; Chang, J.-S. Chemical Kinetic Modelling of Non-Equilibrium Ar-CO_2 Thermal Plasmas. *Jpn. J. Appl. Phys.* **1997**, *36* (Part 1, No. 7B), 4997–5002. https://doi.org/10.1143/JJAP.36.4997.

(193) Mitchell, J. B. A.; Hus, H. The Dissociative Recombination and Excitation of CO^+. *J. Phys. B At. Mol. Phys.* **1985**, *18* (3), 547–555. https://doi.org/10.1088/0022-3700/18/3/029.

(194) McElroy, D.; Walsh, C.; Markwick, A. J.; Cordiner, M. A.; Smith, K.; Millar, T. J. The UMIST Database for Astrochemistry 2012. *Astron. Astrophys.* **2013**, *550*, A36. https://doi.org/10.1051/0004-6361/201220465.

(195) Thoenes, J.; Kurzius, S. C. *Plasma Chemistry Processes in the Closed Cycle EDL.*; ADA083222; 1979. https://apps.dtic.mil/sti/citations/ADA083222.

(196) Woodall, J.; Agúndez, M.; Markwick-Kemper, A. J.; Millar, T. J. The UMIST Database for Astrochemistry 2006. *Astron. Astrophys.* **2007**, *466* (3), 1197–1204. https://doi.org/10.1051/0004-6361:20064981.

(197) Fehsenfeld, F. C.; Schmeltekopf, A. L.; Schiff, H. I.; Ferguson, E. E. Laboratory Measurements of Negative Ion Reactions of Atmospheric Interest. *Planet. Space Sci.* **1967**, *15* (2), 373–379. https://doi.org/10.1016/0032-0633(67)90201-2.

(198) Albritton, D. L. Ion-Neutral Reaction-Rate Constants Measured in Flow Reactors through 1977. *At. Data Nucl. Data Tables* **1978**, *22* (1), 1–89. https://doi.org/10.1016/0092-640X(78)90027-X.

(199) Adams, N. G.; Smith, D.; Grief, D. Reactions of H_nCO^+ Ions with Molecules at 300 K. *Int. J. Mass Spectrom. Ion Phys.* **1978**, *26* (4), 405–415. https://doi.org/10.1016/0020-7381(78)80059-X.

(200) Gudmundsson, J. T.; Thorsteinsson, E. G. Oxygen Discharges Diluted with Argon: Dissociation Processes. *Plasma Sources Sci. Technol.* **2007**, *16* (2), 399–412. https://doi.org/10.1088/0963-0252/16/2/025.

(201) Eliasson, B.; Hirth, M.; Kogelschatz, U. Ozone Synthesis from Oxygen in Dielectric Barrier Discharges. *J. Phys. Appl. Phys.* **1987**, *20* (11), 1421–1437. https://doi.org/10.1088/0022-3727/20/11/010.

(202) Bortner, M. H.; Baurer, T. *Defense Nuclear Agency Reaction Rate Handbook, Second Edition*; AD0763699; 1972. https://apps.dtic.mil/sti/citations/AD0763699.

(203) Hasted, J. B.; Smith, R. A. The Detachment of Electrons from Negative Ions. *Proc. R. Soc. Lond. Ser. Math. Phys. Sci.* **1956**, *235* (1202), 349–353. https://doi.org/10.1098/rspa.1956.0087.

(204) Frommhold, L. Über verzögerte Elektronen in Elektronenlawinen, insbesondere in Sauerstoff und Luft, durch Bildung und Zerfall negativer Ionen (O^-). *Fortschritte Phys.* **1964**, *12* (11), 597–642. https://doi.org/10.1002/prop.19640121102.

(205) Pack, J. L.; Phelps, A. V. Electron Attachment and Detachment. I. Pure O_2 at Low Energy. *J. Chem. Phys.* **1966**, *44* (5), 1870–1883. https://doi.org/10.1063/1.1726956.

(206) Belostotsky, S. G.; Economou, D. J.; Lopaev, D. V.; Rakhimova, T. V. Negative Ion Destruction by $O(^3P)$ Atoms and $O_2(a^1\Delta_g)$ Molecules in an Oxygen Plasma. *Plasma Sources Sci. Technol.* **2005**, *14* (3), 532–542. https://doi.org/10.1088/0963-0252/14/3/016.

(207) McFarland, M.; Albritton, D. L.; Fehsenfeld, F. C.; Ferguson, E. E.; Schmeltekopf, A. L. Flow-drift Technique for Ion Mobility and Ion-molecule Reaction Rate Constant Measurements. III. Negative Ion Reactions of O^- with CO, NO, H_2 and D_2. *J. Chem. Phys.* **1973**, *59* (12), 6629–6635. https://doi.org/10.1063/1.1680043.

(208) Fehsenfeld, F. C.; Ferguson, E. E. Laboratory Studies of Negative Ion Reactions with Atmospheric Trace Constituents. *J. Chem. Phys.* **1974**, *61* (8), 3181–3193. https://doi.org/10.1063/1.1682474.

(209) Eremin, A.; Ziborov, V.; Shumova, V.; Voiki, D.; Roth, P. Formation of $O(^1D)$ Atoms in Thermal Decomposition of CO_2. *Kinet. Catal.* **1997**, *38*, 1–7.

(210) Baber, S. C.; Dean, A. M. Reaction of Atomic Oxygen with Carbon Dioxide behind Reflected Shock Waves. *J. Chem. Phys.* **1974**, *60* (1), 307–313. https://doi.org/10.1063/1.1680785.

(211) Cenian, A.; Chernukho, A.; Borodin, V. Modeling of Plasma-Chemical Reactions in Gas Mixture of CO_2 Lasers. II. Theoretical Model and Its Verification. *Contrib. Plasma Phys.* **1995**, *35* (3), 273–296. https://doi.org/10.1002/ctpp.2150350309.

(212) Tsang, W.; Hampson, R. F. Chemical Kinetic Data Base for Combustion Chemistry. Part I. Methane and Related Compounds. *J. Phys. Chem. Ref. Data* **1986**, *15* (3), 1087–1279. https://doi.org/10.1063/1.555759.

(213) Drummond, L. Shock-Initiated Exothermic Reactions. IV. The Oxidation of Carbon Monoxide. *Aust. J. Chem.* **1968**, *21* (11), 2631. https://doi.org/10.1071/CH9682631.

(214) Baldwin, R. R.; Jackson, D.; Melvin, A.; Rossiter, B. N. The Second Limit of Hydrogen + Carbon Monoxide + Oxygen Mixtures. *Int. J. Chem. Kinet.* **1972**, *4* (3), 277–292. https://doi.org/10.1002/kin.550040305.

(215) Dean, A. J.; Davidson, D. F.; Hanson, R. K. A Shock Tube Study of Reactions of Carbon Atoms with Hydrogen and Oxygen Using Excimer Photolysis of C_3O_2 and Carbon Atom Atomic Resonance Absorption Spectroscopy. *J. Phys. Chem.* **1991**, *95* (1), 183–191. https://doi.org/10.1021/j100154a037.

(216) Wysong, I. J. Measurement of Quenching Rates of $CO(a^3\Pi,v=0)$ Using Laser Pump-and-Probe Technique. *Chem. Phys. Lett.* **2000**, *329* (1–2), 42–46. https://doi.org/10.1016/S0009-2614(00)00967-2.

(217) Skrzypkowski, M. P.; Gougousi, T.; Johnsen, R.; Golde, M. F. Measurement of the Absolute Yield of $CO(a^3\Pi)+O$ Products in the Dissociative Recombination of CO_2^+ Ions with Electrons. *J. Chem. Phys.* **1998**, *108* (20), 8400–8407. https://doi.org/10.1063/1.476267.

(218) Tully, J. C. Reactions of $O(^1D)$ with Atmospheric Molecules. *J. Chem. Phys.* **1975**, *62* (5), 1893–1898. https://doi.org/10.1063/1.430675.

(219) Felder, W.; Morrow, W.; Young, R. A. $CO(a^3\Pi)$: Rate Coefficients for Quenching by $O(^3P)$. *Chem. Phys. Lett.* **1972**, *15* (1), 100–103. https://doi.org/10.1016/0009-2614(72)87026-X.

(220) Abreu, V. J.; Yee, J. H.; Solomon, S. C.; Dalgarno, A. The Quenching Rate of $O(^1D)$ by $O(^3P)$. *Planet. Space Sci.* **1986**, *34* (11), 1143–1145. https://doi.org/10.1016/0032-0633(86)90026-7.

(221) Dunlea, E. J.; Ravishankara, A. R. Kinetic Studies of the Reactions of O(^{1}D) with Several Atmospheric Molecules. *Phys. Chem. Chem. Phys.* **2004**, *6* (9), 2152. https://doi.org/10.1039/b400247d.

(222) Davidson, J. A.; Schiff, H. I.; Brown, T. J.; Howard, C. J. Temperature Dependence of the Deactivation of O(^{1}D) by CO from 113–333 K. *J. Chem. Phys.* **1978**, *69* (3), 1216. https://doi.org/10.1063/1.436657.

(223) Nunnally, T.; Gutsol, K.; Rabinovich, A.; Fridman, A.; Gutsol, A.; Kemoun, A. Dissociation of CO_2 in a Low Current Gliding Arc Plasmatron. *J. Phys. Appl. Phys.* **2011**, *44* (27), 274009. https://doi.org/10.1088/0022-3727/44/27/274009.

(224) Ramakers, M.; Trenchev, G.; Heijkers, S.; Wang, W.; Bogaerts, A. Gliding Arc Plasmatron: Providing an Alternative Method for Carbon Dioxide Conversion. *ChemSusChem* **2017**, *10* (12), 2642–2652. https://doi.org/10.1002/cssc.201700589.

(225) van de Steeg, A. W. *Insight into CO_2 Dissociation Kinetics in Microwave Plasma Using Laser Scattering*; Eindhoven University of Technology, 2022.

(226) Gutsol, A.; Chirokov, A.; Fridman, A.; Worek, W. Numerical Simulation of the Experimental ICP and Microwave Plasma Torches with the Reverse Vortex Stabilization. In *2nd International Conference on Computational Heat and Mass transfer*; Federal University of Rio de Janeiro, Brazil, 2001.

(227) D'Isa, F. A.; Carbone, E. A. D.; Hecimovic, A.; Fantz, U. Performance Analysis of a 2.45 GHz Microwave Plasma Torch for CO_2 Decomposition in Gas Swirl Configuration. *Plasma Sources Sci. Technol.* **2020**, *29* (10), 105009. https://doi.org/10.1088/1361-6595/abaa84.

(228) Viegas, P.; Vialetto, L.; van de Steeg, A. W.; Wolf, A. J.; Bongers, W. A.; van Rooij, G. J.; van de Sanden, M. C. M.; Diomede, P.; Peeters, F. J. J. Resolving Discharge Parameters from Atomic Oxygen Emission. *Plasma Sources Sci. Technol.* **2021**, *30* (6), 065022. https://doi.org/10.1088/1361-6595/ac04bd.

(229) Carbone, E.; D'Isa, F.; Hecimovic, A.; Fantz, U. Analysis of the C_2 (D3Πg−a3Πu) Swan Bands as a Thermometric Probe in CO_2 Microwave Plasmas. *Plasma Sources Sci. Technol.* **2020**, *29* (5), 055003. https://doi.org/10.1088/1361-6595/ab74b4.

(230) Mohsenian, S.; Sheth, S.; Bhatta, S.; Nagassou, D.; Sullivan, D.; Trelles, J. P. Design and Characterization of an Electromagnetic-resonant Cavity Microwave Plasma Reactor for Atmospheric Pressure Carbon Dioxide Decomposition. *Plasma Process. Polym.* **2019**, *16* (2), 1800153. https://doi.org/10.1002/ppap.201800153.

(231) Pachuilo, M.; Levko, D.; Raja, L. L.; Varghese, P. L. Experimental and Numerical Investigations of a Pulsed Nanosecond Streamer Discharge in CO_2. In *55th AIAA Aerospace Sciences Meeting*; American Institute of Aeronautics and Astronautics: Grapevine, Texas, 2017. https://doi.org/10.2514/6.2017-1968.

(232) Wolf, A. J.; Righart, T. W. H.; Peeters, F. J. J.; Groen, P. W. C.; van de Sanden, M. C. M.; Bongers, W. A. Characterization of CO_2 Microwave Plasma Based on the Phenomenon of Skin-Depth-Limited Contraction. *Plasma Sources Sci. Technol.* **2019**, *28* (11), 115022. https://doi.org/10.1088/1361-6595/ab4e61.

(233) Verreycken, T.; van Gessel, A. F. H.; Pageau, A.; Bruggeman, P. Validation of Gas Temperature Measurements by OES in an Atmospheric Air Glow Discharge with

Water Electrode Using Rayleigh Scattering. *Plasma Sources Sci. Technol.* **2011**, *20* (2), 024002. https://doi.org/10.1088/0963-0252/20/2/024002.

(234) van Gessel, A. F. H.; Carbone, E. A. D.; Bruggeman, P. J.; van der Mullen, J. J. A. M. Laser Scattering on an Atmospheric Pressure Plasma Jet: Disentangling Rayleigh, Raman and Thomson Scattering. *Plasma Sources Sci. Technol.* **2012**, *21* (1), 015003. https://doi.org/10.1088/0963-0252/21/1/015003.

(235) Wang, X.; Patel, A.; Shashurin, A. Combined Microwave and Laser Rayleigh Scattering Diagnostics for Pin-to-Pin Nanosecond Discharges. *J. Appl. Phys.* **2021**, *129* (18), 183302. https://doi.org/10.1063/5.0054202.

(236) Long, D. A. *Raman Spectroscopy*; McGraw-Hill: New York, 1977.

(237) van de Steeg, A. W.; Vialetto, L.; Silva, A. F.; Peeters, F. J. J.; van den Bekerom, D. C. M.; Gatti, N.; Diomede, P.; van de Sanden, M. C. M.; van Rooij, G. J. Revisiting Spontaneous Raman Scattering for Direct Oxygen Atom Quantification. *Opt. Lett.* **2021**, *46* (9), 2172. https://doi.org/10.1364/OL.424102.

(238) Grofulović, M.; Klarenaar, B. L. M.; Guaitella, O.; Guerra, V.; Engeln, R. A Rotational Raman Study under Non-Thermal Conditions in Pulsed CO_2–N_2 and CO_2–O_2 Glow Discharges. *Plasma Sources Sci. Technol.* **2019**, *28* (4), 045014. https://doi.org/10.1088/1361-6595/ab1240.

(239) Klarenaar, B. L. M.; Grofulović, M.; Morillo-Candas, A. S.; Bekerom, D. C. M. van den; Damen, M. A.; Sanden, M. C. M. van de; Guaitella, O.; Engeln, R. A Rotational Raman Study under Non-Thermal Conditions in a Pulsed CO_2 Glow Discharge. *Plasma Sources Sci. Technol.* **2018**, *27* (4), 045009. https://doi.org/10.1088/1361-6595/aabab6.

(240) Hummernbrum, F.; Kempkens, H.; Ruzicka, A.; Sauren, H.-D.; Schiffer, C.; Uhlenbusch, J.; Winter, J. Laser-Induced Fluorescence Measurements on the $C_2\Sigma+$–X_2II Transition of the CH Radical Produced by a Microwave Excited Process Plasma. *Plasma Sources Sci. Technol.* **1992**, *1* (4), 221–231. https://doi.org/10.1088/0963-0252/1/4/001.

(241) Doerk, T.; Jauernik, P.; Hädrich, S.; Pfelzer, B.; Uhlenbusch, J. Resonance Enhanced CARS Applied to the CH Radical. *Opt. Commun.* **1995**, *118* (5–6), 637–647. https://doi.org/10.1016/0030-4018(95)00304-Q.

(242) Doerk, T.; Hertl, M.; Pfelzer, B.; Hädrich, S.; Jauernik, P.; Uhlenbusch, J. Resonance Enhanced Coherent Anti-Stokes Raman Scattering and Laser Induced Fluorescence Applied to CH Radicals: A Comparative Study. *Appl. Phys. B Lasers Opt.* **1996**, *64* (1), 111–118. https://doi.org/10.1007/s003400050153.

(243) Hädrich, S.; Pfelzer, B.; Uhlenbusch, J. Coherent Anti-Stokes Raman Scattering Applied to Hydrocarbons in a Microwave Excited Process Plasma. *Plasma Chem. Plasma Process.* **1999**, *19* (1), 91–109. https://doi.org/10.1023/A:1021808000636.

(244) van den Bekerom, D.; Richards, C.; Huang, E.; Adamovich, I. V.; Frank, J. H. 2D Imaging of Absolute Methyl Concentrations in Nanosecond Pulsed Plasma by Photo-Fragmentation Laser-Induced Fluorescence. *Plasma Sources Sci. Technol.* **2022**. https://doi.org/10.1088/1361-6595/ac8f6c.

(245) Carbone, E.; Nijdam, S. Thomson Scattering on Non-Equilibrium Low Density Plasmas: Principles, Practice and Challenges. *Plasma Phys. Control. Fusion* **2015**, *57* (1), 014026. https://doi.org/10.1088/0741-3335/57/1/014026.

(246) van de Steeg, A. W.; Butterworth, T.; van den Bekerom, D. C. M.; Silva, A. F.; van de Sanden, M. C. M.; van Rooij, G. J. Plasma Activation of N_2 , CH_4 and CO_2 : An Assessment of the Vibrational Non-Equilibrium Time Window. *Plasma Sources Sci. Technol.* **2020**, *29* (11), 115001. https://doi.org/10.1088/1361-6595/abbae4.

(247) Espinho, S.; Hofmann, S.; Palomares, J. M.; Nijdam, S. The Influence of the Ar/O_2 Ratio on the Electron Density and Electron Temperature in Microwave Discharges. *Plasma Sources Sci. Technol.* **2017**, *26* (10), 105008. https://doi.org/10.1088/1361-6595/aa8d04.

(248) Klarenaar, B. L. M.; Guaitella, O.; Engeln, R.; Sobota, A. How Dielectric, Metallic and Liquid Targets Influence the Evolution of Electron Properties in a Pulsed He Jet Measured by Thomson and Raman Scattering. *Plasma Sources Sci. Technol.* **2018**, *27* (8), 085004. https://doi.org/10.1088/1361-6595/aad4d7.

(249) Pinhão, N.; Moura, A.; Branco, J. B.; Neves, J. Influence of Gas Expansion on Process Parameters in Non-Thermal Plasma Plug-Flow Reactors: A Study Applied to Dry Reforming of Methane. *Int. J. Hydrog. Energy* **2016**, *41* (22), 9245–9255. https://doi.org/10.1016/j.ijhydene.2016.04.148.

(250) Simpson, C. J. S. M.; Bridgman, K. B.; Chandler, T. R. D. Shock-Tube Study of Vibrational Relaxation in Carbon Dioxide. *J. Chem. Phys.* **1968**, *49* (2), 513–522. https://doi.org/10.1063/1.1670105.

(251) Silva, T.; Morillo-Candas, A. S.; Guaitella, O.; Guerra, V. Modeling the Time Evolution of the Dissociation Fraction in Low-Pressure CO_2 Plasmas. *J. CO2 Util.* **2021**, *53*, 101719. https://doi.org/10.1016/j.jcou.2021.101719.

(252) Kotov, V.; Koelman, P. M. J. Plug Flow Reactor Model of the Plasma Chemical Conversion of CO_2. *Plasma Sources Sci. Technol.* **2019**, *28* (9), 095002. https://doi.org/10.1088/1361-6595/ab3774.

(253) Isola, L. M.; Gómez, B. J.; Guerra, V. Determination of the Electron Temperature and Density in the Negative Glow of a Nitrogen Pulsed Discharge Using Optical Emission Spectroscopy. *J. Phys. Appl. Phys.* **2010**, *43* (1), 015202. https://doi.org/10.1088/0022-3727/43/1/015202.

(254) Booth, J. P.; Guaitella, O.; Chatterjee, A.; Drag, C.; Guerra, V.; Lopaev, D.; Zyryanov, S.; Rakhimova, T.; Voloshin, D.; Mankelevich, Y. Oxygen (^{3}P) Atom Recombination on a Pyrex Surface in an O_2 Plasma. *Plasma Sources Sci. Technol.* **2019**, *28* (5), 055005. https://doi.org/10.1088/1361-6595/ab13e8.

(255) da Silva, M. L.; Guerra, V.; Loureiro, J. Two-Temperature Models for Nitrogen Dissociation. *Chem. Phys.* **2007**, *342* (1–3), 275–287. https://doi.org/10.1016/j.chemphys.2007.10.010.

(256) Kosareva, A.; Kunova, O.; Kustova, E.; Nagnibeda, E. Hybrid Approach to Accurate Modeling of Coupled Vibrational-Chemical Kinetics in Carbon Dioxide. *Phys. Fluids* **2022**, *34* (2), 026105. https://doi.org/10.1063/5.0079664.

(257) Pintassilgo, C. D.; Guerra, V. Power Transfer to Gas Heating in Pure N_2 and in N_2–O_2 Plasmas. *J. Phys. Chem. C* **2016**, *120* (38), 21184–21201. https://doi.org/10.1021/acs.jpcc.6b05463.

(258) Kelly, S.; van de Steeg, A.; Hughes, A.; van Rooij, G.; Bogaerts, A. Thermal Instability and Volume Contraction in a Pulsed Microwave N_2 Plasma at Sub-Atmospheric Pressure. *Plasma Sources Sci. Technol.* **2021**, *30* (5), 055005. https://doi.org/10.1088/1361-6595/abf1d6.

(259) Popov, N. A.; Starikovskaia, S. M. Relaxation of Electronic Excitation in Nitrogen/Oxygen and Fuel/Air Mixtures: Fast Gas Heating in Plasma-Assisted Ignition and Flame Stabilization. *Prog. Energy Combust. Sci.* **2022**, 100928. https://doi.org/10.1016/j.pecs.2021.100928.

(260) Britun, N.; Silva, T.; Chen, G.; Godfroid, T.; van der Mullen, J.; Snyders, R. Plasma-Assisted CO_2 Conversion: Optimizing Performance via Microwave Power Modulation. *J. Phys. Appl. Phys.* **2018**, *51* (14), 144002. https://doi.org/10.1088/1361-6463/aab1ad.

(261) Kozák, T.; Bogaerts, A. Evaluation of the Energy Efficiency of CO_2 Conversion in Microwave Discharges Using a Reaction Kinetics Model. *Plasma Sources Sci. Technol.* **2014**, *24* (1), 015024. https://doi.org/10.1088/0963-0252/24/1/015024.

(262) Berthelot, A.; Bogaerts, A. Modeling of CO_2 Plasma: Effect of Uncertainties in the Plasma Chemistry. *Plasma Sources Sci. Technol.* **2017**, *26* (11), 115002. https://doi.org/10.1088/1361-6595/aa8ffb.

(263) Armenise, I.; Kustova, E. Mechanisms of Coupled Vibrational Relaxation and Dissociation in Carbon Dioxide. *J. Phys. Chem. A* **2018**, *122* (23), 5107–5120. https://doi.org/10.1021/acs.jpca.8b03266.

(264) Alves, L. L.; Bogaerts, A.; Guerra, V.; Turner, M. M. Foundations of Modelling of Nonequilibrium Low-Temperature Plasmas. *Plasma Sources Sci. Technol.* **2018**, *27* (2), 023002. https://doi.org/10.1088/1361-6595/aaa86d.

(265) Bermúdez, J. M.; Ruisánchez, E.; Arenillas, A.; Moreno, A. H.; Menéndez, J. A. New Concept for Energy Storage: Microwave-Induced Carbon Gasification with CO_2. *Energy Convers. Manag.* **2014**, *78*, 559–564. https://doi.org/10.1016/j.enconman.2013.11.021.

(266) Snoeckx, R.; Heijkers, S.; Van Wesenbeeck, K.; Lenaerts, S.; Bogaerts, A. CO_2 Conversion in a Dielectric Barrier Discharge Plasma: N_2 in the Mix as a Helping Hand or Problematic Impurity? *Energy Environ. Sci.* **2016**, *9* (3), 999–1011. https://doi.org/10.1039/C5EE03304G.

(267) Mermoud, F.; Golfier, F.; Salvador, S.; Steene, L. V. de; Dirion, J. L. Experimental and Numerical Study of Steam Gasification of a Single Charcoal Particle. *Combust. Flame* **2006**, *145* (1), 59–79. https://doi.org/10.1016/j.combustflame.2005.12.004.

(268) Ferrari, A.; Hunt, J.; Lita, A.; Ashley, B.; Stiegman, A. E. Microwave-Specific Effects on the Equilibrium Constants and Thermodynamics of the Steam–Carbon and Related Reactions. *J. Phys. Chem. C* **2014**, *118* (18), 9346–9356. https://doi.org/10.1021/jp501206n.

(269) Boehm, H. P. Surface Oxides on Carbon and Their Analysis: A Critical Assessment. *Carbon* **2002**, *40* (2), 145–149. https://doi.org/10.1016/S0008-6223(01)00165-8.

(270) Dias Junior, A. F.; Esteves, R. P.; da Silva, Á. M.; Sousa Júnior, A. D.; Oliveira, M. P.; Brito, J. O.; Napoli, A.; Braga, B. M. Investigating the Pyrolysis Temperature to Define the Use of Charcoal. *Eur. J. Wood Wood Prod.* **2020**, *78* (1), 193–204. https://doi.org/10.1007/s00107-019-01489-6.

(271) Hecht, E. S.; Shaddix, C. R.; Molina, A.; Haynes, B. S. Effect of CO_2 Gasification Reaction on Oxy-Combustion of Pulverized Coal Char. *Proc. Combust. Inst.* **2011**, *33* (2), 1699–1706. https://doi.org/10.1016/j.proci.2010.07.087.

(272) Sánchez, A.; Mondragón, F. Role of the Epoxy Group in the Heterogeneous CO_2 Evolution in Carbon Oxidation Reactions. *J. Phys. Chem. C* **2007**, *111* (2), 612–617. https://doi.org/10.1021/jp065701i.

(273) Hecht, E. S.; Shaddix, C. R.; Lighty, J. S. Analysis of the Errors Associated with Typical Pulverized Coal Char Combustion Modeling Assumptions for Oxy-Fuel Combustion. *Combust. Flame* **2013**, *160* (8), 1499–1509. https://doi.org/10.1016/j.combustflame.2013.02.015.

(274) Palacio, K.; Sanchez, A.; Espinal, J. F. Thermodynamic Evaluation of Carbon Dioxide Gasification Reactions at Oxy-Combustion Conditions. *Combust. Sci. Technol.* **2018**, *190* (9), 1515–1527. https://doi.org/10.1080/00102202.2018.1454916.

(275) Chen, W.-H.; Hsu, C.-L.; Du, S.-W. Thermodynamic Analysis of the Partial Oxidation of Coke Oven Gas for Indirect Reduction of Iron Oxides in a Blast Furnace. *Energy* **2015**, *86*, 758–771. https://doi.org/10.1016/j.energy.2015.04.087.

(276) Dryer, F. L.; Glassman, I. High-Temperature Oxidation of CO and CH_4. *Symp. Int. Combust.* **1973**, *14* (1), 987–1003. https://doi.org/10.1016/S0082-0784(73)80090-6.

(277) Indarto, A.; Choi, J.; Lee, H.; Song, H. Effect of Additive Gases on Methane Conversion Using Gliding Arc Discharge. *Energy* **2006**, *31* (14), 2986–2995. https://doi.org/10.1016/j.energy.2005.10.034.

(278) Wolf, A. J.; Righart, T. W. H.; Peeters, F. J. J.; Bongers, W. A.; van de Sanden, M. C. M. Implications of Thermo-Chemical Instability on the Contracted Modes in CO_2 Microwave Plasmas. *Plasma Sources Sci. Technol.* **2020**, *29* (2), 025005. https://doi.org/10.1088/1361-6595/ab5eca.

(279) Snirer, M.; Toman, J.; Kudrle, V.; Jašek, O. Stable Filamentary Structures in Atmospheric Pressure Microwave Plasma Torch. *Plasma Sources Sci. Technol.* **2021**, *30* (9), 095009. https://doi.org/10.1088/1361-6595/ac1ee0.

(280) Golubovskii, Y. B.; Nekuchaev, V.; Gorchakov, S.; Uhrlandt, D. Contraction of the Positive Column of Discharges in Noble Gases. *Plasma Sources Sci. Technol.* **2011**, *20* (5), 053002. https://doi.org/10.1088/0963-0252/20/5/053002.

(281) Golubovskii, Y. B.; Siasko, A. V.; Nekuchaev, V. O. Peculiarities of Glow Discharge Constriction in Helium. *Plasma Sources Sci. Technol.* **2020**, *29* (6), 065020. https://doi.org/10.1088/1361-6595/ab8fbc.

(282) Hubert, J.; Moisan, M.; Ricard, A. A New Microwave Plasma at Atmospheric Pressure. *Spectrochim. Acta Part B At. Spectrosc.* **1979**, *34* (1), 1–10. https://doi.org/10.1016/0584-8547(79)80016-6.

(283) Gore, J. P. P.; Mahoney, E. J. D.; Smith, J. A.; Ashfold, M. N. R.; Mankelevich, Y. A. Imaging and Modeling C_2 Radical Emissions from Microwave Plasma-Activated

Methane/Hydrogen Gas Mixtures: Contributions from Chemiluminescent Reactions and Investigations of Higher-Pressure Effects and Plasma Constriction. *J. Phys. Chem. A* **2021**, *125* (19), 4184–4199. https://doi.org/10.1021/acs.jpca.1c01924.

(284) Petrov, G. M.; Ferreira, C. M. Numerical Modeling of the Constriction of the Dc Positive Column in Rare Gases. *Phys. Rev. E* **1999**, *59* (3), 3571–3582. https://doi.org/10.1103/PhysRevE.59.3571.

(285) van der Mullen, J. J. A. M.; van de Sande, M. J.; de Vries, N.; Broks, B.; Iordanova, E.; Gamero, A.; Torres, J.; Sola, A. Single-Shot Thomson Scattering on Argon Plasmas Created by the Microwave Plasma Torch; Evidence for a New Plasma Class. *Spectrochim. Acta Part B At. Spectrosc.* **2007**, *62* (10), 1135–1146. https://doi.org/10.1016/j.sab.2007.07.006.

(286) Hait, V. D. Theory of thermal contraction of the current at the anode in a turbulent-flow of thermal plasma. *TVT* **1986**, *24* (2), 209–217.

(287) Eckert, E. R. G.; Goldstein, R. J.; Pfender, E.; Ibele, W. E.; Patankar, S. V.; Ramsey, J. W.; Simon, T. W.; Decker, N. A.; Kuehn, T. H.; Lee, H. O.; Girshick, S. L. Heat Transfer—a Review of 1986 Literature. *Int. J. Heat Mass Transf.* **1987**, *30* (12), 2449–2523. https://doi.org/10.1016/0017-9310(87)90132-3.

(288) Poritskii, P. V. Thermal Contraction of Arc Discharge in Mixtures of Inert Gases: Special Features. *High Temp.* **2006**, *44* (3), 328–335. https://doi.org/10.1007/s10740-006-0042-y.

(289) Kabouzi, Y.; Calzada, M. D.; Moisan, M.; Tran, K. C.; Trassy, C. Radial Contraction of Microwave-Sustained Plasma Columns at Atmospheric Pressure. *J. Appl. Phys.* **2002**, *91* (3), 1008–1019. https://doi.org/10.1063/1.1425078.

(290) Wang, W.; Berthelot, A.; Kolev, S.; Tu, X.; Bogaerts, A. CO_2 Conversion in a Gliding Arc Plasma: 1D Cylindrical Discharge Model. *Plasma Sources Sci. Technol.* **2016**, *25* (6), 065012. https://doi.org/10.1088/0963-0252/25/6/065012.

(291) Böddeker, S.; Bracht, V.; Hermanns, P.; Gröger, S.; Kogelheide, F.; Bibinov, N.; Awakowicz, P. Anode Spots of Low Current Gliding Arc Plasmatron. *Plasma Sources Sci. Technol.* **2020**, *29* (8), 08LT01. https://doi.org/10.1088/1361-6595/aba6a4.

(292) Staack, D.; Farouk, B.; Gutsol, A.; Fridman, A. DC Normal Glow Discharges in Atmospheric Pressure Atomic and Molecular Gases. *Plasma Sources Sci. Technol.* **2008**, *17* (2), 025013. https://doi.org/10.1088/0963-0252/17/2/025013.

(293) Akishev, Y.; Grushin, M.; Karalnik, V.; Petryakov, A.; Trushkin, N. On Basic Processes Sustaining Constricted Glow Discharge in Longitudinal N_2 Flow at Atmospheric Pressure. *J. Phys. Appl. Phys.* **2010**, *43* (21), 215202. https://doi.org/10.1088/0022-3727/43/21/215202.

(294) Hofmann, S.; van Gessel, A. F. H.; Verreycken, T.; Bruggeman, P. Power Dissipation, Gas Temperatures and Electron Densities of Cold Atmospheric Pressure Helium and Argon RF Plasma Jets. *Plasma Sources Sci. Technol.* **2011**, *20* (6), 065010. https://doi.org/10.1088/0963-0252/20/6/065010.

(295) Seo, B. H.; Kim, D. W.; Kim, J. H.; You, S. J. Two-Dimensional Profile Measurement of Plasma Parameters in Radio Frequency-Driven Argon Atmospheric Pressure Plasma Jet. *Phys. Plasmas* **2015**, *22* (9), 093510. https://doi.org/10.1063/1.4931046.

(296) Massey, J. T.; Cannon, S. M. Constricted Discharges in the Rare Gases. I. Spectroscopic and Electrical Measurements. *J. Appl. Phys.* **1965**, *36* (2), 361–372. https://doi.org/10.1063/1.1713996.

(297) Massey, J. T. Constricted Discharges in the Rare Gases. II. Analysis of the Macroscopic Properties of the Discharge. *J. Appl. Phys.* **1965**, *36* (2), 373–380. https://doi.org/10.1063/1.1713997.

(298) Toader, E. I. On the Constricted Neon Positive Column. *J. Phys. Appl. Phys.* **1995**, *28* (1), 75–80. https://doi.org/10.1088/0022-3727/28/1/013.

(299) Castaños-Martínez, E.; Moisan, M.; Kabouzi, Y. Achieving Non-Contracted and Non-Filamentary Rare-Gas Tubular Discharges at Atmospheric Pressure. *J. Phys. Appl. Phys.* **2009**, *42* (1), 012003. https://doi.org/10.1088/0022-3727/42/1/012003.

(300) Cardoso, R. P.; Belmonte, T.; Noël, C.; Kosior, F.; Henrion, G. Filamentation in Argon Microwave Plasma at Atmospheric Pressure. *J. Appl. Phys.* **2009**, *105* (9), 093306. https://doi.org/10.1063/1.3125525.

(301) Ridenti, M. A.; de Amorim, J.; Dal Pino, A.; Guerra, V.; Petrov, G. Causes of Plasma Column Contraction in Surface-Wave-Driven Discharges in Argon at Atmospheric Pressure. *Phys. Rev. E* **2018**, *97* (1), 013201. https://doi.org/10.1103/PhysRevE.97.013201.

(302) Moisan, M.; Pelletier, J. *Physics of Collisional Plasmas*; Springer Netherlands: Dordrecht, 2012. https://doi.org/10.1007/978-94-007-4558-2.

(303) Smirnov, S. A.; Baranov, G. A. Gas Dynamics and Thermal-Ionization Instability of the Cathode Region of a Glow Discharge. Part I. *Tech. Phys.* **2001**, *46* (7), 815–824. https://doi.org/10.1134/1.1387540.

(304) Bychkov, V. L.; Grachev, L. P.; Isakov, I. I. Thermal Ionization Instability of an Air Discharge Plasma in a Microwave Field. *Tech. Phys.* **2007**, *52* (3), 289–295. https://doi.org/10.1134/S1063784207030012.

(305) Fridman, A. A.; Kennedy, L. A. *Plasma Physics and Engineering*; Taylor & Francis: New York, 2004.

(306) Akishev, Y.; Grushin, M.; Karalnik, V.; Kochetov, I.; Napartovich, A.; Trushkin, N. Generation of Atmospheric Pressure Non-Thermal Plasma by Diffusive and Constricted Discharges in Air and Nitrogen at the Rest and Flow. *J. Phys. Conf. Ser.* **2010**, *257*, 012014. https://doi.org/10.1088/1742-6596/257/1/012014.

(307) Shneider, M. N.; Mokrov, M. S.; Milikh, G. M. Dynamic Contraction of the Positive Column of a Self-Sustained Glow Discharge in Molecular Gas. *Phys. Plasmas* **2012**, *19* (3), 033512. https://doi.org/10.1063/1.3694913.

(308) Shneider, M. N.; Mokrov, M. S.; Milikh, G. M. Dynamic Contraction of the Positive Column of a Self-Sustained Glow Discharge in Air Flow. *Phys. Plasmas* **2014**, *21* (3), 032122. https://doi.org/10.1063/1.4869332.

(309) Vialetto, L.; van de Steeg, A.; Viegas, P.; Longo, S.; Van Rooij, G. J.; Van de Sanden, R.; van Dijk, J.; Diomede, P. Charged Particle Kinetics and Gas Heating in CO_2 Microwave Plasma Contraction: Comparisons of Simulations and Experiments. *Plasma Sources Sci. Technol.* **2022**. https://doi.org/10.1088/1361-6595/ac56c5.

(310) Viegas, P.; Vialetto, L.; Wolf, A. J.; Peeters, F. J. J.; Groen, P. W. C.; Righart, T. W. H.; Bongers, W. A.; van de Sanden, M. C. M.; Diomede, P. Insight into Contraction

Dynamics of Microwave Plasmas for CO_2 Conversion from Plasma Chemistry Modelling. *Plasma Sources Sci. Technol.* **2020**, *29* (10), 105014. https://doi.org/10.1088/1361-6595/abb41c.

(311) Zhong, H.; Shneider, M. N.; Mao, X.; Ju, Y. Dynamics and Chemical Mode Analysis of Plasma Thermal-Chemical Instability. *Plasma Sources Sci. Technol.* **2021**, *30* (3), 035002. https://doi.org/10.1088/1361-6595/abde1c.

(312) Zhong, H.; Shneider, M. N.; Mokrov, M. S.; Ju, Y. Thermal-Chemical Instability of Weakly Ionized Plasma in a Reactive Flow. *J. Phys. Appl. Phys.* **2019**, *52* (48), 484001. https://doi.org/10.1088/1361-6463/ab3d69.

(313) Wnukowski, M.; van de Steeg, A. W.; Hrycak, B.; Jasiński, M.; van Rooij, G. J. Influence of Hydrogen Addition on Methane Coupling in a Moderate Pressure Microwave Plasma. *Fuel* **2021**, *288*, 119674. https://doi.org/10.1016/j.fuel.2020.119674.

(314) Magin, T.; Degrez, G.; Sokolova, I. Thermodynamic and Transport Properties of Martian Atmosphere for Space Entry Application. In *33rd Plasmadynamics and Lasers Conference*; American Institute of Aeronautics and Astronautics: Maui, Hawaii, 2002. https://doi.org/10.2514/6.2002-2226.

(315) COMSOL Multiphysics. Chemical Reaction Engineering Module. https://doc.comsol.com/5.4/doc/com.comsol.help.chem/ChemicalReactionEngineeringModuleUsersGuide.pdf (accessed 2022-09-30).

(316) Sanford, G.; McBride, B. J. *Computer Program for Calculation of Complex Chemical Equilibrium Compositions and Applications. Part 1: Analysis*; NASA Reference Publication (RP) 19950013764; NASA Lewis Research Center Cleveland, OH, United States. https://ntrs.nasa.gov/citations/19950013764 (accessed 2022-09-30).

(317) McBride, B. J.; Zehe, M. J.; Sanford, G. NASA Glenn Coefficients for Calculating Thermodynamic Properties of Individual Species., 2002. https://ntrs.nasa.gov/citations/20020085330.

(318) Butler, J. N.; Brokaw, R. S. Thermal Conductivity of Gas Mixtures in Chemical Equilibrium. *J. Chem. Phys.* **1957**, *26* (6), 1636–1643. https://doi.org/10.1063/1.1743596.

(319) Stiel, L. I.; Thodos, G. The Viscosity of Polar Substances in the Dense Gaseous and Liquid Regions. *AIChE J.* **1964**, *10* (2), 275–277. https://doi.org/10.1002/aic.690100229.

(320) Brokaw, R. S. Predicting Transport Properties of Dilute Gases. *Ind. Eng. Chem. Process Des. Dev.* **1969**, *8* (2), 240–253. https://doi.org/10.1021/i260030a015.

(321) Neufeld, P. D.; Janzen, A. R.; Aziz, R. A. Empirical Equations to Calculate 16 of the Transport Collision Integrals $\Omega^{(l,s)*}$ for the Lennard-Jones (12–6) Potential. *J. Chem. Phys.* **1972**, *57* (3), 1100–1102. https://doi.org/10.1063/1.1678363.

(322) Basco, N.; Norrish, R. G. W. VIBRATIONAL DISEQUILIBRIUM IN REACTIONS BETWEEN ATOMS AND MOLECULES. *Can. J. Chem.* **1960**, *38* (10), 1769–1779. https://doi.org/10.1139/v60-242.

(323) Mori, T.; Kanou, K.; Mizuta, K.; Kuramasu, T.; Ishikawa, Y.; Arai, S. Reactions of Highly Excited Oxygen Atoms $O(2p^3 3s,{}^5S)$ with Simple Gas Molecules. *J. Chem. Phys.* **1992**, *97* (12), 9094–9098. https://doi.org/10.1063/1.463336.

(324) Mohanta, A.; Lanfant, B.; Asfaha, M.; Leparoux, M. Optical Emission Spectroscopic Study of Ar/H_2/CH_4 Plasma during the Production of Graphene Nano-Flakes by Induction Plasma Synthesis. *J. Phys. Conf. Ser.* **2017**, *825*, 012010. https://doi.org/10.1088/1742-6596/825/1/012010.

(325) Bolshakov, A. P.; Ralchenko, V. G.; Yurov, V. Y.; Popovich, A. F.; Antonova, I. A.; Khomich, A. A.; Ashkinazi, E. E.; Ryzhkov, S. G.; Vlasov, A. V.; Khomich, A. V. High-Rate Growth of Single Crystal Diamond in Microwave Plasma in CH_4/H_2 and CH_4/H_2/Ar Gas Mixtures in Presence of Intensive Soot Formation. *Diam. Relat. Mater.* **2016**, *62*, 49–57. https://doi.org/10.1016/j.diamond.2015.12.001.

(326) Elliott, M. A.; May, P. W.; Petherbridge, J.; Leeds, S. M.; Ashfold, M. N. R.; Wang, W. N. Optical Emission Spectroscopic Studies of Microwave Enhanced Diamond CVD Using CH_4/CO_2 Plasmas. *Diam. Relat. Mater.* **2000**, *9* (3–6), 311–316. https://doi.org/10.1016/S0925-9635(99)00196-X.

(327) Yoshikawa, M.; Yaguchi, F.; Miyata, Y.; Morimoto, M.; Shima, Y.; Nakashima, Y.; Ichimura, M.; Imai, T.; Yamada, I.; Kawahata, K.; Funaba, H.; Yasuhara, R.; Narihara, K.; Minami, T.; Lee, J. H. Radial Electron Temperature Measurements by Using Newly Installed Thomson Scattering System in GAMMA 10. *J. Instrum.* **2012**, *7* (03), C03003–C03003. https://doi.org/10.1088/1748-0221/7/03/C03003.

(328) Gong, M.; Bao, Y.; Urdahl, R. S.; Jackson, W. M. LIF Measurements of Radiative Lifetimes of the C_2(B’1Σ+g) State. *Chem. Phys. Lett.* **1994**, *217* (3), 210–215. https://doi.org/10.1016/0009-2614(93)E1374-P.

(329) Oliver, J.; Bharadwaj, N.; Sizyuk, T. Laser-Induced Fluorescence of C_2 and C_3 in Colliding Carbon Plasma. *J. Appl. Phys.* **2019**, *125* (7), 073301. https://doi.org/10.1063/1.5078641.

(330) van den Bekerom, D. C. M.; Palomares Linares, J. M.; van Veldhuizen, E. M.; Nijdam, S.; van de Sanden, M. C. M.; van Rooij, G. J. How the Alternating Degeneracy in Rotational Raman Spectra of CO_2 and C_2H_2 Reveals the Vibrational Temperature. *Appl. Opt.* **2018**, *57* (20), 5694. https://doi.org/10.1364/AO.57.005694.

(331) Minea, T.; van den Bekerom, D. C. M.; Peeters, F. J. J.; Zoethout, E.; Graswinckel, M. F.; van de Sanden, M. C. M.; Cents, T.; Lefferts, L.; van Rooij, G. J. Non-Oxidative Methane Coupling to C_2 Hydrocarbons in a Microwave Plasma Reactor. *Plasma Process. Polym.* **2018**, *15* (11), 1800087. https://doi.org/10.1002/ppap.201800087.

(332) Castaños Martinez, E.; Kabouzi, Y.; Makasheva, K.; Moisan, M. Modeling of Microwave-Sustained Plasmas at Atmospheric Pressure with Application to Discharge Contraction. *Phys. Rev. E* **2004**, *70* (6), 066405. https://doi.org/10.1103/PhysRevE.70.066405.

(333) Niu, C.; Chen, Z.; Rong, M.; Wang, C.; Wu, Y.; Yang, F.; Wang, X.; Pang, Q. Calculation of 2-Temperature Plasma Thermo-Physical Properties Considering Condensed Phases: Application to CO_2–CH_4 Plasma: Part 2. Transport Coefficients. *J. Phys. Appl. Phys.* **2016**, *49* (40), 405204. https://doi.org/10.1088/0022-3727/49/40/405204.

(334) Aubreton, J.; Elchinger, M.-F.; Hacala, A.; Michon, U. Transport Coefficients of Typical Biomass Equimolar CO–H_2 Plasma. *J. Phys. Appl. Phys.* **2009**, *42* (9), 095206. https://doi.org/10.1088/0022-3727/42/9/095206.

(335) Yang, A.; Liu, Y.; Sun, B.; Wang, X.; Cressault, Y.; Zhong, L.; Rong, M.; Wu, Y.; Niu, C. Thermodynamic Properties and Transport Coefficients of High-Temperature CO_2 Thermal Plasmas Mixed with C_2F_4. *J. Phys. Appl. Phys.* **2015**, *48* (49), 495202. https://doi.org/10.1088/0022-3727/48/49/495202.

(336) Blanksby, S. J.; Ellison, G. B. Bond Dissociation Energies of Organic Molecules. *Acc. Chem. Res.* **2003**, *36* (4), 255–263. https://doi.org/10.1021/ar020230d.

(337) Hagstrum, H. D. On the Dissociation Energy of Carbon Monoxide and the Heat of Sublimation of Carbon. *Phys. Rev.* **1947**, *72* (10), 947–963. https://doi.org/10.1103/PhysRev.72.947.

(338) Prevosto, L.; Kelly, H.; Mancinelli, B. Modelling of an Atmospheric Pressure Nitrogen Glow Discharge Operating in High-Gas Temperature Regimes. *Plasma Chem. Plasma Process.* **2016**, *36* (4), 973–992. https://doi.org/10.1007/s11090-016-9716-3.

(339) Henrici-Olivé, G.; Olivé, S. The Fischer-Tropsch Synthesis: Molecular Weight Distribution of Primary Products and Reaction Mechanism. *Angew. Chem. Int. Ed. Engl.* **1976**, *15* (3), 136–141. https://doi.org/10.1002/anie.197601361.

(340) Bos, M. J.; Kersten, S. R. A.; Brilman, D. W. F. Wind Power to Methanol: Renewable Methanol Production Using Electricity, Electrolysis of Water and CO_2 Air Capture. *Appl. Energy* **2020**, *264*, 114672. https://doi.org/10.1016/j.apenergy.2020.114672.

(341) Ma, J.; Fang, M.; Li, P.; Zhu, B.; Lu, X.; Lau, N. T. Microwave-Assisted Catalytic Combustion of Diesel Soot. *Appl. Catal. Gen.* **1997**, *159* (1–2), 211–228. https://doi.org/10.1016/S0926-860X(97)00043-4.

(342) Menéndez, J. A.; Arenillas, A.; Fidalgo, B.; Fernández, Y.; Zubizarreta, L.; Calvo, E. G.; Bermúdez, J. M. Microwave Heating Processes Involving Carbon Materials. *Fuel Process. Technol.* **2010**, *91* (1), 1–8. https://doi.org/10.1016/j.fuproc.2009.08.021.

(343) Bo, Z.; Yan, J.; Li, X.; Chi, Y.; Cen, K. Plasma Assisted Dry Methane Reforming Using Gliding Arc Gas Discharge: Effect of Feed Gases Proportion. *Int. J. Hydrog. Energy* **2008**, *33* (20), 5545–5553. https://doi.org/10.1016/j.ijhydene.2008.05.101.

(344) Ranzi, E.; Sogaro, A.; Gaffuri, P.; Pennati, G.; Faravelli, T. A Wide Range Modeling Study of Methane Oxidation. *Combust. Sci. Technol.* **1994**, *96* (4–6), 279–325. https://doi.org/10.1080/00102209408935359.

(345) Lu, N.; Bao, X.; Jiang, N.; Shang, K.; Li, J.; Wu, Y. Non-Thermal Plasma-Assisted Catalytic Dry Reforming of Methane and Carbon Dioxide Over g-C_3N_4-Based Catalyst. *Top. Catal.* **2017**, *60* (12–14), 855–868. https://doi.org/10.1007/s11244-017-0750-z.

(346) Bin, D.; Xiu-ling, Z.; Wei-min, G.; Ren, H. Study on the Methane Coupling under Pulse Corona Plasma by Using CO_2 as Oxidant. *Plasma Sci. Technol.* **2000**, *2* (6), 577–580. https://doi.org/10.1088/1009-0630/2/6/011.

(347) Yao, S. L.; Ouyang, F.; Nakayama, A.; Suzuki, E.; Okumoto, M.; Mizuno, A. Oxidative Coupling and Reforming of Methane with Carbon Dioxide Using a High-Frequency Pulsed Plasma. *Energy Fuels* **2000**, *14* (4), 910–914. https://doi.org/10.1021/ef000016a.

(348) Zhang, J.-Q.; Zhang, J.-S.; Yang, Y.-J.; Liu, Q. Oxidative Coupling and Reforming of Methane with Carbon Dioxide Using a Pulsed Microwave Plasma under

Atmospheric Pressure. *Energy Fuels* **2003**, *17* (1), 54–59. https://doi.org/10.1021/ef020069n.

(349) Mei, D.; Zhang, P.; Duan, G.; Liu, S.; Zhou, Y.; Fang, Z.; Tu, X. CH4 Reforming with CO_2 Using a Nanosecond Pulsed Dielectric Barrier Discharge Plasma. *J. CO2 Util.* **2022**, *62*, 102073. https://doi.org/10.1016/j.jcou.2022.102073.

(350) Liu, J.; Xue, Z.; Zhang, Z.; Sun, B.; Zhu, A. Mechanism Study on Gliding Arc (GA) Plasma Reforming: Unraveling the Decisive Role of CH_4/CO_2 Ratio in the Dry Reforming Reaction. *Plasma Process. Polym.* **2022**. https://doi.org/10.1002/ppap.202200175.

(351) Liu, J.-L.; Park, H.-W.; Chung, W.-J.; Park, D.-W. High-Efficient Conversion of CO_2 in AC-Pulsed Tornado Gliding Arc Plasma. *Plasma Chem. Plasma Process.* **2016**, *36* (2), 437–449. https://doi.org/10.1007/s11090-015-9649-2.

(352) Van Alphen, S.; Slaets, J.; Ceulemans, S.; Aghaei, M.; Snyders, R.; Bogaerts, A. Effect of N_2 on CO_2-CH_4 Conversion in a Gliding Arc Plasmatron: Can This Major Component in Industrial Emissions Improve the Energy Efficiency? *J. CO2 Util.* **2021**, *54*, 101767. https://doi.org/10.1016/j.jcou.2021.101767.

(353) Wolf, A. J.; Peeters, F. J. J.; Groen, P. W. C.; Bongers, W. A.; van de Sanden, M. C. M. CO_2 Conversion in Nonuniform Discharges: Disentangling Dissociation and Recombination Mechanisms. *J. Phys. Chem. C* **2020**, *124* (31), 16806–16819. https://doi.org/10.1021/acs.jpcc.0c03637.

(354) Gutsol, A.; Bakken, J. A. A New Vortex Method of Plasma Insulation and Explanation of the Ranque Effect. *J. Phys. Appl. Phys.* **1998**, *31* (6), 704–711. https://doi.org/10.1088/0022-3727/31/6/018.

(355) Trenchev, G.; Kolev, S.; Bogaerts, A. A 3D Model of a Reverse Vortex Flow Gliding Arc Reactor. *Plasma Sources Sci. Technol.* **2016**, *25* (3), 035014. https://doi.org/10.1088/0963-0252/25/3/035014.

(356) Kalra, C. S.; Cho, Y. I.; Gutsol, A.; Fridman, A.; Rufael, T. S. Gliding Arc in Tornado Using a Reverse Vortex Flow. *Rev. Sci. Instrum.* **2005**, *76* (2), 025110. https://doi.org/10.1063/1.1854215.

(357) den Harder, N.; van den Bekerom, D. C. M.; Al, R. S.; Graswinckel, M. F.; Palomares, J. M.; Peeters, F. J. J.; Ponduri, S.; Minea, T.; Bongers, W. A.; van de Sanden, M. C. M.; van Rooij, G. J. Homogeneous CO_2 Conversion by Microwave Plasma: Wave Propagation and Diagnostics. *Plasma Process. Polym.* **2017**, *14* (6), 1600120. https://doi.org/10.1002/ppap.201600120.

(358) Zaidi, S. H.; Tang, Z.; Yalin, A. P.; Barker, P.; Miles, R. B. Filtered Thomson Scattering in an Argon Plasma. *AIAA J.* **2002**, *40* (6), 1087–1093. https://doi.org/10.2514/2.1756.

(359) Klarenaar, B. L. M.; Brehmer, F.; Welzel, S.; van der Meiden, H. J.; van de Sanden, M. C. M.; Engeln, R. Note: Rotational Raman Scattering on CO_2 Plasma Using a Volume Bragg Grating as a Notch Filter. *Rev. Sci. Instrum.* **2015**, *86* (4), 046106. https://doi.org/10.1063/1.4918730.

(360) Wang, H.; Frenklach, M. A Detailed Kinetic Modeling Study of Aromatics Formation in Laminar Premixed Acetylene and Ethylene Flames. *Combust. Flame* **1997**, *110* (1–2), 173–221. https://doi.org/10.1016/S0010-2180(97)00068-0.

(361) Martin, J. W.; Salamanca, M.; Kraft, M. Soot Inception: Carbonaceous Nanoparticle Formation in Flames. *Prog. Energy Combust. Sci.* **2022**, *88*, 100956. https://doi.org/10.1016/j.pecs.2021.100956.

(362) Devetyarov, R. R. The Formation of Soot on the Walls of the Diesel Combustion Chamber and Its Effect on Heat Transfer in the Cylinder. *IOP Conf. Ser. Mater. Sci. Eng.* **2020**, *862* (6), 062072. https://doi.org/10.1088/1757-899X/862/6/062072.

(363) Pourrezaei, M. H.; Malayeri, M. R.; Hooman, K. Thermal Performance and Mechanisms of Soot Deposition in Foam Structured Exhaust Gas Recirculation Coolers. *Int. J. Therm. Sci.* **2019**, *146*, 106108. https://doi.org/10.1016/j.ijthermalsci.2019.106108.

(364) Roquemore, W. M.; Katta, V.; Stouffer, S.; Belovich, V.; Pawlik, R.; Arstingstall, M.; Justinger, G.; Gord, J.; Lynch, A.; Zelina, J.; Roy, S. Soot Studies of Laminar Diffusion Flames with Recirculation Zones. *Proc. Combust. Inst.* **2009**, *32* (1), 729–736. https://doi.org/10.1016/j.proci.2008.06.104.

(365) Derkaoui, N.; Rond, C.; Hassouni, K.; Gicquel, A. Spectroscopic Analysis of H_2/CH_4 Microwave Plasma and Fast Growth Rate of Diamond Single Crystal. *J. Appl. Phys.* **2014**, *115* (23), 233301. https://doi.org/10.1063/1.4883955.

(366) Delikonstantis, E.; Scapinello, M.; Stefanidis, G. D. Low Energy Cost Conversion of Methane to Ethylene in a Hybrid Plasma-Catalytic Reactor System. *Fuel Process. Technol.* **2018**, *176*, 33–42. https://doi.org/10.1016/j.fuproc.2018.03.011.

Curriculum Vitae

Omar Biondo
Born on October 15, 1991, in Treviso, Italy

2012 – 2016	Bachelor Environment Science and Technology University of Padova (Italy)
2016 – 2018	Master Land and Environment Science and Technology University of Padova (Italy)
2018 – 2019	Pre-doctoral research fellowship University of Padova (Italy)
2019 - present	PhD student University of Antwerp & Eindhoven University of Technology

List of publications

Publications linked to this doctoral thesis

Insights into the limitations to vibrational excitation of CO_2: validation of a kinetic model with pulsed glow discharge experiments
O. Biondo, C. Fromentin, T. Silva, V. Guerra, G. van Rooij, A. Bogaerts
Plasma Sources Sci. Technol., 31, 074003 (2022)
https://doi.org/10.1088/1361-6595/ac8019

Carbon bed post-plasma to enhance the CO_2 conversion and remove O_2 from the product stream
O. Biondo*, F. Girard-Sahun*, G. Trenchev, G. van Rooij, A. Bogaerts
Chemical Engineering Journal 442, 136268 (2022)
https://doi.org/10.1016/j.cej.2022.136268
*Shared first author

Power concentration determined by thermodynamic properties in complex gas mixtures: the case of plasma based dry reforming of methane
O. Biondo, A. Hughes, A. van de Steeg, S. Maerivoet, B. Loenders, G. van Rooij, A. Bogaerts
Plasma Sources Sci. Technol. 32, 045001 (2023)
https://doi.org/10.1088/1361-6595/acc6ec

Flow pattern control avoids solid carbon deposition in plasma-based dry reforming of methane
O. Biondo, C. F. A. M. van Deursen, A. Hughes, A. van de Steeg, W. Bongers, M. C. M van de Sanden, G. van Rooij, A. Bogaerts
In preparation for submission to *Chemical Engineering Journal*

Meta-analysis of CO_2 conversion, energy efficiency and other performance data of plasma-catalysis reactors with the open access PIONEER database
A. Salden, M. Budde, C. A. Garcia-Soto, O. Biondo, J. Barauna, M. Faedda, B. Musig, C. Fromentin, M. Nguyen-Quang, H. Philpott, G. Hasrack, D. Aceto, Y. Cai, F. Azzolina Jury, A. Bogaerts, P. Da Costa, R. Engeln, M. E. Gálvez, T. Gans, T. Garcia, V. Guerra, C. Henriques, M. Motak, M. V. Navarro, V. I. Parvulescu, G. van Rooij, B. Samojeden, A. Sobota, P. Tosi, X. Tu, and O. Guaitella
Submitted to *Journal of Energy Chemistry* on May 22, 2023

Other publications

Study of vibrational kinetics of CO_2 and CO in CO_2–O_2 plasmas under non-equilibrium conditions
C. Fromentin, T. Silva, T. C. Dias, A. S. Morillo-Candas, O. Biondo, O. Guaitella, and V. Guerra
Plasma Sources Sci. Technol. 32, no. 2 (2023): 024001
https://doi.org/10.1088/1361-6595/acb665

Spectroscopic study of self-pulsing discharge with liquid electrode
G. Sretenović, M. Saleem, O. Biondo, G. Tomei, E. Marotta, C. Paradisi
Journal of Applied Physics 129, no. 18 (2021): 183308.
https://doi.org/10.1063/5.0044331

Comparative performance assessment of plasma reactors for the treatment of PFOA; reactor design, kinetics, mineralization and energy yield
M. Saleem, O. Biondo, G. Sretenović, G. Tomei, M. Magarotto, D. Pavarin, E. Marotta, C. Paradisi
Chemical Engineering Journal, 382, 123031 (2020)
https://doi.org/10.1016/j.cej.2019.123031

Air non-thermal plasma treatment of the herbicides mesotrione and metolachlor in water.
A. Giardina, F. Tampieri, O. Biondo, E. Marotta, C. Paradisi
Chemical Engineering Journal, 372, 171-180 (2019)
https://doi.org/10.1016/j.cej.2019.04.098

Kinetics and products of air plasma induced oxidation in water of imidacloprid and thiamethoxam treated individually and in mixture
F. Tampieri, A. Durighello, O. Biondo, M. Gąsior, A. Knyś, E. Marotta, C. Paradisi
Plasma Chemistry and Plasma Processing, 39, no. 3, 545-559 (2019)
https://doi.org/10.1007/s11090-019-09960-1

List of conference contributions

Invited talks

Workshop on Plasma Technology for CO_2 Reforming and *In-Situ* Resource Utilization, 19-20 Sep 2022, Lisbon
“Insights into the limitations to vibrational excitation of CO_2: validation of a kinetic model with pulsed glow discharge experiments”

Torino International Conference on Fundamental Plasma Physics, 21-23 June 2023, Torino
“Towards a fundamental understanding of energy-efficient, plasma-based CO_2 conversion”

Other conference/workshop contributions

International Symposium on Plasma Catalysis for CO_2 Recycling, 13-15 Sep. 2022, Krakow
Oral Presentation: “Insights into the limitations to vibrational excitation of CO_2: validation of a kinetic model with pulsed glow discharge experiments”

17th International Symposium on High Pressure Low Temperature Plasma Chemistry (HAKONE XVII), 21-25 Aug. 2022, Rolduc Abbey (NL)
Poster Presentation: “Gas Heating Dynamics in a CO_2 Pulsed Glow Discharge Resolved by Kinetic Modeling”

PlasmaTech 2022 (Plasma Processing and Technology International Conference), 27-29 Apr. 2022, Barcelona
Oral Presentation: “A modelling investigation of the mechanisms underlying the O/O_2 removal in the afterglow of a CO_2 plasma with a carbon bed”

ERC SCOPE Workshop, online, 31 Aug. 2021
Oral Presentation: "Validation of a CO_2 plasma 0D model with experiments”

Oral presentations at H2020-MSCA-ITN project meetings:

26 Nov. 2021, Sorbonne University, Paris
“Improving the energy efficiency of CO_2 conversion and activation in a microwave plasma by a combination of experiments and modeling”

12 Nov. 2021, TUe, Eindhoven (NL)
“Fundamentals and Mechanisms of CO_2 Plasmas”

2 Dec. 2020, online
“Improving the energy efficiency of CO_2 conversion and activation in a microwave plasma by a combination of experiments and modeling”

Earlier mobility

September ’12 – February ’18: I studied Land and Environment Science and Technology at the University of Padova, Italy, and obtained my bachelor (3 years) and master (2 years) degrees.

February ’18 – October ’19: I joined the group of Prof. Paradisi at the department of Chemistry, University of Padova, Italy, as a pre-doctoral researcher, where I worked on developing and testing plasma reactors for the decontamination of polluted water.

My PhD (November ’19 – May ’23) is a joint PhD between the University of Antwerp (Prof. Bogaerts, PLASMANT) and DIFFER (Prof. van Rooij), with continuous interactions concerning experiments on CO_2 and CH_4 conversion in a microwave discharge and with a secondment of 14 months in Eindhoven (Nov ‘20 – Dec ‘21), followed by several shorter visits for follow-up experiments.

September-October ’22: Research visit in the group of Prof. Guerra at IST Lisbon, Portugal, to strengthen our collaboration and work on the comparison between their chemical kinetic model for simulating CO_2 discharges and mine.